UNIVERSITY OF SOUTHAMPTON

EVOLUTION OF ARTIFICIAL SPACE DEBRIS CLOUDS

by Simon Barrows (B.Eng)

THESIS SUBMITTED FOR DEGREE OF
DOCTOR OF PHILOSOPHY

FACULTY OF ENGINEERING AND APPLIED SCIENCE
DEPARTMENT OF AERONAUTICS AND ASTRONAUTICS

MARCH 1996

It's the final frontier - the place to boldly go where no man has gone before. Well it used to be, anyway. These days space is looking more like the final dustbin, where too many men have been and left all their rubbish behind.

Daily Mirror, September 6, 1994.

UNIVERSITY OF SOUTHAMPTON

ABSTRACT

FACULTY OF ENGINEERING AND APPLIED SCIENCE

DEPARTMENT OF AERONAUTICS AND ASTRONAUTICS

Doctor of Philosophy

EVOLUTION OF ARTIFICIAL SPACE DEBRIS CLOUDS

by Simon Barrows (B.Eng)

Over 120 cases of on-orbit breakups have now been recorded. Many more undetected events are believed to have occurred. Each time an object breaks up, whether by explosion or collision, a cloud of debris is formed. The overall objective of the PhD is to examine the interaction between the debris clouds produced by on-orbit fragmentation events and specific space systems. A breakup event will give rise to concentrations of debris which, for some time after the event, will have spatial densities considerably higher than the background flux. Thus, a detailed knowledge of the extent to which the cloud will grow over a given time period, and an accurate assessment of the risk of collision for a spacecraft passing through it, may prove to be important in mission planning and satellite shielding design.

The SDS (Space Debris Simulation) software suite has been developed to carry out the analysis presented in this thesis and now represents the state-of-the-art in debris cloud modelling. The integrated structure of the developed software enables a wide variety of analyses to be conducted and simulations of both historic and potential future orbital fragmentation events to be performed. Program BREAKUP uses a combination of empirical and analytical models to simulate catastrophic and non-catastrophic collisions, and also variable intensity explosive fragmentations. Included in BREAKUP is a novel parametric model for producing and controlling non-isotropic fragment spreads. TRAJECTORY acts as a test-bed for orbit propagation techniques, providing the facility for convenient and direct method comparison. EVOLUTION enables the complex dynamics of debris cloud growth to be visualised and in particular the effects of propagation method to be examined. Program TARGET employs a novel implementation of the method of probabilistic continuum dynamics to perform collision hazard assessments for spacecraft which encounter debris clouds. Among the additional new developments included in TARGET are the consideration of atmospheric drag, a direct interface with a non-isotropic cloud model, the use of a cellular target spacecraft representation and impact energy-related damage assessment algorithm, and a built-in satellite constellation analysis facility. A number of case studies are presented to illustrate the modelling capabilities of the SDS software suite, including the simulation of several historic fragmentation events and the debris cloud collision risks to ENVISAT-1 and the Iridium^{TM} satellite constellation. The results produced by the models are validated by comparisons with other simulation software and, wherever possible, with actual breakup event, debris impact and spacecraft orbit data.

Contents

List of Tables

List of Figures

Acknowledgements

First of all, a big thank you to Graham for his constant guidance and support over the last three years and for his rapid but diligent proof-reading of the thesis over the last few weeks and months.

Thanks also to Adrian and Walter, my internal and external examiners, whose valuable comments have helped add the finishing polish to the thesis.

Thank you to all the members of academic staff who have endeavoured to fill me with knowledge over the course of my university career and to all the secretarial, administrative and support staff who have helped make life just that little bit easier.

Thank you to my colleagues and friends in the department, both past and present, who have provided an enjoyable and stimulating working environment.

Thanks to the Particle Physics and Astronomy Research Council, the now defunct Science and Engineering Research Council and the British National Space Centre for funding the research. A special thanks to Richard at the DRA for his continued support of the work, in both an advisory and financial sense. Thanks also to my colleagues and friends at DRA Farnborough for making me feel at home over the last few months.

Thank you to everyone who has helped me enjoy life outside work, in particular to Wilma for being such a special friend.

And finally to my parents, without whom none of this would ever have happened. For their unrelenting love and encouragement over the last 26 plus years, I dedicate this thesis to them.

Chapter 1

Introduction

1.1 Background

Since the 'Space Age' began man has continued to pollute the orbital environment. As with other natural Earth resources such as the oceans, the rainforests and fossil fuels, man's combination of a systematic disregard for, and a convenient ignorance of the consequences of his actions has resulted in an unfortunate legacy for future space users. It is only in the last decade or so that the international spacefaring community has begun to recognise the seriousness of the problem.

Following the launch of Sputnik 1 in 1957, the number of objects in orbit has grown steadily (Figure 1.1) [1]. Over 7600 Earth-orbiting objects currently reside in the U.S. Space Command 'official' catalogue [2]. Space debris now represents a significant hazard to future space operations with around 94% of the catalogued population being debris objects [3, 4], having total mass of around 3000 tons [3, 4, 5].

1.1.1 Sources of Space Debris

Space debris can be defined as 'those man-made objects in outer space deemed to be valueless, as evidenced by a lack of operational control' [6]. A more rigorous definition is 'any man-made Earth-orbiting object which is non-functional with no reasonable expectation of assuming or resuming its intended function or any other function for which it is or can be expected to be authorised, including fragments

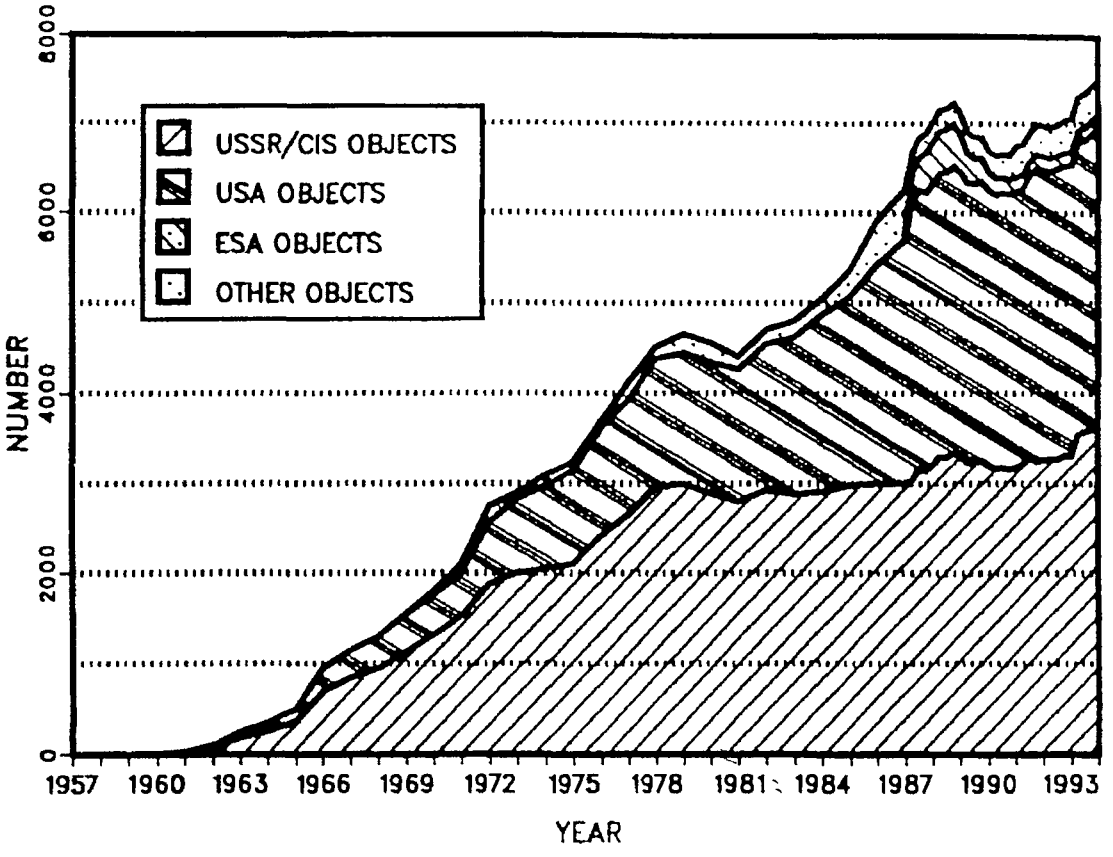

Figure 1.1: Time-history of the catalogued population [1]

and parts thereof' [7]. These definitions encompass the four main sources of space debris, namely inactive payloads, operational debris, fragmentation debris and microparticulate matter. Inactive payloads are those formerly active payloads which can no longer be controlled by their operators. Over 1000 inactive payloads are currently in orbit [4]. Most of these are spent satellites. Operational debris are those objects associated with space activities, which remain in outer space. Most of these objects fall into the category of launch hardware and include rocket bodies, apogee kick motors, satellite fairings and release mechanisms. Also included are items of space trash as jettisoned by both American astronauts and Soviet cosmonauts and various 'odds and ends' ranging from an astronaut's glove to one of the Hubble Space Telescope (HST) solar arrays. Fragmentation debris is produced when space objects breakup up as a result of explosions, collisions or possibly other unknown phenomena. Fragmentation debris accounts for nearly half of all catalogued space

objects [4]. Explosions may be deliberate, to prevent recovery or as part of anti-satellite (ASAT) weapons testing for example, or accidental. Accidental explosions have generally occurred as a result of a propulsion system failure, with 'dead' rocket bodies (e.g. Delta 2nd stage, Ariane V16 3rd stage) containing fuel residuals being historically the worst culprits. Apart from the P-78 (Solwind) U.S. ASAT test in 1985, there have been no fragmentations to date which can be irrefutably classified as being collision-induced. A number of events are suspected of being so, however, most famously the breakup of Cosmos 1275 [8]. Even though the evidence to support the collision theory is very strong in some cases, these events are generally pigeon-holed in the 'unknown' category. The cause of around 40% of the 120 plus recorded on-orbit breakups remains unknown [4]. Microparticulate particles are thought to number somewhere in the billions to trillions and are typically in the μm size range. Such particles are generally produced by exhaust plumes and nozzle erosion from solid-propellant rocket motors (SRMs) and also spacecraft surface degradation, due to radiation exposure, thermal cycling and atomic oxygen erosion. Hypervelocity impacts can also produce very small debris particles.

Disregarding objects beyond geostationary Earth orbit (GEO), space debris is primarily located in three regions of space: low Earth orbit (LEO), geostationary transfer orbit (GTO) and GEO. LEO can be considered as being a spherical shell, bounded below by the Earth's atmosphere at around 200km altitude and above by more-intense regions of the Van Allen radiation belts at around 4000km altitude. LEO is the most densely populated region of space, housing a variety of commercial and military satellites. It is also the region in which manned space activities take place, e.g. shuttle flights, space stations. Approximately two thirds of debris is in LEO (three quarters of that below 2000km) [3], mostly in near-circular orbits [4, 9]. Concentrations of debris exist around the 900-1000km and 1400-1500km [4, 10] altitude bands due to fragmentations close to these altitudes and the lack of orbital 'cleansing' from atmospheric decay (Figure 1.2) [1]. Models of the debris population and its long-term evolution [11, 12, 13, 14, 15] indicate that these regions (the 900-1000km band in particular) may already be unstable. Once a critical density of

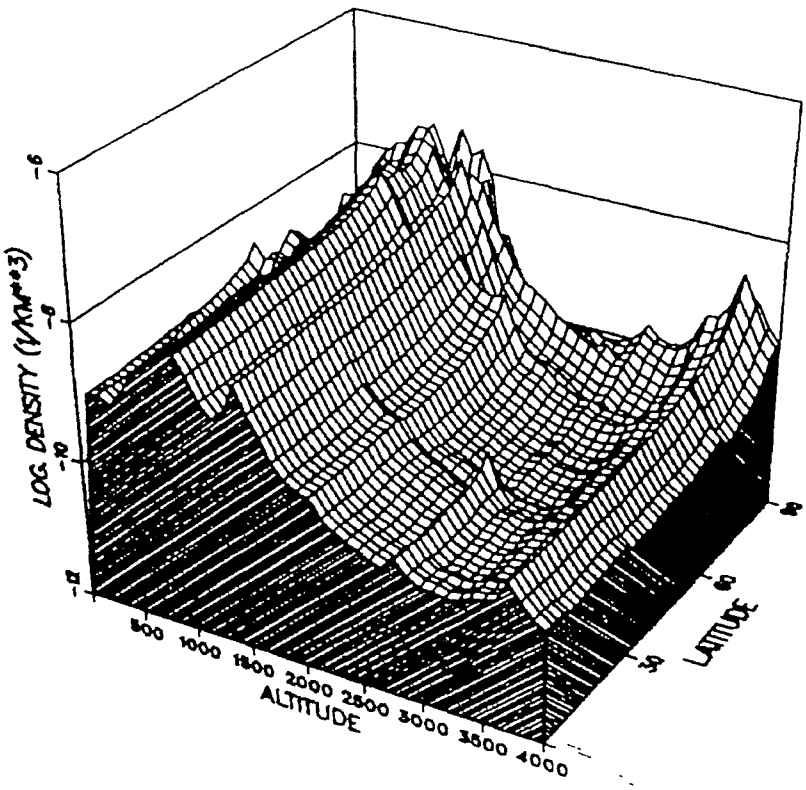

Figure 1.2: Spatial density of debris vs altitude and latitude [1]

objects is reached, the rate of fragment generation from collisions will exceed the rate of removal by atmospheric drag. Hence a 'chain reaction' or 'collisional cascade' will occur and the debris population will increase even if no more objects are placed in orbit. This would render much of near-Earth space unusable. The occurrence and speed of propagation of such a cascade is found to be dependent on the number of 'large' objects in orbit, e.g. satellites, rocket bodies, and their location, since the most likely type of on-orbit collision is 'target-projectile' [11]. This type of collision corresponds to a larger 'target' object being hit by a much smaller piece of debris. Thus the likelihood of a cascade occurring would be reduced by limiting the number of objects left in orbit (e.g. by de-orbiting spent stages/satellites, revising launch practices), placing satellites in less crowded orbital regions and ideally removing existing large items of debris [7, 12, 16, 17].

GTOs are highly elliptical orbits (eccentricity around 0.73) which link low alti-

tude orbits (200-300 km altitude) with GEO. They can be considered to be utility orbits since they do not contain operational spacecraft, but the debris in GTO is important as it interacts with spacecraft in both LEO and GEO. The interactions with LEO spacecraft occur at high relative velocities and on the spacecraft surfaces which are generally the least protected ('trailing' or 'anti-flight' faces) [9, 18]. The lifetimes of objects in GTO can vary enormously (a few months to hundreds of years) and are influenced by atmospheric drag, the Earth's asphericity and luni-solar effects. Current launch practices often lead to rocket upper stages being left in transfer orbits with extremely long lifetimes but through judicious choice of orbital parameters the lifetimes of these objects, and hence any debris they create, can be drastically reduced [9, 19, 20].

GEO is a member of the family of geosynchronous orbits (orbits with a period of rotation equal to that of the Earth). Objects in GEO (approximately 35787 km above the equator) appear to be stationary from the ground. The advantage of such an orbit is that GEO spacecraft have a constant view of a large area of the Earth and are easily tracked with a fixed ground antenna. This has made GEO a very popular operational orbit for a variety of space activities and some orbital regions are already overcrowded. In practice, however, perturbations from the non-spherical shape of the Earth, the gravitational attractions of the Sun and the Moon and solar radiation pressure cause periodic variations in the altitude and inclination of the orbit. To counteract these perturbations, active payloads such as telecommunications satellites must periodically perform station-keeping manoeuvres to remain close to their nominal orbital positions. Inactive payloads and items of space debris are, however, not controlled and hence their orbits are free to be perturbed by the various forces acting [21, 22]. These perturbed orbits cross GEO and so pose a collisional hazard to active payloads, although the relative velocities for such encounters in GEO are typically much less than those in LEO. Supersynchronous 'parking' or 'graveyard' orbits can be employed to remove spent satellites from the GEO region at a cost to the operator but not only is the minimum 'safe' height above GEO a matter of some debate, but also any debris caused by fragmentations in these orbits could still

encroach upon GEO [20, 23, 24].

1.1.2 The Hazards of Space Debris

Debris detection

The space debris environment is not completely defined. The primary source of information on the numbers, sizes and orbits of space debris is the worldwide Space Surveillance Network (SSN) operated by the U.S.-Canadian North American Aerospace Defense Command (NORAD). The SSN was not designed and built with a debris-tracking capability in mind, however, but instead to act as an early-warning defence system. Attempting to track all debris accurately would not only be technically unfeasible (sensor limitations, resource saturation) but would also compromise the primary objectives of the network. The SSN consists of a combination of radars and optical sensing systems and can provide reliable sensing of objects greater than 1m in diameter up to geosynchronous orbit and as small as 8cm at very low altitudes (Figure 1.3, redrawn from [10]). Many of the SSN sensors can operate at a significantly greater resolution than this 'overall' limit but no object can be catalogued unless two or more sensors can reliably track it. The network sensitivity is consequently somewhat less than that of the best sensor in the system.

Large items of space debris have re-entered the Earth's atmosphere and hence posed a small but well publicised threat to people and resources 'on the ground'. The most notable examples have undoubtedly been the re-entries of Skylab (raining debris over Australia) and Cosmos 954 (peppering part of north-west Canada with radioactive fragments) in the late 1970s [25]. These incidents served to increase governmental and public awareness of the dangers of space junk. The greatest hazard posed by space debris, however, is not its re-entry into the atmosphere but its interaction with other 'active' objects in space. From Figure 1.3 it can be seen that objects smaller than about 8cm in diameter cannot be reliably tracked by NORAD at any altitude. Particles of this size are large enough, however, to cause serious or even catastrophic damage to a satellite in a collision. Collision velocities for objects in LEO are on average around 10 km/s [25, 26, 27, 28] and theoretically can be as

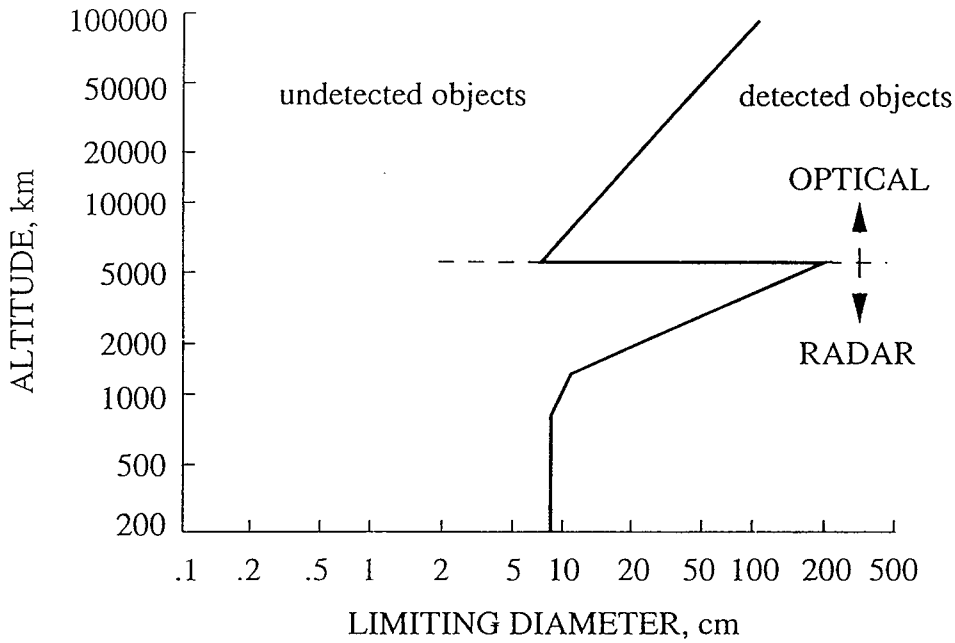

Figure 1.3: Overall sensitivity of the NORAD Space Surveillance Network

high as twice orbital velocity, i.e. around 15 km/s. At these enormous speeds, a piece of debris can possess more destructive power (in the form of kinetic energy) than ten times its equivalent mass in T.N.T. [7]. Herein lies the major hazard of space debris. Large, catalogued objects can (in theory at least) be tracked and avoided and are also relatively few in number. Enormous numbers of small particles exist but these can generally be guarded against by shielding and appropriate spacecraft design (the largest fragment that can be shielded against is thought to be around 1cm in diameter [4, 26]). Debris in the 1-8 cm-size range cannot be reliably tracked or detected and due to spacecraft mass constraints cannot realistically be shielded against. Large numbers of such fragments are thought to exist, possibly several times the catalogued population [4, 10, 15, 29]. The risk to operational spacecraft is dependent on orbit altitude and inclination, spacecraft characteristics and the epoch in question. The probability that a satellite will be hit by a trackable piece of debris in LEO is thought to be less than 0.01% per year [7, 28, 30] but as spacecraft get larger, operational lifetimes increase and the debris environment worsens, so the collision hazard will grow. Collision probabilities in GEO are considerably less than those in LEO due to the smaller numbers of objects and lower relative velocities

involved. The current hazard in GEO is almost certainly underestimated, however, due to the inability to detect objects smaller than around 1m in diameter.

Meteoritic debris

Spacecraft were originally designed to operate in an environment where the primary threat of collisional damage came from meteoroids. These are natural particles which typically range in size from a fraction of a micron to several millimetres in diameter. Meteoroids are in heliocentric orbits and encounter the Earth as a consequence of the intersection of the meteoritic orbits with that of the Earth. They can often be seen as 'shooting stars' in the night sky and the level of meteor activity varies with the time of year as the Earth revolves around the sun. Meteors cross the paths of Earth-orbiting spacecraft at very high speeds, on average around 20km/s [7, 26] (i.e. double the average LEO collision velocity), but have a much lower density than man-made objects (around 0.5g/cm^3 compared with 2.8g/cm^3 for aluminium alloys) [7, 26]. However they are only transient with respect to near-Earth space. Early space activities discovered that the threat from meteors was much less than originally predicted [25] and could be countered with a minimal amount of shielding and appropriate design practices. Artificial orbital debris now markedly exceeds the meteor population for objects larger than 1 mm [5, 7, 26] (Figure 1.4, redrawn from [5]) and as a result is now considered the design environment for manned and unmanned space systems. It is worth noting however that although the threat from natural particles may still dominate in GEO [5] and under 'storm' conditions meteor streams (e.g. Leonid, Perseid) can pose short-lived hazards many times the 'background' debris level [31, 32, 33]. In fact one of the major threats to the survivability of space platforms/stations over time-scales of the order of decades may be the occurrence of meteor storms. The 1993 Perseid outburst caused evasive manoeuvres to be taken by the HST (oriented so as to present the minimum cross-sectional area to the stream), delay of the Discovery STS-51 launch, audible impacts on the Mir-1 space station (with over 2000 impacts recorded for the 24 hours centred about the Perseid maximum) and the probable mission-terminating damage to the

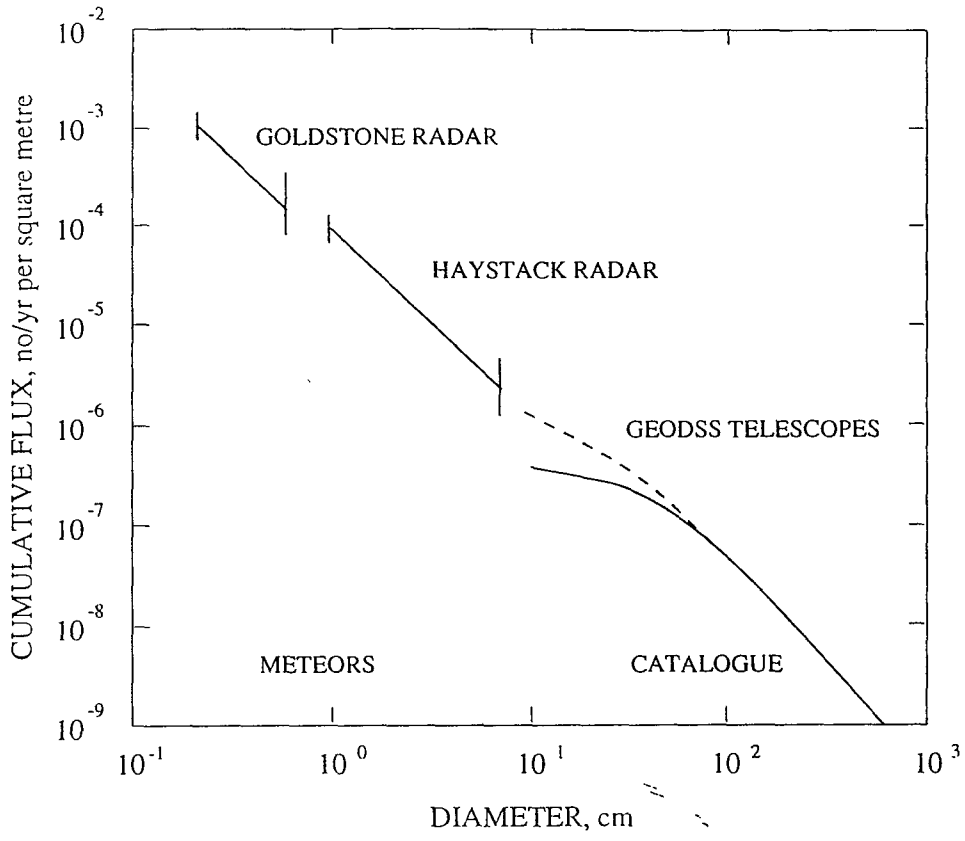

Figure 1.4: Meteoroid environment compared to recent measurements of the orbital debris environment

ESA Olympus satellite. The most likely meteor stream to undergo storm activity during the next 6 years is the Leonids [33].

Evidence from retrieved spacecraft surfaces

Objects returned from space highlight the severity of the combined debris and meteor environment. Most notably these have included NASA's Long Duration Exposure Facility (LDEF), the EUropean REtrievable CArrier (EURECA) and the HST solar array. Returned spacecraft surfaces can be used to analyse the meteor and debris populations and to validate/refine environment models.

LDEF provided, by virtue of an unprecedented area-time product and gravity-gradient stabilisation, a unique study base for identifying debris and meteor flux components. Meteoroids were found to be dominant for particles around 5 microns and greater in dimension, but debris was prevalent for smaller sizes. Also, impact

geometries indicated a clear link between the microparticles encountered and Molniya orbits [34]. Over 30000 craters were discovered on the spacecraft as a whole, ranging from less than a micron to 5mm in size [3, 35]. The East (ram), North and South faces received the majority of the impacts [36], with the ram side dominating the 'lee' side by around a factor of 10 [35, 37] (Figure 1.5, from [37]). Simulations [18, 38] have shown that debris in elliptical orbits are capable of encountering the rear faces of spacecraft such as LDEF. Impact crater chemical analysis suggests that around 10-15% of the impacts on the rear surfaces were caused by orbital debris and probably around double this on the front and side surfaces [5, 39]. The percentage of debris impacting the trailing and 'end' surfaces is much greater than originally predicted, indicating the presence of significant amounts (possibly as much as 30 times the level expected [35]) of debris in highly elliptical, low inclination, orbits [40]. Generally, however, both the meteor and debris fluxes derived from LDEF crater data showed reasonable agreement with model predictions [39, 41].

Data from the EURECA spacecraft supports the LDEF-derived fluxes. EURECA's attitude was sun-pointing and its impact record was found to lie between the LDEF maximum (ram face) and minimum (trailing face) accordingly [42]. Over 1000 impacts were recorded on the EURECA and HST arrays which are visible to the naked eye (the largest craters being in the 0.5-1 cm size range) but there was no functional failure on either EURECA or the Hubble array which can be related to an impact [43]. The impact records of LDEF, EURECA and the HST array suggest that the debris and micrometeor environment is unlikely to cause catastrophic failures on Space Station Alpha, but over the course of its lifetime the station will be hit repeatedly and most likely suffer a number of 'small' failures [35]. The measured crater flux from a French debris/meteor experiment deployed outside the Russian MIR space station was found to be higher than expected when compared with that determined from LDEF, however, even taking into account the differences in orbital altitude and inclination between the two spacecraft. It is possible, therefore, that the environment of a permanently manned space station is populated by a large number of short-lived debris, giving an increase in the debris flux experienced above

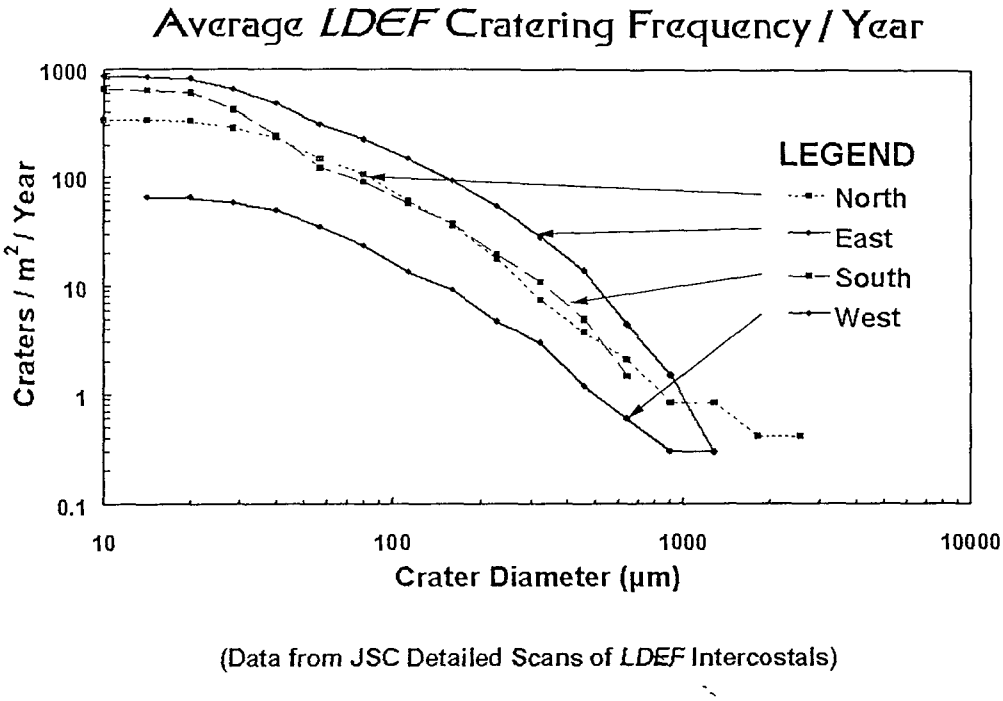

Figure 1.5: LDEF intercostal impact frequency averaged over each of the four primary row directions

the background level [42]. It has also been suggested that the greatest collision risk to Alpha is itself, or more precisely debris created by construction/servicing craft in similar orbits [44].

The LDEF Interplanetary Dust Experiment (IDE) [45] provided a unique spatio-temporal insight into the fluxes of both orbital debris and micrometeoroids, with nearly a year's worth of data being obtained. One of the major findings of the experiment was the discovery of debris in the form of orbiting clouds of micron-sized particles. Most of the 15000 impacts recorded were associated with debris 'swarms', the events occurring at the same place each orbit for a number of successive orbits. The episodic nature of the impacts indicates that the particles were almost certainly man-made (e.g. from SRM burns, spacecraft surface erosion). The highest impact fluxes recorded were thousands of times higher than the background level [36]. This

obviously has serious implications on models which assume that the debris environment is relatively isotropic. The results of IDE experiment are discussed in more detail in Chapter 6.

The U.S. space shuttle

The space shuttle has been both a creator and a victim of space debris. For example, the first 8.2 days of data from the IDE experiment had to be discarded due to contamination from the shuttle (Challenger) which placed LDEF into orbit. This period (2.4% of the experiment duration) produced 36% of the total number of hits recorded on the Earth face low sensitivity detectors, 14% on the West face and 9% on the Space face [45]. Orbital debris, however, has been found to be the cause of the majority of the pits found in the STS outer windows and is responsible for nearly 90% of the 50 plus windows that have required replacement since the shuttle program began in 1981 (the most celebrated case of a debris impact being the STS-7 paint-fleck in 1984) [25, 46]. Shuttle operational practices (Flight Rule 2-77) specify that the orbiter adopt the 'safest' orientation (tail forwards and cargo bay towards Earth) wherever possible, as long as mission objectives are not compromised. Similarly, avoidance manoeuvres are only carried out if objects are projected to encroach into or close to the shuttle's 5x2x2km 'manoeuvre box' (5km in the along-track dimension, 2km in the radial and normal directions), the collision risk is diminished by the manoeuvre (i.e. the probability of moving out of the way of the object is greater than the chance of actually moving into its path through imprecise knowledge of its orbit, or alternatively moving into the path of another object) and mission objectives are not severely affected. Two such encounters occurred in relatively rapid succession in 1991 when Atlantis 'dodged' a 1 tonne plus object on November 19, just three months after Discovery manoeuvred to avoid the Cosmos 955 rocket body. This was the first time that an orbital debris avoidance manoeuvre was performed in the history of spaceflight [25].

Space station Alpha

The increasing hazard of orbital debris means that the policy of disregarding the possibility of a severely damaging or even catastrophic collision is unacceptable for Space Station Alpha. Alpha will be much larger than the shuttle (bigger target), be in-orbit for much longer (larger cumulative debris flux) and also be less able to 'move out of the way' of an on-coming object in the time available (more warning needed). These factors make the collision avoidance problem for the proposed space station quite different from that of the orbiter. An on-board passive optical/IR sensor [47], used in conjunction with an active radar to filter out false alarms (otherwise 'switched off' to save on power), could only provide a few minutes warning of an impending collision. This would only give enough time for the crew to carry out a few emergency procedures to minimise collision damage and risk to life before the potential impact. Another problem would be the number of false alarms that could be registered if the manoeuvre box was set too large. Space station activities will tend to be complex with experiments possibly taking hours to activate/deactivate and extravehicular activity (EVA) and free flyer outings causing long collision-preparation times. The use of a multi-'alert level' safety procedure and carefully chosen 'acceptable-danger' criteria would help to reduce the number of expected manoeuvres to a reasonable level. Improved object detectability technology (both ground and in-orbit) would reduce the number of manoeuvres required and, of course, improve overall mission safety [48]. As stated at the beginning of this section, however, a 'data-gap' currently exists where potentially 'lethal' debris cannot be reliably tracked. It is in this area where modelling of the debris environment is most germane and indeed provides the only real estimates of the collision hazard for spacecraft with these dangerous and extremely numerous 'mid-size' pieces of debris. As fragmentation events are the dominant source for the production of this type of debris, the modelling of on-orbit breakup events, and the risk they pose to existing and future spacecraft, is of vital importance in assessing the hazards to both manned and unmanned space resources.

1.2 Project Description

1.2.1 Project Overview

The funding for the work described in this thesis was initially provided by the BNSC (British National Space Centre) and channeled into a CASE (Cooperative Award in Science and Engineering) PhD project by the DRA (Defence Research Agency) at Farnborough. The main aims of the CASE scheme are to help forge a stronger link between industry and academia, allowing industry to play a driving role in certain key areas of university research and providing students with experience outside the academic environment. The technical objectives of this PhD were, therefore, primarily set out by the needs of the sponsor, the DRA, with the direct usefulness and relevance of the work to the space industry being a major concern. Fortunately, the potentially conflicting interests of the sponsors needs and the PhD's demands for originality of work have been met together through the development of state-of-the-art simulation software. The software produced complements the DRA's existing and developing capabilties and has been written with the requirements of satellite designers and operators firmly in mind. Included in the software are a number of novel developments which also make the work eminently suitable for PhD consideration. The software is as applicable for pure scientific research as it is for the performance of industrially-focussed case studies.

1.2.2 Technical Objectives

The overall objective of the PhD is to examine the interaction between the debris cloud produced by an on-orbit fragmentation event (e.g. a hypervelocity collision or explosion) and specific orbiting space systems (satellites, satellite constellations, space stations). Such a breakup event will give rise to concentrations of debris which, for some time after the event, will have spatial densities considerably higher (possibly by orders of magnitude) than the background flux. Thus, a detailed knowledge of the extent to which the cloud will grow over a given time period, and an accurate assessment of the risk of collision for a spacecraft passing through it, are important

for mission planning and satellite shielding design. Current shielding strategies generally tend to focus on the satellite's ram face, where the majority of debris impacts will normally be registered, and consider only the background debris flux. Quantifying the additional collision risk from debris clouds will help to either support existing spacecraft protection methodologies or show the need for revisions in current practices.

Modelling the evolution of a space debris cloud and the collision risk associated with it is essentially a two-stage process. First of all there is the necessity to simulate the fragmentation event itself. This takes the form of a quantitative description of the event with regard to the distributions of fragments produced and the processing of these distributions to yield a set of parameters which describe the breakup in a form which can serve as input to the second stage of the overall simulation. On receipt of the output from the fragmentation model, the debris cloud propagator can then evolve the cloud forward in time and the desired analysis on the spread of fragments produced can be performed. This analysis may take the form of an investigation into the size, shape and general behaviour of the cloud itself or alternatively may concentrate on the cloud's interaction and possible collision with other orbiting objects.

1.2.3 Software Development

Simulation software has been developed and written, from scratch, to implement both the existing models used and the new ones developed. The SDS (Space Debris Simulation) software suite consists of four main Fortran 77 programs (Figure 1.6), a shared library of 'calculation' modules and a Matlab-based graphical interface with numerous customised data-processing and plotting routines. The integrated structure of the software developed enables a wide variety of analyses to be conducted and simulations of both historic and potential future orbital fragmentation events to be performed. Program BREAKUP uses a combination of empirical and analytical models to simulate catastrophic and non-catastrophic collisions, and also variable intensity explosive fragmentations. Included in BREAKUP is a novel parametric

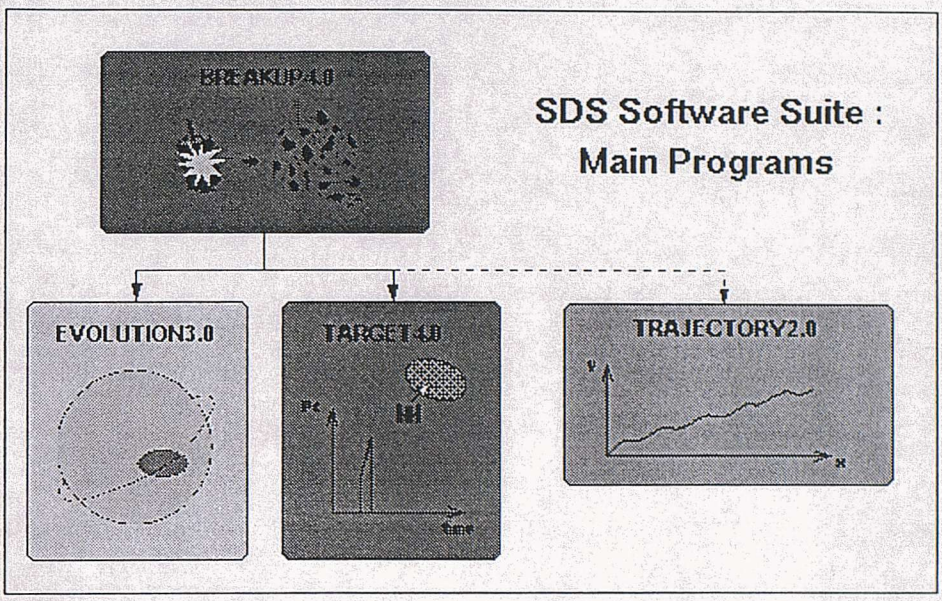

Figure 1.6: SDS software suite

model for producing and controlling non-isotropic fragment spreads. TRAJECTORY acts as a test-bed for orbit propagation techniques, providing the facility for convenient and direct method comparison. EVOLUTION enables the complex dynamics of debris growth to be visualised and in particular the effects of propagation method to be examined. Program TARGET employs a novel implementation of the method of probabilistic continuum dynamics to perform collision hazard assessments for spacecraft which encounter debris clouds. Among the additional new developments available for use in TARGET are the consideration of atmospheric drag, a direct interface with a non-isotropic cloud model, the use of a cellular target spacecraft representation and impact energy-related damage assessment algorithm, and a built-in satellite constellation analysis facility.

The SDS suite constitutes a fully-integrated software package, orginally written to operate in X-Windows on the Sun Sparc workstation cluster in the Department of Aeronautics and Astronautics at the University of Southampton. The software has also been installed at the DRA in Farnborough and has been fully documented according to the retrospective application of the DRA's Informal Software Procedure, which is based upon a derivative of ESA PSS-05 Software Engineering Stan-

dards [49]. The modelling capabilities of the SDS software suite are illustrated and tested through the use of several case studies, including the simulation of several historic fragmentation events and the debris cloud collision risks to ENVISAT-1 and the Iridium^{TM} satellite constellation. The results produced by the software are validated by comparisons with other simulation software and, wherever possible, with actual breakup event, debris impact and object orbit data.

1.3 Thesis Structure

The structure of the thesis follows a logical progression through the various stages of the overall modelling approach and the software developed. Chapter 2 sets the scene for the remainder of the thesis by reviewing the current state-of-the-art in debris cloud modelling, looking at both the simulation of the breakup event and the subsequent evolution of the fragments produced. The various techniques employed to calculate collision probabilities for spacecraft encountering the cloud are also discussed.

Chapter 3 describes the models used to simulate an on-orbit fragmentation event and how these models are implemented into program BREAKUP. The different breakup scenarios are discussed and compared, and the different methods employed to generate a debris cloud from the fragment distributions produced are outlined. Particular attention is given to BREAKUP's novel parametric technique for creating a non-isotropic spread of fragments. Program BREAKUP is then used to simulate a number of actual documented fragmentation events for results validation and to 'showcase' the new non-isotropic cloud model.

Chapter 4 examines a variety of orbit propagation techniques applicable to fragment trajectory calculation. These include two linearised relative motion methods, Keplerian propagation, Keplerian propagation with the analytical addition of perturbation effects and numerical integration. The implementation of these methods, along with a novel second-order state transition matrix method, into program TRAJECTORY creates a unique orbit propagation comparison and analysis facility,

which also serves as a test-bed for the techniques employed in EVOLUTION and TARGET. TRAJECTORY is used to compare the various methods installed for a number of test cases and results validation is conducted through the simulation of actual satellite orbits.

Chapter 5 considers the evolution of a debris cloud under a number of the propagation techniques described in Chapter 4. The implementation of these methods into program EVOLUTION is described and the dynamics of debris cloud growth are analysed, with particular attention given to the cloud's regions of high debris density and the effects of orbital perturbations. The results from EVOLUTION are validated by the comparison of cloud shapes with those generated by another code for a test example and through the coupling of EVOLUTION with the BREAKUP non-isotropic cloud model to produce 'decayed' Gabbard diagrams for actual fragmentation events.

Chapter 6 focuses on the collision hazard the debris cloud poses to spacecraft which fly through it. The novel implementation of the probabilistic continuum dynamics method of collision probability calculation used in program TARGET is described in some detail, as is TARGET's unique 'building-block' spacecraft representation and method of collision damage assessment. Single and multi-target (i.e. satellite constellation) case studies are utilised to illustrate the program's capabilities and assess current spacecraft protective design practices in the context of a debris cloud encounter. Results from other computer codes and data from the LDEF IDE experiment are used for results comparison/validation.

Chapter 7 concludes the main body of the thesis by discussing the results of the work carried out, in particular the novel developments made in breakup modelling and collision hazard assessment. Recommendations for future areas of study/follow-on work are also made.

In the Appendix, the equations of relative motion between a piece of debris and the path of the centre of mass (CM) of the parent object are derived.

Chapter 2

Review of Debris Cloud Modelling Techniques

2.1 Breakup Modelling

2.1.1 Introduction

On-orbit fragmentation events fall into two main categories, explosions and hypervelocity collisions, both of which lead to a number of possible scenarios. Historically, explosive breakups have been the dominant source of fragmentation debris. Explosions can be physical (e.g. a pressure burst), chemical (e.g. battery or propellant related) or even nuclear [50]. Also, a chemical explosion may be high or low-intensity in nature, depending upon how the explosive 'charge' is coupled to the spacecraft structure [51]. The most common type of explosive breakup has been the low-intensity fragmentation of 'dead' rocket bodies, most notably the Delta second stages in the 1970s and more recently the fourth stages of the Russian Proton launch vehicle. The cause of both these event families is thought to be the same, namely hypergolic ignition of residual propellants due to bulkhead failure, probably caused by thermal (i.e. solar) stressing [52]. The fragmentation of the SPOT-1 Ariane V16 third stage in 1986 was a particularly pollutive event, producing nearly 500 trackable fragments [53]. Overpressurization of the rocket body from residual propellants is thought to have been the cause of the breakup. Evidence indicates that other Ariane third stages may have also broken up, the effects being masked by difficult-

to-observe low inclination orbits. In the case of Ariane V16, a hypervelocity collision cannot be completely ruled out, however. A close conjunction between the Cosmos 1680 rocket body and the SPOT-1 Ariane third stage occurred at about the time of the breakup of the Ariane rocket body. Even accounting for orbit propagation errors, it was found that a collision between the two rocket bodies could not have taken place, but there is the possibility that the Ariane stage encountered a piece of debris that was 'accompanying' the Cosmos rocket [54].

To date, there have been no accidental collision-induced fragmentations officially recorded, although the Cosmos 1275 breakup is thought to have possibly been caused by a debris impact [8] and was even briefly classified as such [2]. Determining the cause, location and time of a suspected fragmentation event is generally far from easy. A number of different methods have been proposed for event classification, including methods based upon the optical properties (e.g. albedo) of the debris produced [55], the radar cross-sections (RCS) and area to mass distributions, debris plane change angles and ejection velocity direction distributions [56], and the SAFE (Satellite Fragmentation Event) Tests which examine the debris mass distributions and velocity spreads using weighted 'Gabbard' diagrams [8, 51]. One of the major difficulties of the task is that the greatest difference between the fragment distributions produced by each type of event lies with the very small particles. These particles cannot generally be detected, however, and the trackable fragments do not tend to display a distinctive event-characterising collision or explosion 'signature'. For this reason, a reliable autonomous classification technique has yet to be developed. Pinpointing the location and time of a fragmentation event is also fraught with uncertainties. Errors in orbit determination and propagation mean that even if a cloud of fragments produced by a breakup can successfully be identified, in practice they can never be back-propagated to a single point. If the state vectors of each fragment are simultaneously back dated then the coincidental peaking of different positional difference functions can be used to establish the time of the breakup. The pseudo time-independent method of Dasenbrock et al [57] uses the intersections of the debris orbits with the breakup plane to determine the location

of the fragmentation. In practice, this method is complicated by the effects of orbit perturbations, in particular Earth oblateness effects, and also by the poor definitions of nodal positions due to the relatively small changes in orbit inclination that are produced.

2.1.2 Types of Breakup Model

In general, breakup models can be organised into three families - complex, semi-analytic and empirical. Complex models are based on fundamental physical principles and include hydrodynamic (hydro) codes and structural response programs [58, 59]. Semi-analytic (or semi-empirical) models are developed from theoretical expressions but are normally calibrated through the use of experimental data. These models have a rigorous physics base and can generally be applied to a wide range of breakup scenarios. Empirical models are primarily derived from the curve fitting of data from impact/explosion experiments with some incorporation of analytic expressions. They tend to be based on limited data and are only tenuously based on fundamental physics. They are normally by far the simplest models to use, however, requiring only a few input parameters and negligible computation time. For these reasons, they are the most commonly used for both debris cloud and environment modelling.

The breakup models used and discussed in the remainder of this section will all be of the third of the above three types, i.e. empirical. As stated, these are by far the simplest to use and implement computationally and because of their rapid execution are the most appropriate for both debris cloud and environment modelling.

2.1.3 Fragment Distributions

The cloud of debris produced by a breakup event constitutes the initial conditions (IC) for both short and long-term hazard assessments. The key parameters of the breakup IC are velocity, mass, number and ballistic coefficient distributions. The velocity distribution of the cloud determines its time/spatial evolution whereas the

mass relationship prescribes the 'lethality' of a future impact, i.e. the degree of damage a fragment is likely to cause. The ballistic coefficient distribution has a secondary effect on both the cloud's evolution under the influence of atmospheric drag and the lethality of the fragments [60].

As the physical processes involved in explosions and hypervelocity collisions are so different, each must be modelled separately regarding the ejection velocities and numbers of fragments produced. Collision-induced breakups produce enormous numbers of small debris particles but explosive fragmentations are more effective at producing and dispersing trackable fragments than hypervelocity collisions with equivalent breakup (i.e. kinetic) energy [50]. Relating mass and ballistic coefficient to fragment size can be considered to be a non-event-specific task, however, and so common models may be used.

In many respects, deriving and indeed using empirical breakup models is still very much a 'black-art', with models based on scant, and in some cases inappropriate, data generally being employed for a much wider range of fragmentation scenarios than they were originally intended. No universal, consistent set of fragmentation equations exists, although at least one attempt has been made to bring together a combination of empirical equations and observational data to produce a unified breakup model [61]. Whether a single set of simple equations will ever be able to accurately describe the complete range of potential breakup scenarios is doubtful, however, but more dedicated experimental data is certainly needed to remove many of the large uncertainties in current models.

McKnight [60] provides a comprehensive review of the most common and widely accepted empirical breakup models in current usage. The development histories of the different fragment distribution equations are outlined, and the appendix summarises the most exercised and validated relationships for each distribution, with appropriate disclaimers and cautions with regard to their implementation included.

For explosions, an exponential law is adopted to determine the fragment number distribution,

$$CN = TM_t exp(-UM_f)^{1/2} , \tag{2.1}$$

where CN is the cumulative number of fragments with a mass greater than M_f (in grams), M_t is the target mass (also in grams), and T and U are empirical constants (with nominal, i.e. mean, values of 0.0005 and 0.04 respectively).

For hypervelocity collisions, a power law is used,

$$CN = a(\frac{M_f}{M_e})^{-b} , \tag{2.2}$$

where M_e is the mass of ejecta in grams, and a and b are empirical constants (nominal values of 1.0 and 0.65 respectively). The ejecta mass, M_e, is the mass that would be excavated from the target in a cratering impact, if the target was very much larger than the projectile striking it for example. It is defined as

$$M_e = M_p v_c^2 , \tag{2.3}$$

where M_p is the projectile mass (g) and v_c is the magnitude of the relative collision velocity (km/s). Note that equation (2.3) is dimensionally incorrect. It is an empirically derived relationship which introduces the effect of collision energy variation into the resultant mass distribution. Without the v_c^2 factor, equation (2.2) would produce the same fragment distribution for any projectile/target combination, regardless of the kinetic energy of impact.

The collision is deemed to be catastrophic (i.e. the whole of the target structure fragments as a result of the impact) if M_e exceeds, or is equal to, 10% of the target mass, M_t. In this case it is assumed that the projectile and 10% of the target mass (i.e. M_p+$0.1M_t$) fragment as per equation (2.2), and the remaining 90% of the target breaks up as per a low intensity explosion, the cumulative number distribution of which is described by equation (2.1).

The mass of a particular fragment can be related to its size by the expression

$$M_f = fD^g , \tag{2.4}$$

where D is the fragment's mean diameter in metres and f and g are constants (nominal values 45000 and 2.26 respectively).

Similarly the ballistic coefficient (BC), in m^2/kg, can be found using

$$BC = (1728/f)D^{(2-g)} , \tag{2.5}$$

where BC is defined as

$$BC = C_d X / M_f. \tag{2.6}$$

Here C_d is the drag coefficient of the fragment (a common 'default' value is 2.2), X is its average cross-sectional area (m^2) and M_f is this time expressed in kg. The BC of an object is essentially a measure of its compactness and determines the object's response to atmospheric drag. An object with a small BC will tend to have a longer orbital lifetime than one with a large BC.

For a hypervelocity collision, the velocity distribution of fragments produced is described by

$$log(\frac{v}{v_p}) = A - B[log(\frac{D}{D_m})]^2 \quad if\ D > D_m\ , \tag{2.7}$$

$$and \quad log(\frac{v}{v_p}) = A \quad if\ D < D_m\ , \tag{2.8}$$

where v (in km/s) is the nominal velocity for a fragment of diameter D metres, v_p is the projectile velocity (km/s), the threshold diameter D_m is equal to $E_p^{1/3}/6.194 \times 10^7$, where E_p is the kinetic energy of the projectile (in J), and A and B are constants (nominal value of A is 0.175, B has a fixed value of 0.1022).

For an explosive event, normalisation to a projectile velocity is not possible. Reynolds [62] provides a standardised velocity distribution which is purely a function of debris size, D (m),

$$log\ v = -0.0676[log(D)]^2 - 0.804 log D - 1.514\ . \tag{2.9}$$

A spread is usually made about whichever of the above nominal velocity curves is used. This is done to model the fact that all the fragments of a given size will not have the same velocity. The NASA triangular spreading function bounds the velocity distribution between 1.3 and 0.1 of the nominal, the peak probability velocity being the nominal case (Figure 2.1). These limits have been found to agree favourably with a number of on-orbit collisions and explosions [62].

Tedeschi et al [58] updates and refines several of McKnight's [60] expressions and also introduces a new, energy-based, criterion for determining if an impact causes a complete breakup of the target object.

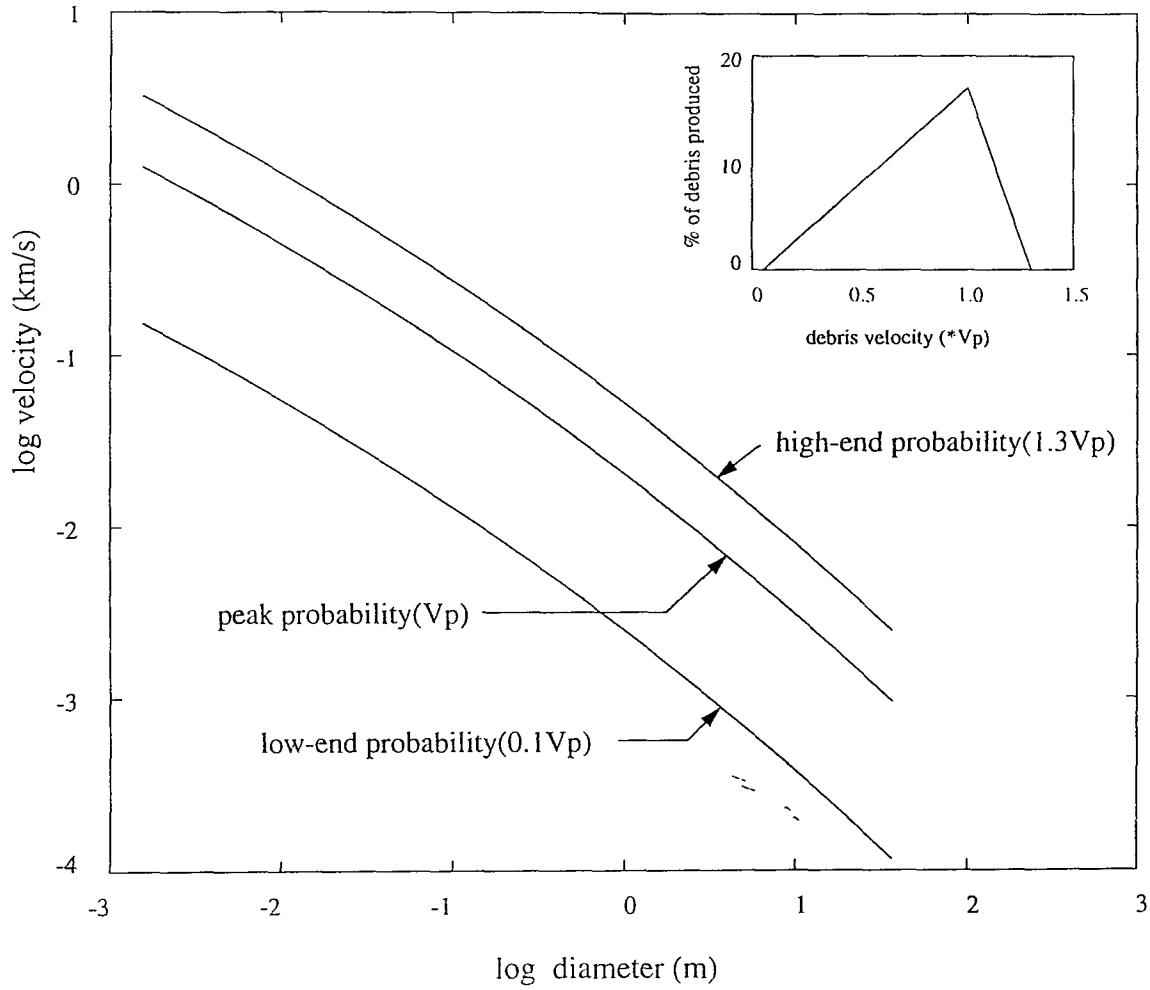

Figure 2.1: Standardised debris ejection velocity distribution

For a catastrophic hypervelocity collision, the cumulative number of fragments larger than a given mass, M_f is expressed using the following power law,

$$CN = C(\frac{M_f}{M_t})^{-B} . \tag{2.10}$$

The parameter B is defined as,

$$B = 0.6 + 0.15P(1 - 40M_t/E_p), \tag{2.11}$$

where P is the fraction of the target mass encountered by the projectile, M_t is expressed in grams and E_p is given in Joules. The value of P will depend on the structural nature of the target and its fuel loading and is typically in the range 0.5-0.9. The constant C in equation (2.10) is set so as to conserve mass.

The collision is deemed to be catastrophic if the following energy criterion is met,

$$E_p/M_t \; > \; 40 \; (J/gram). \tag{2.12}$$

For complete breakups, the size of the errors incurred in using equation (2.10) are $< 10\%$ [58].

For a hypervelocity collision, the following velocity distribution is recommended,

$$(\frac{v}{v_c}) \; = \; A(\frac{q}{[100D+q]}), \tag{2.13}$$

where A is a constant (nominal value 1.3) and the parameter q is given by,

$$q \; = \; 0.00048[\frac{M_p}{PM_t}]{E_p}^{1/2}. \tag{2.14}$$

Here D is expressed in metres, M_p and M_t in grams and E_p in Joules, as before.

The above expressions can be used to describe the resulting fragment distributions from a breakup event but note should be made that mass, momentum and energy are not all explicitly conserved. Through judicious choice of the various parameters available, approximate balances between the pre- and post-collision states can be made, but this is a far from ideal method. A more rigorous approach is to constrain the event to obey the conservation laws from the outset. This is the method employed in the Aerospace Corporation 'kinematic' model [63]. The kinematic model is discussed in more detail in Chapter 3.

Jonas et al [64] compares the breakup models used in three U.S. computer codes. The three codes examined are the breakup module in the NASA EVOLVE long-term population model, the Aerospace Corporation's IMPACT (version 2.0) and Kaman Sciences' FAST (Fragmentation Algorithms for Satellite Targets). The models used in each code are compared side-by-side in equation form and the fragment distributions produced by each are also compared graphically. The paper does not attempt to recommend any one model in preference to the others but aims simply to compare and contrast the different approaches currently adopted as a reference for other researchers. It was found that many of the models, although similar in form, could often produce quite different fragment distributions through the use of

different parameters/model constants. The greatest discrepancies found related to the ejection velocity distributions. The uncertainties here have strong implications on both debris cloud and long-term environment modelling.

Although the results from simulation codes have been shown to be in reasonable agreement with actual observational data from recorded breakup events (for example in [65]), any uncertainties in the models will tend to propagate through into predictions of both the current and future orbital environments. The modelling of fragmentation events has been shown to have a significant impact on the predicted debris population in LEO for example [66]. Factors such as the percentage of target mass converted into small debris, and the mass-area relationships and velocity distributions used, all influence the shape (i.e. slopes and peaks) of the resulting spatial density vs altitude distributions [67]. Current ejection velocity models may overestimate the spread velocities given to fragmentation debris, as the density-altitude profiles obtained from simulations [68] have been found to be considerably 'flatter' than those derived from recent Haystack observational data. This has obvious implications on the debris density levels at the 'critical' orbital altitudes described in Chapter 1.

2.1.4 Generation of the Debris Cloud

Fragment distributions generated using the above expressions are of no real use to a debris cloud propagation or a collision hazard analysis program in the form quoted. Firstly, each distribution is continuous. These continuous distributions must be quantised to produce a set of discrete fragments, each with their corresponding masses and velocities. The cumulative number distribution must also be converted into a number distribution, detailing how many fragments there are of a given size, or, alternatively, in a given diameter range. The 'velocity' distributions described above are also only really speed distributions, i.e. no distribution of ejection directions is specified. The fragment distributions thus require a degree of 'processing' before they can be used as input to a debris cloud or environment model.

The simplest way of modelling a debris cloud is to assume that the fragments are

ejected isotropically from the breakup point. The shape of the cloud is, therefore, initially spherical. By setting maximum and minimum debris size limits, the number of fragments produced by the breakup can be determined by using an appropriate CN distribution, e.g. one of those shown above. From the smallest fragment size (and the velocity spreading function used, e.g. the NASA triangular), the maximum debris ejection velocity or Δv can be determined. This scales the cloud dimensionally. A mean value of the debris density at a given time can be calculated by dividing the number of fragments in the cloud by the cloud's volume. To model a cloud with variable density and a variable growth rate, a number of concentric cloud 'shells' or Δv bins can be employed. Three such shells were used in [63] and [69] to represent three categories of objects, those that were trackable, those that were non-trackable but potentially lethal and finally those that were non-trackable but could be shielded against. The cloud's density-Δv profile will depend upon the number of shells used, their spacing and, of course, the type of event in question. Debris densities are usually highest near the cloud's centroid, however, and decrease rapidly towards the outer extremities of the cloud (volume dilution effect) [70, 71].

Typically, on-orbit explosions and collision-induced breakups will produce quite different debris clouds. This is due to the difference in fragmentation energies and mechanisms associated with the two types of event [50]. Collision-induced events generate enormous quantities of very small fast-moving fragments and hence produce very large debris clouds. In contrast, explosions tend to produce mostly large fragments with generally lower Δvs. So, although the chance of collision with any fragment is higher for a collision-induced debris cloud, the risk of a collision with a large (and hence potentially damaging) fragment may be greater for an explosive breakup [72]. Highly energetic breakups may also not necessarily be the most hazardous. More satellites may encounter the cloud than for a low-energy fragmentation due the cloud's size, but lower debris densities will reduce the collision risk in each case [27].

The type of model outlined above considers the debris cloud as a continuum, a three-dimensional envelope in space inside which all the debris is contained. No

details on individual fragments are provided. Debris density is the primary cloud descriptor. This type of representation is best suited to collision hazard analysis which uses spatial density to calculate values of collision probability. For cloud propagation only the envelope boundaries are evolved and the internal cloud structure is 'smoothed' though the use of mean or representative fragment Δvs and BCs. Anisotropy and information on individual debris objects (e.g. orbital parameters, orbital lifetime) can only be introduced through the creation of 'actual' fragments from the breakup model. This requires some degree of random selection of mass, Δv etc from the fragment distribution spreads and also a method of assigning ejection velocity directions. All directions can be selected completely at random or follow a direction/anti-direction coupling so as to conserve angular momentum [63]. Using the magnitude of the fragment Δv, its direction, and the orbital position and velocity vectors of the parent object at breakup, the orbit of the fragment can be determined. The orbits of the individual fragments (and hence the whole debris cloud) can then be evolved using a standard orbit propagator. This approach is particularly suited to assessments of the cloud's long-term effects on the environment and the integration of fragmentation debris into a considered orbital object population. The effects of the cloud's internal structure on its dynamics and growth can also be investigated. As each fragment orbit is processed individually, a lower limit on debris size has to be set for computational practicality. This limit can, for example, be taken to correspond with the minimum trackable debris size. Smaller particles need not be ignored, however, but can be considered on a 'macro' level. A typical 'macro-fragment' is taken as being representative of a number of particles of a given size.

2.2 Debris Cloud Evolution and Collision Hazard Analysis

2.2.1 Introduction

Modelling the evolution of a space debris cloud has been the subject of a considerable amount of research over the last few years. The quest for a computationally fast model has always forced a number of simplifying assumptions to be made to make the problem manageable. Such approximations are almost always made at the expense of accuracy, however. Many of these simplifying assumptions have been removed in the most recent models, enabling more accurate, and more realistic, simulations to be performed.

The main driver for accurately modelling the evolution of a debris cloud is to be able to investigate its interaction with other orbiting objects and ultimately calculate the probability that a 'target' object will collide with a debris object from the fragmentation. Here the 'target' is considered to be, say, an operational spacecraft in a prescribed orbit. Many of the techniques discussed in what follows are purely propagation methods and offer no inherent facility for cloud-target encounter detection or collision probability calculation. Crude approximations or complicated geometrical calculations are then required to determine the volume of the cloud and whether or not the target is 'inside' it at any given time. Other methods, most notably probabilistic continuum dynamics, have a direct coupling between their method of cloud propagation and collision probability calculation. As such, the two topics can be considered to be inter-dependent and so will be discussed together here.

The equation generally used in the literature for calculating collision probability (P_c) is,

$$P_c = \rho A v t, \tag{2.15}$$

where ρ is the spatial density of debris, A is the collision cross-sectional area of the target, v is the relative velocity between the target and the debris and t is the duration of the time interval being considered. This equation is derived from the kinetic theory of gases and Poisson statistics [51]. It assumes that the debris behaves

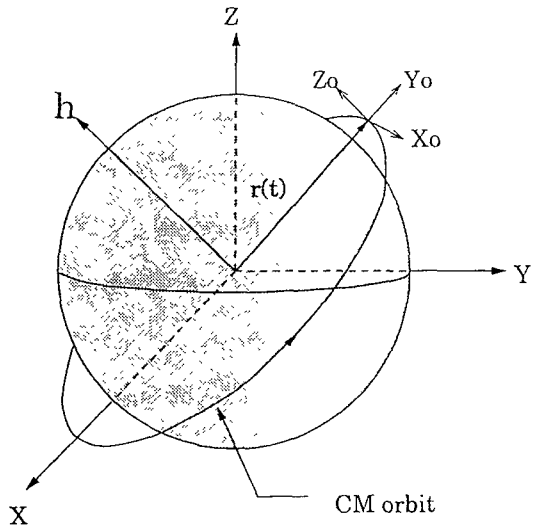

r(t) is the position vector of the system CM at time t
h is the angular momentum vector of the CM orbit

X points towards the Vernal Equinox
Z points North
Y completes the right-hand set

Yo points in the same direction as r(t)
Zo points parallel to h
Xo completes the right-hand set

Figure 2.2: Orbital coordinate frames

like a rarefied gas and that P_c is very small (i.e. the probability of more than one collision is negligible).

2.2.2 Linearised State Transition Matrix Methods

Undoubtedly the simplest short-term model is that pioneered by Chobotov [63, 65, 69] and based on the Clohessy-Wiltshire (CW) rendezvous equations [73]. These are the linearised equations of relative motion between an object, in this case a debris object, and a given circular reference orbit (taken as being the orbit of the breakup object pre-breakup). These equations are derived in full in the Appendix. The equations can be expressed in matrix form as follows,

$$\mathbf{r} = \mathbf{M}\,\dot{\mathbf{r}}_o\,, \tag{2.16}$$

where $\mathbf{r}$ is the particle position vector, $\dot{\mathbf{r}}_o$ is the initial particle velocity vector and $\mathbf{M}$ is known as the state transition matrix. The position and velocity vectors are both given relative to an orthogonal orbiting reference frame, the origin of which is located at the system's centre of mass (CM). The frame's orientation with respect to the geocentric inertial frame chosen is dictated by the CM's orbit radius and angular momentum vectors (Figure 2.2). The state transition matrix $\mathbf{M}$ can also be used to calculate cloud volume. This is discussed in more detail in section 2.2.7.

Using the above model, the cloud shape formed in relative coordinates is that of a pulsating ellipsoid which stretches out along the CM orbit path due to the different orbital periods of the fragments generated. 'Pinch' locations are formed at the full and half revolution points which, in the absence of perturbations, cause the cloud's volume to collapse to zero. A 'pinch point' occurs at the location of the fragmentation because all debris must pass through this point, although not at the same time. Similarly, a 'pinch line' occurs along a radial in the satellite orbit plane 180 degrees from the pinch point because all debris must pass through the orbit plane along this line. These pinch zones are termed 'stationary' as they are fixed inertially by the model's equations of motion. Jenkin [74] examines the phenomenon of debris cloud pinch zones in more detail and shows that a 'non-stationary' pinch zone exists. Identifying and locating pinch zones is important as these are regions of high debris density and as such pose a significant threat of collision to orbiting spacecraft passing through them. The non-stationary pinch zone is found to drift inertially as the debris cloud 'flies' through it. The location of this pinch zone and the behaviour of the debris around it are investigated first by the examination of debris cloud evolution plots and then, more mathematically, through the study of Jacobians. The non-stationary pinch zone is not a true singularity because fragment positions do not intersect simultaneously. It only occurs after the cloud centroid has completed one full orbital revolution and then approaches the half-revolution pinch zone asymptotically. The effects of orbital eccentricity and orbit perturbations are neglected throughout the analysis.

The Chobotov model is very quick and easy to use but is somewhat restricted in its application to circular orbits only. In reality, of course, orbits are never truly circular. In fact the circular orbit model can be used for orbital eccentricities of up to about 0.05 at which point the effects of eccentricity can no longer be neglected. To extend the range of the above model's capability Spencer [75] uses the expressions derived by Anthony and Sasaki [76] to incorporate the effects of low eccentricities ($e<0.25$) through the differential addition of linear eccentricity terms to the circular

case solutions. This produces a solution of the form,

$$\mathbf{r} = \mathbf{r}_C + \delta\mathbf{r}_{Sp} = \mathbf{M}_{Sp}\,\dot{\mathbf{r}}_o\,, \tag{2.17}$$

where $\mathbf{r}$ is the resultant particle position vector, $\mathbf{r}_C$ is its position vector as predicted by the CW equations, $\delta\mathbf{r}_{Sp}$ is the differential correction due to eccentricity, $\mathbf{M}_{Sp}$ is the modified state transition matrix and $\dot{\mathbf{r}}_o$ is the initial velocity vector as before. The linearised trajectories of fragments are compared with those obtained using the full equations of motion and the approximate solutions are found to be reasonable (error <1 n.m.) for Δvs less than 100m/s (for two orbit revolutions only). The eccentricity-extended linear state transition matrix is used in cloud volume calculations for a number of orbital eccentricities and breakup locations. Cloud volume is found to be highly dependent on both parameters.

In Chobotov et al [63], Spencer also introduces perturbation effects (J_2 and atmospheric drag) into the simple circular form of the Chobotov model by perturbing the elements of the transition matrix M. This allows estimates of the cloud's longer-term characteristics to be made and also succeeds in removing the troublesome cloud volume singularities incurred by the Chobotov model at integer half-revolution multiples after the breakup. The justification for adding perturbation effects to a model which is only really valid in the short-term (a few revolutions post-breakup for 'small' Δvs, i.e. tens of m/s or less), however, seems somewhat questionable.

2.2.3 Multi-Phase Models

Chobotov's model, with or without Spencer's modifications, can only consider the very short-term evolution of a debris cloud and so on its own is inadequate for most cases. It can, however, be used as the first phase in a multi-phase model. This is the approach adopted by McKnight [77] who considers the collision risk posed by such a cloud in three distinct phases of its growth, ellipsoid, toroid and band (Figure 2.3). To account for variable density/different particle sizes throughout the cloud, three concentric overlapping sub-clouds are used in each of the three phases. Collision probabilities are calculated for each of the cloud's phases for satellites

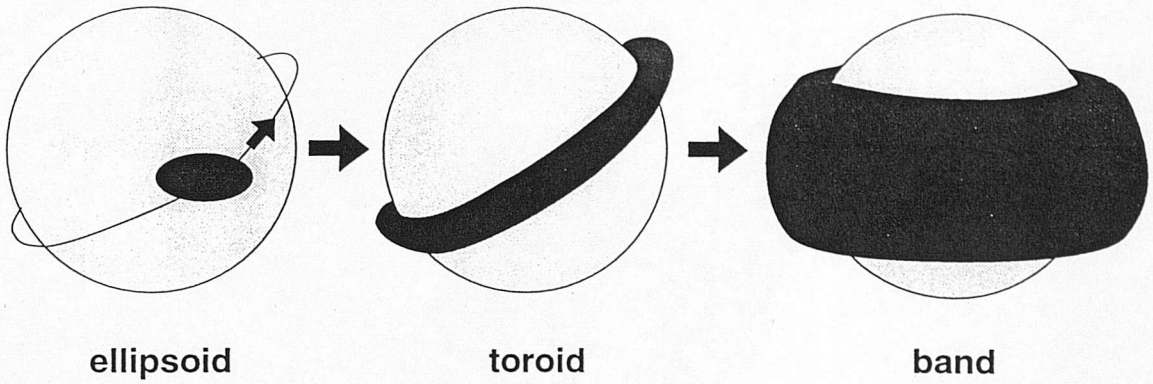

Figure 2.3: Three phase debris cloud evolution

passing through the cloud and can be summed to yield an overall, long-term value. Written to implement the model, program SCREEN, therefore, represents a simple and hence computationally fast method of determining the collision risks due to debris clouds. The method is quite crude, however, particularly with respect to debris density calculation and the criteria used to trigger transition between phases, especially toroid to band.

Jehn [78] adopts a similar approach to McKnight but introduces an extra phase between the toroid and the band. The time taken for the effects of the Earth's asphericity to dismantle the toroid to form a band will generally be of the order of several years and so Jehn uses an opening toroid as a bridging phase to model this gradual transition (Figure 2.4). The opening toroid is modelled using a Monte-Carlo simulation of trackable and untrackable objects and an orbit propagation tool. This phase is considered complete when the distributions of fragment ascending nodes and argument of perigees are uniform.

2.2.4 Toroidal Models

Program DEBRIS was developed by the Aerospace Corporation to model short-term debris cloud dynamics and to compute the probability of collision between satellites of concern and fragments in orbiting debris clouds. Early releases of DEBRIS (versions 1.0,1.1 [63, 65, 69]), used a superposition of overlapping constant density toroidal sub-clouds to model a cloud of variable density. Entry and exit

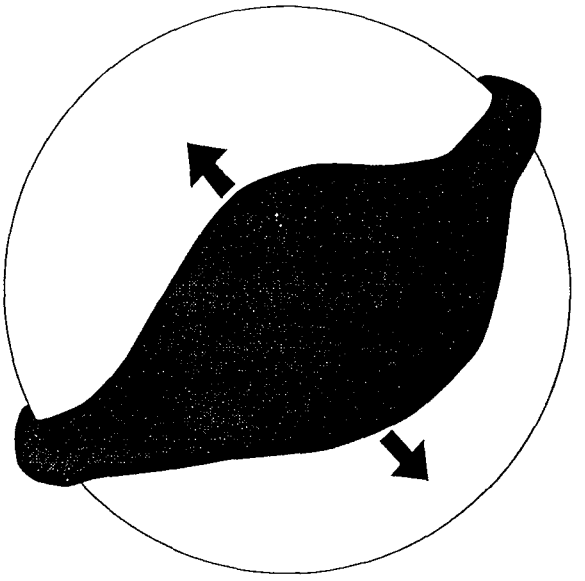

Figure 2.4: Opening toroid

times were computed for objects passing through the cloud from the geometry of the cloud structure and the orientation of the encounter. This model produced conservative but reasonable results for breakups with small maximum spread velocities. The linearisations used to describe the debris cloud motion, and hence the dimensions of the toroidal cloud sections, meant, however, that the model became increasing invalid as the maximum spread velocities were increased.

Crowther [79] develops an analytical model to describe the short-medium term evolution of a debris cloud in a circular orbit. The evolving cloud is treated as two limbs, one which advances ahead of the parent satellite locus (orbital energy less than the parent) and one which retreats behind it (orbital energy greater than the parent). The model represents the pulsating nature of the debris cloud without the volume singularities of the Chobotov model. It predicts that the volume of the retreating limb will generally be larger than the advancing limb and that the maxima and minima of the cloud's total volume occur at different times as compared with the 'pinch' locations of the Chobotov model. The 'limb' nature of the model makes it relatively easy to determine when the cloud intersects with the orbits of other spacecraft but its use of toroidal (albeit half) cloud sections tends to overestimate cloud volume and hence underestimate debris density and thus collision probabilities.

Frye [80] also uses a toroidal model to represent a debris cloud. The problem of determining collision probabilities for objects passing through the cloud is reduced to a two-dimensional consideration of objects passing through the debris cloud mid-plane. The 'area-rule' approach requires the complex geometric computation of target entry and exit times for passages through the cloud. The approximation of the cloud to that of a section of the debris-bounding torus does, of course, overestimate the cloud's volume, as is stated in the paper. The claim that this leads to a conservative approach (by registering more encounters) seems somewhat dubious, however, as the underestimates of debris density made by this approach are likely to dominate over the contribution of any 'extra' cloud encounters. As a plus point, the model seems computationally rapid. A sample problem (16 clouds and 32 targets) is included in the paper to illustrate the approach's capability for conducting simulations well into the long-term (years). For the example included, a run time of around 10 seconds for a 3 day simulation is quoted (FORTRAN code, Sun Sparc workstation).

2.2.5 Non-Linear State Transition Matrix Methods

An alternative to using a multi- or second-phase model is to enhance the validity range of a linear transition matrix method through a non-linear extension. Hujsak [81] presents a non-linear dynamical model of relative motion for debris cloud evolution simulation. The linearised Clohessy-Wiltshire equations [73] are generalised and secular J_2 and second order relative distance terms are combined into a single state transition matrix formulated in equinoctial orbital elements [82]. The non-linear matrix is then used first for fragment evolution and then cloud spatial density computation. For the latter analysis, the inverse of the state transition matrix is used as an approximate solution to the Gauss-Lambert problem (the problem of orbit determination given two position vectors and a transfer time). The non-linear extensions to the linearised state transition matrix are shown to provide a significant improvement in fragment position calculation (at least for the short time period and moderate Δvs of the example). The use of the non-linear matrix for

spatial density calculation (or more precisely the calculation of the spread velocity volume that corresponds to a fixed volume surrounding the target position in position space) breaks down at and around the cloud's pinch locations but it does at least provide a pointer to the order of magnitude of density variations that can be present within a debris cloud at any given instant.

2.2.6 Keplerian Propagation

Non-linear corrections can be used to extend the useful lifetime of linear models, but only up to a point. Such a model will eventually break down after a number of orbits and the improved performance is offset by an increase in model complexity. If a longer term analysis is required or the eccentricities of the orbits being considered are large (e.g. for GTO or Molniya orbits) then the full equations of motion must be used, i.e. Keplerian propagation in the ideal, two-body, case. In contrast to the state transition matrix methods described previously, Keplerian propagation deals with individual orbits in the geocentric inertial frame. Jenkin and Sorge [83] use Keplerian propagation to investigate the effects of eccentricity on the growth and general behaviour of debris clouds. The behaviour of a cloud resulting from a breakup in an eccentric orbit is far more complex than that of the circular case. The variable orbit tangential velocity significantly complicates the cloud dynamics and causes the behaviour of the cloud shape to be highly dependent upon the orbital position of the breakup with respect to perigee. Large along-track density variations are also observed purely as a result of the variable orbit rate. For highly elliptic orbits, these variations can be as large as two orders of magnitude.

2.2.7 Probabilistic Continuum Dynamics

In some of the earliest work on the subject, the methods of statistical mechanics were employed to examine the evolution of a debris cloud, its spatial density and even to attempt to determine its breakup origin. Both Dasenbrock et al [57] and Heard [84] consider the cloud as an ensemble of non-interacting particles and although both initially embark on completely general solutions, both choose to concentrate on the

simplest of cases, that of slow dispersion from an initially circular orbit. This, in fact, results in an alternative derivation of the CW rendezvous equations and a model that is essentially identical to that of Chobotov. The methods of probabilistic continuum dynamics, however, have been employed again recently to produce more accurate debris cloud models. In the probabilistic continuum method, debris cloud motion is treated as a time-dependent mapping from spread velocity space at the time of breakup to position space at the time of interest. The spatial density of debris at any given position can then be obtained using the Jacobian that relates spread velocity space to position space [85]. The determination of the point at which to evaluate the Jacobian involves, for Keplerian motion, the solution of the classical Gauss-Lambert problem. This can be taken to correspond to the calculation of a fragment's initial velocity vector from its position vector at a given, later time. In practice, there can be more than one such velocity vector which satisfies a given Gauss-Lambert problem. The total debris density is obtained by summing the contributions from each solution.

For example [70], consider a breakup at time t=0 and position $\mathbf{r}_0$. The spatial density of debris at a particular position $\mathbf{r}$ at time t can be found as follows. If $\dot{\mathbf{r}}_0$ represents an initial velocity vector which enables a fragment to perform the orbital transfer $\mathbf{r}_0$ to $\mathbf{r}$ in time t, then the number of fragments contained in a small volume element $d\mathbf{r}$ at time t will be equal to the number of fragments which had ejection velocities in a corresponding velocity element $d\dot{\mathbf{r}}_0$. That is,

$$\rho(\mathbf{r})d\mathbf{r} \;=\; f_v(\dot{\mathbf{r}}_0)d\dot{\mathbf{r}}_0, \tag{2.18}$$

where f_v, the distribution of initial velocities, is defined such that $f_v(\dot{\mathbf{r}}_0)d\dot{\mathbf{r}}_0$ is the number of fragments with initial velocities in the element $d\dot{\mathbf{r}}_0$. The elements $d\mathbf{r}$ and $d\dot{\mathbf{r}}_0$ are related by

$$d\mathbf{r} \;=\; |J|d\dot{\mathbf{r}}_0, \tag{2.19}$$

where J is the Jacobian of the transformation from $\dot{\mathbf{r}}_0$ to $\mathbf{r}$, i.e. the determinant of the state transition matrix $\Phi(\mathbf{r}, \dot{\mathbf{r}}_0) \;=\; \partial\mathbf{r}/\partial\dot{\mathbf{r}}_0$. The debris density at $\mathbf{r}$ due to $\dot{\mathbf{r}}_0$ is

then given by,

$$\rho(\mathbf{r}) = \frac{1}{|J|} f_v(\dot{\mathbf{r}}_0[\mathbf{r}]). \tag{2.20}$$

It should be noted that the state transition matrix methods described earlier and the probabilistic continuum dynamics method are conceptually identical. For example, M, used in the Chobotov model described previously (equation 2.16), is merely a linearised version of Φ. A distinction is made between the two, however, since the former implementations of the method dealt purely with cloud evolution and simple estimates of cloud volume, while the latter has primarily been utilised as a tool for debris density and hence collision probability calculation, with debris propagation carried out only implicitly.

Cloud volume can be calculated in a similar way to spatial density. The above approach, although completely general for any type of fragment trajectory and spatial distribution of spread velocities, is in fact only valid for small regions of spread velocity space and hence position space. In such small regions, the transition matrix can be assumed to be constant. When the entire cloud is relatively small, then the volume of the whole cloud can be evaluated using this technique, i.e.

$$V = |J|V_v = |det(\Phi)|V_v, \tag{2.21}$$

where V is the volume of the cloud, V_v is the volume of spread velocity space and the transition matrix is referenced to the centre of spread velocity space, i.e. the state of the breakup object at breakup. When the cloud increases in size, however, the approximation that the state transition matrix is constant throughout the cloud cannot be used and the cloud volume must be obtained by integrating over all of spread velocity space, i.e.

$$V = \int_{R_v} |J| dV_v, \tag{2.22}$$

where R_v denotes a spread velocity space of arbitrary shape.

Hujsak [86] uses the method of probabilistic continuum dynamics to calculate debris density maps. The method of Gooding [87] is used for solution of the Gauss-Lambert problem and the algorithm of Goodyear [88] is employed for state transition

matrix and hence Jacobian calculation. The paper's theoretical development contains a number of fundamental mistakes, however, and a 'bug' in Hujsak's computer code caused errors in his density plots (although apparently corrected in a 'revised' version of the paper) [89].

Housen [70] tackled the same problem but did so with a greater degree of success. He also used Goodyear's [88] algorithm in the calculation of the Jacobian but chose the algorithm of Sun et al [90] to solve the Gauss-Lambert problem. His analysis revealed order of magnitude density variations throughout the cloud with the highest densities occurring, as expected, near the pinch locations. For the 'low-velocity' breakup model used, he showed that the cloud density peaks produced can exceed the background level by up to two orders of magnitude.

A debris density calculation algorithm like that outlined above can also be used in the calculation of collision probabilities for a target object which passes through the debris cloud. Interactions with the debris cloud formed by a fragmentation event produce 'spikes' in the target object's overall (i.e. background debris environment plus cloud) instantaneous collision probability versus time curve. For an analysis which focuses on the collision risk to a target object due to a debris cloud rather than on the cloud itself, values of debris density need only be calculated at positions along the target's orbit. If, for given time step, the target object is physically outside the bounds of the debris cloud, then the spatial density of debris will be zero . If it lies inside the cloud, then a non-zero value will be returned. Hence, not only is the value of debris density determined for subsequent calculation of the collision probability at each point, but an implicit and accurate detection method is established for determining if/when any encounters between the target and the debris cloud actually occur. The technique can be applied to any scenario and can even employ a completely arbitrary breakup model.

Jenkin [71] describes the methods used in the Aerospace Corporation's program DEBRIS, version 3.1. A generalised, numerical implementation of the above method is employed. In DEBRIS3.1, the two-point boundary value problem (the Gauss-Lambert problem in two-body dynamics) is solved using a generalised vector root

solving algorithm and the state transition matrix is calculated numerically by determining the perturbations in position space that result from small perturbations in spread velocity space. Two numerical examples are used to show the program in operation. In the first example, the target satellite passes close to a debris cloud's first whole-revolution pinch point (i.e. breakup location). The collision probabilities calculated are found to increase by several orders of magnitude as the target passes close to the breakup point.

Chapter 3

Modelling of the Fragmentation Event

3.1 Introduction

A general introduction to the field of breakup modelling was given in the previous chapter. That will not be repeated here. Instead, specific details on the breakup models actually used will be provided and also how these have been implemented into program BREAKUP. As well as describing the existing approaches that have been adopted, special attention will be given to the novel developments made, particularly in the area of non-isotropic fragment ejections, and the validation of simulation results with actual data from on-orbit fragmentations.

3.2 Collision-Induced Breakups

3.2.1 Scenario 1

Two different collision models (scenarios) are available for use in program BREAKUP. Scenario 1 uses a selection of the fragment distribution equations that were described in the previous chapter. The fragment cumulative number versus mass distribution used is equation (2.10). This model is best for complete target fragmentations although it can also be used for non-catastrophic breakups. If the collision is non-catastrophic then the mass of the portion of the target spacecraft which fragments

(M_{tot}) is determined using,

$$M_e = E_p/40, \tag{3.1}$$

and

$$M_{tot} = M_e + M_p \tag{3.2}$$

(from [64]), where 40 (J/gram) is the threshold debris impact energy to target mass ratio for a complete breakup (equation (2.12)), M_e is the ejecta mass in grams, E_p is the projectile kinetic energy in Joules, M_p is the projectile mass in grams, and the target mass which breaks up, M_{tot}, is also expressed in grams. If the collision is catastrophic (i.e. $E_p/M_t \geq 40$ (J/gram)) then M_{tot} is simply $M_t + M_p$.

To add an element of unpredictability and hence a touch of realism to the distributions produced, a random spread is introduced about the above, nominal, distribution. Hence, within specified bounds, a different distribution of debris can be generated every time (by using a different integer seed), thus catering for the complex mechanisms involved in the collision process which make getting exactly the same set of fragments more than once for a given fragmentation event virtually impossible. The randomised CN distribution can then be scaled to conserve mass, ensuring that the sum of the fragment masses post-collision is equal to the breakup mass M_{tot}.

The ejection velocity distribution used is given in equation (2.13), and the mass and ballistic coefficient-to-size relationships employed are shown in equations (2.4) and (2.5) respectively. The nominal curves are used for the mass and BC distributions but a triangular spread is made about the nominal Δv curve as described in Figure 2.1.

3.2.2 Scenario 2

Scenario 1 provides a simple representation of a hypervelocity collision, but only mass is explicitly conserved. Scenario 2 employs a modified version of the Aerospace Corporation's kinematic model [63] which explicitly sets out to conserve not only mass but also energy and both translational and angular momentum. The model

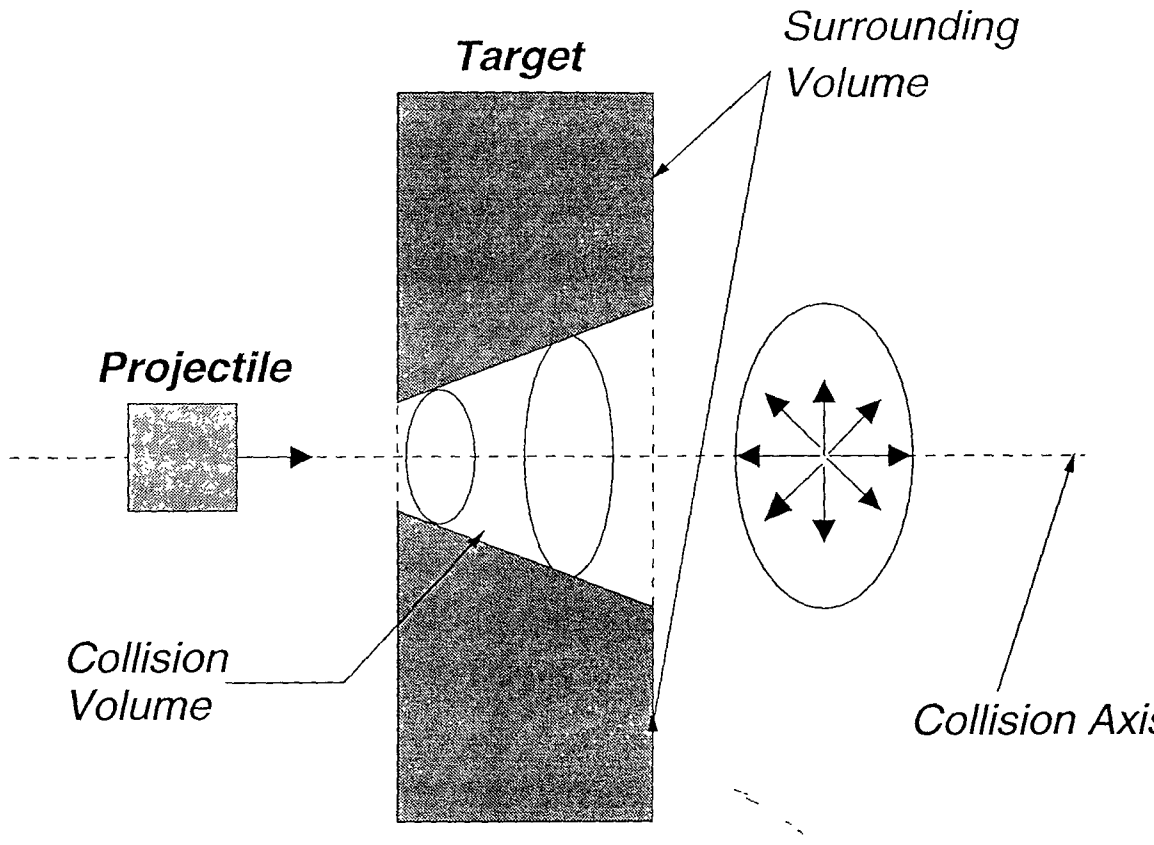

Figure 3.1: Collision schematic

conveniently avoids the complexities involved in simulating a hypervelocity collision from first principles by using a number of parameters which qualitatively describe the degrees of freedom associated with the collision dynamics. The sensitivity of the post-collision state with respect to these parameters can then be evaluated by the definition of a system of transfer functions relating the pre- and post-collision states, as constrained by the conservation laws. In this way, the range of possible outcomes of an event can be examined without the necessity of modelling each condition individually. By choosing the model parameters to have clear physical significance, improved knowledge of collision dynamics can easily be incorporated into the model.

The general properties of a collision are depicted schematically in Figure 3.1 (adapted from [63]). The volume of the target object is divided into two regions as shown. The central (unshaded) region is the collision volume and corresponds to the part of the target that participates directly in the collision, i.e. is directly in

the path of the expanding collision front. The shaded region is the surrounding or non-involved target volume.

Nearly all of the momentum transfer is confined to the collision volume. Energy is transferred to the non-involved volume in a secondary interaction that involves shock waves, collisions and both shear and explosive forces. If the collision is catastrophic, the shock front propagates through the target until the collision volume exits the surrounding mass. At this point the internal energy of the collision is released in a radial expansion of the now unconfined collision volume material in fragments in the solid, liquid and gaseous states. The non-involved volume experiences a lower intensity, explosive, breakup into fragments of various sizes, which are accelerated radially from its centre of mass and the collision axis by the fraction of collision energy transferred to it. If the target is sufficiently large and 'deep' along the collision axis with respect to the projectile dimensions, then the collision is fully absorbed and a crater is formed on the target surface at the point of the impact.

Qualitative studies on a variety of test cases show [63] that, for a catastrophic collision, the fragments are organised into two basic groups. There is a rapidly expanding radial distribution of large numbers of fragments about the centroid velocity of the collision mass, and a less energetic expansion of smaller numbers of larger fragments about a centroid close to the target velocity. It is this feature which gives rise to the bimodal fragment distribution used in the kinematic model.

Consider, in an inertial frame, two objects of mass M_1 and M_2 which approach their joint centre of mass with velocities $\mathbf{V}_1$ and $\mathbf{V}_2$ respectively, as shown in Figure 3.2 (adapted from [63]).

It is convenient to describe the motion of the system of particles relative to the system CM. Taking advantage of symmetry, the CM coordinate system is chosen with one axis oriented along the relative velocity vector, $\mathbf{V}_{rel} = \mathbf{V}_1 - \mathbf{V}_2$. If $\mathbf{U}$ is the velocity of M_1 and $\mathbf{V}$ that of M_2 in the transformed system, then

$$\mathbf{U} = \frac{M_2}{M_1 + M_2}\mathbf{V}_{rel} \tag{3.3}$$

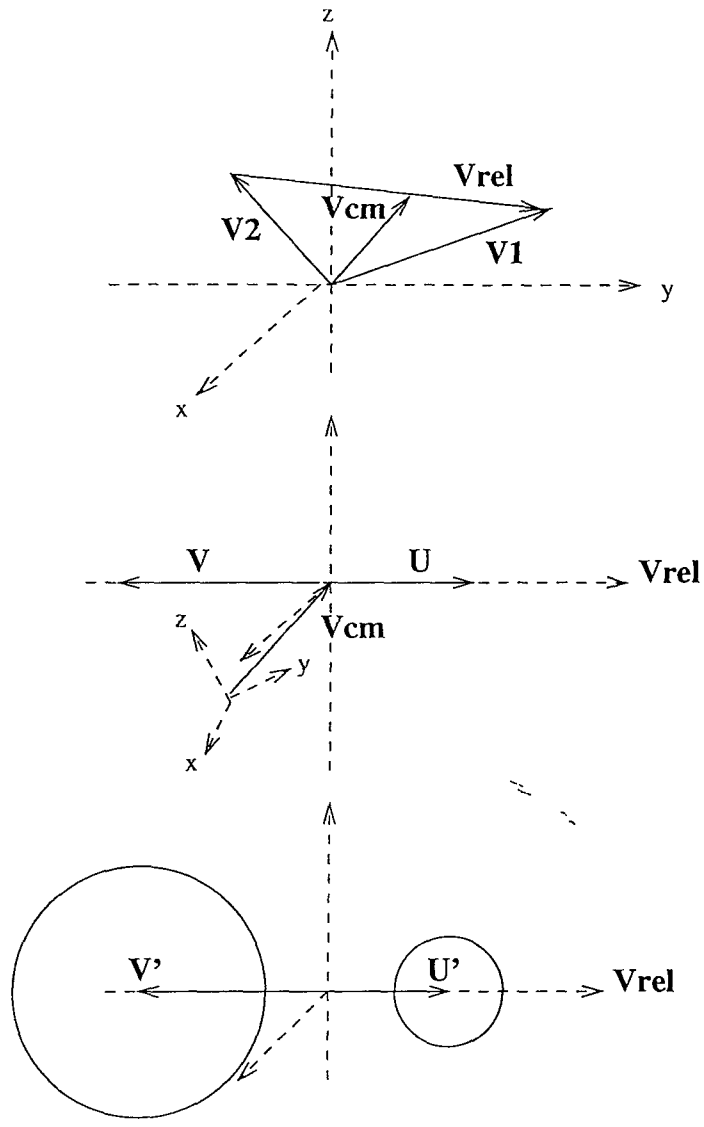

Figure 3.2: Incident and resultant collision geometries

and

$$\mathrm{V} = \frac{-M_1}{M_1 + M_2}\mathrm{V}_{rel} \ . \tag{3.4}$$

In CM coordinates, the total linear momentum of the system is zero,

$$M_1\mathrm{U} + M_2\mathrm{V} = 0 \ , \tag{3.5}$$

and the total system kinetic energy (KE) is

$$KE_{sys} = \frac{1}{2}(M_1U^2 + M_2V^2) \ . \tag{3.6}$$

Accelerations during the collision are assumed to be instantaneous.

Immediately after the collision, the system is described as consisting of two translating, non-rotating (dictated by conservation of angular momentum), expanding spheres. These spheres represent the respective mass distributions of the non-involved and collision volumes.

If the quantities (M_1',$\mathbf{U}'$,$KE'_{spread1}$) and (M_2',$\mathbf{V}'$,$KE'_{spread2}$) represent the mass, centroid translational velocity and spread KE of each of the two spheres in the CM system, then the application of the conservation laws provides the following constraints,

$$M_1' + M_2' = M_1 + M_2 \text{ (conservation of mass)} , \tag{3.7}$$

$$M_1'\mathbf{U}' + M_2'\mathbf{V}' = 0 \text{ (conservation of linear momentum)} , \tag{3.8}$$

and

$$KE_{sys} = KE'_{trans} + KE'_{spread} + Q_{loss} \text{ (conservation of energy).} \tag{3.9}$$

Here KE'_{trans} represents the translational KE of the sphere centroids (equal to $\frac{1}{2}(M_1'U'^2 + M_2'V'^2)$), KE'_{spread} represents the spread KE of the fragments about the sphere centroids and Q_{loss} accounts for the KE dissipated in the collision, i.e. converted to other forms (heat, light, etc). Note that KE'_{spread}, as defined above, also includes terms due to the dot products of the centroid velocities and the fragment spread velocities relative to the sphere centroids. As a spherical spread of fragments is assumed for each volume, however, these terms sum to zero.

A system of transfer functions can now be defined which express the post-collision state (M_1',M_2',$\mathbf{U}'$,$\mathbf{V}'$,$KE'_{spread1}$,$KE'_{spread2}$) in terms of the pre-collision state (M_1,M_2,$\mathbf{U}$,$\mathbf{V}$) as well as a set of independent parameters governing the system degrees of freedom. If M_1 is the target mass, M_2 is the projectile mass and a parameter γ is defined as the fraction of M_1 directly involved in the collision ($0 < \gamma < 1$), then the mass of the non-involved target volume is given by

$$M_1' = (1-\gamma)M_1 , \tag{3.10}$$

and the mass of the collision volume by

$$M_2' = M_2 + \gamma M_1 , \tag{3.11}$$

from equation (3.7).

The combination of equations (3.10) and (3.11) with equation (3.8) places upper limits on the magnitudes of the resultant centroid translational velocities in the CM system,

$$|\mathbf{U}'| \leq |\mathbf{U}|, \tag{3.12}$$

and

$$|\mathbf{V}'| \leq \frac{(1-\gamma)M_2}{M_2+\gamma M_1}|\mathbf{V}|. \tag{3.13}$$

These upper limits are achieved if, in the collision, no translational kinetic energy is converted to kinetic energy of expansion.

If a momentum transfer parameter, ϵ , is defined as the fractional part of the pre-collision translational momentum not converted into post-collision spread KE $(0 < \epsilon < 1-\gamma)$ then,

$$\mathbf{U}' = \frac{\epsilon}{(1-\gamma)}\mathbf{U}, \tag{3.14}$$

and

$$\mathbf{V}' = \frac{\epsilon}{(1+\gamma\frac{M_1}{M_2})}\mathbf{V}\,. \tag{3.15}$$

A third parameter, ζ, is defined as the fraction of the energy theoretically available to KE'_{spread} which is actually delivered to KE'_{spread}, i.e. which is not absorbed by Q_{loss}, $(0 < \zeta < 1)$. Hence, from equation (3.9),

$$KE'_{spread} = \zeta[KE_{sys} - KE'_{trans}]\,. \tag{3.16}$$

Finally, a fourth parameter, μ, is defined as the fraction of KE'_{spread} transferred to M'_1 , $(0 < \mu < 1)$. Thus the spread KE can be apportioned between the two masses as follows,

$$KE'_{spread1} = \mu KE'_{spread} \tag{3.17}$$

and

$$KE'_{spread2} = KE'_{spread} - KE'_{spread1}\,. \tag{3.18}$$

The method used above to determine the two spread KEs is a novel simplification of that outlined in the original kinematic model. The above method arrives at

essentially the same end point, using the same four system parameters, but manages to avoid virtually all the intermediate stages and the associated, quite complex, algebra contained in the original. It is this modified version of the kinematic model which is used in program BREAKUP.

As the collision and non-involved volumes are considered individually by the kinematic model, a different CN distribution to equation (2.10) must be used, as this expression is effectively a combination of a collision-type power law and an explosion-type exponential. Equation (2.2) is employed instead as it describes solely collision-produced fragments. The CN distribution of the non-involved volume can be modelled by the exponential described in equation (2.1).

Rather than using the velocity distribution described in equation (2.13), the kinematic model actually makes use of the spread KEs of the two volumes explicitly in determining the fragment velocities. Once the total number of fragments in each of the two volumes is known then the average spread KE for each fragment can be calculated. For all but the smallest fragments (<1 mm say) the kinetic energy imparted to each fragment can be assumed to be equal, since the shock wave front, which is hemispherical in shape, applies equal pressure at a given time. The assumption of equi-partitioning of KE has been shown to be in general agreement with a number of laboratory experiments [65]. Hence the material is assumed to break up into fragments of unequal size but with equal KE. So, given the mass of each fragment and the volume-average (i.e. collision or non-involved) KE per fragment, the (nominal) velocity of the fragment can be found. The equal-KE assumption breaks down, though, for smaller fragments as the effectiveness of the shock wave is reduced. Hence, an upper bound is imposed upon the velocity distribution obtained to allow for this, with the spread velocities of the smallest fragments being limited to 1.3 times the relative impact velocity.

Fragment mass and ballistic coefficient distributions are generated as per scenario 1. Random and triangular spreads are also made about the nominal CN and Δv distributions respectively, again as in scenario 1.

3.3 Explosive Fragmentations

Two explosion models are also employed. Scenario 3 simulates a low-intensity fragmentation using equation (2.1). Scenario 4 models a high or variable-intensity explosive fragmentation with the following equation [64],

$$CN = Vexp(-WM_f)^{1/2}, \tag{3.19}$$

where W=0.0012(E_{exp}/M_{tot}), E_{exp} being the energy released in the explosion (J). The breakup mass, M_{tot}, and the fragment mass, M_f, are both expressed in grams. The parameter V is set to conserve mass.

As with scenarios 1 and 2, equations (2.4) and (2.5) are used to generate the fragment mass and BC distributions respectively, and random CN and triangular $\triangle$v spreads are utilised.

3.4 Generation of the Debris Cloud

3.4.1 Isotropic Continuum Cloud Model

An outline of the two main cloud model options was given in section 2.1.4. As stated there, the simplest method of generating a debris cloud is to assume that the fragments are ejected isotropically from the breakup origin and to treat the debris as a continuum as opposed to discrete particles. Such a representation is designated as cloud type 1 in program BREAKUP. It should be noted that for a given breakup scenario, either of the two cloud models can be used. The decoupling of fragment distribution generation and cloud model is possible because even though the different breakup scenarios are described by different CN and $\triangle$v equations, the same four fragment distributions (CN, $\triangle$v, mass, BC) are used irrespective of the event type. The only exception to the rule is scenario 2, the kinematic collision model. The kinematic model produces two spherical clouds which, if the isotropic continuum model is employed, must be treated individually.

Fragment distributions are generated in program BREAKUP by evaluating each

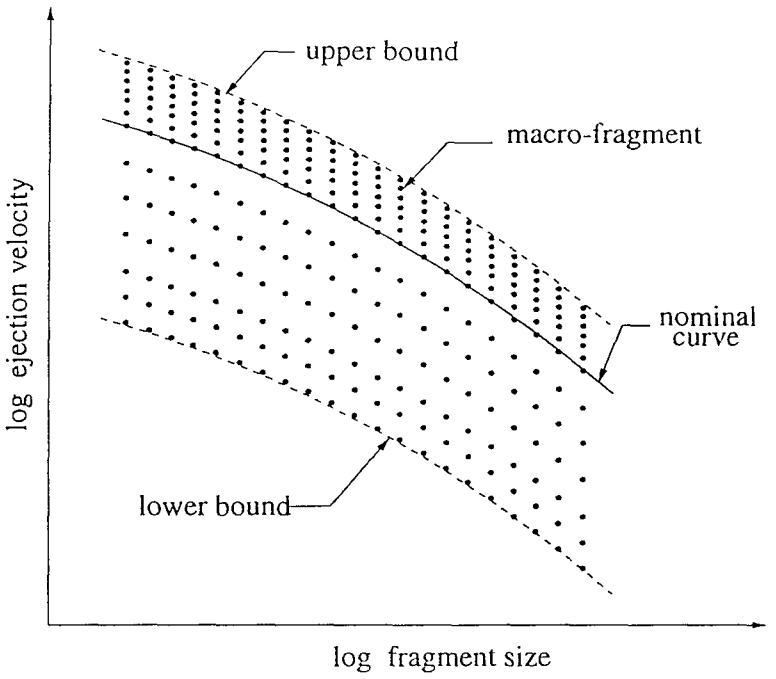

Figure 3.3: Macro-fragments

of the relevant equations for a set of fragment sizes over the range 1μm -1m. This produces a set of 'pseudo-continuous' distributions. The CN curve can then be used to form a discrete number distribution by calculating the difference between successive CN values (working in the direction of decreasing fragment size) and then attributing the number obtained to the mean fragment size in the corresponding size range. Hence, from $j + 1$ data points used to produce the pseudo-continuous distribution, j discrete fragment sizes are generated. The mass, BC and velocity curves are sampled directly to yield the masses, BCs and Δvs that correspond to these fragments. The fragment number distribution is randomised about the nominal by using a random number generator to select a value between user-specified upper and lower bounds. The randomised distribution is then scaled either up or down to conserve mass. A triangular spread of velocities is also introduced about each nominal Δv value [62]. For each discrete size, the debris is grouped into several macro-fragments (13 samples are used), with the velocity and number of particles in each determined from the relevant spreading function sample (Figure 3.3). For collisions, an upper-bound of 1.3 times the impact velocity is imposed upon the Δvs. For scenario 2, which considers the pre- and post-collision energy balance and assigns

$\triangle$vs through the equi-partitioning of KE assumption, the $1.3\mathbf{V}_{rel}$ truncation results in a large loss of KE from KE'_{spread}. By definition, all of KE'_{spread} is used in fragment spreading, with the energy losses associated with the breakup being accounted for in Q_{loss}. To ensure that KE'_{spread} is fully assigned, scenario 2 calculates average fragment KEs and hence $\triangle$vs iteratively.

Firstly, the average fragment KE must be weighted to allow for the triangular velocity spread. The average spread KE per fragment for cloud i (i=1.2) is given simply by,

$$\overline{KE'}_{spread,i} = \frac{KE'_{spread,i}}{N_{frags,i}}, \tag{3.20}$$

where $N_{frags,i}$ is the number of fragments in cloud i. Hence for each fragment size (D_j),

$$\overline{KE'}_{spread,i} = \frac{1}{2} M_j \triangle V_{i,j}^2, \tag{3.21}$$

where M_j is the fragment mass and $\triangle V_{i,j}$ is its nominal ejection velocity. For a triangular velocity spread with k samples, equation (3.21) becomes,

$$\overline{KE'}_{spread,i} = \frac{1}{2} M_j \triangle V_{i,j}^2 \sum_k \delta_{1k}\ \delta_{2k}^2, \tag{3.22}$$

where $\delta_{1k} = N_{frags,k}/N_{frags,j}$ and $\delta_{2k} = \triangle V_k / \triangle V_{i,j}$. Hence, the nominal ejection velocity for fragment mass M_j is given by,

$$\triangle V_{i,j} = \sqrt{\frac{2\ \overline{KE'}_{spread,i}}{M_j \sum_k \delta_{1k}\ \delta_{2k}^2}}. \tag{3.23}$$

Secondly, the above procedure must be repeated until all of $KE'_{spread,i}$ is accounted for. Once $\triangle V_{i,j}$ has been evaluated for each fragment size D_j, the size at which the $1.3\mathbf{V}_{rel}$ truncation occurs (D_{trunc}) can be determined as can the number of fragments with size $> D_{trunc}$ (Figure 3.4). Hence the shortfall in spread KE can be determined. This shortfall is added to the spread KE of the fragments whose $\triangle$vs have not been truncated and the average spread KE and nominal $\triangle$vs are recalculated for these particles. A new value for D_{trunc} is determined and the new spread KE shortfall calculated. The iteration is completed when the KE shortfall reaches zero or, in more practical terms, becomes less than a specified tolerance.

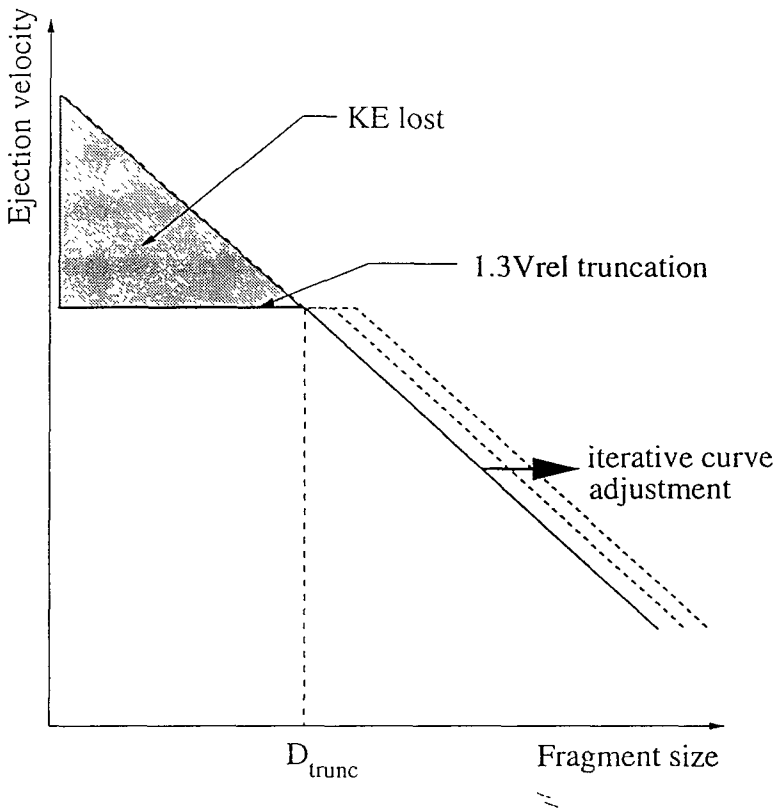

Figure 3.4: Use of KE equi-partitioning to calculate fragment Δvs

Once the fragment distributions have been produced and the CN and Δv distributions have been randomised and triangularised respectively, the next step is to use the distributions to generate the debris cloud. For cloud type 1, this involves partitioning the fragments into the desired number of cloud shells. The isotropic cloud model in program BREAKUP can utilise up to 8 spherical Δv shells. The number of fragments in each shell is determined from the fragment Δvs and the shell inner and outer bounding velocities. Once the assignment of fragments to shells is completed, the spatial density of debris in each shell can be calculated, as can a weighted average shell BC. These parameters, along with the bounding shell Δvs, fully describe the continuum cloud. As stated in section 2.1.4, this type of cloud representation is best suited to collision hazard analyses. Cloud propagation corresponds to the evolution of the shell boundaries, not the orbits of individual fragments. If the latter form of analysis is required then the second cloud type should be adopted, which is discussed in the following subsection.

3.4.2 Random Fragment Generation

Overview

In contrast to the isotropic continuum cloud outlined above, the non-isotropic cloud model described here deals with the orbits of individual fragments or, for the smaller particles, representative macro-fragments. This type of approach lends itself much better to long-term forecasts of the debris' dispersion and lifetime than the continuum model, and also enables direct comparisons to be made with recorded fragmentation events. On-orbit breakups are generally described by their Gabbard diagrams. Developed by John Gabbard, these depict the intensity of the breakup, and hence the initial character of the debris cloud, by plotting each fragment's apogee and perigee against its orbital period. The Gabbard diagram can also provide graphical clues as to the cause of the fragmentation by virtue of the orderedness/asymmetry of the points plotted and their degree of dispersion. Gabbard diagrams and the analysis of them are explained in some detail in [51].

Although cloud type 2 is ideally suited to the analysis of the fragments' orbits, and hence the cloud's orbital evolution, such a model can also be used for collision hazard analysis if debris density can be calculated for a given region of the cloud. Whereas the isotropic cloud was partitioned into concentric spherical shells in spread velocity space, to maintain the additional directional information necessary for anisotropy, the non-isotropic model must divide spread velocity space into a three-dimensional grid or cell structure. The simplest, and indeed most suitable, method of achieving this is to use a spread velocity space divided up into cells using spherical polar coordinates. Such a representation enables the straightforward assignment of fragments to cells and the calculation of debris density, and also facilitates close comparison with the isotropic model. A non-isotropic debris spread can be formed within the bounds of the spherical grid structure because each cell will generally contain a different collection of fragments. Different cells corresponding to the same $\triangle$v band may contain different numbers of different sized fragments. Some cells may even be empty.

By assuming that the debris from a breakup is ejected uniformly in all directions, an isotropic cloud model smoothes out the effects of regions of high/low fragment density in the breakup (not to be confused with the cloud's subsequent pinch locations). Hence, an isotropic model can either underestimate or overestimate values of collision probability. The errors incurred by the assumption of isotropic fragment ejections have never been quantified. The development and use of a non-isotropic cloud model will enable the importance of considering fragment ejection directions to be assessed.

Fragment selection

A non-isotropic cloud model requires some method of selecting debris masses, Δvs etc from the fragment distributions. The macro-fragment distribution shown in Figure 3.3 can be used directly in the selection process as it offers a range of Δvs for each fragment size and a randomised number of particles in each macro-fragment. Two threshold fragment sizes are also utilised. D_{min} is the smallest fragment that is considered in the cloud generation procedure. This enables the smaller particles to be neglected either for computational practicality/convenience or alternatively to represent a spacecraft's shielding capability. All the fragments deemed to be too small to cause significant damage to the spacecraft (even at the highest possible impact velocity in question) can thus be filtered out of the analysis at the outset. D_{ind} is the limit for the smallest fragment that is treated individually. Again this limit has two main uses. Collisions produce too many debris objects for them all to have ejection directions assigned, orbits determined etc. So, if D_{min} is set so as to include 'all' the debris in the macro-fragment distribution, then D_{ind} is needed to set a practical limit on the number of fragments considered individually. The second use of D_{ind} is to represent the trackable debris threshold. This is particularly useful when comparing simulated results (e.g. Gabbard diagrams) with data from actual on-orbit fragmentations. Observational data from recorded events is restricted by the sensitivity of the sensors in question (Figure 1.3) and so there is a size limit on the debris objects that are considered. Setting D_{ind} to be approximately equal to this

threshold allows a virtually direct comparison of results to be made. Debris which falls in the size range $D_{min} \leq D < D_{ind}$ is considered on a macro-fragment level, with the ejection direction selected and the orbit determined for the macro-fragment taken to be representative of all the particles within the macro-fragment.

In the macro-fragment distribution, and the randomised fragment number distribution used to create it, mass is conserved between the pre- and post-collision states. These distributions do not deal with whole numbers of fragments, however, and so in each macro-fragment there is not, in general, an integer number of particles. If the real numbers of fragments were simply rounded down to the nearest integer in the fragment selection procedure then a significant amount of mass would be 'lost' in the process. Hence, before it is used in the fragment selection procedure, the real number macro-fragment distribution is converted to a mass-equivalent integer distribution. The process takes place in two stages. Firstly, for each fragment size, the difference between $int(\sum_{k=1}^{13} N_{frags,k})$ and $\sum_{k=1}^{13} int(N_{frags,k})$ is calculated (where $int(N)$ is the integer part of the real number N) and the whole number of fragments in the difference are each randomly placed in the 13 triangular spread Δv bins. The mass discrepancy that still exists is determined and passed on to stage two of the process. This works from the largest fragment size down, calculating, for each fragment size, the whole number of fragments of that size that can be produced given the mass left to assign. Working from the largest (and hence most massive) fragments downwards assigns the remaining mass the most quickly and does so without creating enormous numbers of extra fragments. The smaller fragments enable the mass balance to be established almost exactly. Each new fragment generated in this way is again randomly assigned one of the 13 possible Δvs for its size. Thus a modified distribution of fragments is produced. It should be noted that, for true mass conservation, the procedure is carried out on the entire fragment distribution, i.e. is not limited by D_{min} or D_{ind}.

Ejection direction biasing

As stated in section 2.1.4, the velocity, or $\triangle$v, distributions only give the magnitude of each fragment's ejection velocity. Hence, some method of assigning ejection directions is needed. The simplest method is to attribute directions completely at random. There are two main drawbacks with this approach, however. Firstly, angular momentum will not be conserved. This is not a major problem, though, because only one of the four breakup scenarios described earlier in this chapter actually considers momentum conservation. Moreover, the changes in angular momentum will generally be much smaller than the total orbital angular momentum of system. Secondly, a completely random selection process offers no control over the choice of ejection directions. If the effects of anisotropy are to be investigated then a method of biasing the ejection directions must be utilised so that a variety of cases can be examined. Also, a truly random assignment of directions is actually itself isotropic. Anisotropy is only observed in practice due to the limited number of fragments and hence directions selected, and also any numerical biasing in the random number generator used. Program BREAKUP uses a novel parametric model for controlling the characteristics of the fragment ejections. The model is both simple and versatile and enables a wide variety of different scenarios to be explored.

Ejection directions are most simply specified by two angles referenced to a standard orthogonal coordinate frame, for example the standard polar angles α and β shown in Figure 3.5a. Hence, the selection of a direction can be considered as the selection of these two angles. α and β can be worked with directly but the parametric model in BREAKUP instead deals with the angles ϕ and θ shown in Figure 3.5b. ϕ controls the initial X-Y plane projection of the vector and has the range $0^o \leq \phi < 360^o$. θ then rotates the vector about the ejection X-axis. θ also has the range $0^o \leq \theta < 360^o$. Hence ϕ can be thought of as the vector's 'X-axis cone angle', and θ can be defined as the 'X-axis revolution angle'. Note that for the angle ranges specified, each vector position is essentially defined twice. This is not a problem, however, as each angle is given half the probability value it would be assigned if ϕ was used in the range $0^o \leq \phi < 180^o$, for example. Defining both

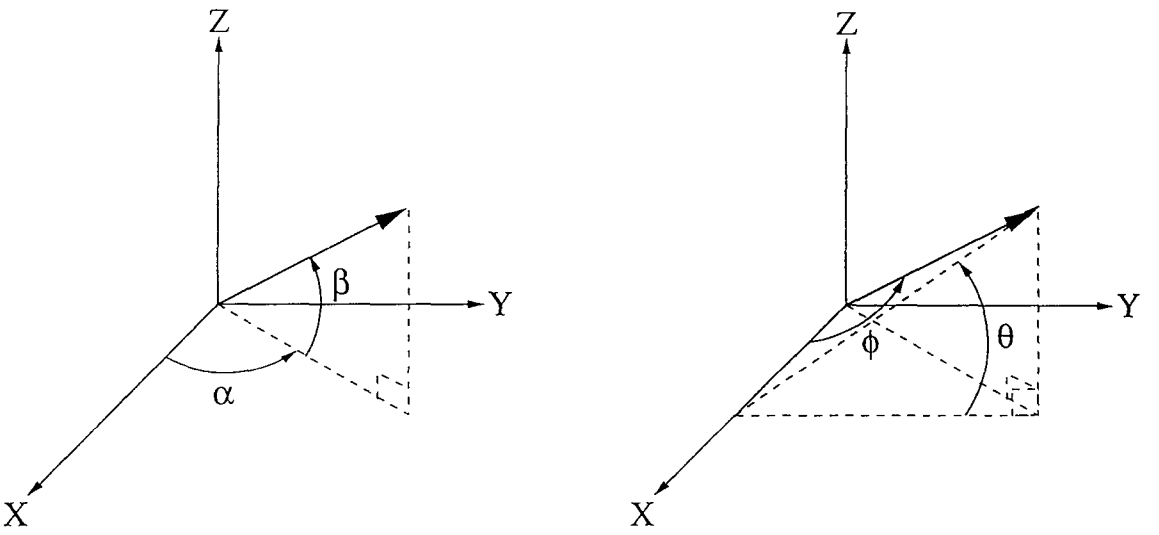

a) standard polar angles

b) X-axis cone and revolution angles

Figure 3.5: Angles used for ejection direction specification

angles in the range $0^o - 360^o$ is conceptually more straightforward and also enables the probability weighting of the angles' selection (discussed next) to be visualised graphically more effectively.

The angles ϕ and θ are selected using a random number generator and two probability 'lines'. The probability lines contain, for each angle, the cumulative probability of selecting an angle up to that value. The random number generator produces a random number between 0 and 1 individually for ϕ and θ, and the angle whose cumulative probability bin the random number falls into is selected in each case. The simplest probability line for each corresponds to a uniform probability distribution (e.g. for θ in Figure 3.6). In this case the likelihood of choosing any angle is the same. Note that the largest angle selectable shown on Figure 3.6 is 359^o. This is because the angular distribution used is discrete, with integer values only considered, i.e. 0^o, 1^o, 2^o, ... 359^o. If the probability distributions for both ϕ and θ were uniform then the spread of ejection directions would be theoretically isotropic, as discussed above.

Anisotropy is introduced into the ejection selection process by weighting the angular probability distributions. Three model parameters are used. Firstly, E_{fb} is

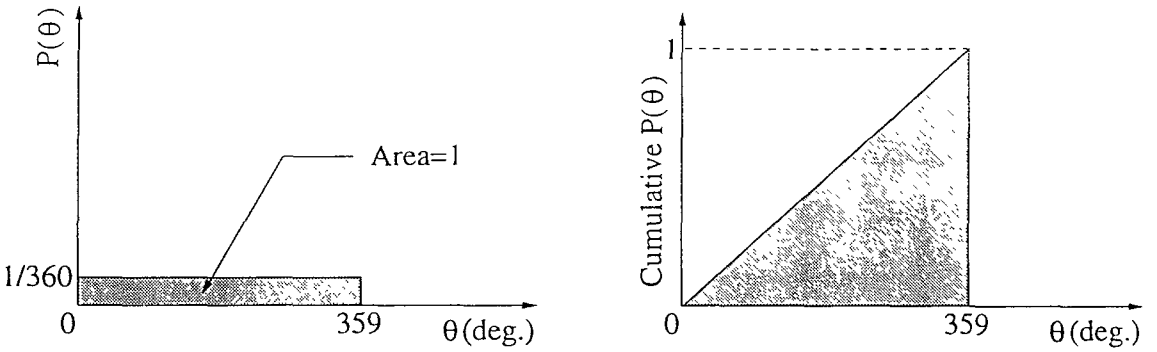

a) angular probability distribution b) cumulative probability distribution

NOTE: a) and b) are not to scale

Figure 3.6: Uniform probability distribution

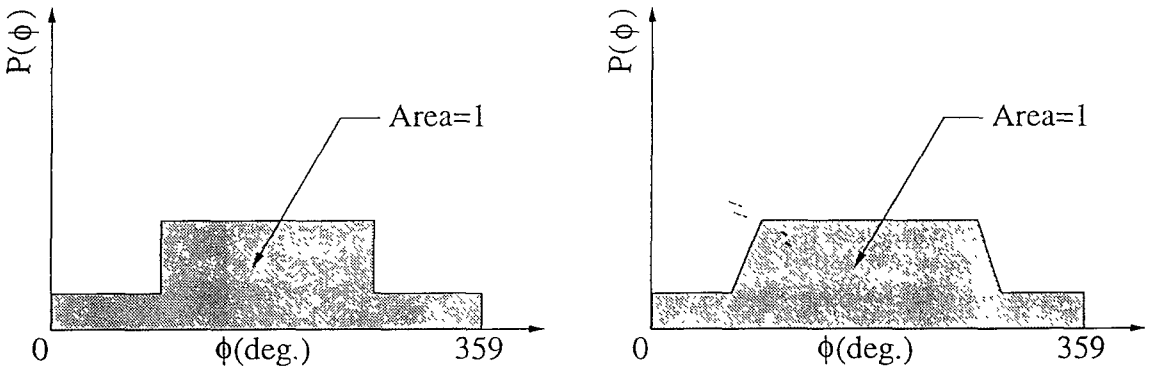

a) stepped forward bias b) ramped forward bias

Figure 3.7: Forward/backward ejection biasing

used to introduce a forward/backward bias into the fragment Δvs. 'Forward' is defined as being in the negative ejection X-axis direction. This definition is adopted to achieve commonality between the ejection coordinate system and the orthogonal orbiting axis frame defined in Figure 2.2. The 'default' condition adopted considers the two reference frames to be coincident. In the orthogonal orbiting axis frame, the X-axis can be qualitatively regarded as being in the anti-flight direction, i.e. backwards with respect to the orbital motion of the object in question. The range $90^o \leq \phi < 270^o$, therefore, corresponds to the forward direction. E_{fb} scales up the probabilities of all the values of ϕ in the forward sector by the factor $2E_{fb}/(E_{fb}+1)$. E_{fb}=1 represents no forward/backward biasing and positive values of E_{fb} greater than one represent a dominance in the forward direction. To ensure that the cu-

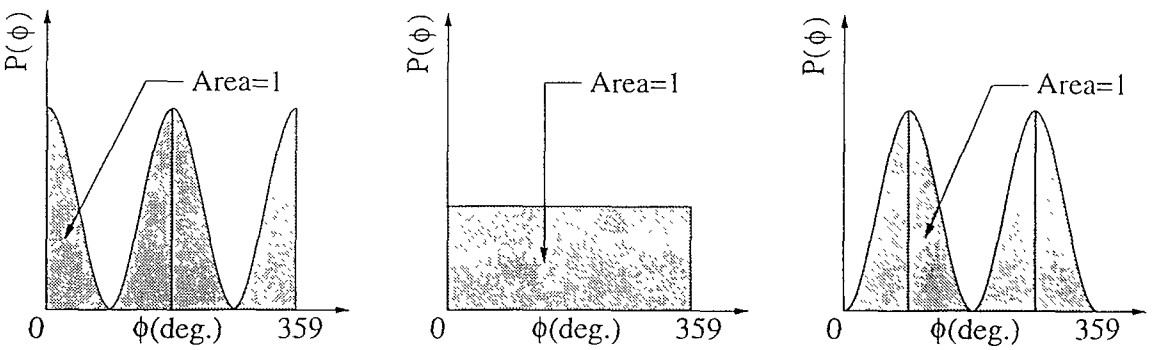

a) maximum tangential bias b) no bias (i.e. isotropic) c) maximum radial bias

Figure 3.8: Radial spread function

mulative angular probability remains equal to 1, the probabilities of the backward angles are scaled down accordingly (i.e. by $2/(E_{fb}+1)$. This produces a 'step' type probability distribution as shown schematically in Figure 3.7a. With this approach, however, adjacent ejection angles 89^o and 90^o, and also 269^o and 270^o, have markedly different probabilities of selection. This discontinuity in the distribution is not physically meaningful and so 'ramps' are introduced into the distributions to produce a more gradual transition (Figure 3.7b).

Secondly, the parameter E_{tr} is employed to provide the facility for biasing the ejection directions in either the tangential (i.e. $\pm X$) or radial ($\pm Y$) sense. This is achieved by superimposing the following function on the above 'ramped' distribution,

$$f = acos^2\phi + bsin^2\phi, \tag{3.24}$$

where $a = 1 + E_{tr}$ and $b = 2 - a$. E_{tr}=1 produces the maximum accentuation of the tangential angle probabilities (angles of ϕ around 0^o and 180^o) by putting the $sin^2\phi$ term to zero in f (Figure 3.8a). Conversely, E_{tr}=-1 causes the $cos^2\phi$ term to become zero and hence allows $\phi = 90^o$ and 270^o to dominate (Figure 3.8c). E_{tr}=0 produces a flat, and hence isotropic, angular probability distribution (Figure 3.8b). Values of E_{tr} between 1 and -1 produce varying degrees of tangential/radial ejection dominance.

Using the above two parameters to weight $P(\phi)$, and adopting a uniform (i.e. flat) distribution for $P(\theta)$, creates an ejection direction probability space which is a

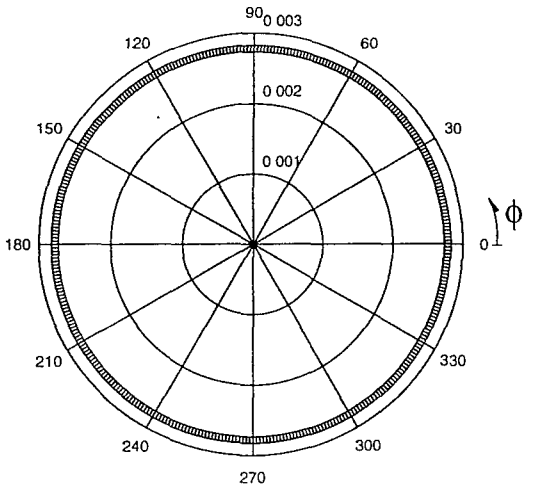

a) Polar plot of P(ϕ) vs ϕ (deg.)

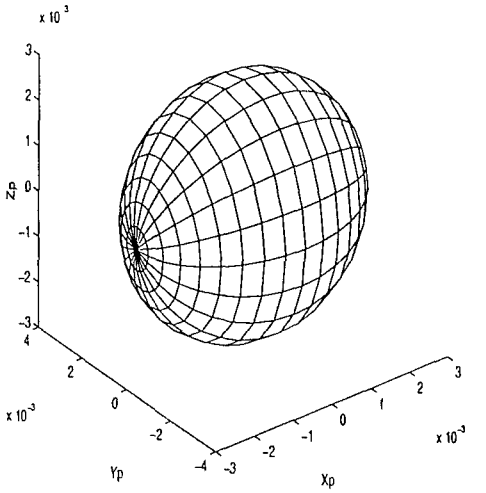

b) Ejection direction probability space

Figure 3.9: Isotropic fragment spread

solid of revolution about the ejection X-axis. The directional probability weighting can be visualised on either 2D polar or 3D Cartesian plots. The simplest example is that of an isotropic spread, where E_{fb}=1 and E_{tr}=0. A polar plot of $P(\phi)$ vs ϕ is then a circle, the radius of which is $P(\phi)$ (Figure 3.9a). In 3D, the shape of ejection direction probability space (Xp,Yp,Zp), and hence spread velocity space, is a sphere (Figure 3.9b). The radius of each point is the probability of selecting the direction that it represents.

If a forward ejection dominance is introduced, then the radii of the forward points on the two plots will be increased. For example, Figure 3.10 shows the case where E_{fb}=5 and E_{tr}=0. Here, a fragment is 5 times more likely to be ejected in the forward direction (i.e. $90^o \leq \phi < 270^o$) than in the backward direction. No tangential/radial biasing is present, however, and so each half of the polar plot is a semi-circle and each half of the 3D plot is a hemisphere, except for the bridging (ramp) function which joins the two sections.

If E_{tr} is then set to 1 to bias the ejections in the tangential direction, the fragment spread pattern shown in Figure 3.11 is produced. Alternatively, setting E_{tr} equal to

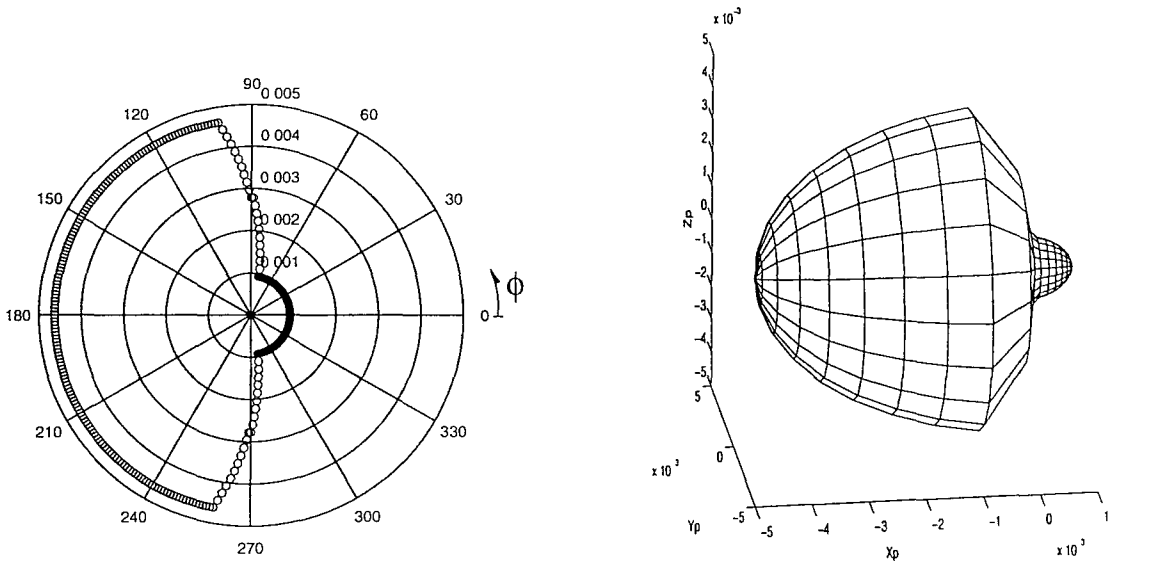

a) Polar plot of P(ϕ) vs ϕ (deg.) b) Ejection direction probability space

Figure 3.10: Fragment spread with forward biasing

-1 produces a radial ejection dominance (Figure 3.12).

Using a large (positive) value of E_{fb} and E_{tr}=1, the ejection of fragments can be directed into a jet along the negative ejection X-axis. Even under these conditions, however, significant radial ejections can exist which serve to diminish the focus of the jet. The thickness of the jet can be reduced using the third model parameter E_{jet}. This acts to thin the tangential probability 'lobes' by transferring probability from the radial to the tangential angular regions. Two phases are used in the process to emphasise the thinning. Probability is transferred from the radial regions to the tangential regions according to the following formula,

$$P(trans) = P(\phi_{-})\frac{E_{jet}}{(E_{jet}+1)}, \tag{3.25}$$

where $P(trans)$ is the probability to be transferred and $P(\phi_{-})$ is the probability of selecting 'radial' angle ϕ_{-}. E_{jet}=0, therefore, produces no enhancement. $P(trans)$ is subtracted from $P(\phi_{-})$ and added to $P(\phi_{+})$. $P(\phi_{+})$ and $P(\phi_{-})$ are paired together to create the maximum enhancement. The parameter E_{jet} has no upper bound, but its effectiveness diminishes as it is increased, as $E_{jet}/(E_{jet}+1) \rightarrow 1$. An upper limit of 10 is, therefore, recommended. If further jet-focusing is required, additional

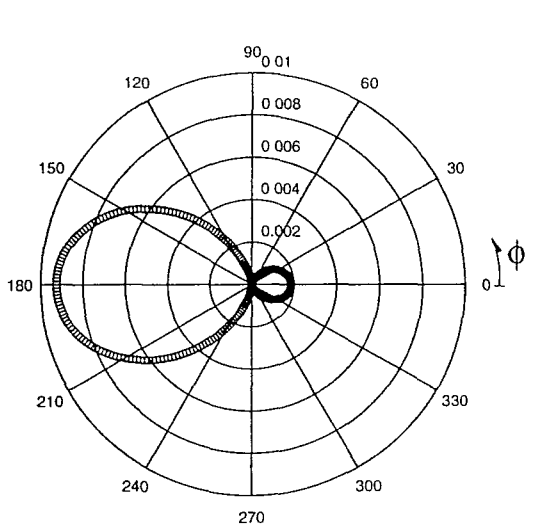

a) Polar plot of P(ϕ) vs ϕ (deg.)

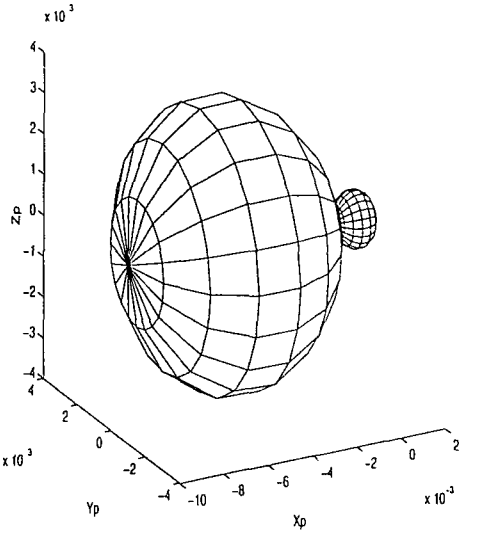

b) Ejection direction probability space

Figure 3.11: Fragment spread with forward and tangential biasing

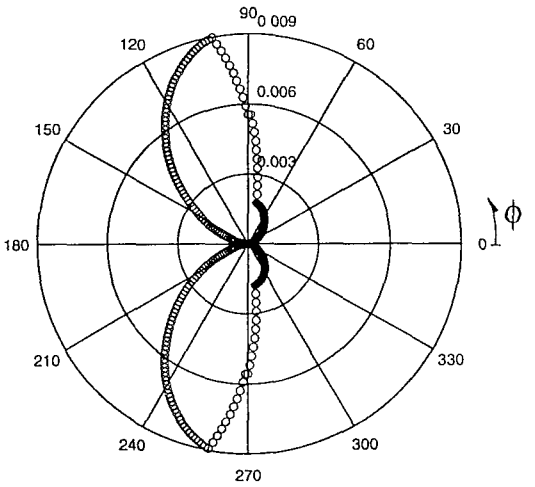

a) Polar plot of P(ϕ) vs ϕ (deg.)

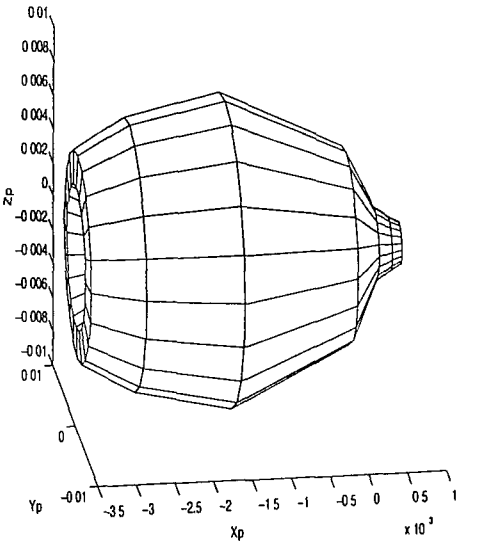

b) Ejection direction probability space

Figure 3.12: Fragment spread with forward and radial biasing

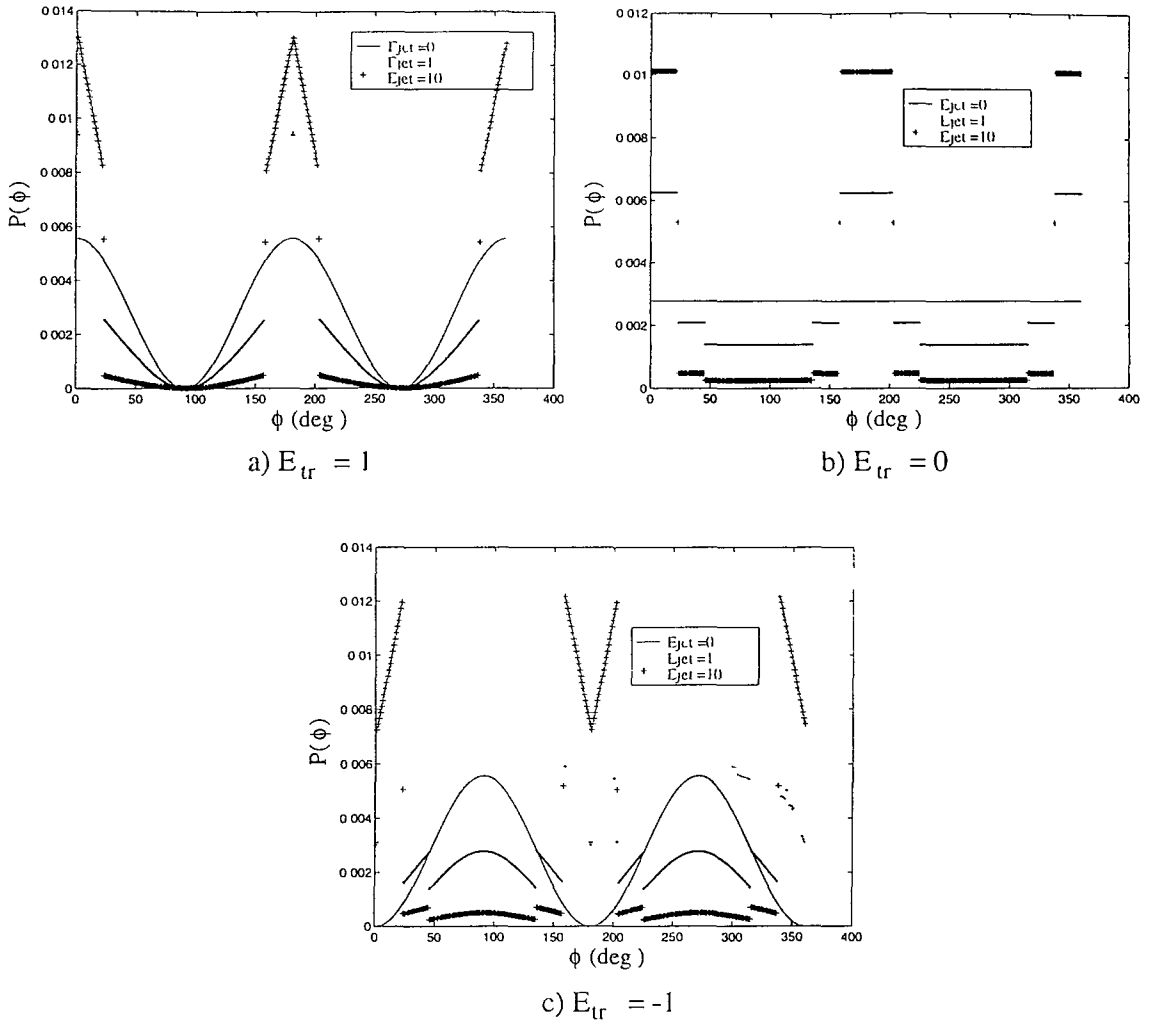

Figure 3 13: Influence of E_{jet} on $P(\phi)$

stages can be introduced into the probability redistribution process.

The influence of E_{jet} on $P(\phi)$ is shown in Figure 3.13 for several different values of E_{tr}. E_{fb}=1 in each case. Figure 3.13a corresponds to the most appropriate and meaningful use of E_{jet}, i e when E_{tr} has its maximum tangential value (=1). E_{jet} increases and sharpens the peaks of the unenhanced $P(\phi)$ vs ϕ curve and flattens down the regions surrounding the radial troughs. When E_{tr}=0, the original $P(\phi)$ vs ϕ curve is flat and so the jet-enhanced probability distribution does not have sharp peaks. The highest probability in Figure 3.13b is around 30% lower than that in Figure 3.13a but is sustained across virtually the whole tangential angle range. Figure 3 13c shows the effect of E_{jet} on an initially radial-dominated probability

distribution. E_{jet} acts out of phase with the initial distribution and so produces 'inverse' peaks in the tangential angle regions. The highest probabilities are, therefore, registered at the extremities of the tangential angle regions. It can be seen from Figure 3.13 that no measures are taken to smooth out the curve discontinuities as is done with E_{fb}. The purpose of E_{jet} is to produce a more highly focussed spread of fragment ejection directions and so the discontinuities produced in the distribution of $P(\phi)$ actually represent the desired effect.

The 3 parameters described so far determine the spread of fragment ejection velocities with respect to the ejection axis system. With E_{fb}, there is only provision to introduce an ejection dominance in the forward direction. Also E_{tr} and E_{jet} can only bias the selection of directions in the tangential and radial directions. For greater model flexibility, and to allow jet-like ejections in any direction to be produced, the ejection X-axis (and hence the ejection probability space solid of revolution) can be pointed in any direction relative to the orbiting axis frame using $\mathbf{X}_{ej}$. From the three vector components of $\mathbf{X}_{ej}$ in the orbiting frame, the polar angles α_{xej} and β_{xej} can be calculated. These are then added to the polar angles of each fragment's ejection direction with respect to the ejection frame (i.e. α and β) to yield the resultant direction in the orbiting frame. It is important to combine the X-axis pointing offset with each fragment's ejection frame $\triangle$v direction in this manner because if the directions are combined in terms of ϕ and θ and then the resultant is transformed to α_{res} and β_{res}, the X-axis pointing information is 'washed out' in the process. For explosions, $\mathbf{X}_{ej}$ can be set to any direction. For collision-induced breakups, however, the velocity vector of the projectile relative to the target defines the collision axis of the system (Figure 3.1) and so is taken as specifying the positive ejection X direction.

Cloud description

The debris cloud generated by the breakup is described by two fragment 'catalogues'. All debris larger than D_{min} is included in the breakup 'cell catalogue'. This describes the cloud in terms of numbers of fragments, debris densities and cell-average ballistic

coefficients using a 256 cell, spherical polar coordinate structure ($8\alpha \times 4\beta \times 8\triangle$v). Each cell can contain a mixture of individual and macro-fragments. Once a fragment's (or macro-fragment's) ejection velocity vector has been calculated (from the magnitude of its $\triangle$v and the ejection direction selected) then the bounding values of α, β and $\triangle$v which describe each cell, i.e. (α_{min}, α_{max}, β_{min}, β_{max}, $\triangle v_{min}$, $\triangle v_{max}$), are used to determine into which of the 256 cells the fragment(s) fall. The number of fragments in the cell and the total cell BC are then updated accordingly. At the end of the fragment generation procedure, the number of fragments in each cell is used along with the cell volume and the total cell BC to calculate the spatial density of debris in the cell and its average BC. The form of output that is produced is most useful for collision hazard analysis as this type of investigation deals primarily with debris fluxes/spatial densities. It can also be used to investigate how the density of debris within a cloud varies over time and space as the cloud evolves, enabling potentially dangerous high-density regions to be identified. Both these aspects of debris cloud analysis are discussed later, in Chapters 6 and 5 respectively.

The second type of debris cloud representation is the 'fragment catalogue'. This contains information (orbital parameters, fragment mass, size and BC) on all the individual fragments produced, i.e. those larger than D_{ind}. For each debris object, the ejection velocity vector is used, along with the cloud centroid velocity vector (if the kinematic model is being used) and the orbital velocity vector of the breakup CM, to determine the fragment's orbital velocity vector. This, in conjunction with the breakup position vector, enables the fragment's orbital parameters to be calculated. The fragment catalogue can thus be used to plot the Gabbard diagram for the breakup.

3.5 Program BREAKUP

3.5.1 Programming issues

BREAKUP4.0 is the latest version of program BREAKUP and is the first program in the SDS software suite, version 2.1. The program is run via two input files,

break4_control and *frag_dist_params*. *break4_control* is the main input control file and contains details on the orbit of the breakup object pre-breakup and the projectile in the case of a collision-induced fragmentation, and also the event scenario being modelled and type of cloud output to be used. In addition, *break4_control* includes the various run parameters, for example γ, ϵ, ζ and μ used in the kinematic model, and E_{fb}, E_{tr}, E_{jet} and $\mathbf{X}_{ej}$ for the non-isotropic cloud model. Inputs are changed by simply editing the relevant parameter values in *break4_control*, using a standard Text Editor for example, and re-saving the file containing the new inputs (Figure 3.14). *frag_dist_params* contains the values to be used for the breakup model fragment distribution parameters. As with *break4_control*, the parameters in *frag_dist_params* can be altered by editing the values in the file.

breakup4.0.f is the main Fortran calculation and control program. The majority of the program's work is carried out in external subroutines, also written in Fortran, which are linked to the main program in its compilation by a makefile. The program only takes input from the two files described above and can either be run from a command line or via the BREAKUP4.0 X-Windows menu. All four SDS programs can be menu-driven. The menus contain options for input file/program editing, program compilation, program running and initiation of the Matlab-SDS graphical interface. Each menu is constructed from a C program running in an xterm. The BREAKUP4.0 menu is shown in Figure 3.15.

Program run information describing the pre- and post-breakup states is written either to the screen or to file *break4_info*. The main output from the program, however, is written to a number of data files. These can then be used by the dedicated Matlab-SDS plotting routines, for example, for results visualisation. The fragment distributions produced are written to file *break4_dist.dat*. This is common for both isotropic and non-isotropic cloud types. The isotropic cloud model only generates one extra results file, *break4_iso.dat*, containing numbers of fragments, debris densities and average BCs in shell (i.e. $\triangle$v bin) format. The non-isotropic model produces five additional output files. *break4_phi.dat* and *break4_dir.dat* detail the ejection angle probability distributions and the directions selected respectively

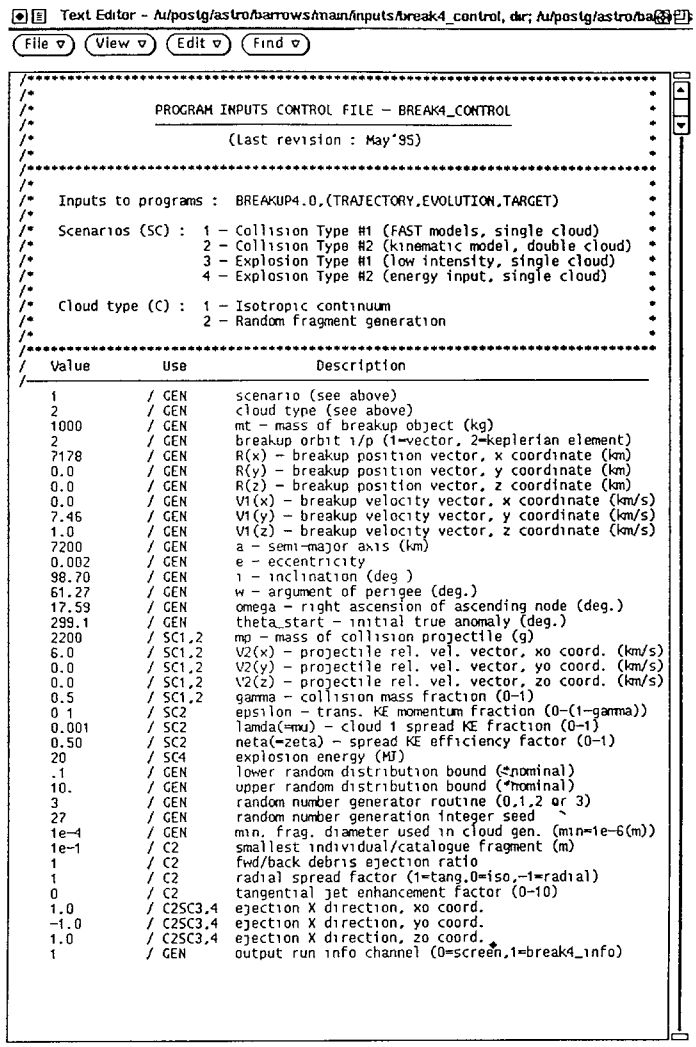

Figure 3.14: BREAKUP4.0 input control file *break4_control*

break4_phi.dat was used, along with routines *phiplot* and *phiplot3* to produce Figures 3.9- 3.12. *break4_cells.dat* and *break4_fcat.dat* contain the cell and fragment catalogues. *break4_forb.dat* contains fragment orbit information.

A simplified flow-diagram for the program is shown in Figure 3.16. Also, more on the output and visualisation of results from the program is included in the next section.

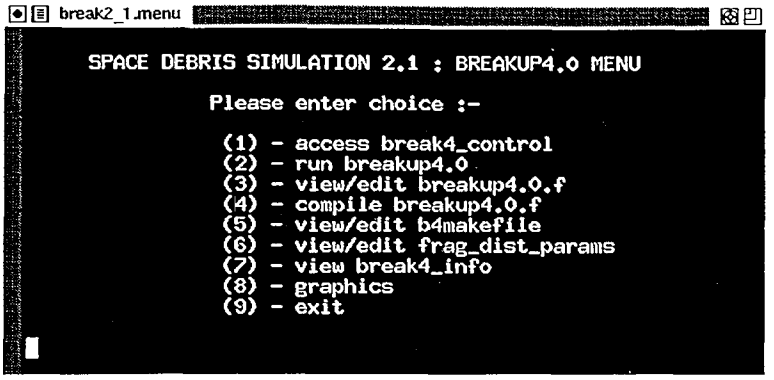

Figure 3.15: BREAKUP4.0 menu

3.5.2 Results Validation

Overview

The validation of results from any piece of simulation software is extremely important and is essentially a two-stage process. Firstly one must ensure that the code does what it is programmed to do, i.e. the code contains no bugs, is a direct translation of the models/algorithms in question and operates to the required level of accuracy in the results that it produces. Once satisfied that this has been achieved, one must then address the second question, namely how well does the program actually model what it is attempting to simulate? One can compare different simulation codes but the only true test of the quality of the model is how well the simulation results compare with 'real' data. In the case of program BREAKUP4.0, the main source of suitable data on actual, recorded, orbital fragmentation events are the event Gabbard diagrams, for example those in [91]. These are produced from the observed orbits of the fragments generated by the breakup. Care must be taken when using Gabbard diagrams, however, as factors such as sensor sensitivity and the time taken to detect the cloud can affect the number of fragments observed and can also produce an incomplete or distorted picture of the event. For breakups in LEO, atmospheric drag will cause the debris in the leading portion of the cloud to decay most quickly, and many of the fragments may even re-enter before they are observed. This may lead to a 'drooping' of the left-hand limbs of the Gabbard diagram or alternatively may give the false impression that the majority of the frag-

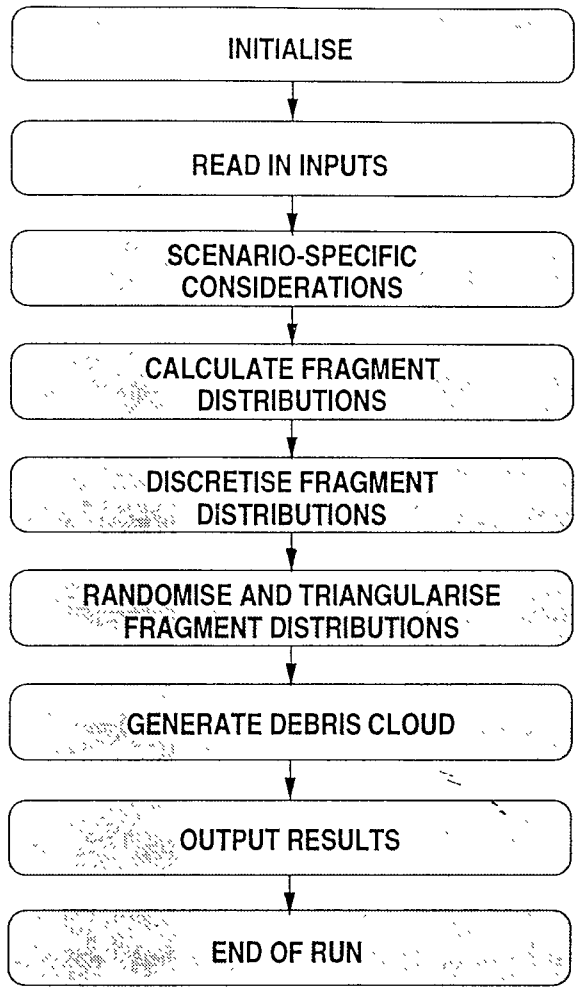

Figure 3.16: BREAKUP4.0 flowchart

ments were ejected in the forward direction. These influences must, therefore, be borne in mind when attempting to match simulated results with actual event data.

Model comparison

The first step in validating the results produced by BREAKUP4.0 is to ensure that the fragment distributions generated are 'correct', i.e. a faithful reproduction of the original model equations. This is a straightforward process and can be achieved quite simply by visually comparing the distribution plots produced by BREAKUP4.0 with those in the literature [58, 60, 64].

Another and perhaps more interesting test is to compare the distributions produced by the two collision and explosion scenarios for the same breakup event. The

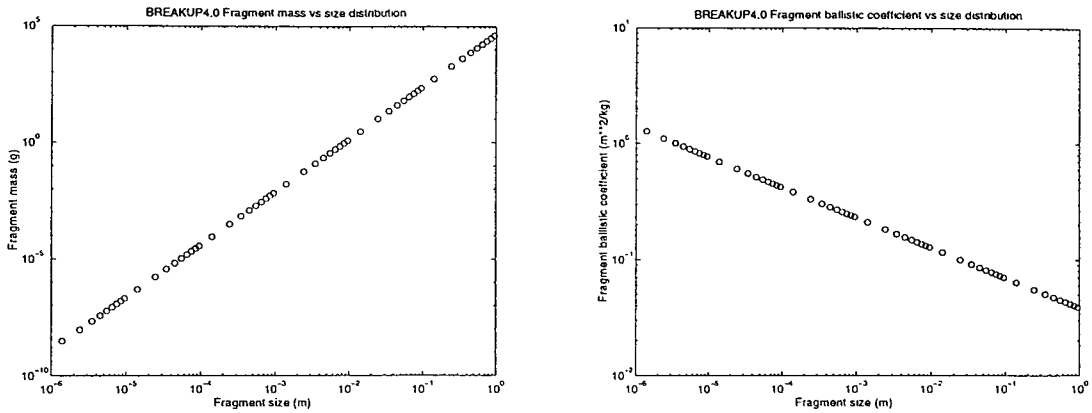

a) Fragment mass distribution

b) Fragment BC distribution

Figure 3.17: Fragment mass and ballistic coefficient distributions

collision example chosen was that of a 500kg LEO satellite impacted by a 1kg piece of debris at 10km/s. The debris impact energy to target mass ratio for the impact is, therefore, 100 (J/gram) and so the target satellite fragments completely as a result of the collision. The mass versus size and ballistic coefficient versus size distributions for the event are shown in Figure 3.17. These distributions are event-independent and so are the same for both the collision scenarios. Figure 3.18a shows the fragment number distributions for scenarios 1 and 2. The scenario 2 distribution is produced by summing the contributions from both cloud volumes. The two number distributions are quite similar (same randomised spread about the nominal) but noticeable differences are present at the low size end. These discrepancies are somewhat masked by the logarithmic scale. Figure 3.18b shows the ejection velocity distributions. The $\triangle$v curves for both scenario 2 clouds are considerably higher than the scenario 1 curve. This is caused by the amount of the collision kinetic energy that is made available to fragment spreading in the kinematic model energy conservation equation, and also the apportionment of spread KE between the two clouds. Using ζ=0.99 results in the scenario 2 simulation attributing over twice the energy to fragment ejections compared with scenario 1 (the scenario 1 figure is obtained by summing the KEs of all the fragments generated). Also, even though in this example only 5% of the total spread KE available is assigned to cloud 1, the small number of (relatively large) fragments in the non-involved cloud volume

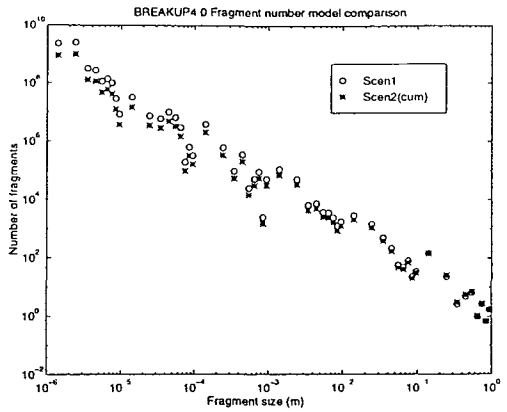

a) Fragment number distributions

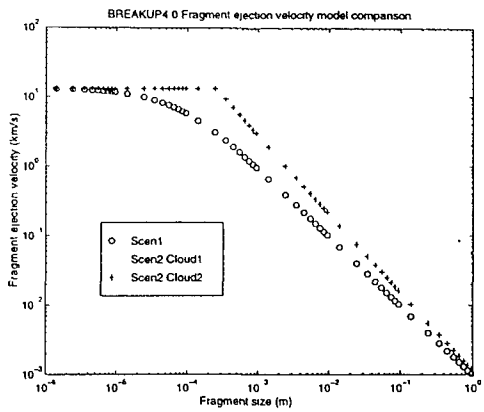

b) Fragment ejection velocity distributions

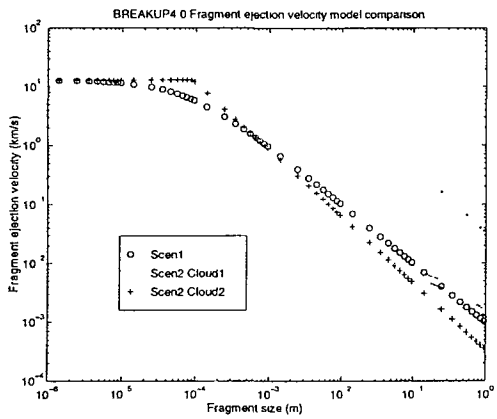

c) Fragment ejection velocity distributions

Figure 3.18: Fragment number and $\triangle$v comparisons for scenarios 1 and 2

means that the average KE per fragment is much larger in this cloud than in the collision volume and hence the $\triangle$vs produced are higher. Figure 3.18c shows the $\triangle$v curves for the same example but with ζ=0.40 for scenario 2. This value of ζ results in the fragment spread KE being virtually the same for both scenarios. The scenario 1 and scenario 2 (cloud 2) curves are much closer together as a result.

The explosion example also considers the breakup of a 500kg LEO satellite. The fragment number distributions for model scenarios 3 and 4 are shown in Figure 3.19a. As with Figure 3.18a above, the same randomisation process is carried out on both distributions. The explosion energy utilised for scenario 4 is 10MJ. This produces fewer fragments than the scenario 3 across the whole size range indicating that, in this example, the explosion energy implicitly associated with scenario 3 is greater. Figure 3.19b shows the common $\triangle$v curve for both explosion scenarios. The mass

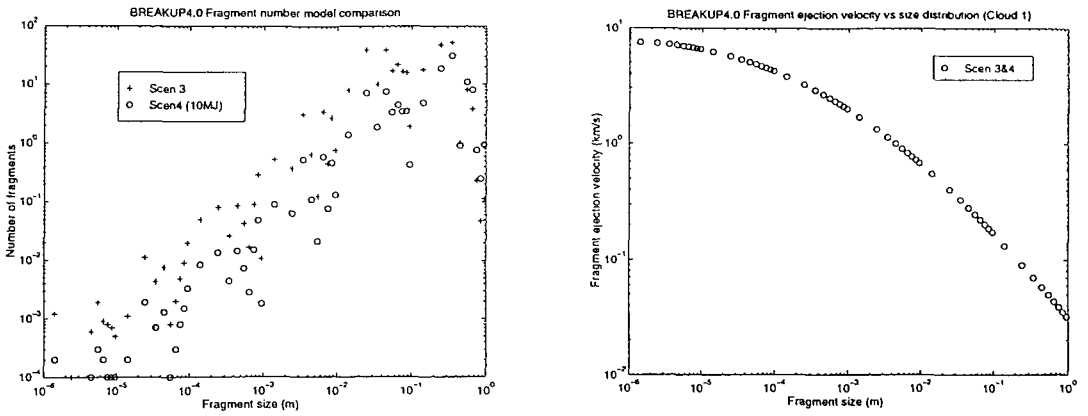

a) Fragment number distributions

b) Fragment ejection velocity distributions

Figure 3.19: Fragment number and Δv comparisons for scenarios 3 and 4

and BC curves for scenarios 3 and 4 are as shown in Figure 3.17.

Event simulation

A number of the breakup events documented in [91] are used here as test cases for program BREAKUP4.0. As stated above, the main method of results validation is the visual comparison of the actual event and the BREAKUP4.0-simulated Gabbard diagrams. Although a largely qualitative procedure in terms of the general shape of the diagrams and the spread of the debris, comparison of the number of fragments produced and the length of the diagram limbs (measure of maximum Δvs) does allow some degree of quantitative results matching to be attempted.

The first example is that of the explosive breakup of the NOAA-3 Delta second stage rocket body which fragmented in 1973 producing 182 trackable pieces of debris. The cause of the breakup is believed to be the hypergolic ignition of residual propellant, brought about by failure of the propellant-oxidiser separating bulkhead, most likely due to thermal (solar) stressing. Figure 3.20a shows the Gabbard diagram for the event [91]. The fragment spread is reasonably ordered, with an apparent bias towards the prograde (i.e. forward) direction. Drooping of the left-hand limb is apparent due to the effects of atmospheric drag and the bulk of the radial features (departure of points from the tangential ejection limbs) are found around the right-hand, forward ejection, limb. The event is simulated by BREAKUP4.0 using

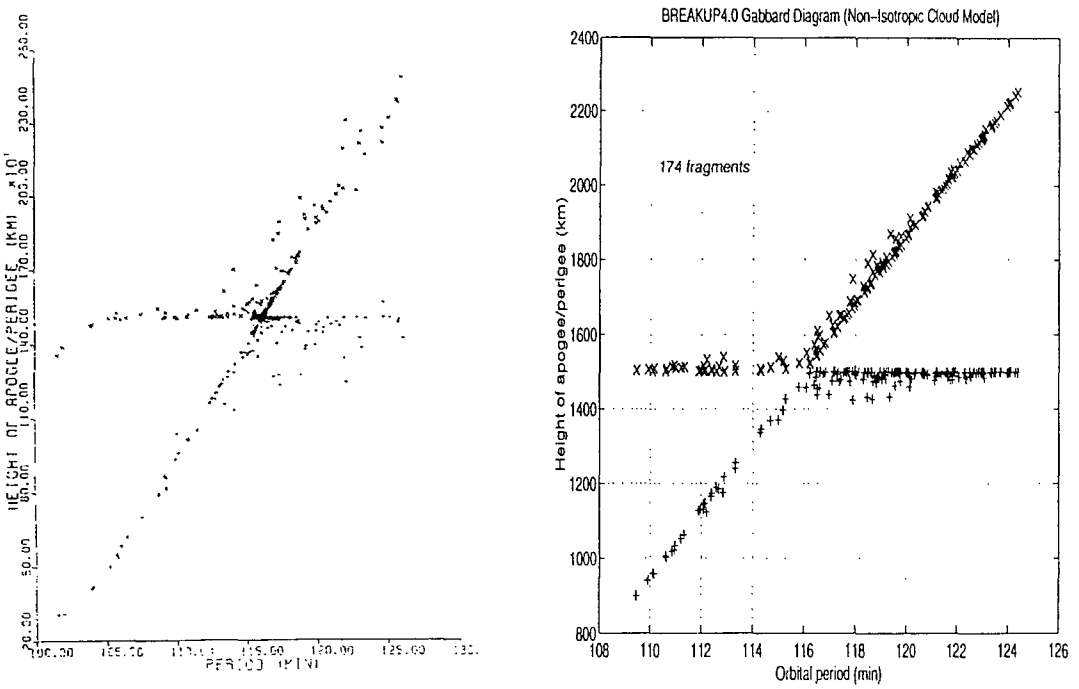

a) Event Gabbard diagram

b) Simulated Gabbard diagram

Figure 3.20: Gabbard diagrams for the NOAA-3 breakup

explosion scenario 3 with E_{fb}=3 and E_{tr}=0.2. These values give the fragment ejections the forward dominance suggested by Figure 3.20a and also a slight tangential characteristic. The value of D_{ind} used is 10cm, taken to represent the trackable debris size at the NOAA-3 altitude of around 1500km. The Gabbard diagram produced by the BREAKUP4.0 simulation is shown in Figure 3.20b, which is generated by the Matlab-SDS plotting function *gabplot* from the output file *break4_fcat.dat*. 174 fragments of 10cm in size and greater are produced by the simulation, as is stated in Figure 3.20b. The simulated results are good. The general shape and scaling of the simulated Gabbard diagram are close to the original and the required forward bias is achieved. This can also be seen from Figure 3.21 which shows the spread of (in-plane) ejection velocities generated. The effect of the 3:1 forward to backward ejection weighting can clearly be seen, as can the slight bias towards the tangential ($\pm X_o$) directions. Although the right-hand limbs on both diagrams are virtually the same length, there are more debris ejections at high Δvs predicted by BREAKUP4.0 than were observed for the actual event. This is a direct result of

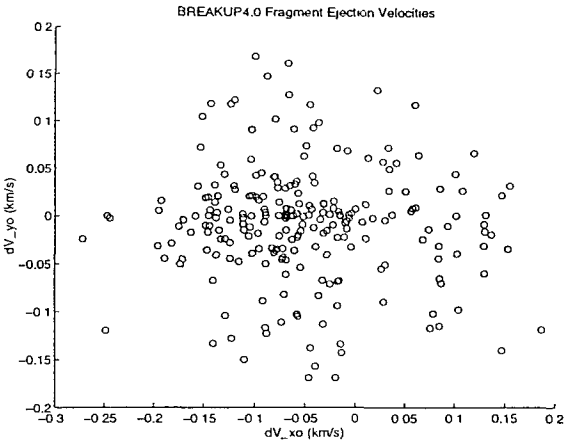

Figure 3.21: Simulated fragment ejection directions for the NOAA-3 breakup

the $\triangle$v distribution used by BREAKUP4.0 (Figure 3.19b) which has a tendency to overestimate the magnitudes of fragment ejection velocities.

The next example is that of the suspected intentional fragmentation of the Cosmos 1654 satellite. The Cosmos 1654 breakup occurred while the Shuttle mission STS-18 was in orbit and, although no fragments from the events were officially catalogued, over 300 debris fragments from the event were detected. The value of E_{tr} employed in the BREAKUP4.0 simulation was 0.8 as the limbs of the event Gabbard diagram are relatively thin, showing a high proportion of tangential ejection directions. The low orbit of Cosmos 1654 (around 250km altitude) meant that many of the fragment orbits decayed quickly and the prograde dominance of the event's Gabbard diagram (Figure 3.22a) is at least partly a result of this. A value of 10 for E_{fb} was used to model the breakup (Figure 3.22b). While this value enables a reasonable match between the actual and simulated plots to be achieved, it is unlikely that the true value for the event was this high. Figure 3.22b shows the orbits of the 398 debris objects larger than D_{ind} (=5cm) generated by BREAKUP4.0 as they are immediately after the event. To obtain a true insight into the nature of the event, the two Gabbard diagrams that are being compared should correspond to the same epoch. In the case of the Cosmos 1654 breakup this would involve the propagation of the simulated fragment orbits forward a number of hours/days to allow the debris in the leading portion of the cloud to re-enter the atmosphere as it quite obviously

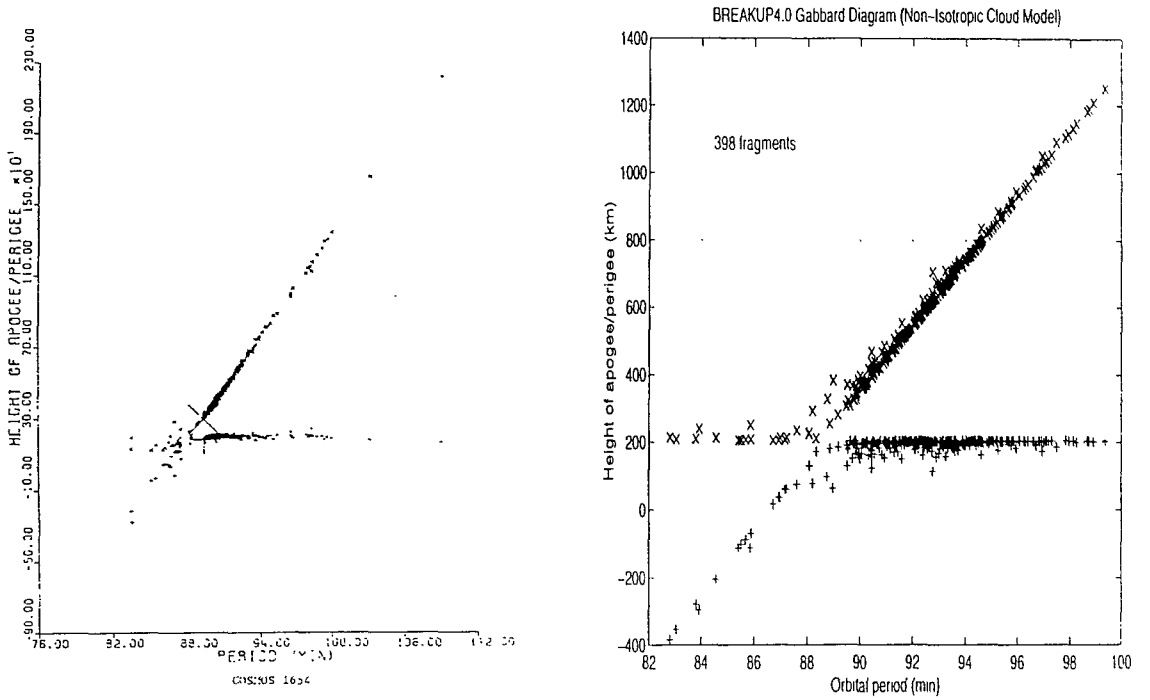

a) Event Gabbard diagram

b) Simulated Gabbard diagram

Figure 3.22: Gabbard diagrams for the Cosmos 1654 breakup

has done in Figure 3.22a. Hence the selection of E_{fb} would be an iterative process (choose value, evolve simulated debris, compare with event data, revise value and iterate again/accept), with the appropriate value for the event being that which matched the real and simulated fragment spreads at the same reference epoch. This type of two-stage simulation approach is covered in more detail in Chapter 5.

The third example looks at the breakup of the Cosmos 1275 satellite. As stated in both Chapters 1 and 2, this fragmentation is suspected of being caused by a hypervelocity impact. To investigate this possibility, several BREAKUP4.0 simulations were performed, treating the breakup as either an explosion or the result of a hypervelocity collision. The explosion simulation (scenario 3) shown in Figure 3.23b uses E_{fb}=4, E_{tr}=0.5 and $\mathbf{X}_{ej}$=(0,0,1). The prograde ejection dominance can be assumed to be real in this case as Cosmos 1275 operated at a much higher altitude than Cosmos 1654 (around 1000km compared with 250km) where the effects of atmospheric drag are much less severe. Using $\mathbf{X}_{ej}$=(0,0,1) thins and shortens the limbs of the Gabbard diagram by reducing the in-plane components of the fragments'

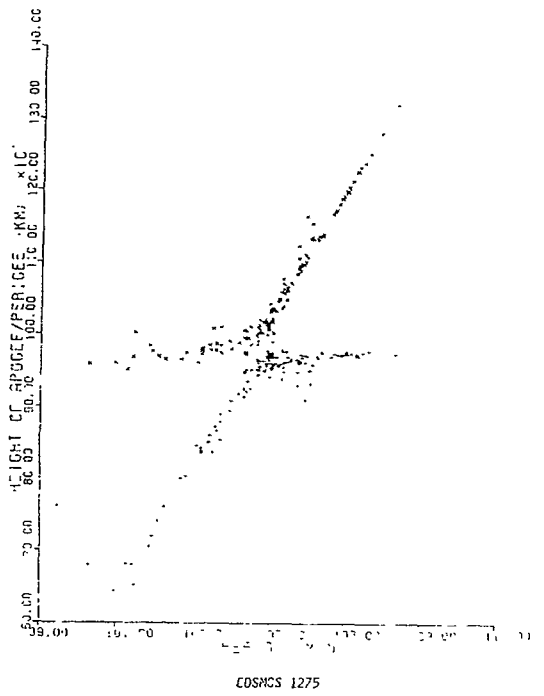

a) Event Gabbard diagram

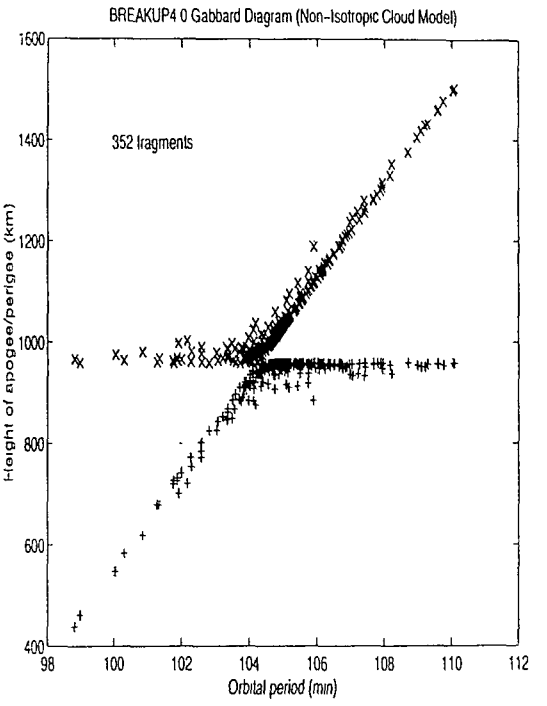

b) Simulated Gabbard diagram - Explosion

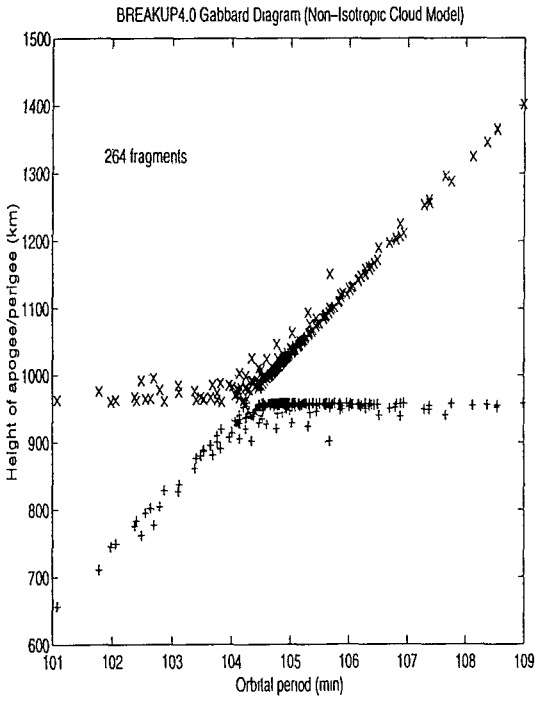

c) Simulated Gabbard diagram - Collision #1

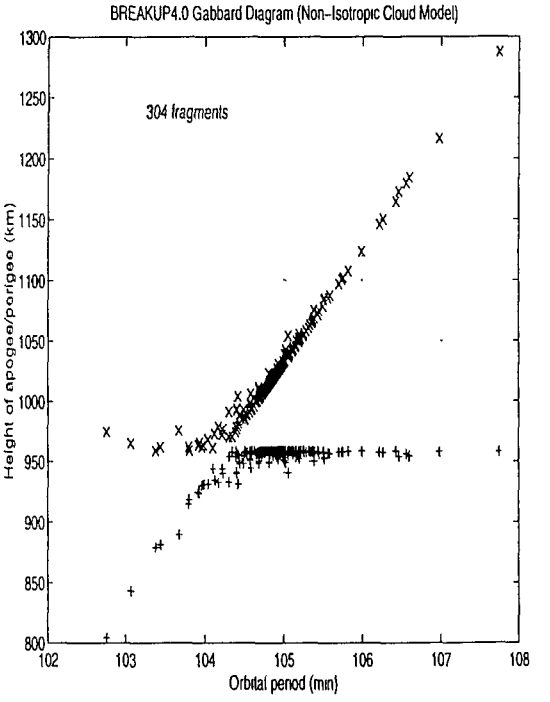

d) Simulated Gabbard diagram - Collision #2

Figure 3.23: Gabbard diagrams for the Cosmos 1275 breakup

$\triangle$vs. Reducing the in-plane velocities in this manner also fills in the central region of the diagram, i.e. that close to the cloud CM. More fragments are produced by the simulation than were originally catalogued (352 versus 242). Not all fragments of catalogue size are catalogued in practice, however, and the number of fragments associated with an event can sometimes rise over time. In the case of Cosmos 1275, the tally of catalogued fragments increased to over 300 [25]. As with the NOAA-3 breakup above, the maximum $\triangle$vs predicted are higher than those recorded for the event, this time despite the effect of $\mathbf{X}_{ej}$.

Figure 3.23c shows the Gabbard diagram for the scenario 1 simulation of the event. A collision between Cosmos 1275 and a 10kg projectile (e.g. debris object) at a relative velocity of 6km/s was found to provide a good match with the event diagram, with 264 catalogue-size fragments being produced. The same cloud model parameters were used as for the scenario 3 simulation, with the relative velocity vector of the projectile chosen to orient the ejection X-axis in the orbiting axis Z direction, as per the scenario 3 run.

The third of the Cosmos 1275 simulations made use of the kinematic collision model (scenario 2). The same collision example considered in the scenario 1 simulation above was used. The values of the four kinematic model parameters (γ, ϵ, ζ and μ) chosen can significantly influence the spread of debris produced. γ, ζ and μ control the amount of collision kinetic energy that is available for fragment spreading, and how the KE is apportioned between the two debris clouds. These three parameters, therefore, determine the magnitude of the maximum fragment $\triangle$vs and also which fragments (i.e. from which cloud) are given the largest ejection velocities. The larger the value of ϵ, the greater the two cloud centroid velocities. If these are large enough (O(10m/s) and greater, for example) then the directional weighting of the fragment ejections can be swamped by the vector addition of the cloud centroid velocities. The BREAKUP4.0 run shown in Figure 3.23d uses a relatively small value of ϵ (=0.1) to stop this occurring. The values of the other kinematic parameters are γ=0.5, ζ=0.5 and μ=0.001. The value of μ employed means that only 0.1% of the available fragment spreading energy is assigned to the non-involved fragments

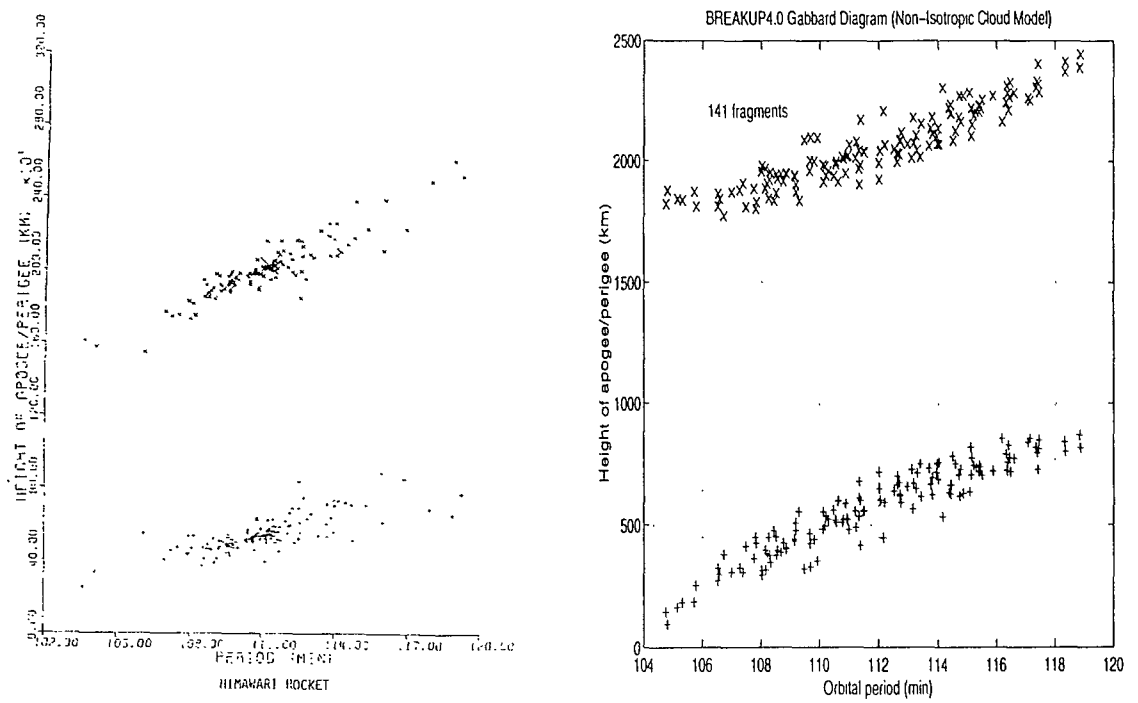

a) Event Gabbard diagram

b) Simulated Gabbard diagram

Figure 3.24: Gabbard diagrams for the Himawari breakup

(cloud number 1). This results in comparable Δvs for the fragments in both debris clouds. 304 individual fragments are produced in this run and once again the general shape and scaling of the simulated diagram is a reasonable match to the real thing, this time with slightly smaller Δvs predicted than for the actual event.

The above simulations of the Cosmos 1275 breakup are inconclusive with regard to identifying the cause of the event. Both the explosive and collision-induced scenarios produced quite reasonable matches to the real event, although the two collision simulations, and in particular that due to the kinematic model, actually produced the better results. Uncertainties in the various fragment distribution models involved throughout all the simulations mean that no firm conclusions can be drawn concerning the reason for the fragmentation, but the simulations do show that in terms of the debris produced by the event, a hypervelocity collision is a distinct possibility.

The fourth breakup example is that of the explosive fragmentation of the Hi-

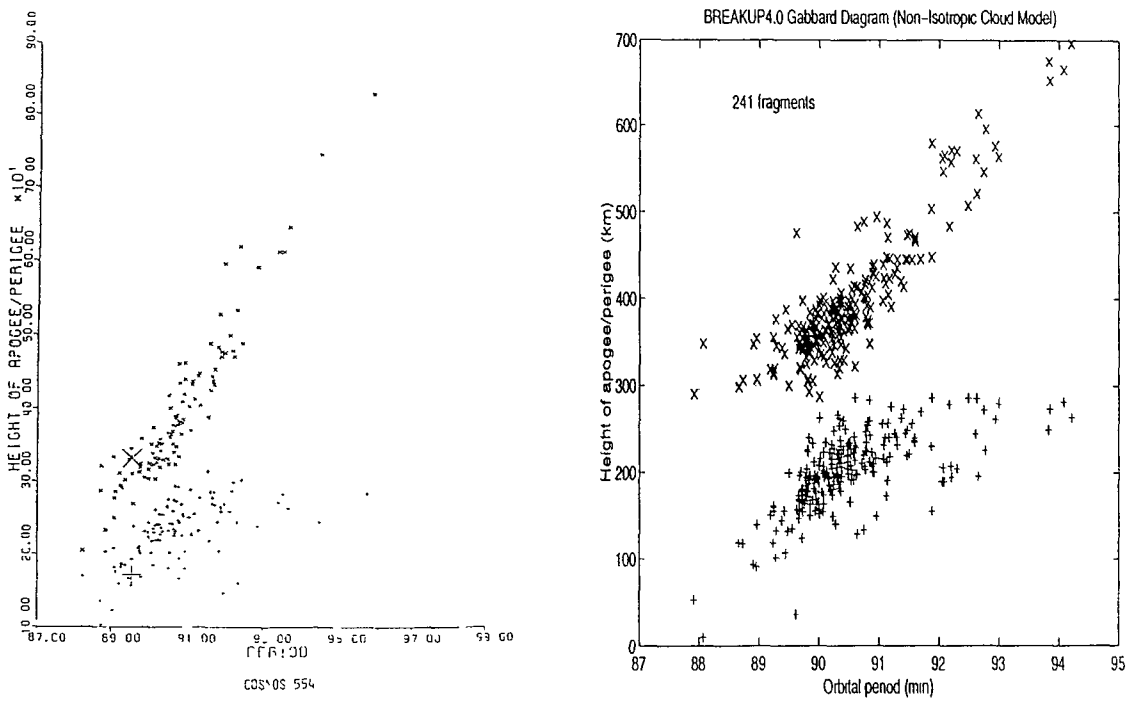

a) Event Gabbard diagram

b) Simulated Gabbard diagram

Figure 3.25: Gabbard diagrams for the Cosmos 554 breakup

mawari Delta 2nd stage rocket body. The cause of the Himawari Delta stage fragmentation is believed to be the same as that of the NOAA-3 rocket in the first example, i.e. hypergolic ignition of residual propellant. The Himawari rocket was in a considerably more elliptic orbit than the NOAA-3 stage, however, (eccentricity of 0.1 compared with 0.001) and broke up at a true anomaly of 108^o along its orbit. The eccentricity of the Himawari rocket orbit and the location of the breakup on the orbit combine to produce a markedly different Gabbard diagram to those seen in the first three examples. The classic skewed cross shape is replaced by two distinct apogee and perigee point clusters. This type of event does not require a special modelling approach and the BREAKUP4.0 simulation run shown in Figure 3.24b did not employ any ejection direction biasing. From Figure 3.24 it can be seen that the simulated fragment data is once again a good match to that observed from the actual event. The simulation produces 141 individual fragments compared with the 148 catalogued from the event. As before, however, the largest fragment Δvs predicted by BREAKUP4.0 are a little higher than those recorded.

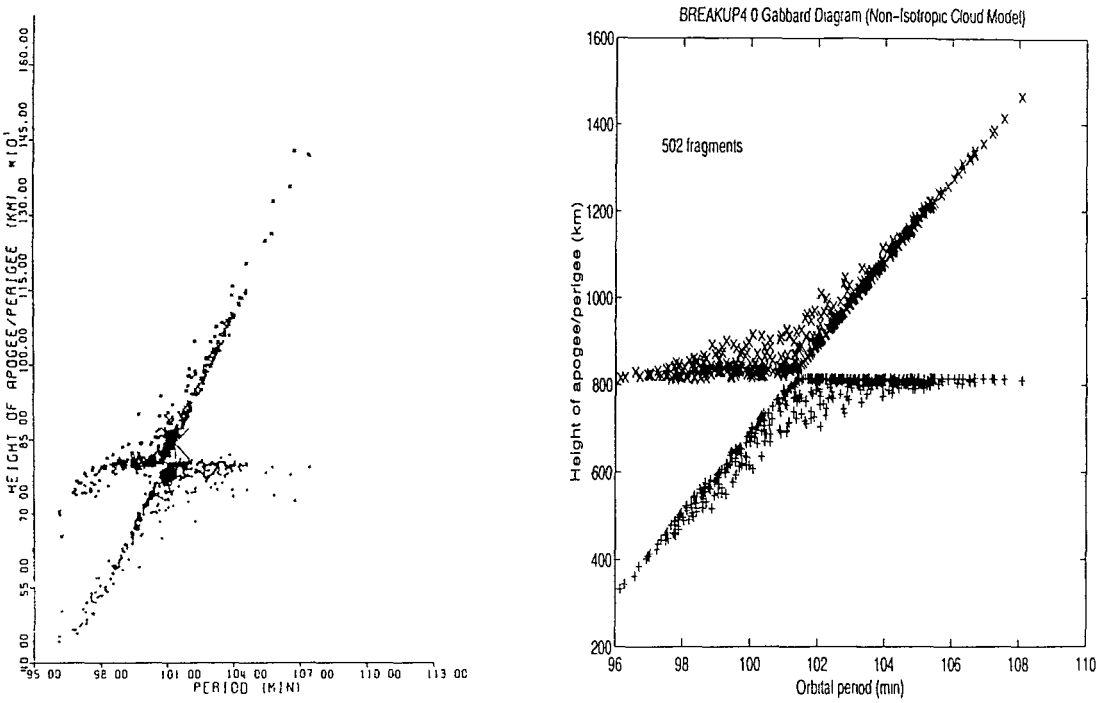

a) Event Gabbard diagram

b) Simulated Gabbard diagram

Figure 3.26: Gabbard diagrams for the SPOT-1 Ariane breakup

The fifth fragmentation case to be examined is the intentional breakup of the Cosmos 554 satellite. From Figure 3.25a it can be seen that the fragmentation was highly anisotropic, even taking into account the rapid decay of fragments from the cloud's leading edge. There are also no clearly discernible tangential ejection limbs on the diagram. As with the Cosmos 1654 example above, the true ejection pattern can only really be modelled by combining a cloud evolution tool with the initial fragment ejection conditions. Figure 3.25b is obtained by using E_{fb}=10 to and E_{tr}=-1 to directly simulate the remaining collection of fragments. Again, the non-isotropic ejection model in BREAKUP4.0 is shown to be capable of dealing with highly unordered fragmentations. The general shape of the diagram is matched very well and 241 'large' fragments are produced by the simulation compared with the 196 catalogued. The breakup of Cosmos 554 is examined further in Chapter 5.

The sixth and final breakup example is that of the SPOT-1 Ariane third stage rocket body which broke up violently in November 1986 generating around 500 catalogued fragments [53]. This breakup was described in some detail in Chapter

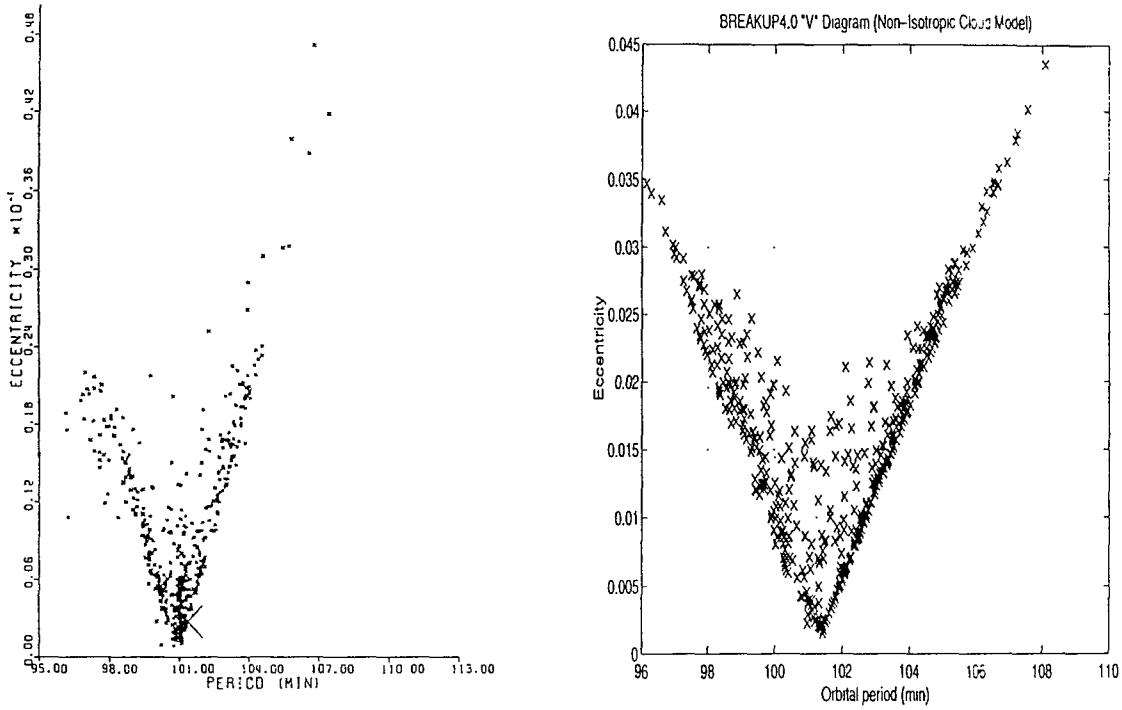

a) Event 'V' diagram

b) Simulated 'V' diagram

Figure 3.27: 'V' diagrams for the SPOT-1 Ariane breakup

2. The height of the orbit concerned (around 800km) meant that the event was particularly pollutive, with many of the fragments generated having long orbital lifetimes. Gabbard, 'V' (eccentricity versus period) and inclination versus period diagrams for the event are included in [53] allowing comparison with BREAKUP4.0 simulation data. The event Gabbard diagram shown in Figure 3.26a suggests a relatively uniform breakup, with drooping visible on the low-period apogee limb due to the effects of atmospheric drag. E_{fb}=1 and E_{tr}=1 are used for the simulation.

The 'V' diagram is essentially an alternative to the Gabbard diagram. Figure 3.27 clearly shows that the highest ejection velocities were in the prograde, or forward, direction. The debris on the inside of the 'V' have experienced significant radial $\triangle$vs.

The Gabbard and 'V' diagrams only really provide information about the breakup in two-dimensions, e.g. in the breakup CM orbital plane. The out-of-plane velocity components do, of course, contribute to the eccentricity and period changes of the

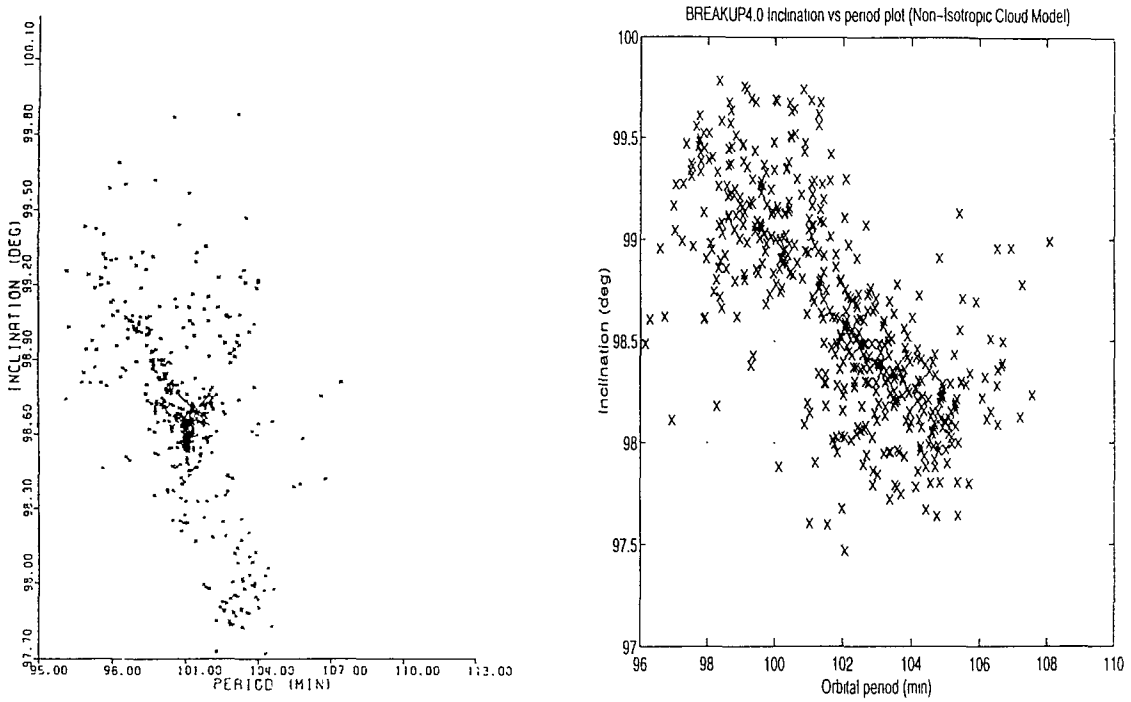

a) Event inclination vs period plot

b) Simulated inclination vs period plot

Figure 3.28: Inclination vs period plots for the SPOT-1 Ariane breakup

fragments' orbits but information on the out-of-plane ejection directions cannot be directly obtained. From Figure 3.28a, a curious asymmetry in the debris ejection pattern can be observed, with the breakup seemingly concentrated in two directions; one to the rear, up, and left of the velocity vector and the other in the opposite direction. $\mathbf{X}_{ej}$=(1,-1,1) was used to model this dual-jet like behaviour. E_{jet} was kept at 0, however, as the jets were observed to be relatively thick. The ejection directions obtained are shown in Figure 3.29 and 3.28b. These clearly show how the $\mathbf{X}_{ej}$ ejection pointing facility allows fragment ejections to be biased in any direction, in or out of the breakup orbit plane. The inclination extremities of Figure 3.28b contain more debris than present in the real event. This is also true of the Gabbard and 'V' diagrams, however, and is once again a consequence of the larger-than-observed $\triangle$vs predicted by BREAKUP4.0.

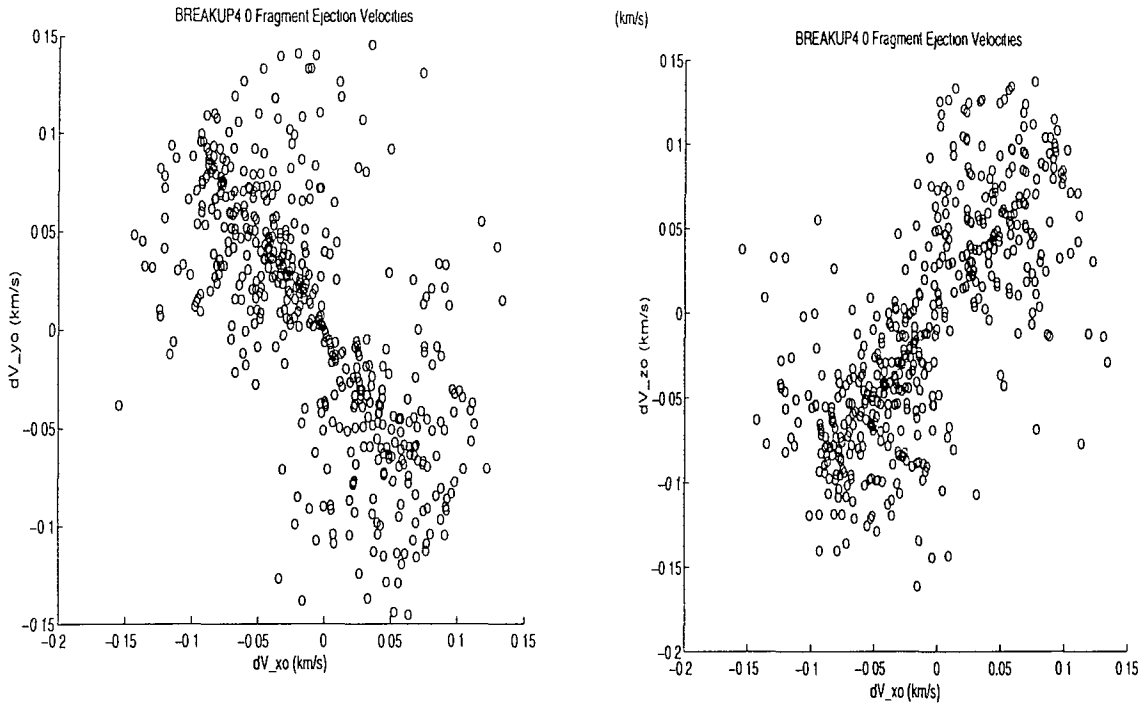

a) Ejection velocities in the orbiting frame X-Y plane

b) Ejection velocities in the orbiting frame X-Z plane

Figure 3.29: Simulated fragment ejection directions for the SPOT-1 Ariane 3 breakup

Summary

The model comparisons and event simulations discussed above show that BREAKUP4.0 can simulate a variety of different fragmentation events, and can do so with a considerable degree of realism. BREAKUP4.0 can act as a stand-alone program, for the generation of Gabbard diagrams or fragment distributions for example, or can be used in conjunction with cloud propagation program EVOLUTION or collision hazard assessment program TARGET. The use of BREAKUP4.0 with these two second-stage programs is discussed in Chapters 5 and 6 respectively.

Chapter 4

Calculation of Fragment Trajectories

4.1 Introduction

Given the velocities of the fragments produced by a breakup event, the investigation of the extent to which the debris cloud disperses is essentially a problem of orbit propagation, whether it be of 'actual' individual fragments (e.g. for the BREAKUP non-isotropic cloud model) or the debris cloud bounding envelope (e.g. the BREAKUP isotropic cloud model). Accurate determination of the positions and velocities of debris at a given time after a breakup is fundamental to the assessment of the collision risk posed to other spacecraft. A number of different methods exist for the determination of the trajectory/orbit of an object from its orbital parameters at a reference epoch. These techniques vary in complexity and accuracy, and can be split into three general categories: state transition matrix methods, analytical orbit propagation and numerical integration.

The main methods available for object trajectory calculation are discussed here, as is a Fortran code written to implement them, program TRAJECTORY. TRAJECTORY serves two main purposes. Firstly, TRAJECTORY acts as a test-bed for the orbit propagation schemes employed in EVOLUTION and TARGET. The main driver for an orbit propagator to be used in debris cloud evolution and collision hazard assessment studies is speed of operation because both applications involve

the propagation of large numbers of orbits. The aim here, then, is not to produce the most accurate orbit propagator possible, but instead identify and implement the scheme which offers the optimum compromise of speed of execution and quality of output. Only orbit perturbations due to the Earth's oblateness and atmospheric drag are modelled because these are the dominant perturbation forces for the orbital regimes and fragment sizes generally considered. All the analyses performed in the thesis consider objects and debris in low Earth orbit and very small particles ($< .1mm$) are generally ignored to concentrate upon potentially damaging debris. Secondly, the program constitutes a unique orbit propagation method comparison tool. TRAJECTORY is used in this chapter to compare the different propagation options available for a number of test cases.

The results produced by TRAJECTORY are validated by modelling the orbits of several spacecraft and comparing the simulated orbits produced with actual orbital flight data.

4.2 Orbital Motion

4.2.1 Ideal Orbital Theory

An orbit is the periodically repeated trajectory of one body (satellite) around another, generally more massive, primary body [92]. The trajectories of the planets around the Sun, and Moons around the planets of the solar system are all basically orbital, as are the trajectories of the majority of free bodies in space. Orbital motion is due to the mutual gravitational attraction between two bodies, which is generally the main force experienced in the space environment. The attractive force F, between two bodies of masses m_1 and m_2, is defined by Newton as

$$F = G\frac{m_1 m_2}{r^2}, \tag{4.1}$$

where r is the distance between their centres of mass, and G is Newton's Gravity constant ($G \approx 6.672 \times 10^{-14} m^3 s^{-2} kg^{-1}$).

The motions of the bodies of the solar system have been observed for many cen-

turies, with increasingly higher degrees of accuracy. Many researchers have theorised about the laws of motion that they obey. Johannes Kepler empirically formulated three laws of planetary motion from Tycho Brahe's planetary observations. These are [93]:

(1) The orbit of each planet is an ellipse with the Sun at one focus.

(2) For any planet, the rate of description of area by the radius vector joining the planet to the Sun (dA/dt) is constant, i.e.

$$\frac{dA}{dt} = \frac{1}{2}r^2\dot{f} = \frac{h}{2} = constant \tag{4.2}$$

where r is the orbital radius, $\dot{f}$ is angular velocity, and h is orbital angular momentum.

(3) The cube of the semi-major axis of a planetary orbit is proportional to the square of the planet's period of revolution about the Sun.

Kepler's three laws of planetary motion and Newton's law of universal gravitation form the basis for the equations of ideal orbital motion. These formulae assume that the two attracting bodies are point masses with the satellite of negligible mass when compared to the primary body, and that the two body system is isolated. This is a reasonable first approximation for the majority of bodies in the solar system, and produces the elliptic trajectory of Kepler's First Law. The basic formulae for an ideally orbiting body are [93],

$$\text{Energy equation} : \frac{v^2}{2} - \frac{\mu}{r} = -\frac{\mu}{2a}, \tag{4.3}$$

$$\text{Orbital period} : \tau = 2\pi\sqrt{\frac{a^3}{\mu}}, \quad (n^2a^3 = \mu), \tag{4.4}$$

$$\text{Orbital radius} : r = \frac{a(1-e^2)}{1+ecos(f)}, \tag{4.5}$$

$$\text{Kepler's equation} : E - esinE = M = n(t - t_p), \tag{4.6}$$

$$\text{True anomaly} : tan(\frac{f}{2}) = (\frac{1+e}{1-e})^{\frac{1}{2}} tan(\frac{E}{2}). \quad (4.7)$$

Here $\mu = Gm_1$ where m_1 is the mass of the primary body, v is the orbital velocity, a is the semi-major axis of orbital ellipse, τ is the orbital period, n is the mean motion, e is the eccentricity, f is the true anomaly, E is the eccentric anomaly, M is the mean anomaly, t is time and t_p is the time of periapsis (perigee) passage. The equations describe the conditions of the orbiting body within the plane of the ellipse. To fully describe an orbit, the orientation of the orbital ellipse needs to be described with respect to a suitable reference frame. For Earth orbiting satellites, the orbit orientation is most commonly defined by the following parameters : (1) The orbital inclination i is the angle between the orbit plane and the equatorial plane, measured at the ascending node. Here a 'node' is the point on the orbit where the satellite crosses the equator and the 'ascending node' is the location where the satellite crosses the equator going South to North. (2) The right ascension of the ascending node, Ω, is the geocentric angle from the Vernal Equinox around the equator to the ascending node, measured Eastwards [93]. This is also referred to commonly by the acronym RAAN. (3) The argument of perigee, ω, is the geocentric angle from the ascending node around the orbit to the perigee position, measured in the direction of motion.The orbital elements a, e, f, i, ω and Ω therefore describe both the current location and the trajectory of the ideally orbiting body relative to the Earth. The geometry of an Earth orbit is shown in Figure 4.1.

4.2.2 Predicting a Realistic Orbit.

With the invention of higher precision tracking equipment it became apparent that the actual paths followed by the orbiting bodies of the solar system differed from those predicted by equations (4.3)-(4.7). The deviations are due to the satellite experiencing forces other than the simple central gravitational force of equation (4.1). These perturbations to the ideal orbit occur because the two bodies cannot be approximated by point masses, but must be given shape and a density distribution. Also, the two-body system is not completely isolated. Massive bodies other than

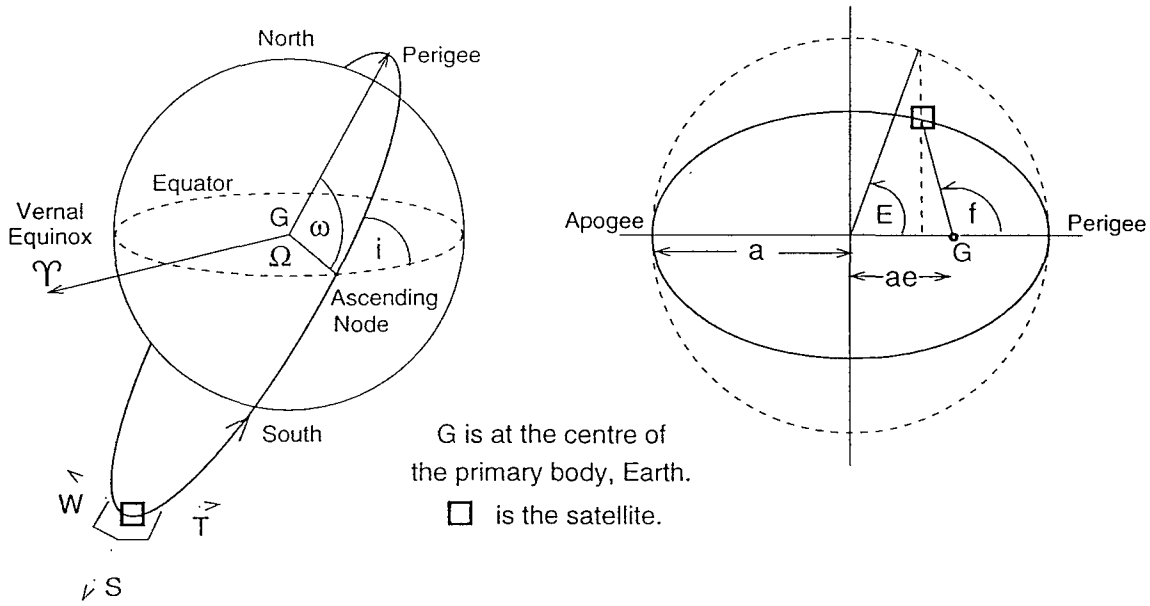

Figure 4.1: Geometry of an Earth orbiting body.

the primary exert gravitational force on the satellite, for example the Sun and the Moon.

The deviation of the actual path from the ideal path can be interpreted as a gradual change in orbit, similar to the low impulse manoeuvres performed by some modern artificial satellites. So the orbital motion can be represented by the instantaneous elements (a, e, f, i, ω and Ω) and the rate of change of the elements with time ($\dot{a}$, $\dot{e}$, $\dot{f}$, $\dot{i}$, $\dot{\omega}$ and $\dot{\Omega}$). The equations of Lagrange relate the rates of change of the elements to the forces experienced by the satellite. The Lagrange equations [94] expressed in terms of the force components in the satellite's radial (S), tangential (T) and out-of-plane (W) directions, as shown in Figure 4.1, are,

$$\frac{da}{dt} = \frac{2}{n\sqrt{1-e^2}}(Sesin(f) + T(1 + ecos(f))), \tag{4.8}$$

$$\frac{de}{dt} = \frac{(1-e^2)^{1/2}}{na}(Ssin(f) + T(cos(E) + cos(f))), \tag{4.9}$$

$$\frac{di}{dt} = \frac{Wrcos(\omega + f)}{na^2\sqrt{1-e^2}}, \tag{4.10}$$

$$\frac{d\Omega}{dt} = \frac{sin(\omega + f)}{sin(i)} \frac{Wr}{na^2\sqrt{1-e^2}}, \tag{4.11}$$

$$\frac{d\omega}{dt} + \frac{d\Omega}{dt}cos(i) = \frac{(1-e^2)^{1/2}}{nae}(-Scos(f) + T(\frac{2+ecos(f)}{1+ecos(f)})sin(f)), \tag{4.12}$$

$$\frac{dn}{dt} = -\frac{3}{2}\sqrt{\frac{\mu}{a^5}}\frac{da}{dt}. \tag{4.13}$$

The orbital elements at time t are given by the sum of the elemental values at time t_0 and the integral of the rate of change of the elements from t_0 to t. That is

$$(a, e, f, i, \omega, \Omega)_t = (a, e, f, i, \omega, \Omega)_{t_0} + \int_{t_0}^{t} (\dot{a}, \dot{e}, \dot{f}, \dot{i}, \dot{\omega}, \dot{\Omega})dt. \tag{4.14}$$

Accurate modelling of the forces encountered by the satellite is, therefore, required to predict the orbit at a time t after the satellite orbit is observed at t_0. Due to the periodic nature of an orbit, and the orbits of the other bodies of the solar system, the variation of the orbital elements often tend to be periodic themselves. The variation of orbital elements can, therefore, be divided into three main categories : (1) short period (those with a period of oscillation of less than or about one orbital revolution), (2) long period (those having a period of oscillation greater than one revolution but less than the life time of the satellite) and (3) secular (an apparently non-oscillatory variation). The periodic nature of the variation of the elements has given rise to essentially two definitions of the orbital elements : (1) osculating elements (the instantaneous values of the elements, as discussed thus far) and (2) mean elements (the elements that would best fit the actual orbit but remain constant for a complete orbital revolution). Using mean elements serves to remove the effects of the short period terms, which appear as noise in long period analyses.

4.3 Methods of Orbit Propagation

4.3.1 State Transition Matrix Methods

Several different state transition matrix methods were described in Chapter 2. These dealt with the relative motion of an object with respect to an orbiting reference frame. The simple matrix representations of these models were given in section 2.2 and the equations of motion used to derive them are described in full in the Appendix. The state transition matrix method can also be directly applied to motion in the geocentric inertial frame, for example using Goodyear's [88] formulation of the state transition matrix. Only relative coordinate models are considered here, however, with three such methods implemented into program TRAJECTORY.

Propagation option 1 is the linearised model of Chobotov outlined in equation (2.16). Spencer's [75] eccentricity-corrected version of Chobotov's linearised model is propagation method 2 in TRAJECTORY. This is described in equation (2.17). The third state transition matrix propagation option is a novel non-linear method. Spencer's eccentricity-corrected transition matrix model is further improved by the incorporation of the effects of second order relative distance terms. Using the method described in Anthony and Sasaki [76], a further differential correction is added, this time to the linear eccentricity-corrected solution,

$$\mathbf{r} = \mathbf{r}_{Sp} + \delta\mathbf{r}_B = \mathrm{M}_{Sp}\,\dot{\mathbf{r}}_o + \mathrm{N}\,\mathbf{q}_o, \tag{4.15}$$

where $\delta\mathbf{r}_B$ is the differential correction in position due to second order relative distance terms, N is the second order correction matrix and $\mathbf{q}_o$ is a vector of second order velocity products. The development of the above model is described in more detail in the Appendix.

4.3.2 Analytic Orbit Propagation

Keplerian propagation

Most conventional methods of orbit propagation operate in the geocentric inertial frame. The simplest of these is Keplerian propagation, which deals with the ideal

(i.e. two-body) orbital motion discussed in section 4.2.1. This is propagation method 4 in program TRAJECTORY.

Motion around the oblate Earth

Orbital perturbations can be added analytically to the ideal solutions, to account for the effects of the Earth's oblateness and atmospheric drag, for example. First order secular perturbations due to the asphericity of the Earth (i.e. the J_2 gravitational potential term [93]) cause Ω and ω to drift in value. This can be modelled very simply by the following variation equations [93, 95],

$$\Omega = \Omega_0 + \dot{\Omega}(t - t_0), \text{ where } \dot{\Omega} = -\frac{3nJ_2R_e^2cos(i)}{2p^2}, \tag{4.16}$$

$$\omega = \omega_0 + \dot{\omega}(t - t_0), \text{ where } \dot{\omega} = \frac{3nJ_2R_e^2}{2p^2}[2 - \frac{5}{2}sin^2(i)], \tag{4.17}$$

where p is the semi-latus rectum of the elliptic orbit ($= a(1 - e^2)$), R_e is the radius of the Earth and $J_2 \approx 1.08 \times 10^{-3}$. The RAAN regresses (i.e. moves in the opposite direction to the orbiting body) and the perigee precesses around orbit. a, e and i, however, remain constant with respect to secular J_2 effects. The above representation of secular J_2 perturbations, superimposed on ideal Keplerian motion, is propagation option 5 in TRAJECTORY.

Motion through the Earth's atmosphere

Accounting for the decay of an orbit due to atmospheric drag is considerably more complex than determining its perturbation due to the gravity field. It not only requires expressions which describe how the elements of a given orbit vary over time, but also some form of atmospheric model. Given the requirement for speed of propagation discussed earlier, a relatively straightforward analytical approach is adopted for detemining the variations of orbit elements and a greatly-simplified version of the CIRA-72 [96] reference atmosphere is used for calculating atmospheric density.

Sterne [97] gives the following equations which detail how a, e and i are influenced

by drag,

$$(\frac{da}{dE})_D = -2b\rho a^2 \frac{x^{3/2}}{y^{1/2}}[1 - \frac{yd}{x}]^2, \tag{4.18}$$

$$(\frac{de}{dE})_D = -2b\rho a(1-e^2)\sqrt{\frac{x}{y}}[1 - \frac{yd}{x}]\{cos(E) - \frac{yd(2cos(E) - e - ecos^2(E))}{2(1-e^2)}, \tag{4.19}$$

$$(\frac{di}{dE})_D = -\frac{1}{2}b\rho a w_s \frac{sin(i)}{n}(1-e^2)^{-1/2}(1 + cos(2u))y^{5/2}x^{1/2}[1 - \frac{yd}{x}], \tag{4.20}$$

where

$$b = \frac{C_D A}{2m_s} = \frac{BC}{2}, \tag{4.21}$$

$$d = \frac{w_s cos(i)}{n}(1-e^2)^{1/2}, \tag{4.22}$$

$$x = 1 + ecos(E), \tag{4.23}$$

$$y = 1 - ecos(E), \tag{4.24}$$

and ρ is atmospheric density, E is the perturbed (e.g. by J_2) eccentric anomaly, u is the perturbed argument of latitude ($= w + f$), w_s is the Earth's rotation rate, m_s is the mass of the orbiting body, C_D is its drag coefficient and A is the satellite cross-sectional area consistent with C_D. The dominant effects are the diminishing size and circularisation of the satellite orbit, i.e. $\triangle$a and $\triangle$e are negative and the orbit perturbations are primarily in the orbit plane. Although $(di/dE)_D$ above produces a shift in the orientation of the orbit plane, this effect is very small when compared with the in-plane perturbations.

King-Hele [94] derives similar but slightly different expressions for $(da/dE)_D$ and $(de/dE)_D$, again working from Lagrange's planetary equations but this time assuming that only a tangential drag force component acts on the satellite. $(di/dE)_D$ is, therefore, zero in this case. King-Hele's expressions for $(da/dE)_D$ and $(de/dE)_D$ are,

$$(\frac{da}{dE})_D = -2b\rho a^2 \frac{x^{3/2}}{y^{1/2}}[1 - \frac{d(1-e)}{(1+e)}]^2, \tag{4.25}$$

$$(\frac{de}{dE})_D = -2b\rho a(1-e^2)\sqrt{\frac{x}{y}}[1 - \frac{d(1-e)}{(1+e)}]^2 cos(E), \tag{4.26}$$

which may be compared to equations (4.18) and (4.19). The differences between the two sets of equations can be attributed to their respective differences in modelling the

drag force and the orbital velocity vector with respect to the rotating atmosphere [94, 97].

The combined analytical modelling of secular J_2 and atmospheric drag perturbations is TRAJECTORY propagation option 6. Once the drag model has been chosen (Sterne/King-Hele), two further implementation details remain. Firstly, there is the question of whether to re-evaluate the derivatives da/dE, de/dE and di/dE at every time-step (i.e. at every point along the satellite orbit being considered) or alternatively to use orbit-averaged mean variations. Mean element variations can be determined by numerically integrating the derivatives around a nominal reference orbit (e.g. Keplerian with secular J_2 perturbations) and dividing the integrals by 2π. For example,

$$\overline{(\frac{da}{dE})}_D = \frac{\triangle a}{2\pi} = \frac{1}{2\pi}\int_0^{2\pi}(\frac{da}{dE})_D dE, \tag{4.27}$$

where $\triangle a$ is the total change in semi-major axis over the course of the reference orbit and $\overline{(\frac{da}{dE})}_D$ is the mean value. The same procedure is carried out to obtain $\overline{(\frac{de}{dE})}_D$ and $\overline{(\frac{di}{dE})}_D$. As the semi-major axis a of the orbit is perturbed by the drag force, n, τ and p must all be updated every time new values of a and e are determined. The change in mean motion can be found from the following relationship,

$$\overline{(\frac{dn}{dE})}_D = -\frac{3n}{2a}\overline{(\frac{da}{dE})}_D. \tag{4.28}$$

The orbital period τ is recalculated using the updated value of n, and p is redetermined directly from the new values of a and e. The mean rates of change are used to predict the variation of a, e and i (and related parameters) over a number of revolutions. If a large number of orbital revolutions are to be considered then the mean values can be recalculated periodically to ensure that the desired degree of accuracy is attained. The alternative to using mean element variations is to use 'exact' values of the derivatives, i.e. freshly calculated at each point of interest. If a long duration analysis is required, with the orbital elements only being updated once per orbit, for example, then the mean element approach is appropriate as element variations within a given orbit are unimportant. Only the net change per orbit is of concern. If orbital element values are required at a number of points in each revolution, then the

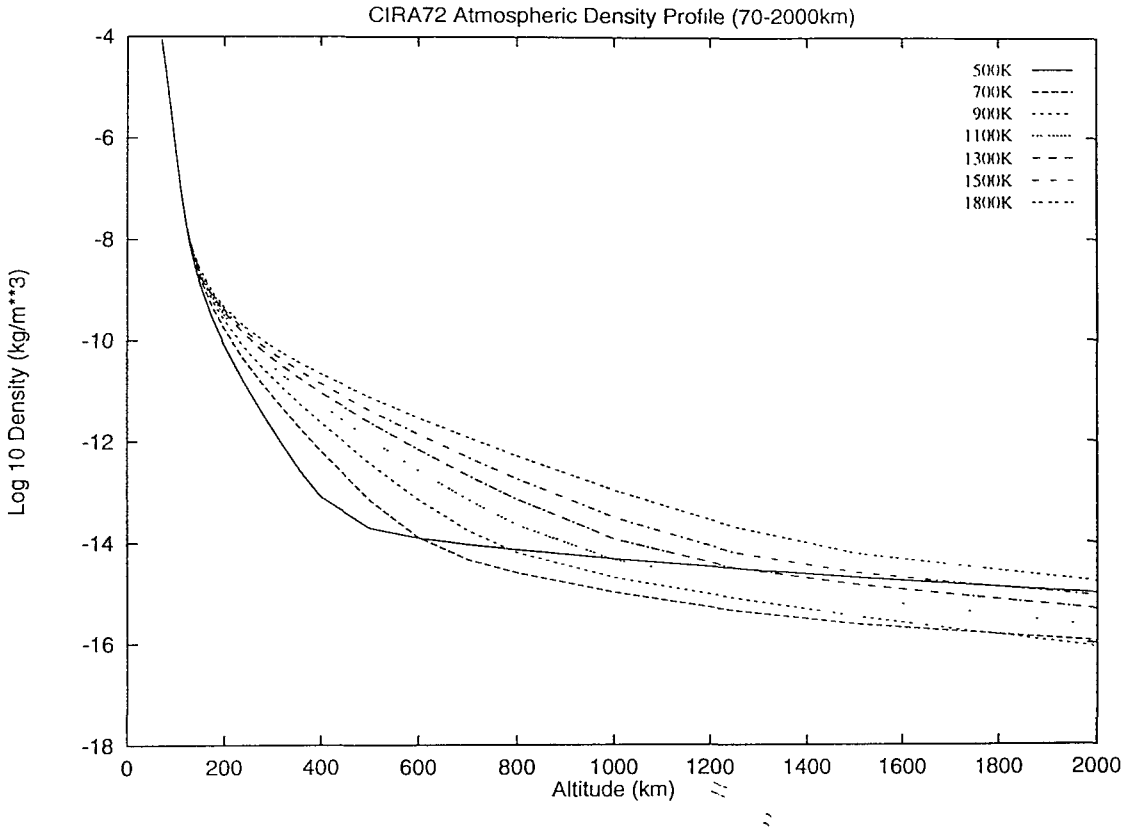

Figure 4.2: CIRA-72 density vs altitude profiles, for a range of exospheric temperatures

exact variation technique may be necessary. Care should be taken, however, when using exact variations with the phasing of the calculation points with respect to the satellite's orbital period. Because all the drag variation derivatives are dependent upon ρ, they are greatest in magnitude where ρ is highest, i.e. at perigee, and vary with distance from the Earth over the course of each orbit. If a set of exact derivatives is calculated near perigee and then applied over a large portion of the orbit, the change in elements may be significantly overestimated, for example. Similarly, using a set of derivatives determined near apogee will result in a smaller element variation than should be the case. The element variation time-histories produced will also be far from smooth, with large gradient changes possible from time-step to time-step. When using exact variations, then, a relatively small time-step with respect to τ should be used and the elements updated every time-step. This ensures that the exact variations do provide the additional intra-orbit accuracy intended.

The value of ρ at any given time is dependent upon the atmospheric model

adopted. The atmospheric model used is completely independent of the element variation equations and can be either analytical or empirical in nature, and as simple or as complex as desired. The model installed in program TRAJECTORY is a simplified version of the CIRA-72 [96] reference atmosphere. Atmospheric density is taken to be solely a function of altitude and exospheric temperature, as shown in Figure 4.2. At a given height, ρ generally increases with exospheric temperature T_{ex}. The ρ profile observed in Figure 4.2 for T_{ex}=500K appears to be anomalous, but this is a result of the manner in which the mix of atmospheric gases is modelled at that temperature. In the CIRA-72 atmosphere, hydrogen is not present below around 500km altitude but at low exospheric temperatures is the dominant species above this height. This causes a levelling-out of the density versus altitude profile. As T_{ex} increases, however, the number density of hydrogen falls below that of Helium and atomic Oxygen and so its influence on ρ is diminished. T_{ex} is a function of solar activity and is dependent upon the smoothed 10.7cm wavelength solar flux $\overline{F}_{10.7}$ ($10^4 Jy$) and the diurnal factor D according to the equation [96],

$$T_{ex} = D(379 + 3.24\overline{F}_{10.7}), \tag{4.29}$$

where T_{ex} is in Kelvin. The value of $\overline{F}_{10.7}$ to be used is input to TRAJECTORY and is held constant for the duration of the simulation. D varies periodically between 1.0 (nighttime minimum) and 1.3 (daytime maximum) over the course of each orbit according to the local solar time. D is set at a constant value of 1.15 in TRAJECTORY, however, which smoothes out the diurnal density variations. $\rho(r, T_{ex})$ is defined for altitudes in the range 70-2000km. Above this height, ρ is taken to be zero, i.e. atmospheric drag is deemed to have no effect on the satellite orbit. In practice, the exact height at which re-entry begins is not exactly defined [98]. To account for this, and to allow the effects of different re-entry heights to be investigated, a variable 'cut-off' altitude is employed. Once below this height, the orbiting body is considered to have begun re-entry and the simulation is stopped. The minimum value cut-off altitude is set by the density model, i.e. at 70km.

Short period J_2 effects

In addition to the secular effects described above, the Earth's oblateness also produces short period perturbations to a satellite orbit. These result from the variation of mean anomaly M around the orbit and take the form of oscillations about the mean orbit. TRAJECTORY propagation method 7 uses the expressions developed by Kozai [99] and reproduced in [93] to perturb the orbital elements (a, e, i, Ω, ω, M). These expressions, again derived from Lagrange's planetary equations, give the instantaneous perturbations of the osculating orbit with respect to the mean orbit. These expressions are :

$$\Delta a_{sp} = \frac{J_2 R_e^2}{a}\{(1-\frac{3}{2}sin^2(i))[(\frac{a}{r})^3-(1-e^2)^{-3/2}]+\frac{3}{2}(\frac{a}{r})^3 sin^2(i)cos2(f+\omega)\} \quad (4.30)$$

$$\begin{aligned}\Delta e_{sp} = & \frac{3J_2R_e^2(1-e^2)}{2a^2e}\{\frac{1}{3}(1-\frac{3}{2}sin^2(i))[(\frac{a}{r})^3-(1-e^2)^{-3/2}] \\ & +\frac{1}{2}(\frac{a}{r})^3 sin^2(i)cos2(f+\omega)\} \\ & -\frac{3J_2R_e^2 sin^2(i)}{4ape}[cos2(f+\omega)+ecos(f+2\omega)+\frac{1}{3}ecos(3f+2\omega)]\end{aligned} \quad (4.31)$$

$$\Delta i_{sp} = \frac{3J_2R_e^2 sin(2i)}{8p^2}[cos2(f+\omega)+ecos(f+2\omega)+\frac{1}{3}ecos(3f+2\omega)] \quad (4.32)$$

$$\Delta\Omega_{sp} = -\frac{3J_2R_e^2 cos(i)}{2p^2}[f-M+esin(f)-\frac{1}{2}sin2(f+\omega)-\frac{e}{2}sin(f+2\omega)-\frac{e}{6}sin(3f+2\omega)] \quad (4.33)$$

$$\begin{aligned}\Delta\omega_{sp} = & -\frac{3J_2R_e^2}{2p^2}\{(2-\frac{5}{2}sin^2(i))(f-M+esin(f)) \\ & +(1-\frac{3}{2}sin^2(i))[\frac{1}{e}(1-\frac{1}{4}e^2)sin(f)+\frac{1}{2}sin(2f)+\frac{e}{12}sin(3f)] \\ & -\frac{1}{e}[\frac{1}{4}sin^2(i)+(\frac{1}{2}-\frac{15}{16}sin^2(i))e^2]sin(f+2\omega) \\ & +\frac{e}{16}sin^2(i)sin(f-2\omega)-\frac{1}{2}(1-\frac{5}{2}sin^2(i))sin2(f+\omega) \\ & +\frac{1}{e}[\frac{7}{12}sin^2(i)-\frac{1}{6}(1-\frac{19}{8}sin^2(i))e^2]sin(3f+2\omega) \\ & +\frac{3}{8}sin^2(i)sin(4f+2\omega)+\frac{e}{16}sin^2(i)sin(5f+2\omega)\}\end{aligned} \quad (4.34)$$

$$\Delta M_{sp} = -\frac{3J_2R_e^2(1-e^2)^{1/2}}{2ep^2}\{-(1-\frac{3}{2}sin^2(i))$$

$$\times[(1-\frac{e^2}{4})sin(f)+\frac{e}{2}sin(2f)+\frac{e^2}{12}sin(3f)]$$
$$+sin^2(i)[\frac{1}{4}(1+\frac{5}{4}e^2)sin(f+2\omega)-\frac{e^2}{16}sin(f-2\omega)$$
$$-\frac{7}{12}(1-\frac{e^2}{28})sin(3f+2\omega)-\frac{3}{8}esin(4f+2\omega)$$
$$-\frac{e^2}{16}sin(5f+2\omega)]\}. \tag{4.35}$$

The mean values of the above perturbations are not zero, with the exception of those of a. Their mean values with respect to M are :

$$\overline{\Delta a_{sp}} = 0 \tag{4.36}$$

$$\overline{\Delta e_{sp}} = \frac{J_2R_e^2}{4p^2}sin^2i(\frac{1-e^2}{e})\overline{cos(2f)}cos(2\omega) \tag{4.37}$$

$$\overline{\Delta i_{sp}} = -\frac{J_2R_e^2}{8p^2}sin(2i)\overline{cos(2f)}cos(2\omega) \tag{4.38}$$

$$\overline{\Delta\Omega_{sp}} = -\frac{J_2R_e^2}{4p^2}cos(i)\overline{cos(2f)}sin(2\omega) \tag{4.39}$$

$$\overline{\Delta\omega_{sp}} = \frac{3J_2R_e^2}{2p^2}[sin^2i(\frac{1}{8}+\frac{1-e^2}{6e^2}\overline{cos(2f)})+\frac{1}{6}cos^2(i)\overline{cos(2f)}]sin(2\omega) \tag{4.40}$$

$$\overline{\Delta M_{sp}} = -\frac{3J_2R_e^2}{2p^2}(1-e^2)sin^2(i)(\frac{1}{8}+\frac{1e^2/2}{6e^2}\overline{cos(2f)})sin(2\omega), \tag{4.41}$$

where $\overline{cos(2f)}$ is given by

$$\overline{cos(2f)} = (\frac{-e}{1+\sqrt{1-e^2}})^2(1+2\sqrt{1-e^2}). \tag{4.42}$$

4.3.3 Numerical Integration

The alternative to correcting the solutions to Keplerian motion analytically to account for perturbation effects is to deal with the perturbation forces directly in the equations of motion and solve for orbital positions, velocities and elements numerically. This is the approach adopted by propagation option 8 in program TRAJECTORY.

From equation (4.1), the second order ordinary differential equation (ODE) which represents unperturbed orbital motion is,

$$\ddot{\mathrm{r}}+(\frac{\mu}{r^3})\mathrm{r} = 0. \tag{4.43}$$

The motion described is in the standard geocentric inertial frame. In the perturbed case, equation (4.43) becomes

$$\ddot{\mathbf{r}} + (\frac{\mu}{r^3})\mathbf{r} = \mathbf{f}_{pert}, \tag{4.44}$$

where $\mathbf{f}_{pert}$ is the resultant perturbing acceleration. Equation (4.44) can be split up into two first order ODEs thus,

$$\dot{\mathbf{r}} = \mathbf{v}, \tag{4.45}$$

and

$$\dot{\mathbf{v}} = \mathbf{f}_{pert} - (\frac{\mu}{r^3})\mathbf{r}. \tag{4.46}$$

Equations (4.45) and (4.46) are solved in TRAJECTORY directly using a simple fourth-order Runge-Kutta numerical integration scheme [100]. A fourth-order Runge-Kutta scheme is employed because it is a well-established technique and is relatively straightforward to implement. The main purpose of propagation method 8 is to validate the results from method 7 and so a more complex, higher precision integration scheme is not required. For commonality with method 7, propagation option 8 only models the perturbative effects due to J_2 and atmospheric drag.

The effects of atmospheric drag are modelled quite simply using [94]

$$\mathbf{f}_{drag} = -\frac{1}{2}\rho\delta v\mathbf{v}, \tag{4.47}$$

where $\mathbf{f}_{drag}$ is the acceleration due to drag and δ $(= \frac{AC_D}{m})$ is the orbiting body's ballistic coefficient (BC). The atmospheric density, ρ, is calculated from the CIRA-72 atmosphere as before.

The perturbations resulting from the Earth's oblateness are represented as follows [101],

$$\text{Radial component} : \mathbf{f}_{J_2(S)} = J_2^* \ (1 - 3sin^2(i)sin^2(u)), \tag{4.48}$$

$$\text{Tangential component} : \mathbf{f}_{J_2(T)} = J_2^* \ sin^2(i)sin(2u), \tag{4.49}$$

$$\text{Normal component} : \mathbf{f}_{J_2(W)} = J_2^* \ sin(2i)sin(u), \tag{4.50}$$

where

$$J_2^* = \frac{-3\mu J_2 R_e^2}{2r^4}. \tag{4.51}$$

The total perturbing acceleration is then given by,

$$\mathbf{f}_{pert} = \mathbf{f}_{J_2} + \mathbf{f}_{drag}, \tag{4.52}$$

where $\mathbf{f}_{J_2}$ is the resultant J_2 acceleration transformed to the geocentric frame.

4.4 Program TRAJECTORY

4.4.1 Programming Issues

TRAJECTORY2.0 is the latest version of program TRAJECTORY and is the second main module in the SDS software suite. As with BREAKUP, the program runs from input files which are modified by the user with a standard Text Editor. The orbit of the breakup CM is taken from BREAKUP input file *break4_control*. All positions in the orbiting frame are given relative to the breakup CM orbit, which is propagated using Keplerian motion (method 4). *traj2_control* contains the main program inputs, including the initial Δv of the fragment/object in question relative to the reference orbit. If this is set to 0 then TRAJECTORY2.0 simply propagates the CM orbit. The inputs in *traj2_control* also set the simulation start time (post-breakup), the time-step to be used in the orbit propagation and the number of time-steps to be considered. The remaining inputs set the BC for the object, describe the orbital environment in terms of solar activity and re-entry altitude and define the propagation option to be adopted (Figure 4.3). TRAJECTORY2.0 can run in either single-simulation or multi-method automatic modes. The mode in which it is to be operated is determined by the third input file *traj2_auto*. The single-simulation mode simply runs the program once with the inputs given in *break4_control* and *traj2_control*. If auto-mode is selected then the program is run for the given inputs for each of the orbit propagation methods indicated. This feature enables the effects of the propagation method to be investigated quickly and efficiently for the same input example. This facility is used in the next section.

As with BREAKUP4.0, TRAJECTORY2.0 outputs to a number of data files. Propagation options 1-3 (the state transition matrix methods) output the fragment

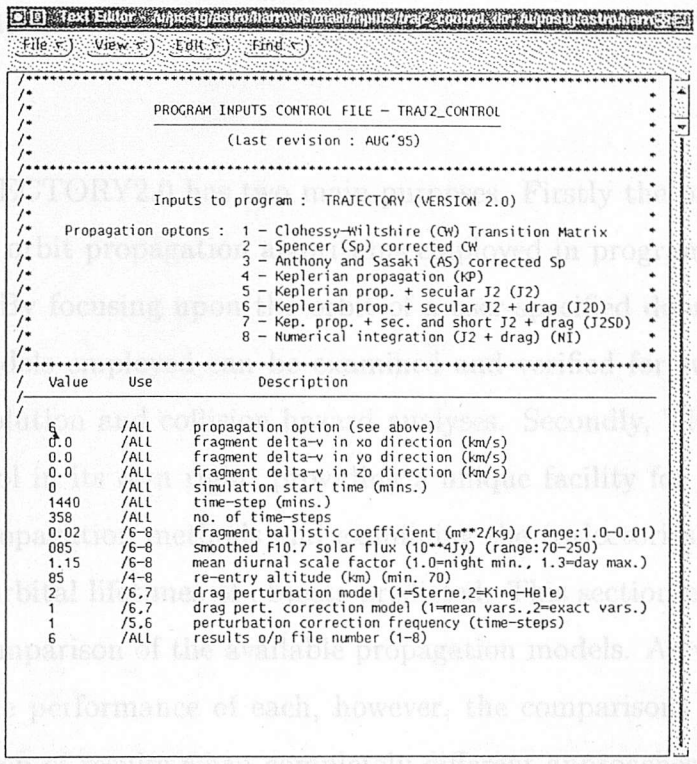

```
Text Editor - /u/postg/astro/hamowe/main/inputs/traj2_control - in: /u/postg/astro/hamowe/main
File ▾   View ▾   Edit ▾   Find ▾

/*****************************************************************
/*                                                               *
/*              PROGRAM INPUTS CONTROL FILE - TRAJ2_CONTROL      *
/*                                                               *
/*                      (Last revision : AUG'95)                 *
/*                                                               *
/*****************************************************************
/*                                                               *
/*                Inputs to program :  TRAJECTORY (VERSION 2.0)  *
/*                                                               *
/*   Propagation optons :  1 - Clohessy-Wiltshire (CW) Transition Matrix  *
/*                         2 - Spencer (Sp) corrected CW         *
/*                         3 - Anthony and Sasaki (AS) corrected Sp  *
/*                         4 - Keplerian propagation (KP)        *
/*                         5 - Keplerian prop. + secular J2 (J2)  *
/*                         6 - Keplerian prop. + secular J2 + drag (J2D)  *
/*                         7 - Kep. prop. + sec. and short J2 + drag (J2SD)  *
/*                         8 - Numerical integration (J2 + drag) (NI)  *
/*                                                               *
/*****************************************************************
/  Value     Use            Description
/-----------------------------------------------------------------
/
    6         /ALL     propagation option (see above)
    0.0       /ALL     fragment delta-v in xo direction (km/s)
    0.0       /ALL     fragment delta-v in yo direction (km/s)
    0.0       /ALL     fragment delta-v in zo direction (km/s)
    0         /ALL     simulation start time (mins.)
    1440      /ALL     time-step (mins.)
    358       /ALL     no. of time-steps
    0.02      /6-8     fragment ballistic coefficient (m**2/kg) (range:1.0-0.01)
    085       /6-8     smoothed F10.7 solar flux (10**4Jy) (range:70-250)
    1.15      /6-8     mean diurnal scale factor (1.0=night min., 1.3=day max.)
    85        /4-8     re-entry altitude (km) (min. 70)
    2         /6,7     drag perturbation model (1=Sterne,2=King-Hele)
    1         /6,7     drag pert. correction model (1=mean vars.,2=exact vars.)
    1         /5,6     perturbation correction frequency (time-steps)
    6         /ALL     results o/p file number (1-8)
```

Figure 4.3: TRAJECTORY2.0 input control file *traj2_control*

position after each time-step in relative coordinates only. The output channel to be used is specified in *traj2_control*. Eight channels are available, corresponding to the eight propagation methods. In auto-mode, the results from each propagation method are written to the corresponding channel number. In single-simulation mode, any of the eight channels can be used for each run. Relative position data is output to file *traj#.dat* where # corresponds to the channel number. Propagation methods 4-8 also output the orbit positions in geocentric inertial coordinates to file *traj#i.dat* and the variation of orbital elements over the run to file *traj#ev.dat*. As with BREAKUP and the other SDS programs, data visualisation is achieved through dedicated Matlab plotting routines. In the next two sections, TRAJECTORY is used to illustrate the difference between the various propagation methods available in terms of predicted orbits, and results from the program are compared with real satellite orbital data.

4.4.2 Comparison of Propagation Methods

Overview

Program TRAJECTORY2.0 has two main purposes. Firstly the program acts as a test-bed for the orbit propagation algorithms employed in programs EVOLUTION and TARGET. By focusing upon the orbit of a user-specified debris fragment, the propagation models employed can be examined and verified for subsequent use in debris cloud evolution and collision hazard analyses. Secondly, TRAJECTORY2.0 is a valuable tool in its own right, providing a unique facility for comparing a variety of orbit propagation methods and examining the trajectories, orbital element variations and orbital lifetimes of objects predicted. This section explicitly concentrates on the comparison of the available propagation models. As well as providing a measure of the performance of each, however, the comparisons also produce an implicit validation of results when completely different approaches are found to be in good agreement; for example a state transition matrix method with Keplerian propagation or analytical orbit propagation with numerical integration.

State transition matrix methods and Keplerian propagation

Four test cases are used here to compare the orbital trajectories produced by the the three state transition matrix methods with those generated using Keplerian propagation. The three state transition matrix methods are all approximations to ideal, two-body, motion, formulated in the relative orbiting frame as opposed to geocentric inertial coordinates. How they perform when compared with Keplerian propagation, therefore, gives an indication of how good the approximations are and how useful the methods are for propagating fragment orbits. The breakup, or reference, orbit used in all of the four cases is the same as that of the SPOT-1 Ariane third stage pre-breakup. That is, it is a 800km altitude, near-circular orbit with an inclination of 98.7 degrees. In each case, a fragment is given a Δv relative to the breakup state, and its trajectory relative to the breakup orbit is examined.

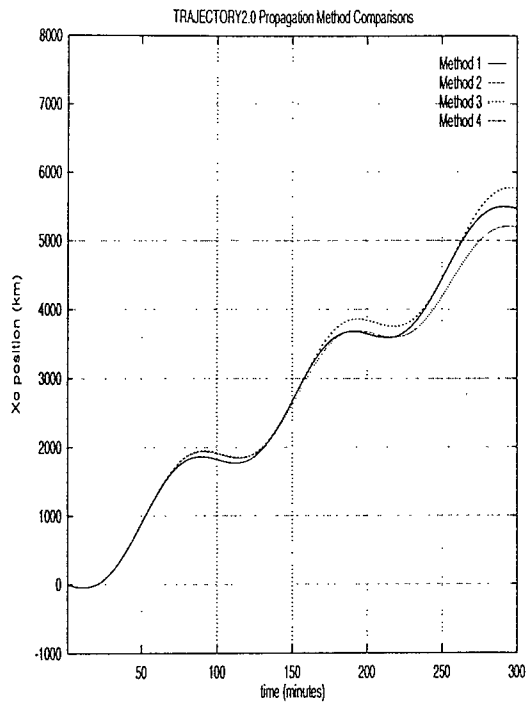

a) Xo position vs time comparison

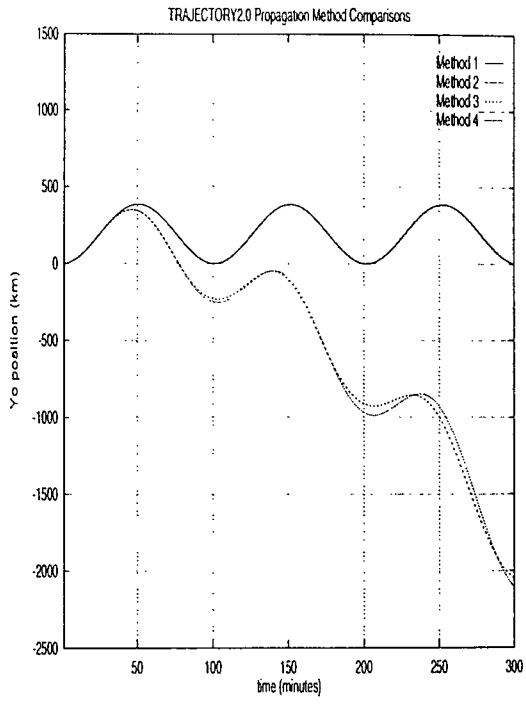

b) Yo position vs time comparison

Figure 4.4: Comparison of state transition matrix methods with Keplerian propagation : Case 1

Case 1

In this, the fragment is given a 100m/s Δv in the forward tangential direction, i.e. a prograde ejection. This direction corresponds to the negative orbiting frame X-axis, or $-X_o$. The motion of the fragment relative to the breakup orbit is, therefore, restricted to the breakup orbit plane as the effects of orbital perturbations are not considered. The size of the Δv is comparable to the largest ejection velocities recorded for the SPOT-1 fragmentation. This, of course, only includes the fragments actually detected. Figure 4.4 shows the orbital trajectories produced for case 1 for the first 300 minutes post-breakup. From Figure 4.4a it can be seen that all four methods exhibit the same general behaviour and the transition matrix methods appear to offer a reasonable approximation to the full ideal equations of motion. Methods 1 and 2 are essentially identical for the cases considered here since the breakup orbit in question is near-circular and so the eccentricity-corrections applied by method 2 to the method 1 solutions are virtually non-existent. Figure 4.4b is

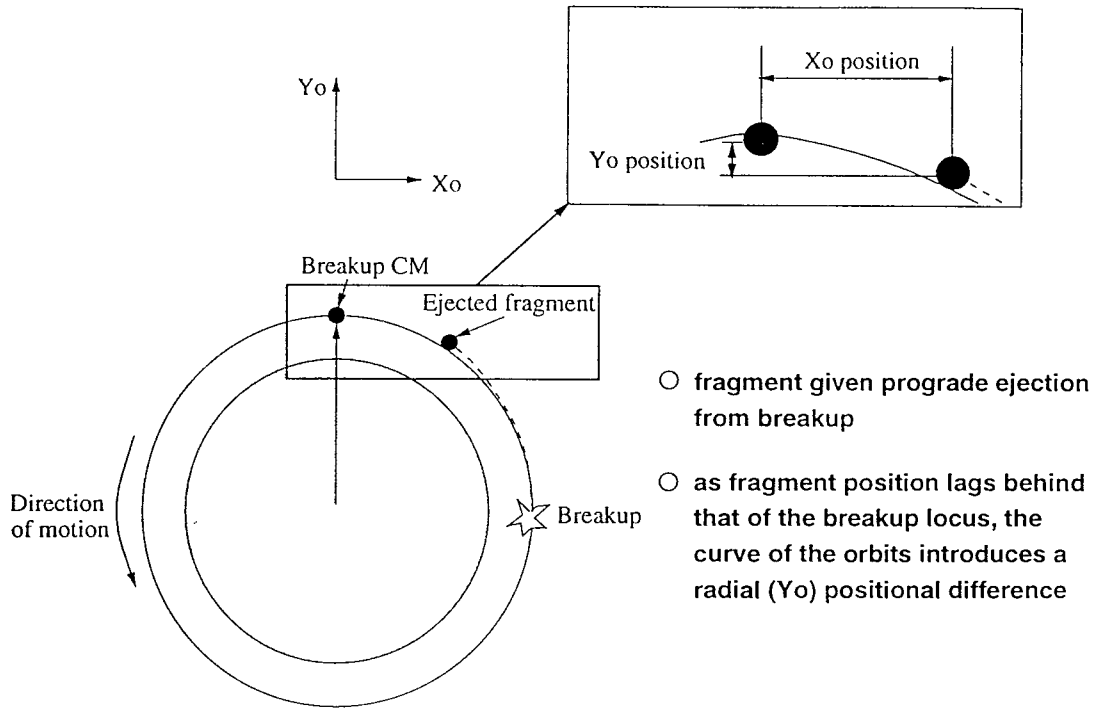

Figure 4.5: Curl of fragment relative trajectory around breakup orbit

considerably more revealing. The linearised approximations of the first two methods are unable to cope with the large radial deviations from the breakup orbit locus. Here the dramatic improvement of the novel second order model over these techniques is clearly evident. The consideration of second order relative distance terms enables the 'curl' of the fragment relative position around the breakup orbit to be accounted for as the along-track positional difference increases. This phenomenon can be visualised quite clearly when a cloud of fragments is considered (see Chapter 5). The situation is also shown schematically in Figure 4.5.

Case 2

Case 2 considers a radial fragment ejection ($+Y_o$), also of 100m/s. The radial ejection results in a much smaller departure for the fragment from the breakup locus than for case 1, with eccentricity being the main orbital parameter altered by the Δv. This produces the periodic relative distance time-histories shown in Figure 4.6. All three state transition matrix methods are seen to be capable of following the method 4 trajectory.

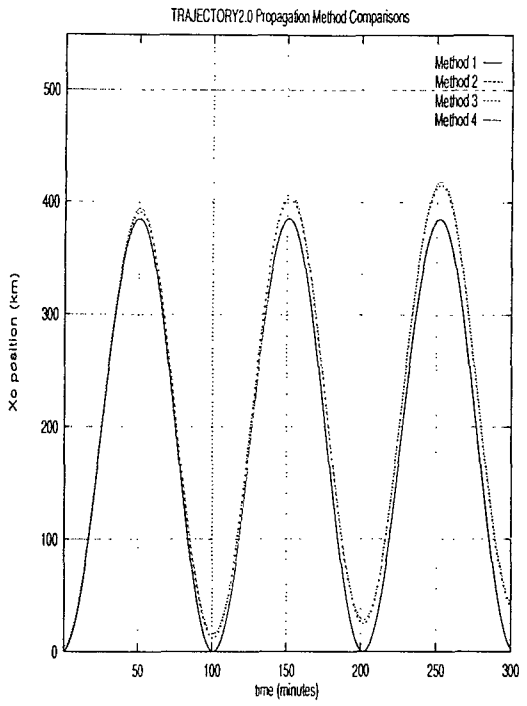

a) Xo position vs time comparison

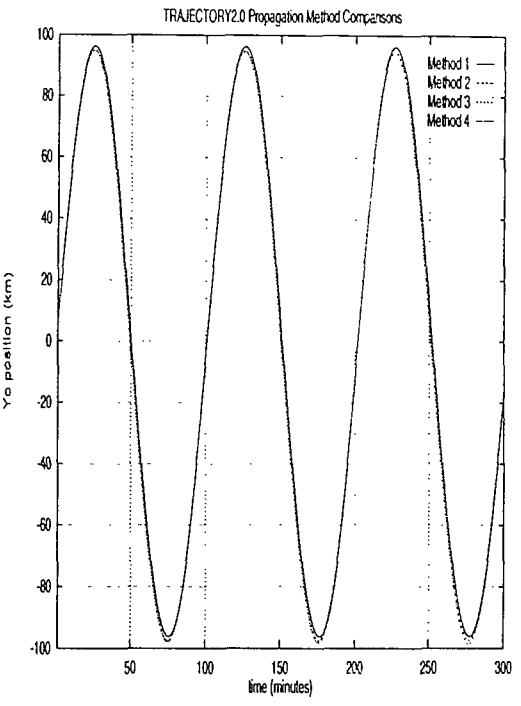

b) Yo position vs time comparison

Figure 4.6: Comparison of state transition matrix methods with Keplerian propagation : Case 2

Case 3

Here, the ejection velocity is directed out of the breakup plane, in the $+\mathbf{Z}_o$ direction. The Δv is once again 100m/s. The primary effect of such an ejection is to change the orbit plane of the fragment. This results in the periodic out-of-plane position variation shown in Figure 4.7. The out-of-plane motion produced by the four propagation methods is virtually identical. Although the Δv is directed completely out of the breakup plane, it does nonetheless have an effect in-plane. The vector addition of the fragment Δv to the breakup orbital velocity vector produces a fragment velocity vector with a greater magnitude than that of the breakup CM, thus throwing the fragment into a higher energy orbit. This can be seen in the method 3 and 4 curves on Figure 4.8. The fragment lags behind the breakup locus and has the greater orbit radius. Methods 1 and 2 de-couple in-plane and out-of-plane motion and so fail to exhibit this true behaviour. Method 3, however, makes no such simplification and again is able to provide a good match to the ideal curve.

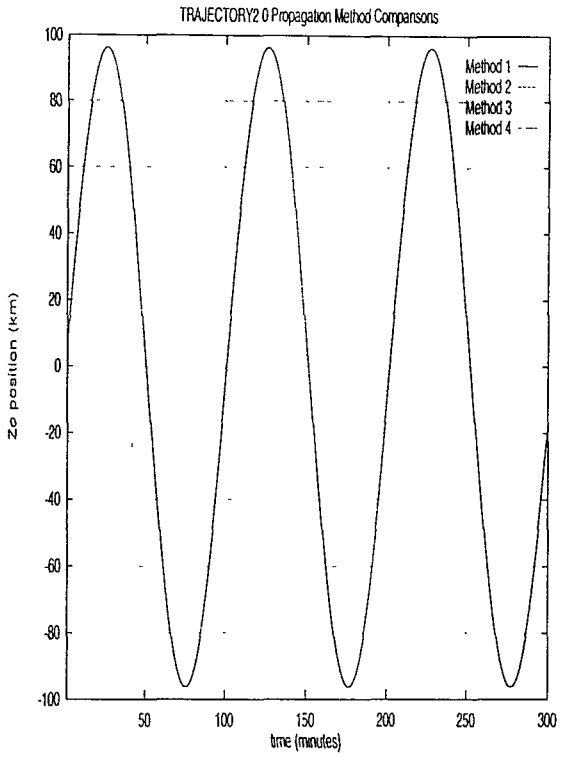

Figure 4.7: Comparison of state transition matrix methods with Keplerian propagation : Case 3, out-of-plane motion

Case 4

This is essentially a repeat of case 1 but with a higher ejection velocity. This time the Δv in the -$\mathbf{X}_o$ is 500m/s. Such a Δv could be considered to correspond to a small, untrackable, piece of debris. The higher Δv accelerates the fragment's departure from the breakup locus. In this example, the matching of methods 3 and 4 finally breaks down. The second order relative distance corrections are able to 'keep pace' with the ideal solution for little more than an hour, before the two trajectories diverge rapidly (Figure 4.9). This loss of results matching is caused by the second order model's inability to cope with the 'curling' of the relative distances involved once the breakup locus and the fragment position are separated by an angle of more than $\pi/2$ (this phenomenon is discussed again in the next chapter). So, although an undoubted improvement over methods 1 and 2 in the majority of cases, method 3 ceases to become useful as an adequate approximation for Keplerian propagation for Δv s of more than around 100m/s.

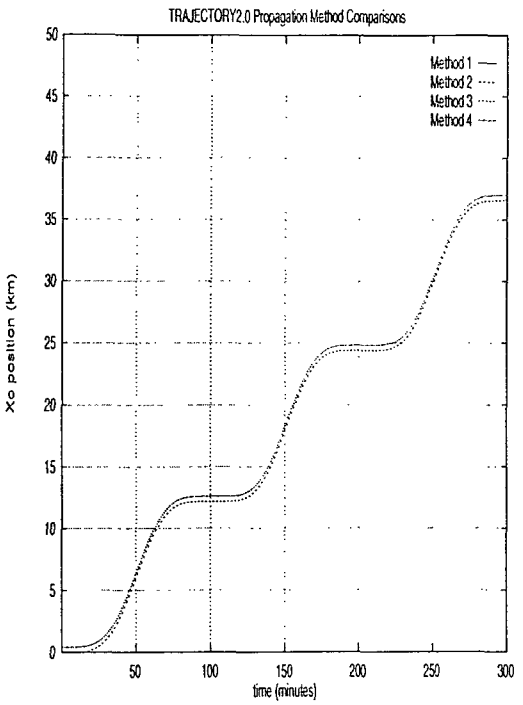

a) Xo position vs time comparison

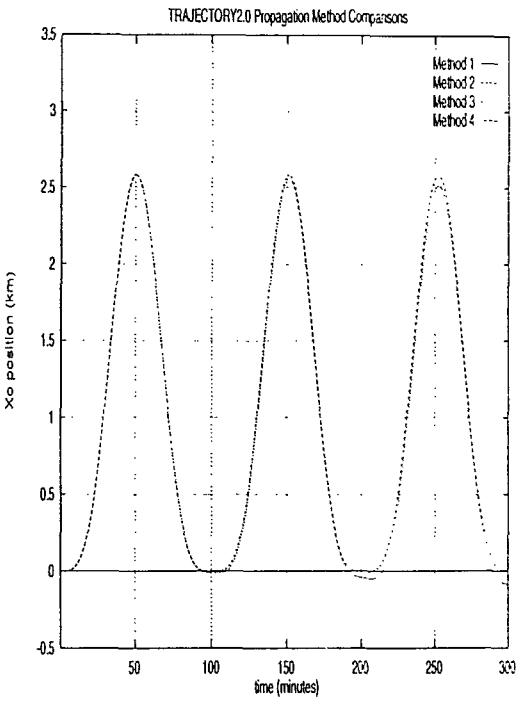

b) Yo position vs time comparison

Figure 4.8: Comparison of state transition matrix methods with Keplerian propagation : Case 3, in-plane motion

Unperturbed and perturbed orbital motion

An additional test case is employed here to compare the four methods of analytic orbit propagation and numerical integration. The breakup orbit chosen is considerably lower than that of the four cases in the previous section, the aim being to illustrate the effects of atmospheric drag as well as the J_2 geopotential term. The orbit selected is at 300km altitude, near-circular and with an inclination of 28.5 degrees. The trajectory of a fragment ejected at 100m/s in the prograde direction is examined for 1 day with 1 minute time-steps. TRAJECTORY2.0 auto-mode is used to run the case for methods 4-8. Each output file number, therefore, directly corresponds to the method number. Matlab-SDS plotting functions *trajcomp* and *elvcomp* are used to graphically compare the trajectories and orbital element variations produced.

Figure 4.10 shows the fragment trajectories produced by methods 4 and 5. The consideration of secular J_2 effects by method 5 introduces positional differences of

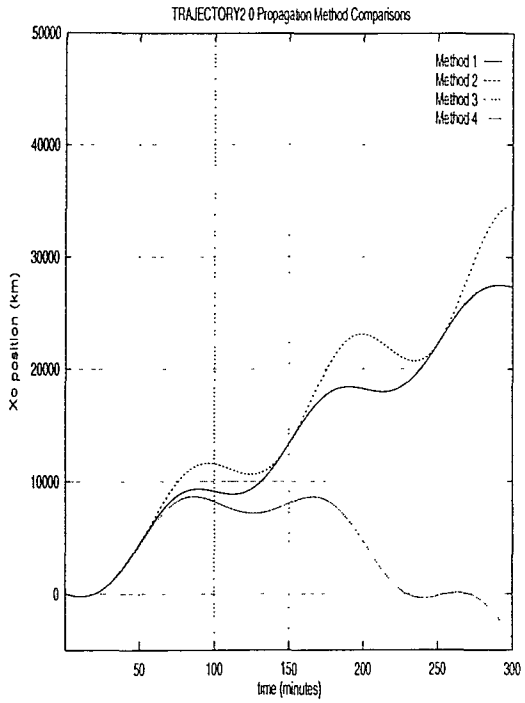

a) Xo position vs time comparison

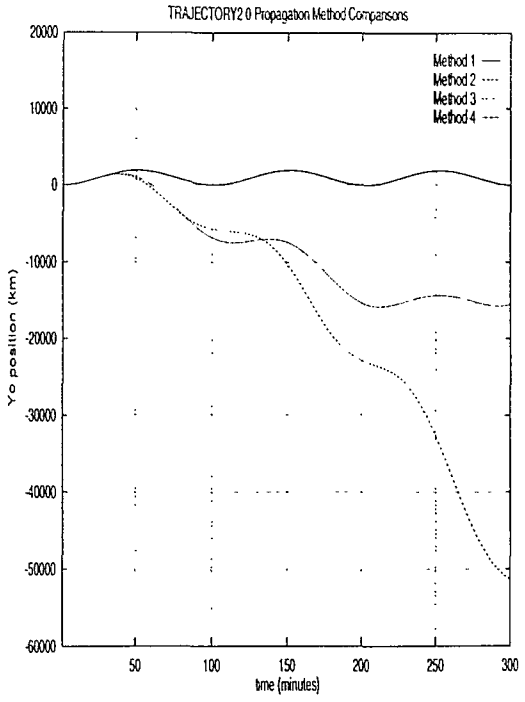

b) Yo position vs time comparison

Figure 4.9: Comparison of state transition matrix methods with Keplerian propagation : Case 4

the order of several hundred km by the end of the the simulation, both in and out of the breakup orbit plane. The Xo and Yo position time-histories show a common behaviour but as the perigee of the method 5 fragment orbit precesses, the two curves in each case begin to diverge towards the end of the run. The most noticeable difference between the two predicted trajectories is in the out-of-plane motion. The modelling of J_2 effects introduces a periodic, increasing, oscillation of the Zo coordinate. This is due to the regression of the fragment orbit's ascending node which results in the orbit plane rotating about the inertial frame Z axis. The breakup and method 4 orbit planes, however, remain fixed in space. As the angle between the fragment orbit plane and the breakup orbit plane increases, so does the amplitude of the Zo oscillations.

The decay of the fragment orbit under the influence of atmospheric drag is modelled by method 6 using the Sterne drag model, with mean drag variations applied every time-step. A ballistic coefficient of $0.1\text{m}^2/\text{kg}$ is assumed for the fragment.

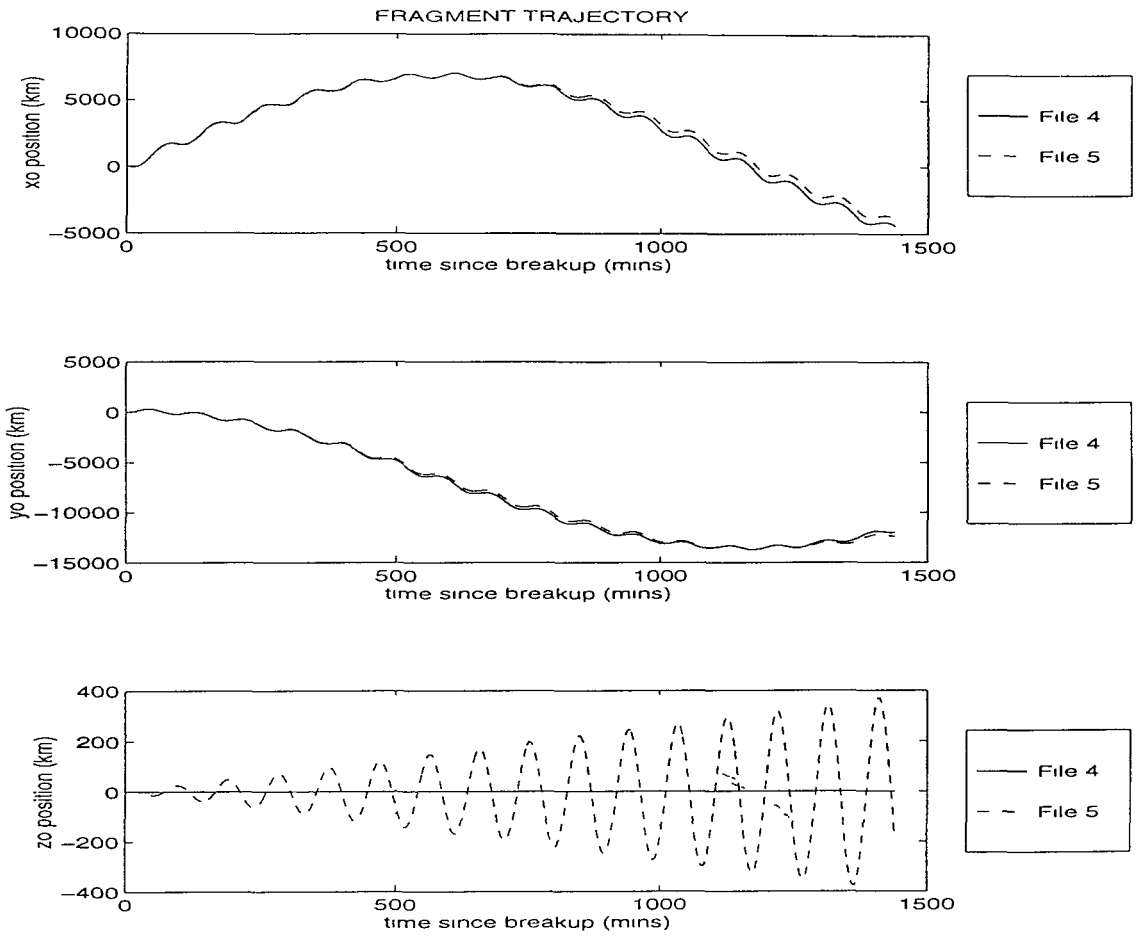

Figure 4.10: Comparison of orbit propagation techniques : Methods 4 and 5

The variation in the orbital elements predicted by methods 5 and 6 is shown in Figure 4.11. Drag causes both the fragment semi-major axis and eccentricity to fall over the course of the simulation. As the orbit mean motion is dependent upon the semi-major axis, this is seen to increase over time. The changes in a, e and n are quite small and at first glance would suggest a correspondingly small positional discrepancy between the two methods. This is, however, not the case because as the fragment orbit looses energy to work done against the atmosphere, the fragment moves ahead of the breakup locus due to its reduced orbital period. Only a very small difference in true anomaly is needed for a large positional difference to be produced. The difference in this case is small enough to be masked by the scale on the true anomaly plot on Figure 4.11 but large enough ($\approx$2 degrees) to produce an

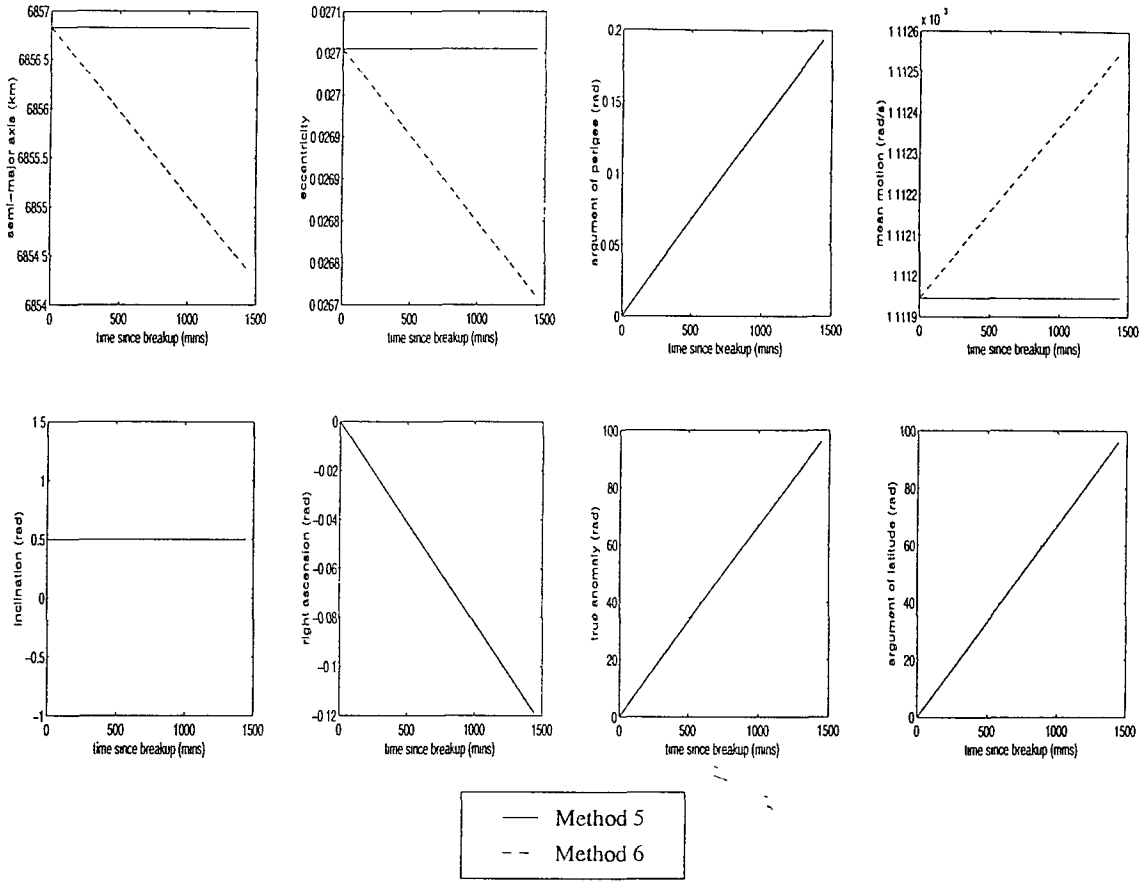

Figure 4.11: Comparison of orbit propagation techniques : Methods 5 and 6

along-track positional difference between the two methods of nearly 300km.

TRAJECTORY propagation method 6 has a number of drag modelling options available. These are compared for the scenario in question in Figure 4.12. The baseline condition is that used in Figure 4.11 above, i.e. mean drag variations calculated using Sterne's drag model (equations (4.18)-(4.24)). The use of King-Hele's expressions for $(da/dE)_D$ and $(de/dE)_D$ (equations (4.25) and (4.26)) produces a negligible difference compared to the Sterne results, even when exact variations are applied at every time-step. The Sterne and King-Hele models can, therefore, be considered to be virtually interchangeable. For the moderate drag perturbations of case 5, applying mean drag variations throughout the simulation is shown to be an adequate approximation to applying exact variations at every time-step. In certain situations, using mean variations is actually the 'safest' option, i.e. the least likely to produce spurious results. This is illustrated by the fourth line in Figures 4.12a

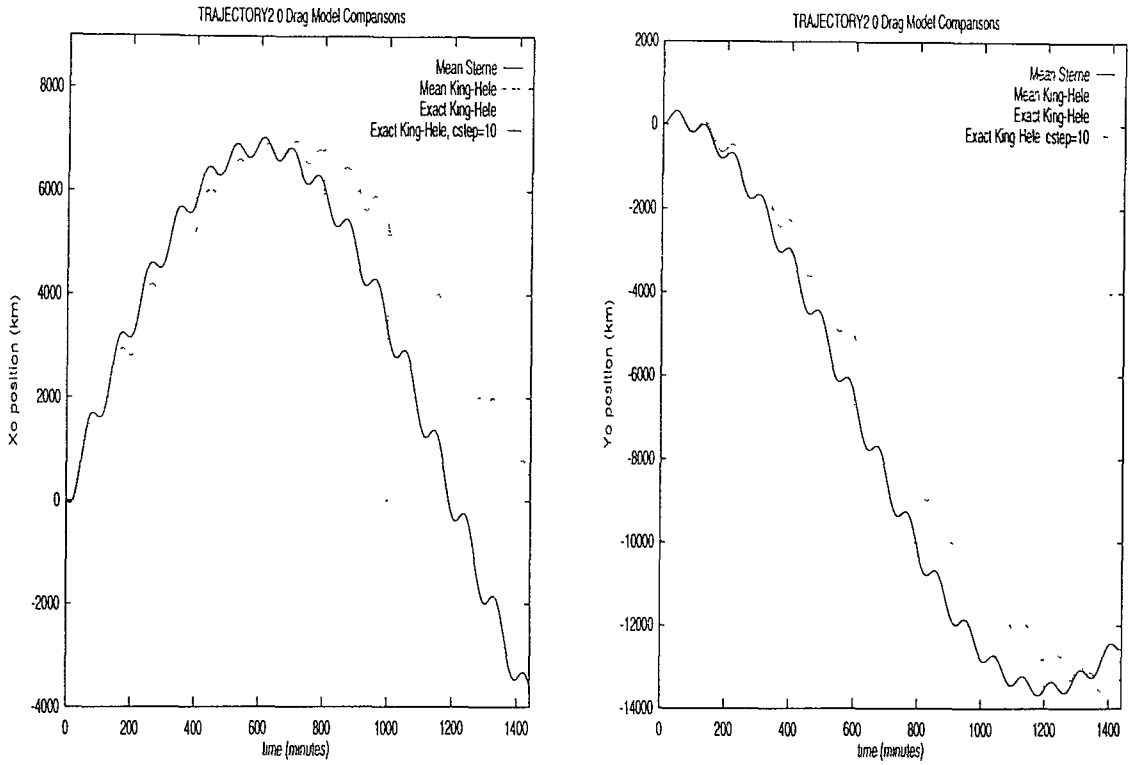

a) Xo position time-histories b) Yo position time-histories

Figure 4.12: Comparison of method 6 drag models

and 4.12b. Here exact variations are employed with the King-Hele model but are only applied every 10 time-steps (correction step, *cstep*, =10). Values of $(da/dE)_D$ and $(de/dE)_D$ are thus used for much longer than strictly applicable, with extended use of the drag variations calculated near perigee and apogee in particular producing the divergent trajectory shown.

Propagation method 7 superimposes short period J_2 effects onto the secular J_2 plus atmospheric drag model of method 6. The consideration of short period J_2 element variations raises the issue of how to deal with the osculating orbit of method 7 in relation to the orbits of methods 4, 5 and 6, which are all implicitly mean. The approach adopted by TRAJECTORY2.0 is to treat the breakup orbit input from *break4_control* as defining the mean orbit state at the breakup epoch. In the case of propagation methods 4,5 and 6, the breakup location lies on the breakup mean orbit, and it is the mean orbit of the ejected fragment that is subsequently propagated. For method 7, short period J_2 perturbations are calculated from and added to the

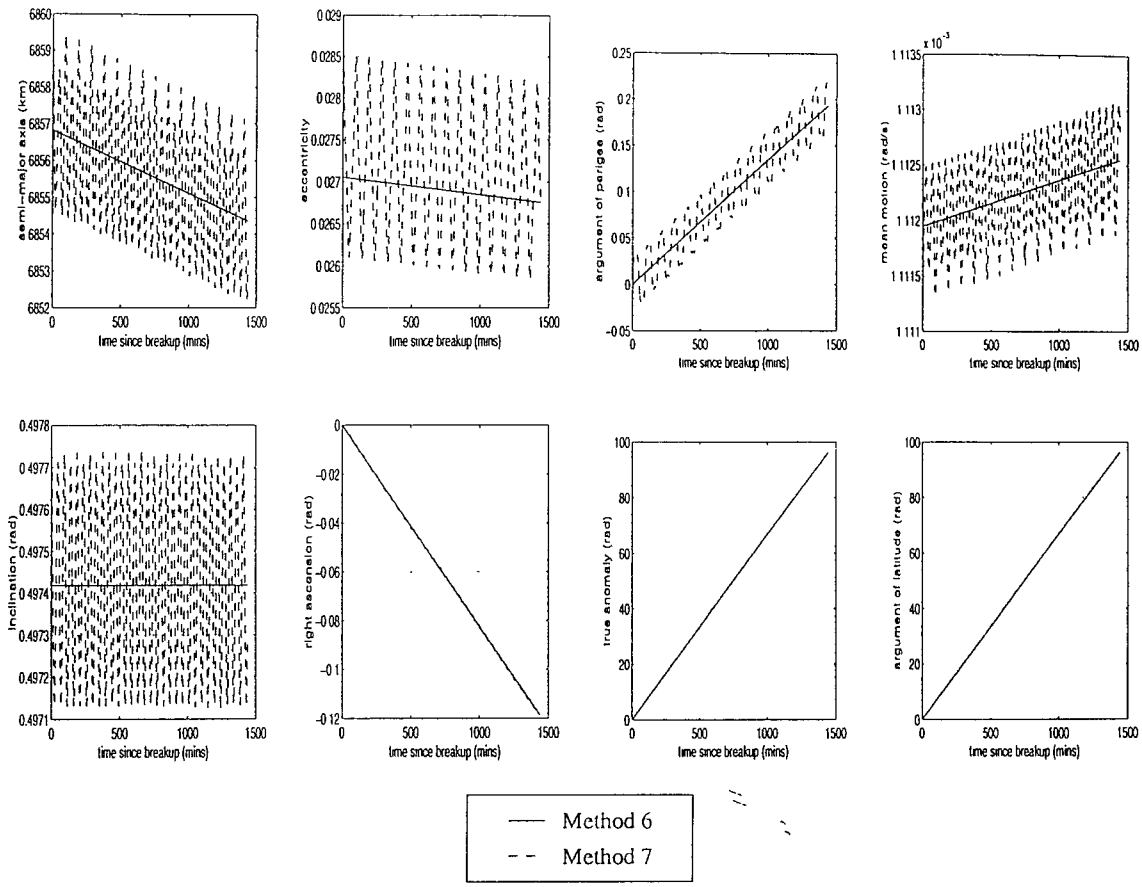

Figure 4.13: Comparison of orbit propagation techniques : Methods 6 and 7

mean fragment orbital element values to define the initial osculating orbit. This ensures that method 7 and methods 4-6 consider the same mean orbit, and hence are directly comparable. Figure 4.13 shows the method 6 and 7 element variations for case 5. The short-period perturbations are clearly evident as oscillations about the mean element values. The positional differences between the two trajectories are also found to be periodic and are less than 10km in magnitude.

The last of the eight TRAJECTORY2.0 propagation methods is a simple numerical integration scheme which considers J_2 and atmospheric drag in its force model. This technique propagates an orbit in a completely different way to the analytic approaches of methods 4-7. Instead of calculating orbital positions and velocities from orbital elements, which are updated/perturbed every *cstep* time-steps, method 8 uses the position and velocity vectors to drive the orbit, and element values are only calculated incidently for making model comparisons. The excellent matching

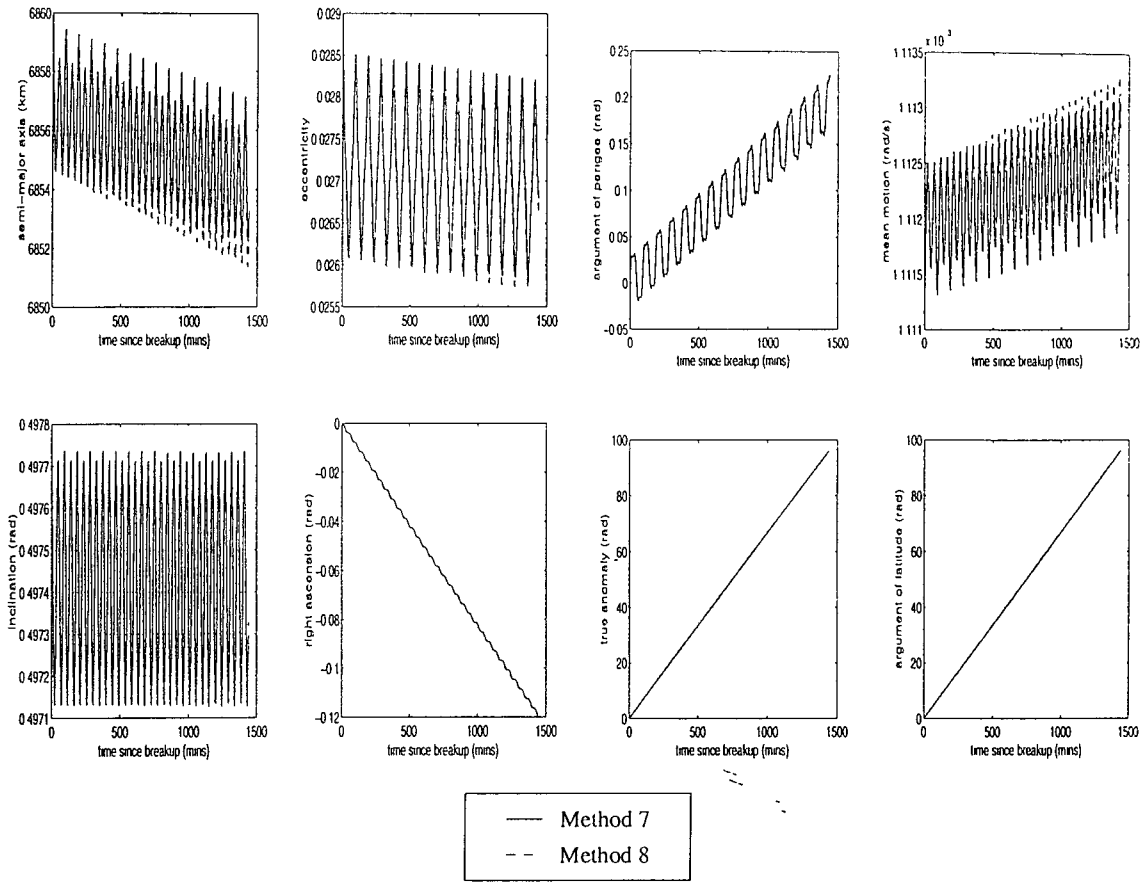

Figure 4.14: Comparison of orbit propagation techniques : Methods 7 and 8

of the method 7 and 8 element variations shown in Figure 4.14 ,therefore, provides a mutual validation of both sets of results.

Summary

The novel second order state transition matrix method (propagation method 3 in TRAJECTORY2.0) offers a considerable improvement over the linearised approximations offered by methods 1 and 2. Method 3 quickly looses accuracy, however, when compared with Keplerian propagation for cases with high fragment ejection velocities. It is also limited in terms of the eccentricity of the breakup orbit that can be considered because it uses the first order eccentricity corrections employed by method 2. Method 3 represents the useful limit of extension of the original linearised state transition matrix model. The formulation of the second order model is considerably more complex than the simple linearised case and although more

accurate results are produced, it is debatable whether the increase in accuracy (and hence increase in length of simulations possible) is sufficient to justify the added complexity of implementation. All three state transition matrix methods examined, therefore, are found to have only limited practical use.

Methods 4-7 offer relatively straightforward analytical methods of orbit propagation which, in terms of the perturbation effects modelled, are in increasing order of accuracy and realism. Results from method 7, agree well with the numerical integration approach of method 8. This mutual results-validation, in particular, lends support to utility of the trajectories produced by the analytical methods. The consideration of short period J_2 perturbations in method 7 is found to provide only a minor periodic positional difference to the trajectories produced by method 6. Method 6 can, therefore, be considered as being the 'best' TRAJECTORY2.0 (mean) orbit propagator. This is not only for dedicated fragment trajectory calculation purposes, but also as an embedded algorithm for debris cloud evolution (in program EVOLUTION3.0) and collision hazard assessment (in program TARGET4.0).

4.4.3 Comparison of Results with Actual Orbital Data

Overview

The orbits of three satellites are used here to validate the output from TRAJECTORY propagation option 6. In each case, TRAJECTORY2.0 is used to simulate the orbit of the satellite in question and the predicted variation of orbital elements over the simulation period is compared with the actual variation of elements observed.

China 2 rocket

The first example looks at the orbit of the China 2 rocket body (1971-18B) over the period July 2 1971 to January 28 1972, as documented in [102]. Orbital parameters are given at 36 epochs over the 7 month period enabling a direct comparison to be

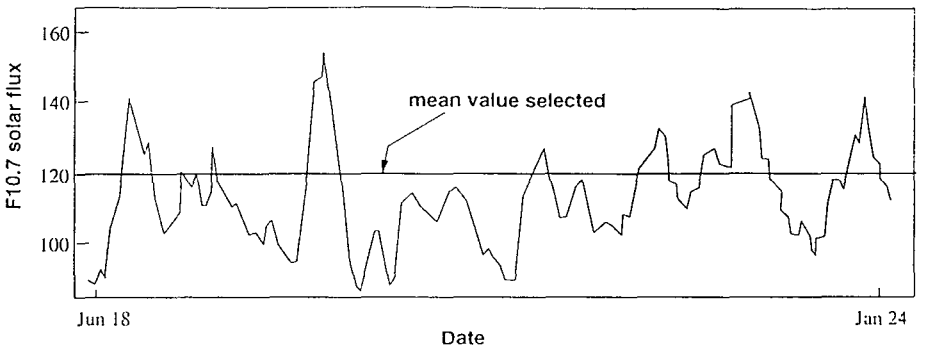

Figure 4.15: $F_{10.7}$ solar flux data for the China 2 rocket analysis

made with the element variations predicted by TRAJECTORY2.0. The cylindrical rocket body is quoted as having a BC of approximately $0.017\text{m}^2/\text{kg}$, and solar flux ($F_{10.7}$) data is provided for the time period in question. The variation of $F_{10.7}$ is shown in Figure 4.15. A constant value of 120 for $F_{10.7}$ is adopted for the simulation and this is used in place of $\overline{F}_{10.7}$ in equation (4.29). This corresponds to an average exospheric temperature of $\approx$ 883 degrees Kelvin. The King-Hele drag model is used for the run, with mean drag variations applied every time-step. A time-step of 1 day is used and the simulation is run for the full 210 day time-span for which orbital data is provided.

Figure 4.16 shows the orbital decay of the China 2 rocket in terms of the decrease in semi-major axis and orbit eccentricity. In both cases the actual and simulated variations are plotted on the same graph. From Figure 4.16a it can be seen that the TRAJECTORY2.0 simulation overestimates the decay of semi-major axis by just over 10km. The eccentricity variations shown in Figure 4.16b match extremely well for the first 100 days of the simulation but then begin to diverge. So, the general decay and circularisation trends of the rocket orbit are adequately predicted by TRAJECTORY2.0 and comparison with the actual element variations yield reasonable approximations.

The effects of the Earth's oblateness on the rocket orbit are shown in Figure 4.17. The actual regression of the orbit ascending node shown in Figure 4.17a follows almost exactly the secular variation predicted by TRAJECTORY2.0. Similarly, the actual and simulated perigee precessions in Figure 4.17b are virtually indistinguish-

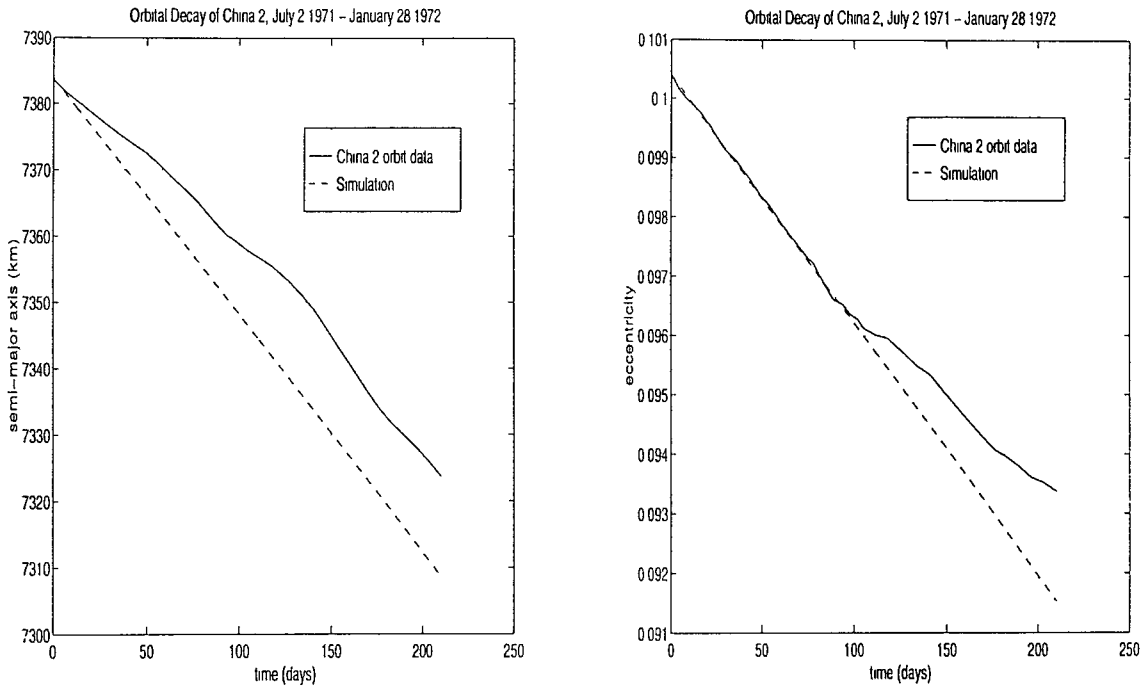

a) China 2 semi-major axis variation

b) China 2 eccentricity variation

Figure 4.16: Orbital decay of China 2 rocket

able. For simulations of this length, then, the simple secular J_2 variations in Ω and ω given in equations (4.16) and (4.17) seem to be perfectly adequate for predicting the evolution of the orbit under the influence of the Earth's gravity field.

Skylab 1

The second satellite modelled is Skylab 1 (1973-27A), the time period considered being its final decay into the Earth's atmosphere from June-July 1979. The orbital data for this example comes from [103]. Orbital parameters are provided at 21 epochs during a 14 day period from June 27. From the information given on the satellite mass and dimensions, a ballistic coefficient of $0.007 \mathrm{m}^2/\mathrm{kg}$ is estimated. As with the China 2 study above, a mean value of the $F_{10.7}$ solar flux is adopted for the simulation (Figure 4.18). Using $F_{10.7}$=180 in equation (4.29) sets a constant exospheric temperature of $\approx$1107 degrees Kelvin. Two simulation runs are performed for this example, both of which use the King-Hele drag model. The first run uses mean drag variations and 1 day time-steps, as per the China 2 analysis. The second

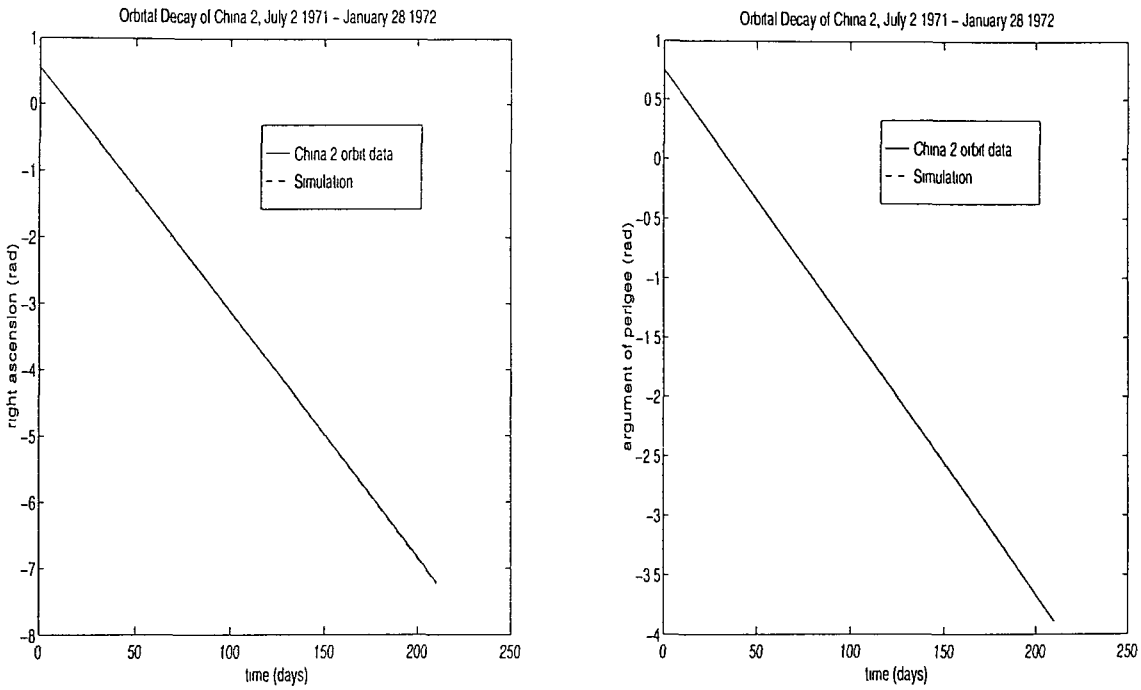

a) China 2 RAAN variation

b) China 2 argument of perigee variation

Figure 4.17: Nodal regression and perigee precession of China 2 rocket orbit

run uses 0.01 day (14.4 minute) time-steps and applies exact drag variations.

Figure 4.19 shows the orbital decay of Skylab 1. From Figure 4.19a it can be seen that using exact drag variations, with an appropriately small time-step, provides a much better match of TRAJECTORY2.0 results to the actual Skylab 1 curve. This is due to the low orbital altitude in question and the rapid decay of Skylab's orbit towards the end of the simulation. The mean drag variations are calculated at the start of the simulation when Skylab is at a height of around 250km, and are held constant throughout the run. As its orbit decays, atmospheric density increases rapidly, accelerating the satellite's downward spiral towards re-entry. Using exact variations enables these large changes in atmospheric density to be accounted for. Hence, exact drag variations should always be used for such scenarios. Mean drag variations and large time-steps are perfectly adequate at higher altitudes, but such approximations are only valid for short time-spans near re-entry. Figure 4.19b shows that the discrepancy between the actual and simulated eccentricity variations is reduced by using exact variations, but the difference remains sizeable with respect

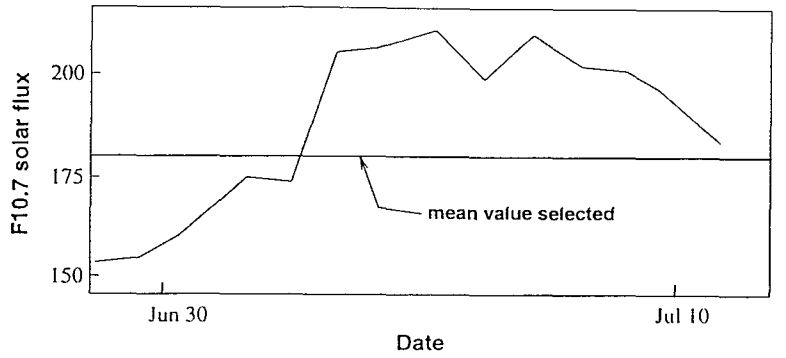

Figure 4.18: $F_{10.7}$ solar flux data for the Skylab 1 analysis

to the values of eccentricity involved. The eccentricities in question are very small, however, and so such discrepancies result in relatively small positional errors.

The nodal regression of the Skylab 1 orbit is shown in Figure 4.20a. As with the China 2 results previously, the matching of simulation and actual orbit curves is almost exact. The situation with the two argument of perigee variations shown in Figure 4.20b is somewhat different, however. The linear perigee precession predicted by TRAJECTORY2.0 is apparently not adhered to by the Skylab 1 orbit. In fact, ω is actually found to fall over the time period in question due to the dominance of drag effects over those of the secular J_2 perturbations. As the eccentricity of the Skylab orbit becomes very small, ω also becomes increasingly less well defined.

LDEF

The third and final example is LDEF (1984-34B). Two-line element (TLE) data is given for LDEF's first year in orbit in [37]. From the spacecraft specifications given in [37], a ballistic coefficient of $0.020\text{m}^2/\text{kg}$ is calculated. LDEF was launched during a period of low solar activity. A mean $F_{10.7}$ solar flux value of 85 is assumed for the simulation ($T_{ex} \approx 753$ degrees Kelvin). The King-Hele drag model is used for the run, with mean drag variations applied every time-step. A time-step of 1 day is employed and the simulation is run for one year post-deployment.

Figure 4.21a shows the decay of LDEF's semi-major axis. The actual decay is matched well by TRAJECTORY2.0's predicted mean variation. The eccentricity

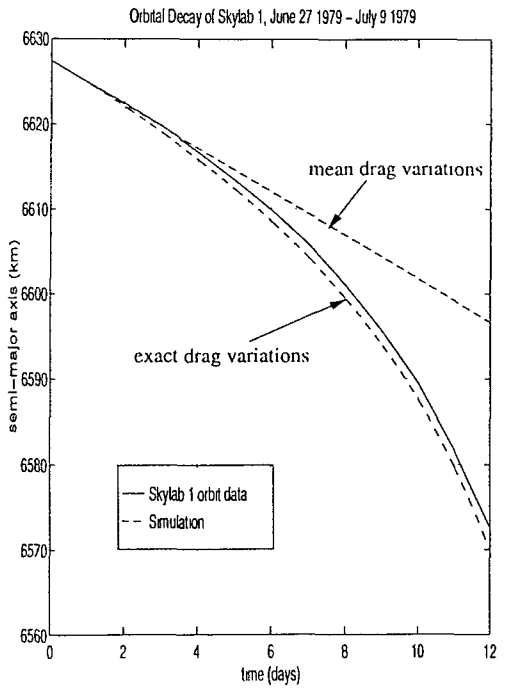

a) Skylab 1 semi-major axis variation

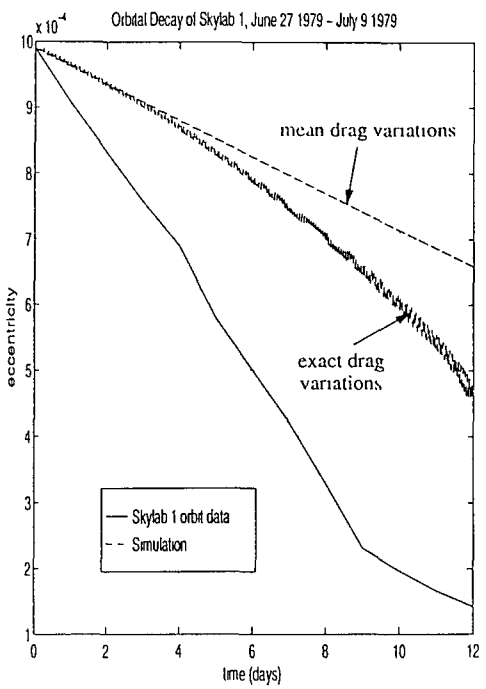

b) Skylab 1 eccentricity variation

Figure 4.19: Orbital decay of Skylab 1

curve for LDEF shown in Figure 4.21b is very noisy. The simulation smoothes out this jagged variation leaving only the underlying decreasing trend. Figure 4.22 indicates once again that the first order secular J_2 variations in Ω and ω predicted by TRAJECTORY2.0 generally provide an excellent match to the element variations actually observed.

Summary

The three examples above show that the orbits predicted by TRAJECTORY2.0 propagation method 6 are generally in good agreement with those of satellites observed. The modelling of J_2 perturbation effects is found to be particularly impressive. Attempting to model accurately the effects of atmospheric density is an extremely complicated task but the relatively simple approach employed by TRAJECTORY2.0 provides a reasonable approximation to actual orbital data. The analytical method of adding perturbation effects to Keplerian propagation is shown to offer a good compromise between computational speed and quality of results.

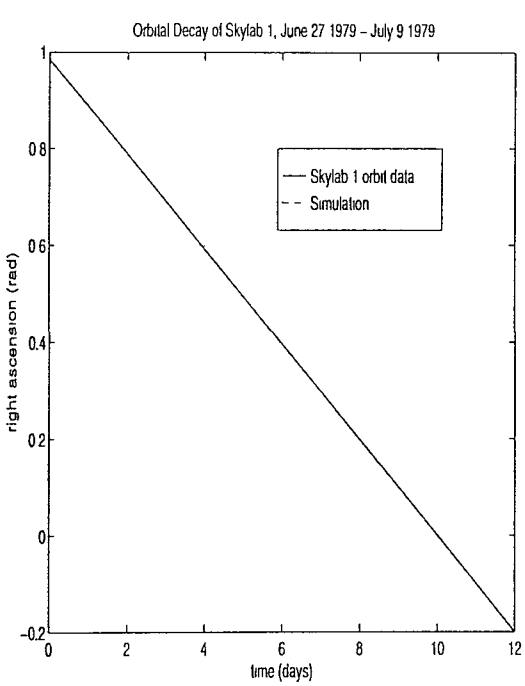

a) Skylab 1 RAAN variation

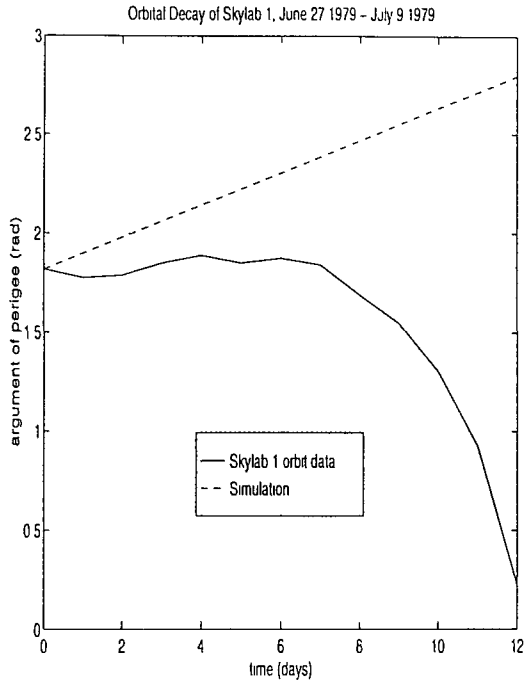

b) Skylab 1 argument of perigee variation

Figure 4.20: Nodal regression and perigee precession of Skylab 1

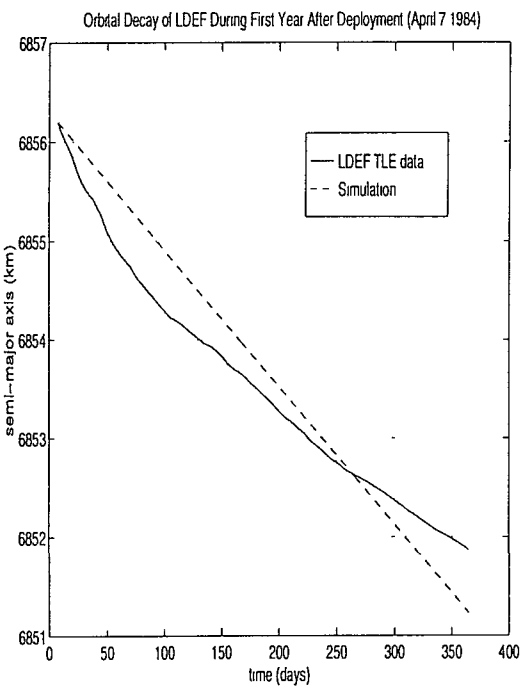

a) LDEF semi-major axis variation

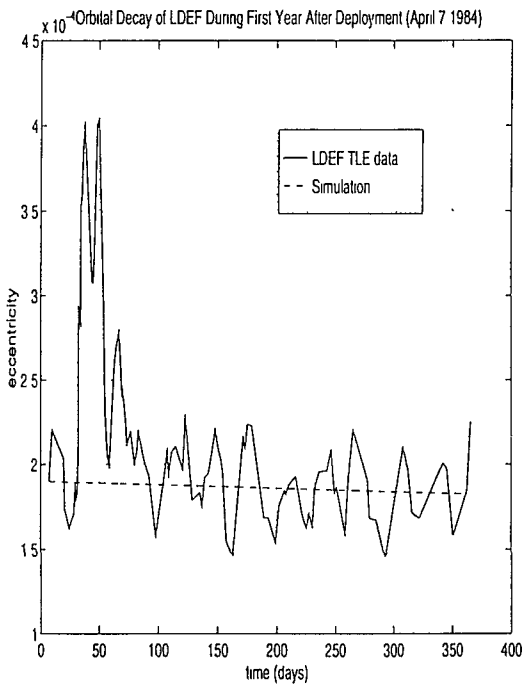

b) LDEF eccentricity variation

Figure 4.21: Orbital decay of LDEF

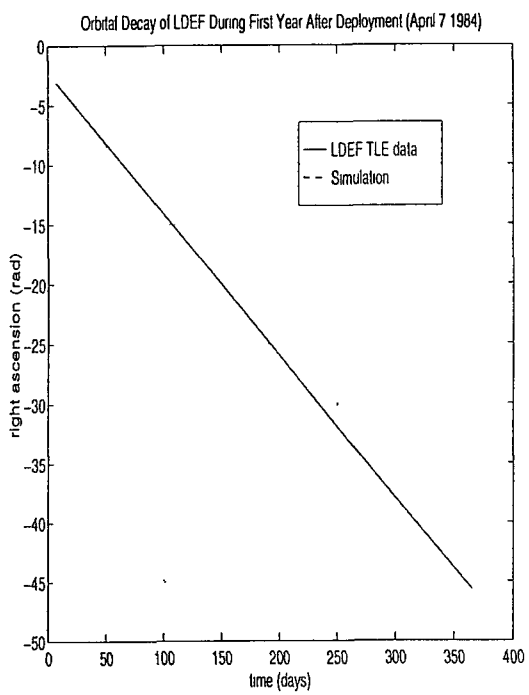

a) LDEF RAAN variation

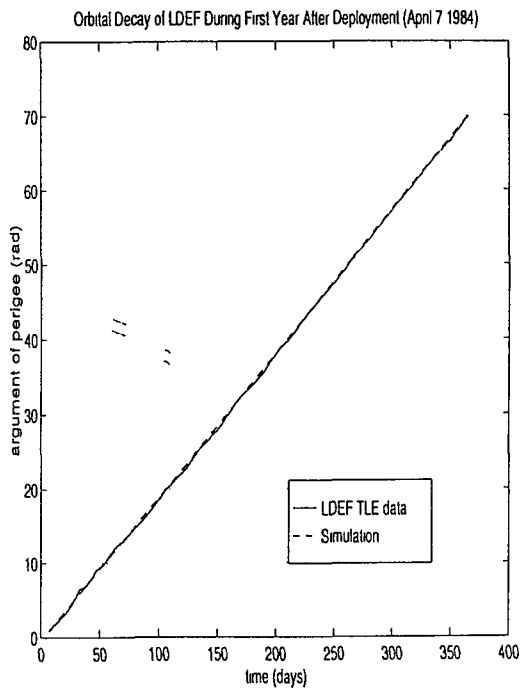

b) LDEF argument of perigee variation

Figure 4.22: Nodal regression and perigee precession of LDEF

Chapter 5

Debris Cloud Evolution

5.1 Introduction

Given a method of trajectory calculation, the evolution of a debris cloud is essentially a matter of propagating the fragment orbits over the desired period of time. As discussed previously (section 2.1.4), debris cloud evolution can take two main forms, depending upon the type of breakup model employed. If the spread of fragments from the breakup is modelled as an isotropic continuum, then cloud propagation takes the form of evolving the cloud boundaries over time. 'Pseudo-fragments' are used to represent points on the bounding cloud envelope and the extent to which the debris inside the cloud disperses around the globe is gauged by examining the growth of the outer cloud shell. If a catalogue of individual or macro-fragments is produced by the fragmentation model, then the actual orbits of these debris can be propagated and considered collectively to form the cloud.

In this chapter, the techniques employed to utilise the orbit propagation methods described in Chapter 4 for debris cloud evolution are discussed and program EVOLUTION3.0 is presented. EVOLUTION3.0 can use any one of the first six TRAJECTORY2.0 propagation methods discussed in the previous chapter, and taking initial cloud data direct from program BREAKUP4.0, can evolve either of the two cloud types described above. EVOLUTION3.0 is used to investigate the complex dynamic behaviour of a debris cloud and to compare the clouds produced by the different propagation methods available. The results from EVOLUTION3.0 are val-

idated by comparison with another model on a simple test case, and through the production of 'decayed' Gabbard diagrams, as described in Chapter 2.

5.2 Application of Fragment Propagation Techniques

The spread of fragment Δvs generated by a breakup model describe the initial conditions for the debris cloud. Given a fragment Δv relative to the breakup CM and the CM orbital velocity vector, simple vector addition can be used to produce the fragment's orbital velocity vector. This, used in conjunction with the position vector of the breakup, defines the fragment's initial orbit, which can then be propagated using any one of the methods outlined in the previous chapter.

The above technique can be applied directly to the fragment catalogue produced by a non-isotropic fragmentation model, such as BREAKUP4.0 cloud type 2, as each fragment has an ejection direction assigned. The isotropic continuum cloud model does not provide any explicit information on debris directions, however. By its very definition the model assumes a uniformity of ejections in all directions, but to make use of the model a method of assigning a uniform set of fragment ejection directions needs to be employed. The problem, then, is one of determining a set of direction cosines which map onto the surface of a sphere. One method is to use the vertices of a polyhedron to define the directions. For example, an icosahedron (12 vertices and 20 faces) was employed in [63]. The distance from any vertex to the geometric centre of the icosahedron is the same. Hence, if a sphere was circumscribed about an icosahedron, the geometric centres of the two bodies would coincide and the 12 vertices of the icosahedron would all lie on the surface of the sphere. Such a method provides a truly uniform spread of ejection directions. As all the adjacent vertices of the icosahedron are equi-distant, all the points on the the surface of the sphere are equally-spaced. To provide a good definition of the 3-dimensional cloud envelope, particularly once it has spread significantly around the globe, a large number of points on the sphere are required. Using a polyhedron with hundreds of sides would

be a complicated affair and so the most practical method of describing a uniform fragment spread is to use spherical polar coordinates. Using equal angular increments for both polar angles to define the spherical direction grid does not produce an equal spacing of ejection directions. This is not generally a major concern, however, and the ease of implementation of the method, combined with the added flexibility of being able to change the number of directions used without significant alteration to the model, considerably out-weigh any disadvantages the method may have. This approach is adopted in program EVOLUTION3.0. One thousand pseudo-fragments are used to evolve the isotropic breakup model outer cloud boundary, with the ejection directions projected onto the surface of the initial cloud sphere using 50 angular increments of $2\pi/50$ in the breakup plane and 20 increments of $\pi/20$ out-of-plane. The highest direction resolution is used in-plane as this is where the greatest cloud spreading occurs.

Once the initial conditions of the cloud have been determined, including the fragment ballistic coefficients, then it can be evolved over the required time period. The process involves applying the chosen propagation technique N times each timestep, where N is the number of fragments left in the cloud. At every epoch, the position of each fragment is calculated and if a fragment falls below the specified re-entry altitude then it is deleted from the cloud. So, although the cloud may initially contain 1000 fragments, for example, the number still in orbit will generally decrease over time. If the breakup occurs in a low orbit and especially if the debris ejection velocities are high, many of the fragments may re-enter almost immediately.

5.3 Program EVOLUTION3.0

5.3.1 Programming Issues

EVOLUTION3.0 is the third program in the SDS software suite and operates in a similar fashion to BREAKUP4.0 and TRAJECTORY2.0. As with TRAJECTORY2.0, the orbit of the breakup CM is taken from BREAKUP4.0 input file *break4_control*. This is the reference orbit and all positions in the orbiting frame are

given relative to the ideal propagation of this orbit. *evol3_control* contains the main program inputs, including the propagation method to be employed, the simulation start time (post-breakup), the time-step to be used and the number of time-steps to be considered. Program EVOLUTION3.0 uses TRAJECTORY2.0 orbit propagation methods 1-6. Method 6 employs the King-Hele drag model with mean element variations. The remaining program inputs from *evol3_control* define the orbital environment in terms of solar activity and re-entry altitude, and specify the cloud type to be evolved. If the isotropic cloud model is chosen (cloud type 1) then initial cloud data is read from BREAKUP4.0 output file *break4_iso.dat*. For cloud type 2, files *break4_forb.dat* and *break4_fcat.dat* are used.

EVOLUTION3.0 outputs to a number of data files. Propagation options 1-3 (the state transition matrix methods) output fragment positions after each time-step in relative coordinates only. The output channel to be used is specified in *evol3_control*. Relative position data is output to file *evol#.dat* where # corresponds to the channel number. Propagation methods 4-6 also output cloud position data in geocentric inertial coordinates to file *evol#i.dat*. If cloud type 2 is selected, the Gabbard diagram for the end-of-run cloud state is output to file *evol#_gab.dat*. This enables the effects of atmospheric decay on the initial fragment spread to be examined and is particularly useful for comparing results with actual event data. Gabbard diagrams from on-orbit fragmentations are generally compiled from data obtained some time after the event. For breakups in LEO, many of the fragments from the breakup may have re-entered during this period and so, as stated in section 3.5.2, the only way to make true comparisons with such data is to evolve the breakup epoch Gabbard diagrams to the equivalent point in time. This technique is applied in section 5.3.3 to three of the fragmentation examples examined in Chapter 2.

5.3.2 Analysis of Debris Cloud Dynamics

General cloud behaviour

Immediately after an on-orbit fragmentation event, the cloud of debris will be compact, dense and roughly spherical in shape, assuming an isotropic spread of fragment

ejections. The cloud rapidly stretches out along the orbit of the breakup CM due to the different fragment orbital periods. Eventually, the leading edge of the cloud will catch up with the trailing end thereby encircling the Earth. As the cloud continues to evolve, it wraps around on itself, taking the form of spiral which is pinched in two locations. A spiral is formed because the fragments in the leading portion of the cloud are in lower orbits than those at the rear. A pinch point occurs at the location of the breakup because, in the absence of perturbations, all debris must return through this point. A pinch line occurs along a radial in the breakup orbit plane at the half-revolution point because all debris must pass through the breakup plane along this line. The pinched regions are important as the density of debris at and around these regions is typically several orders of magnitude higher than elsewhere in the cloud.

Without the effects of orbital perturbations, the cloud would retain the pinched-spiral shape indefinitely. In reality, however, perturbing forces are present and these have a significant effect on the long-term evolution of the cloud. The oblateness of the Earth has two main secular effects. Firstly, it causes the argument of perigee, ω, to precess, rotating the major axes of the debris orbits in their orbital planes. Secondly, a regression occurs in the right ascension of the ascending node Ω. As the rates of change of these elements are dependent on the semi-major axis, inclination and eccentricity of the orbit in question, the variations are generally different for each fragment orbit. The values of ω and Ω for the debris in the cloud, therefore, tend to spread out over time. As a consequence, the debris concentrations at the pinched locations are smeared out. The continued spreading in the arguments of perigee has the effect of transforming the pinched spiral into a torus. At the same time, the dispersion of the nodes causes the cloud to evolve into a band which encircles the Earth and is latitude-limited by the inclinations of the debris orbits. While the cloud evolves as outlined above under the influence of the Earth's gravity field, in low Earth orbit air drag causes the fragment orbits to decay and spiral in towards the Earth. All or many of the fragments which constitute the cloud may re-enter long before the evolution to a band shape can occur. The combined effects

of drag and Earth gravity result in the spatial density of debris in the cloud steadily decreasing over time.

Comparison of propagation methods

The method chosen to propagate the orbits of the fragments in a debris cloud has a significant impact on the errors incurred in the simulation of the cloud's evolution. Figure 5.1 shows a debris cloud at it's first pinch point, one full CM orbit revolution post-breakup. The debris cloud in this example is formed by an explosive breakup in an orbit of semi-major axis 7000km, eccentricity 0.001 and inclination 28.5 degrees. The fragmentation occurs at the perigee of the breakup object orbit, and the cloud envelope is modelled by a uniform fragment spread of Δv equal to 125m/s. Figures 5.1a and 5.1b show the cloud produced by propagation methods 2 and 3 respectively, the fragment positions being given in the relative coordinates of the orbiting axis frame (Figure 2.2) with all distances given in km. Four cloud views are shown in each case, a 3-dimensional overview and the 3 axis-plane projections. From Figure 5.1a it can be seen that the linearised equations of motion employed by method 2 cause the cloud to collapse to virtually one dimension at the first full-revolution pinch location. The relative axis scalings show that the cloud is essentially a line along the orbiting frame X-axis, i.e. tangential to the breakup CM orbit. The XY view of Figure 5.1b indicates how the cloud should curve around the breakup orbit. The linearised equations of motion of method 2 do not allow this, but the second order terms considered by method 3 enable the cloud to curve around the CM orbit path as it spreads along-track. This, of course, is the correct behaviour. Method 2 also does not produce a distinct pinch point, whereas method 3 does as is seen clearly on the 3D and XZ views of Figure 5.1b. As stated in the previous section, this point corresponds to the breakup location and as orbital perturbations are neglected by both of the methods considered here, all the debris passes through this point. The uniform spread of debris into orbits of higher and lower inclinations, and greater and smaller orbital periods, produces the characteristic 'bow-tie' or 'butterfly' effect shown in Figure 5.1b.

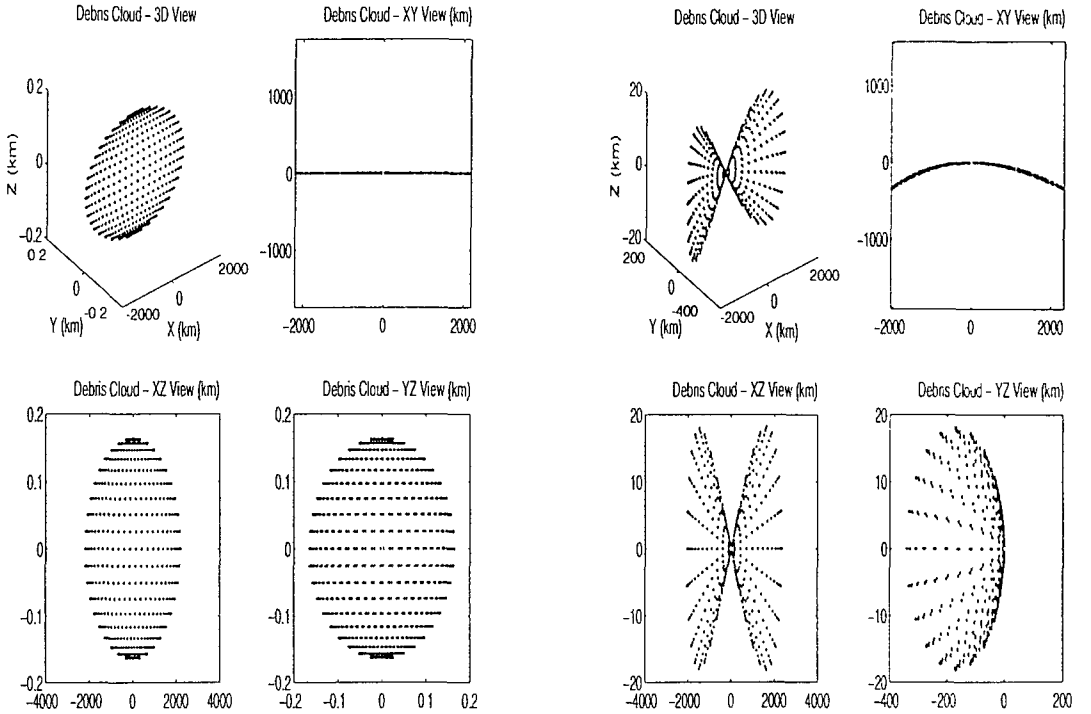

a) Example 1 cloud after 1 orbit : Method 2

b) Example 1 cloud after 1 orbit : Method 3

Figure 5.1: Example 1 : Comparison of propagation methods 2 and 3 after 1 orbit

Figure 5.2 compares the method 3 cloud shown in Figure 5.1b with that produced by Keplerian propagation (method 4). The uniform fragment spreads of methods 1-3 are constructed in the orbiting axis frame. This is evident from the fragment alignment along lines of constant Z in Figure 5.1a which correspond to Z-plane fragment 'rings' in the initial spread velocity distribution. Each of these rings corresponds to different orbital inclination and hence to a particular orbit plane. The distribution of fragments is symmetrical about the orbiting frame XY plane. Methods 4-6, however, construct their spread velocity distributions in geocentric coordinates. There is, therefore, only a direct one-to-one fragment mapping between the two techniques for orbits of zero inclination. The curvature of the fragment lines on the Z-plane 'butterfly wings' on the 3D and XZ views of Figure 5.2b is produced by the 28.5 degree breakup orbit inclination. With this difference in mind, the comparison between the two methods is extremely good. The second order transition matrix method provides an excellent match to the cloud shape predicted by Keplerian propagation.

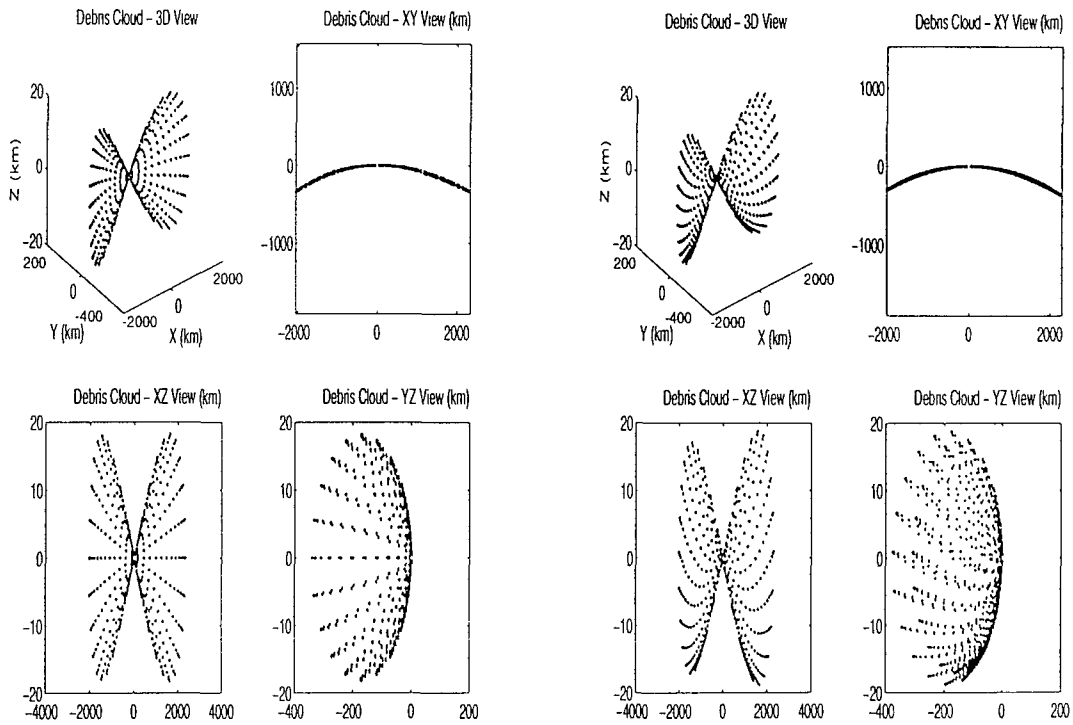

a) Example 1 cloud after 1 orbit : Method 3

b) Example 1 cloud after 1 orbit : Method 4

Figure 5.2: Example 1 : Comparison of propagation methods 3 and 4 after 1 orbit

Figure 5.3 shows the same debris cloud after 10 CM orbit revolutions. Propagation methods 3 and 4 are again compared. This time, however, the comparison is less favourable. As stated in the previous chapter, the second order model can accommodate radial positional differences relative to the reference orbit caused by orbit curvature, but only up to a point. In this example, after 10 orbits the debris cloud has almost encircled the Earth. This is evident from the XY cloud view in Figure 5.3b, which shows the characteristic cloud spiral described in the previous section. The second order model cloud cannot curve completely around the CM orbit, however, and is left in the elongated and inverted U-shape shown in the XY view of Figure 5.3a. As a result, the method 3 cloud out-of-plane butterfly wings remain open, bent only partially around the CM orbit. The use of the second order model for cloud evolution is thus limited to cases where the cloud is stretched along only a minor arc of the CM orbit, i.e. for relatively small Δvs and for just a few hours post-breakup.

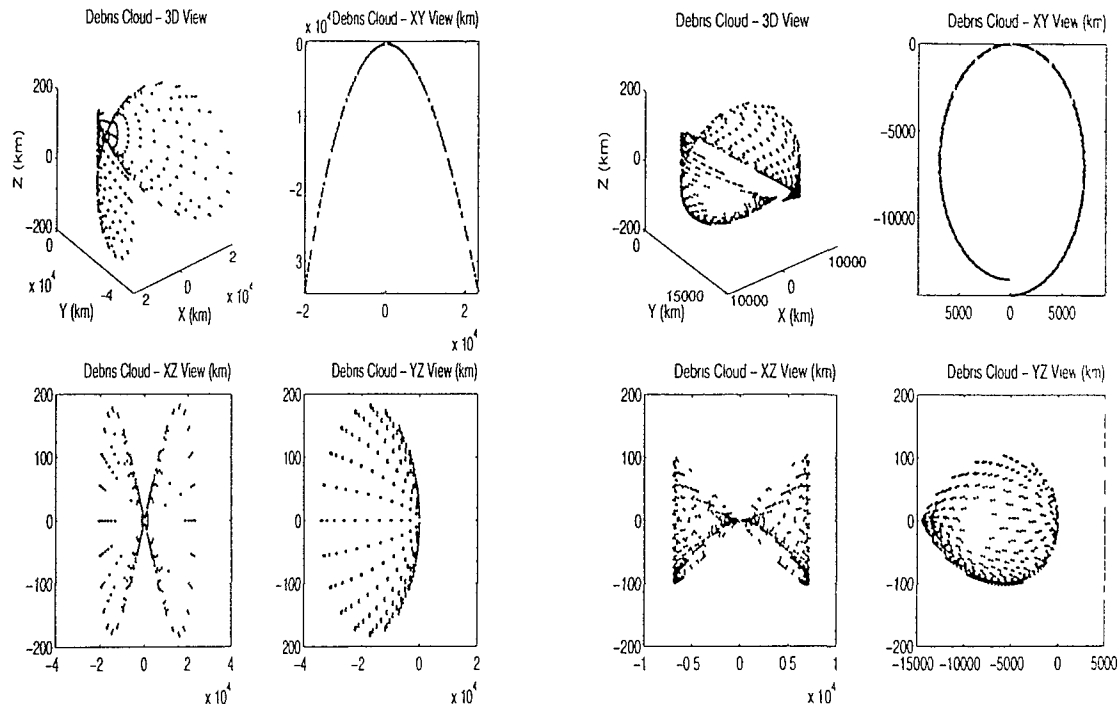

a) Example 1 cloud after 10 orbits : Method 3

b) Example 1 cloud after 10 orbits : Method 4

Figure 5.3: Example 1 : Comparison of propagation methods 3 and 4 after 10 orbits

To illustrate the effects of orbital perturbations on debris cloud growth, a second example is employed Example 2 is identical to the Example 1 above except that the orbit semi-major axis is decreased to 6678km. This measure is taken to emphasise the effects of atmospheric drag. Figure 5.4 shows the debris cloud produced by propagation methods 5 and 6 at 20 minutes after breakup, as projected onto the breakup plane. The ringed arrangement of the debris is consequence of the initial spread of fragment Δvs and the orbit inclination The method 5 cloud shown in Figure 5.4a is still complete, containing all the 1000 envelope-describing pseudo-fragments. Due to the different fragment orbital periods, the shape of the cloud has transformed from its initial breakup epoch sphere to an ellipsoid, with the debris in the lower rear portion of the cloud having been ejected into lower energy orbits than the breakup CM It is this debris that is most affected by atmospheric drag as can be seen from the missing cloud section in Figure 5.4b Over a quarter of the fragments have already re-entered by this stage and many more are en-route as

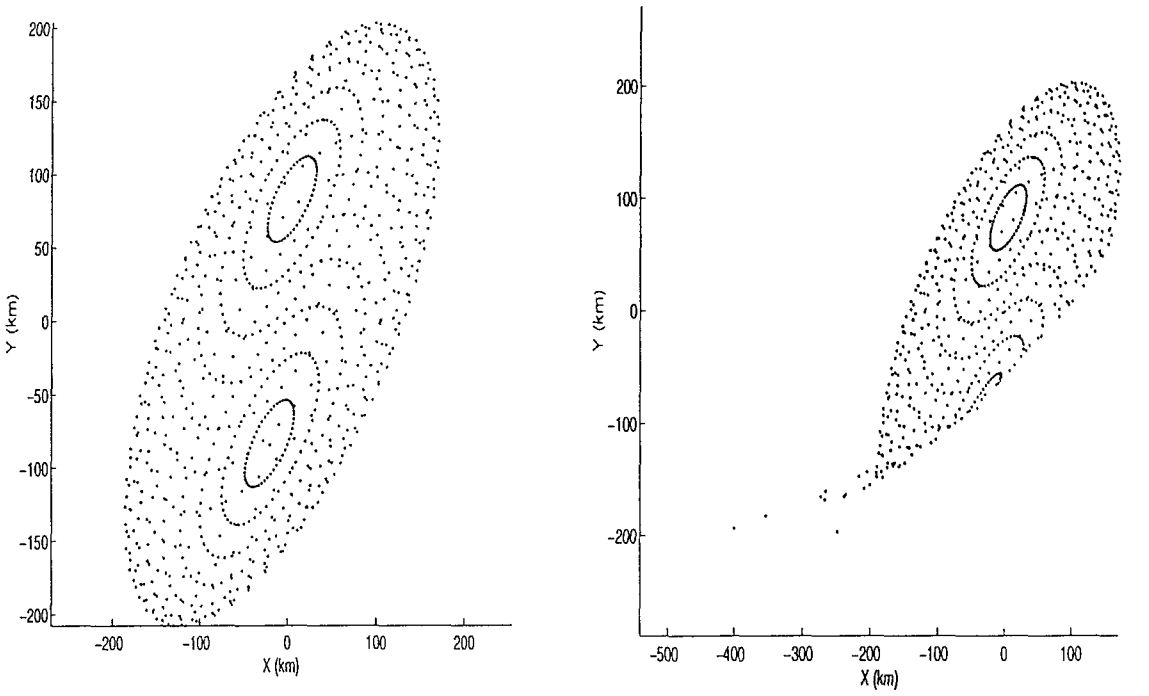

a) Example 2 cloud after 20 minutes : Method 5 b) Example 2 cloud after 20 minutes : Method 6

Figure 5.4: Example 2 : Comparison of propagation methods 5 and 6 after 20 minutes

can be seen from the trail of debris 'peeling off' from what will eventually form the cloud's leading edge.

Figure 5.5 shows the cloud at its first pinch point. The clouds produced by methods 4, 5 and 6 all exhibit the characteristic out-of-plane butterfly behaviour. There are a number of important differences between the 3 plots, however. The method 4 cloud shape shown in Figure 5.5a is essentially symmetrical about both the Z and X axes, and the cloud pinch point coincides with the origin of the orbiting axis frame, which in this case corresponds to the breakup location. The method 5 cloud in Figure 5.5b exhibits the same XZ plane shape as the method 4 cloud but has been translated and rotated relative to the orbiting frame under the influence of J_2 perturbations. The resultant effect of the perigee precession and nodal regression of the fragment orbits is to shift the pinch point around 25km out of the breakup orbit plane, in the positive Z axis direction. Consideration of the effects of atmospheric drag on the cloud's evolution, however, does not have a noticeable effect on the

location of the cloud's pinch point but the definition of the pinch point is made less clear before the cloud CM reaches the full revolution point due to the loss of debris from the cloud's leading edge. By the first full revolution point, the front (-ve X) portion of the method 6 cloud shown in Figure 5.5c has lost over 300 fragments to the atmosphere. The fragment's passing through the cloud's pinch point at this time, however, are in higher energy orbits and so are much less affected by drag. This maintains the general pinch point cloud structure and means that the pinch point itself does not receive a significant drag perturbation.

In the long-term (months to years) the debris cloud disperses and the pinch zones smear out, more fragments are lost to the atmosphere and eventually the debris in the cloud becomes an indistinguishable part of the background environment. The degree to which the long-term dispersal of a simulated debris cloud occurs is again governed by the method chosen to propagate the fragment orbits. The debris cloud from the first example (a=7000km) is evolved for one year using propagation methods 4 and 5. The clouds produced are shown in Figures 5.6 and 5.7 in geocentric coordinates, with and without the Earth depicted respectively. The method 4 cloud encircles the Earth but maintains a pinched spiral shape and does not spread significantly out of the breakup orbit plane. The J_2 perturbations modelled by method 5, however, cause the cloud to disperse fully around the CM orbit and to form a latitude-limited band which wraps completely around the Earth.

5.3.3 Results Validation

Model comparison

One way of validating the results from a simulation is to use a similar or equivalent model for comparison purposes. The cloud evolution example included in Jenkin [71] is adopted here as a benchmark for comparison. The research conducted at The Aerospace Corporation in the field of debris cloud modelling is well established and documented in the literature. The results given in [71] can, therefore, be considered to be reliable.

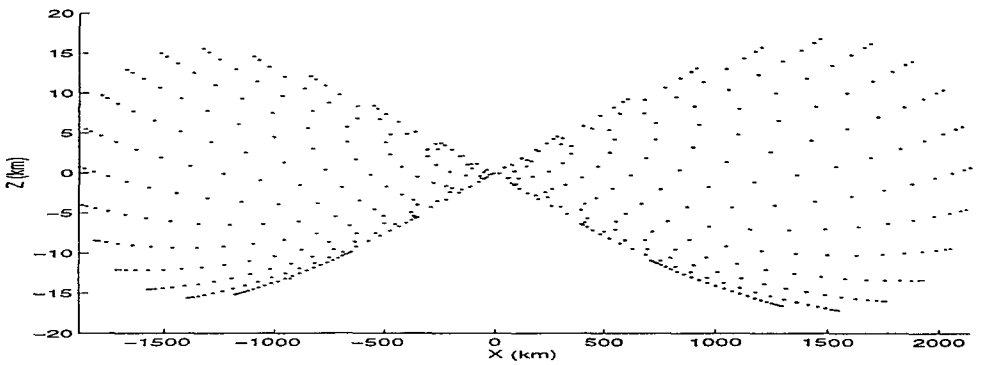

a) Example 2 cloud after 1 orbit : Method 4

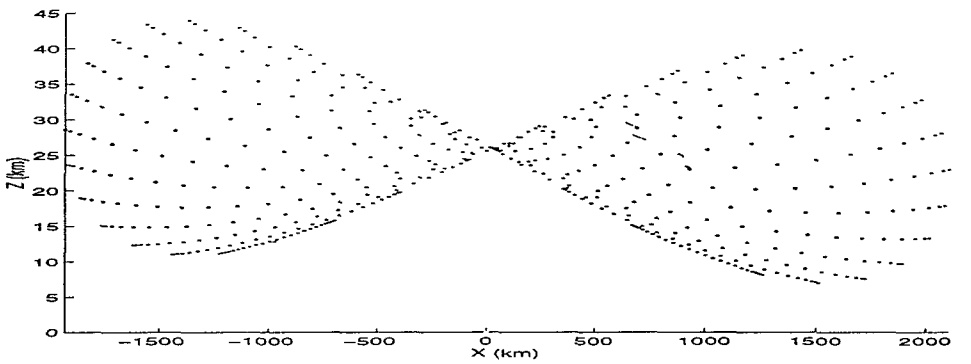

b) Example 2 cloud after 1 orbit : Method 5

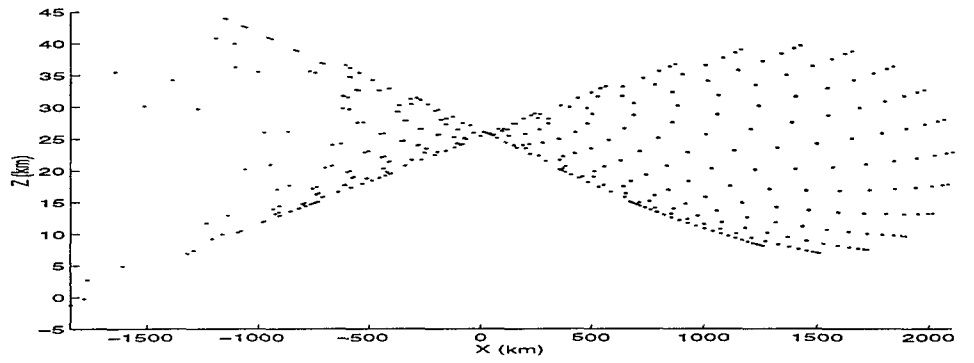

c) Example 2 cloud after 1 orbit : Method 6

Figure 5.5: Example 2 : Comparison of propagation methods 4, 5 and 6 after 1 orbit

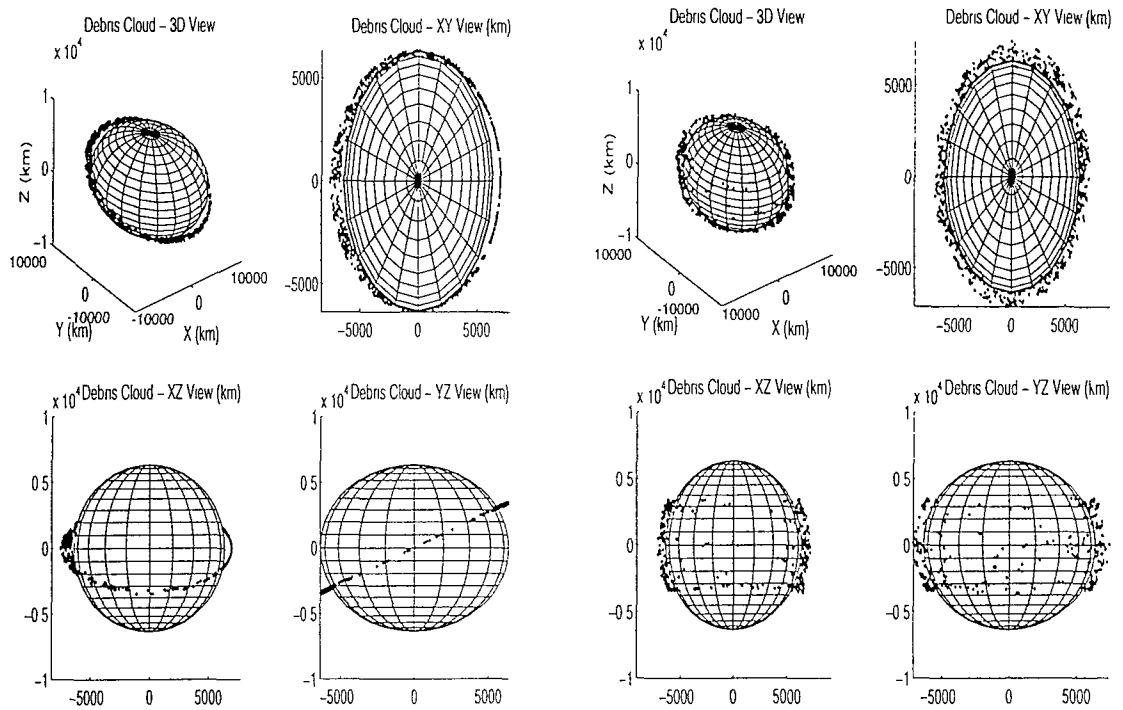

a) Example 1 cloud after 1 year : Method 4

b) Example 1 cloud after 1 year : Method 5

Figure 5.6: Example 1 : Comparison of propagation methods 4 and 5 after 1 year

The example used is that of a breakup which takes place in a 400km altitude circular orbit of inclination 28.5 degrees. The spread velocity distribution is isotropic and the maximum spread velocity is 1.6 km/s. The cloud in [71] is formed by distributing the velocity vectors of 1296 fragments uniformly in the plane of the cloud centroid, and evolving the fragment orbits using a propagator which considers the secular effects of the J_2 zonal gravitational harmonic, but neglects the effect of atmospheric drag. Only the motion of the cloud in the plane of the breakup is considered. The example is recreated using EVOLUTION3.0 with propagation method 5 on a cloud of equivalent maximum spread velocity produced by the BREAKUP4.0 isotropic model.

Figures 5.8-5.11 show the debris clouds produced by the two models at four different epochs during the first 4 orbit revolutions of the cloud CM post-breakup. The cloud shape from [71] and the EVOLUTION3.0 equivalent are compared side by side in each case. The re-entry of fragments is ignored to enable the complete

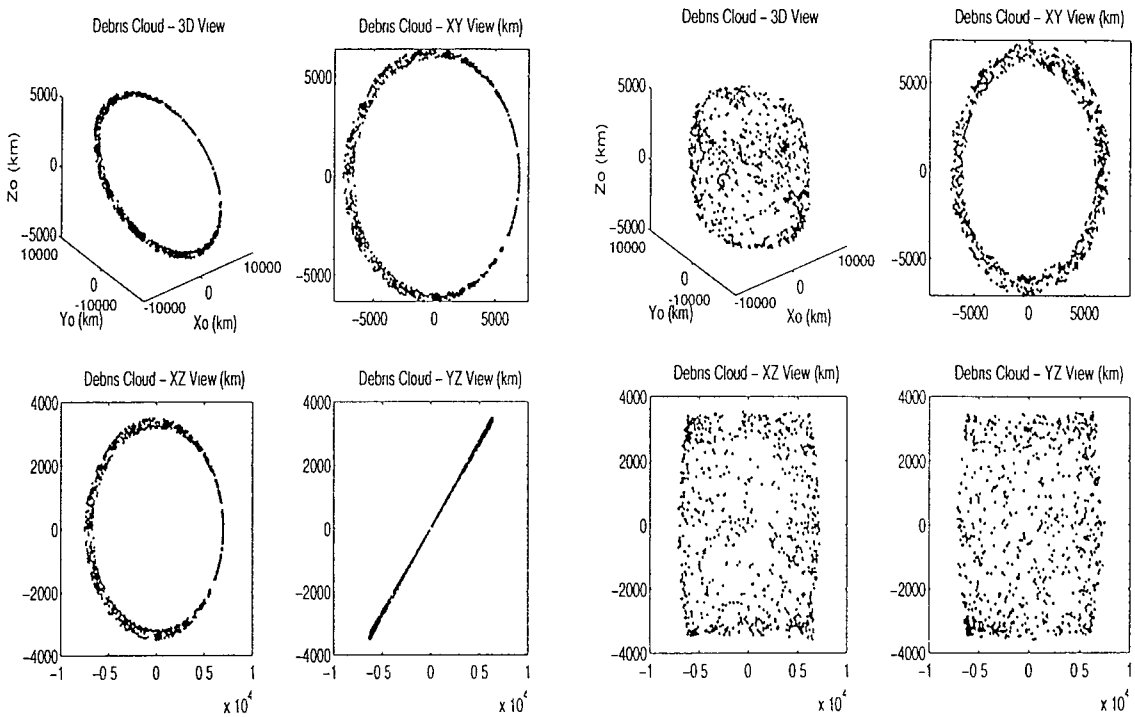

a) Example 1 cloud after 1 year : Method 4

b) Example 1 cloud after 1 year : Method 5

Figure 5.7: Example 1 : Comparison of propagation methods 4 and 5 after 1 year

cloud to be viewed. The circle shown on each plot represents the Earth.

The matching of results between the two models is excellent. More fragments are distributed in the breakup plane in the Jenkin model, which produces the denser clouds shown, and the way the spread velocities are assigned is also different, producing the different internal cloud structures displayed. The shapes of the bounding cloud envelopes predicted by the two models are, however, virtually identical.

Figure 5.8 shows the cloud when its centroid is 90 degrees past the breakup point. From the fragments which lie inside the Earth circle it can be seen that a large proportion of the debris has already re-entered. At the half-revolution point (Figure 5.9), the cloud has begun to curve significantly around the Earth and the debris in the cloud's leading edge is beginning to compress as it approaches the first whole-revolution pinch point. Figure 5.10 shows the debris cloud when the centroid is 360 degrees past the breakup location, i.e. at the pinch point. The cloud has spread around the orbit to such an extent that the trailing edge is still

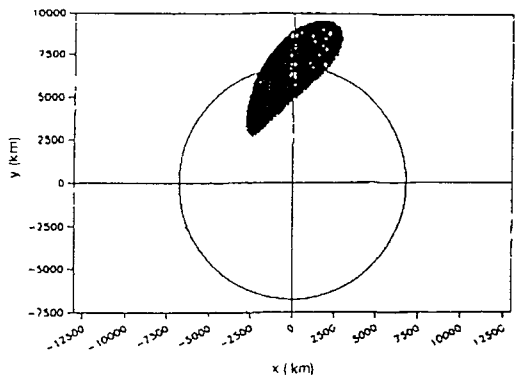

a) Cloud after 1/4 revolution : from Jenkin

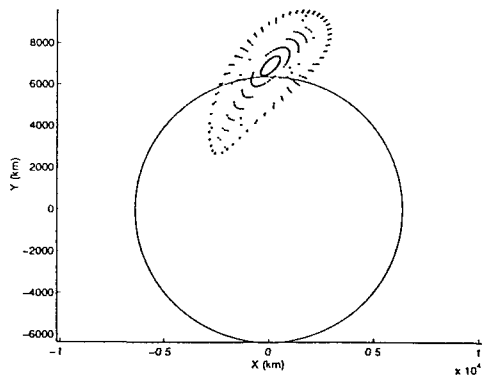

b) Cloud after 1/4 revolution : EVOLUTION3.0

Figure 5.8: Comparison of Jenkin and EVOLUTION3.0 debris clouds : 1/4 orbit

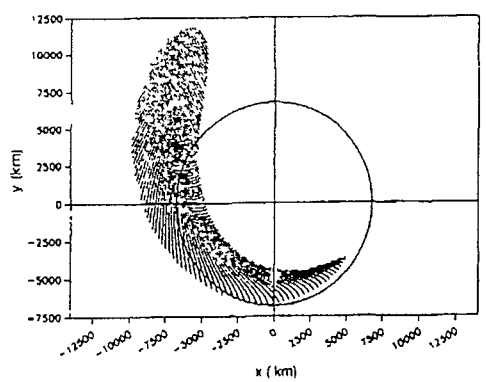

a) Cloud after 1/2 revolution : from Jenkin

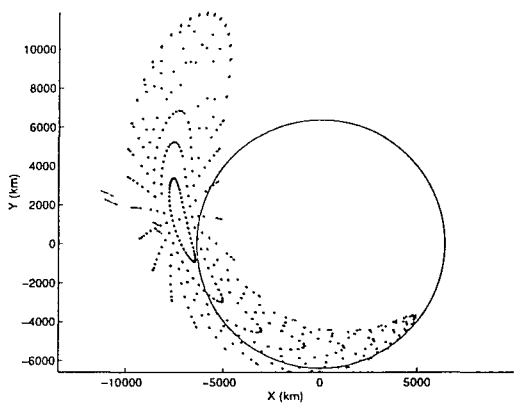

b) Cloud after 1/2 revolution : EVOLUTION3.0

Figure 5.9: Comparison of Jenkin and EVOLUTION3.0 debris clouds : 1/2 orbit

passing through the half-revolution pinch line. Furthermore, the leading edge of the cloud has passed through the first non-stationary pinch zone, a phenomenon which is caused by the internal rotation of the debris cloud [74]. The cloud is thus pinched simultaneously in three separate places. After four orbits of the cloud centroid, the cloud has wrapped around the Earth four times, yielding five pinched layers on the opposite side of the orbit to the breakup (Figure 5.11).

Gabbard diagram decay

Another method of results validation is to compare the debris clouds produced by EVOLUTION3.0 with those derived from actual orbital data. On-orbit fragmen-

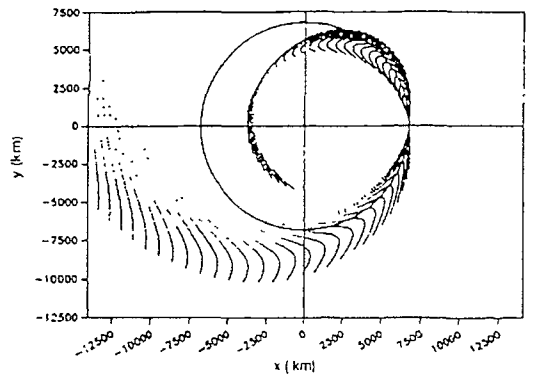

a) Cloud after 1 revolution : from Jenkin

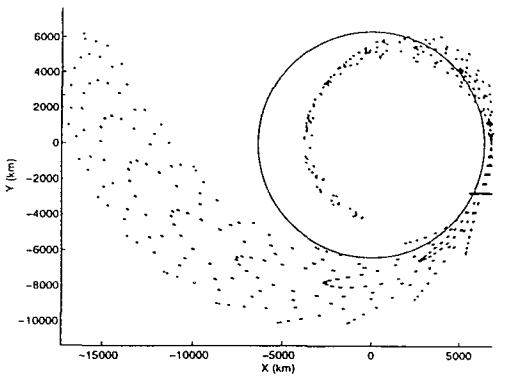

b) Cloud after 1 revolution : EVOLUTION3.0

Figure 5.10: Comparison of Jenkin and EVOLUTION3.0 debris clouds : 1 orbit

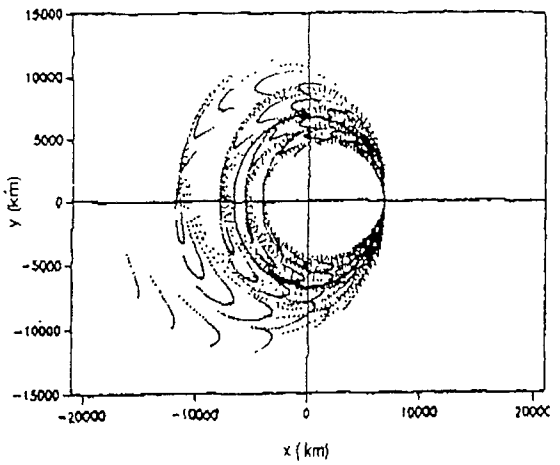

a) Cloud after 4 revolutions : from Jenkin

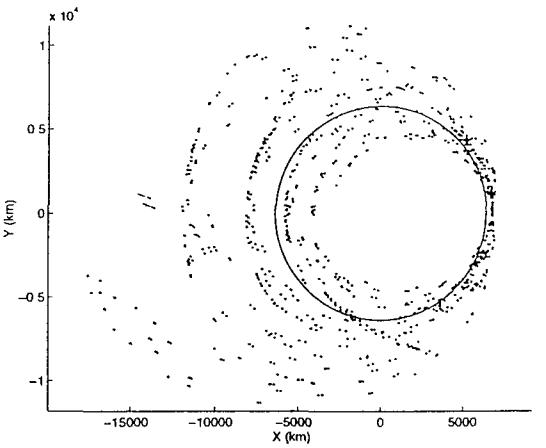

b) Cloud after 4 revolutions : EVOLUTION3.0

Figure 5.11: Comparison of Jenkin and EVOLUTION3.0 debris clouds : 4 orbits

tations are most commonly represented by their Gabbard diagrams, and so these provide arguably the best means of comparing the spread of fragments from real breakup events with the results produced by a simulation. This technique has already been employed in section 3.5.2, where fragment spreads produced by the BREAKUP4.0 non-isotropic cloud model were compared with actual breakup event Gabbard diagrams. Such comparisons do contain a degree of subjectivity, but the comparison of the number of fragments produced, and the length and shape of the diagram limbs does allow some degree of quantitative results matching to be attempted.

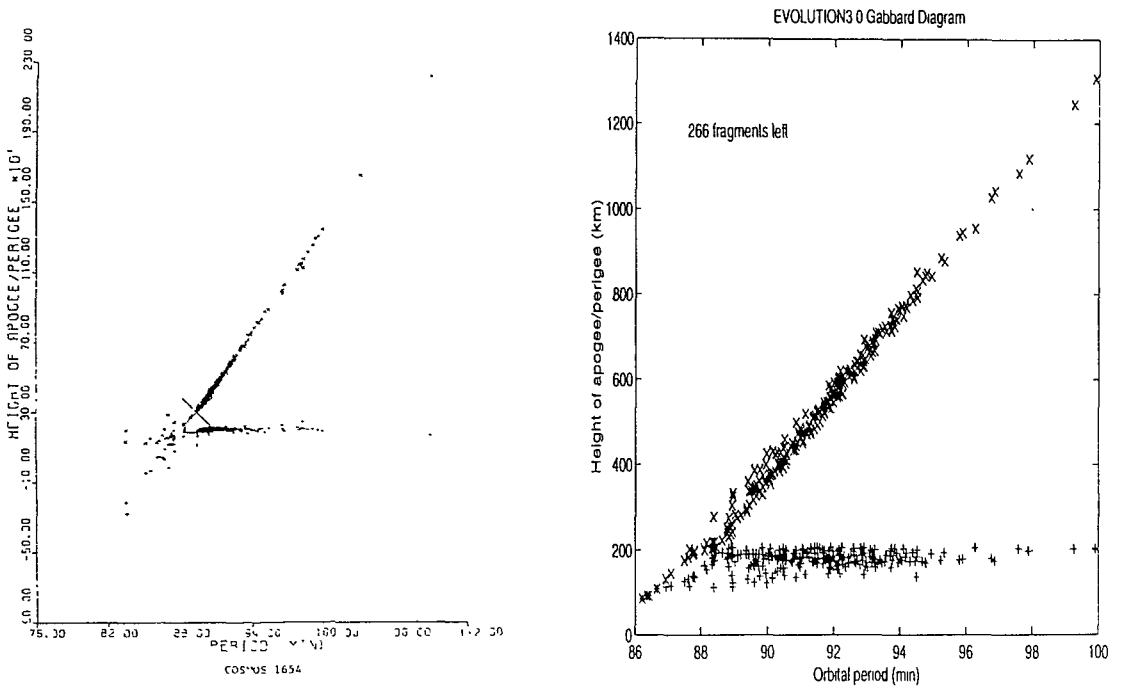

a) Event Gabbard diagram

b) Simulation Gabbard diagram (1 hour post-breakup)

Figure 5.12: Gabbard diagrams for the Cosmos 1654 breakup

Because it often takes anything from a few hours to several weeks to compile a Gabbard diagram from flight data, the orbital evolution and possible decay of fragments over this time period should be accounted for when making results comparisons. Three of the examples looked at in section 3.5.2 are re-examined here using EVOLUTION3.0 to evolve the initial spread of fragments produced by BREAKUP4.0. Propagation method 6 is employed in each case.

The first example here is the breakup of the Cosmos 1654 satellite. The apparent prograde ejection dominance of the event Gabbard diagram was originally modelled by BREAKUP4.0 using a prograde-retrograde ejection bias of 10:1. The real cause of the sparseness of fragments on the lower limb of the event Gabbard diagram, however, is the rapid decay of debris from cloud's leading edge. The low orbit of Cosmos 1654 (around 250km altitude) meant that fragments ejected into orbits of lower energy than the cloud centroid rapidly decayed into the Earth's atmosphere. Figure 5.12b shows the revised BREAKUP4.0-EVOLUTION3.0 simulation of the event. Here the fragmentation is modelled by BREAKUP4.0 with no

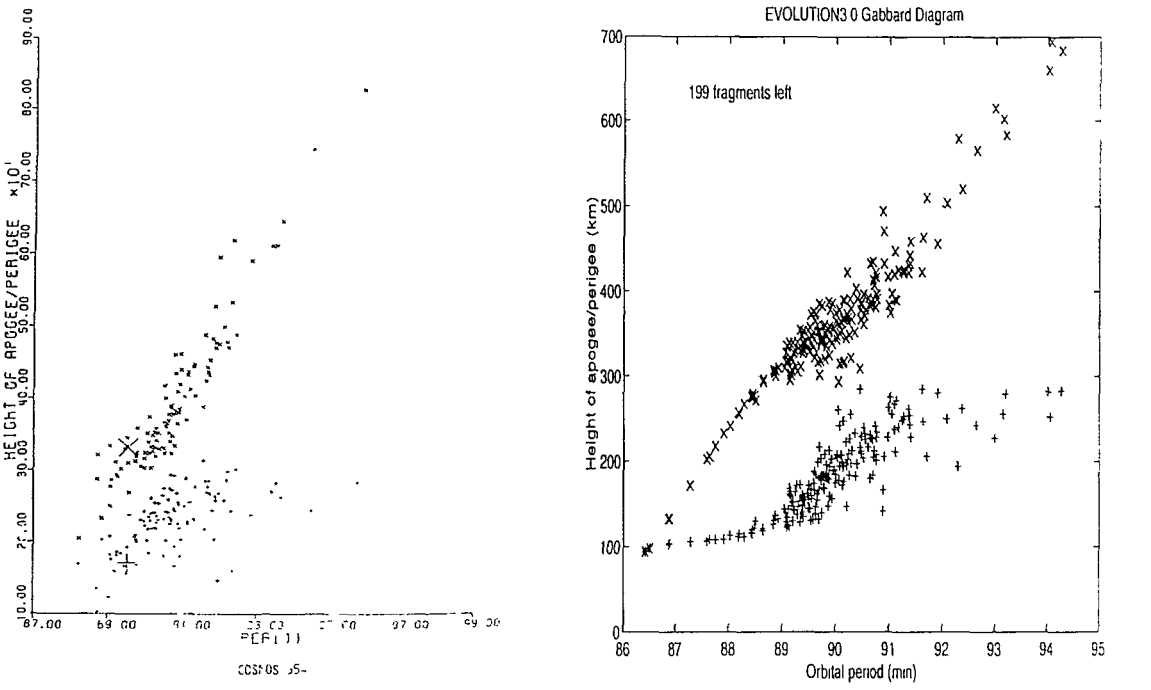

a) Event Gabbard diagram

b) Simulation Gabbard diagram (1 hour post-breakup)

Figure 5.13: Gabbard diagrams for the Cosmos 554 breakup

prograde-retrograde ejection bias, but instead the cloud of fragments is evolved by EVOLUTION3.0 for 1 hour after the breakup. 398 fragments greater than 5cm in size are initially generated by BREAKUP4.0 for the event. After one hour, only 266 fragments are left in orbit (c.f. the 300 or so fragments that were detected from the actual fragmentation). As predicted, almost all the debris from the lower Gabbard diagram limb has decayed, producing the highly asymmetrical spread of fragments shown. The matching of the simulated Gabbard diagram with the event data is extremely good.

The second example re-visited is the breakup of the Cosmos 554 satellite. As with the Cosmos 1654 breakup above, the prograde-dominated event Gabbard diagram was originally modelled in Chapter 3 using a prograde:retrograde ejection bias factor of 10. Again though, fragment decay is undoubtedly the greatest contributor to the asymmetrical pattern of debris ejections seen on the event Gabbard diagram (Figure 5.13a). The fragmentation is modelled again using BREAKUP4.0 with no prograde ejection biasing and the cloud produced is evolved by EVOLUTION3.0 for

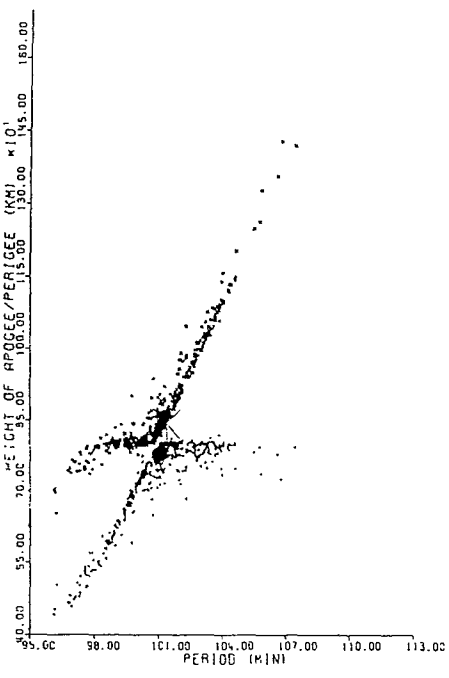

a) Event Gabbard diagram

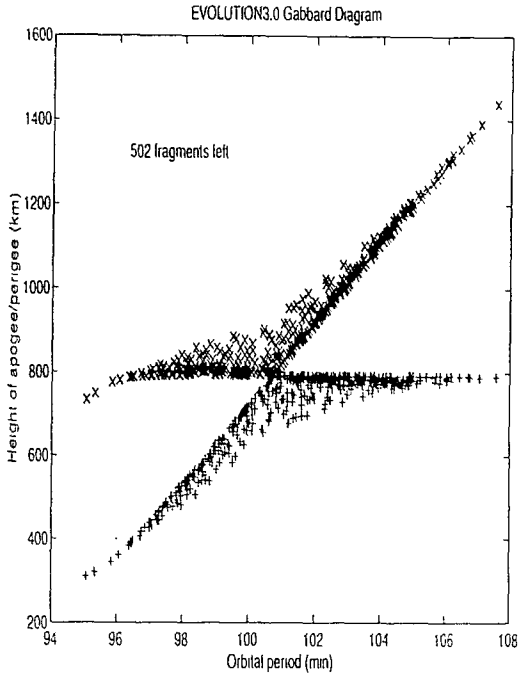

b) Simulation Gabbard diagram (3 months post-breakup)

Figure 5.14: Gabbard diagrams for the SPOT-1 Ariane breakup

1 hour after the breakup. Of the 241 fragments 10cm in size and greater generated by BREAKUP4.0, 199 are still in orbit after 1 hour. This number compares well with the 196 fragments from the breakup actually catalogued. The Gabbard diagram for the low period end of the simulation (Figure 5.13b) shows fragments peeling off from the left of the clusters around the centroid orbit into a 'decay corridor'. As the cloud continues to orbit, more and more fragments will be drawn down this path of decreasing semi-major axis which leads ultimately to re-entry.

The final example re-modelled is the fragmentation of the SPOT-1 Ariane third stage. In contrast to the first two examples above, the SPOT-1 rocket fragmentation occurred in an orbit only slightly perturbed by atmospheric drag. The 800km altitude of the breakup and it's relatively low intensity meant that the fragments produced, of catalogue-size, had long orbital lifetimes. The in-plane spread of fragments for the event shown in Figure 5.14a is still fairly uniform and there is only a slight 'drooping' of the low period limb several months after the event, which is when the 'snapshot' of the cloud shown was taken. The breakup was originally

modelled in section 3.5.2 using an even prograde-retrograde ejection spread. The same BREAKUP4.0 modelling parameters are used for the simulation re-run as for the original in Chapter 2, and the cloud is propagated using EVOLUTION3.0 for 3 months after the event. The evolved Gabbard diagram for the simulation is shown in Figure 5.14b. No fragments have re-entered during this time, and a noticeable drooping of the low period limb has occurred, which matches very well with that shown in Figure 5.14a.

Summary

In summary, then, the combination of EVOLUTION3.0 with BREAKUP4.0 creates a realistic and integrated satellite fragmentation and debris cloud evolution simulation capability. Together, these two programs enable good comparisons between actual and simulated debris cloud data to be made, as is shown above in a number of different test cases.

Chapter 6

Collision Hazard Analysis

6.1 Introduction

For some time after a breakup event, the fragmentation debris produced may pose a significant threat of collision to orbiting spacecraft which encounter the cloud. The collision hazard due to the debris cloud acts in addition to that routinely experienced from the background debris environment and the natural particulate population. In the early stages of its evolution, the density of debris in the cloud may be several orders of magnitude higher than the background level. Interaction with the debris cloud produced by the fragmentation event may result in considerable 'spikes' in a satellite's overall (i.e. background plus cloud) collision probability versus time curve. If such order of magnitude increases above the background level were predicted to occur often enough, and be of sufficient severity, they could influence mission planning and the shielding strategies employed in the design of a future satellite.

This chapter examines the collision hazard to an orbiting 'target' object resulting from an on-orbit fragmentation event. The aim is to quantify the risk of a collision with debris experienced by a chosen target object (or objects), as a direct result of the fragmentation event (Figure 6.1). This type of study is in contrast to those which strive to model the debris environment as a whole and the subsequent danger that the background population poses to orbiting spacecraft. A shorter-term analysis, one which considers a specific debris cloud and is concerned with time-spans of hours to days, as opposed to years, can also be regarded as complementary to such long

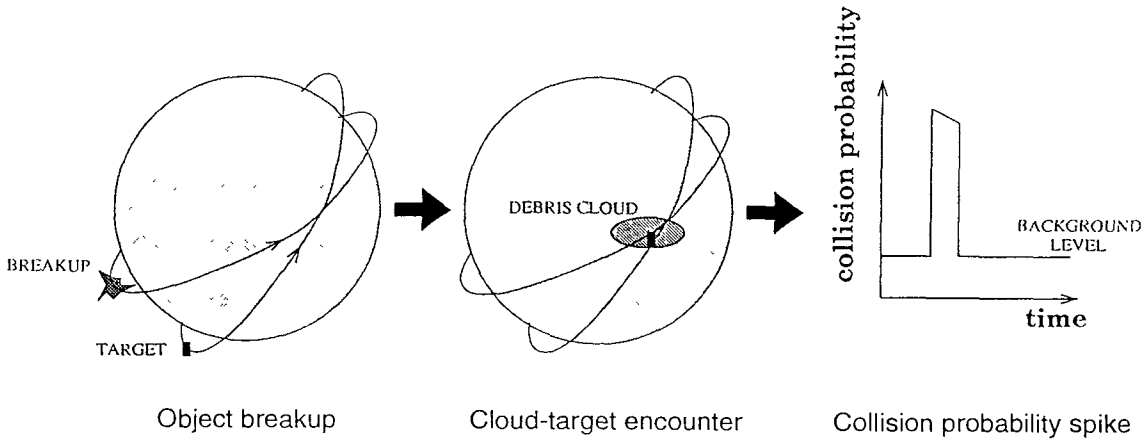

Figure 6.1: Target problem outline

term investigations.

The approach described in this chapter is an implementation of the probabilistic continuum dynamics method of exact debris density calculation described in section 2.2.7, as applied to the cloud-target collision hazard assessment problem. The general methodology of this approach is outlined in Chapter 2 and so will not be repeated here. Instead, the discussion will focus upon the novel implementation of the technique in program TARGET, and how TARGET can be applied to a variety of different scenarios, examining the collision risk posed to both single and multiple target objects. TARGET is used to assess the potential collision risk to the ESA polar platform ENVISAT-1, and also to investigate the possibility of runaway collisional fratricide in satellite constellations. The results from TARGET are validated by comparison with those from a similar model, The Aerospace Corporation's program DEBRIS, on several test cases and also through the use of data returned from the Interplanetary Dust Experiment on LDEF.

6.2 Calculation of Collision Probability

6.2.1 Overview

A review of the various methods employed for debris cloud propagation and collision hazard assessment was given in Chapter 2. By far the simplest method of cloud

propagation and assessment of the collision hazard to spacecraft resulting is the linearised state transition matrix method of Chobotov [63, 65, 69]. Although quick and easy to use and implement, such a technique has only limited use and and offers no means of detecting whether or not the target object is actually inside the cloud envelope at any given time. Toroidal cloud models [63, 65, 69, 79, 80] have also been employed in an attempt to tackle the problem. These methods are still limited by the necessity to make certain simplifying assumptions in their analyses, however, and serve to illustrate the difficulties encountered when using an approach that assumes a cloud shape and looks to compute entry and exit times for objects passing through it. The simplifying assumptions that make such analyses manageable may also be sources of errors in the results that they produce. The most serious of these over-simplifications is the common assumption of average cloud (or sub-shell) densities. The use of probabilistic continuum dynamics [70, 84] has shown that the spatial density of fragments within a cloud can vary by several orders of magnitude at a given epoch. As collision probability is directly proportional to debris density (equation (2.15)), the adoption of mean density values can give rise to errors of several orders of magnitude in the determination of collision risk. Such errors will generally swamp any inaccuracies that may be present in other parts of the analysis.

As discussed in section 2.2.7, the method of probabilistic continuum dynamics can be directly applied to the cloud-target collision hazard problem. The technique is both powerful and versatile. Debris density is calculated 'exactly' at the point of interest, and information on the direction of the debris flux relative to the target object and the size of fragments encountered can also be determined. This allows the potential lethality of a collision to be ascertained. No assumptions are made about the cloud shape or the breakup model used and any target, or number of targets, can be considered.

6.2.2 Method Implementation

Procedure

The implementation of the probabilistic continuum dynamics (PCD) technique for collision hazard assessment is a multi-stage process. Given a debris cloud and a target object and orbit, the determination of collision probability at a point on the target orbit takes place in three main parts. These correspond to the calculation of ρ, A and v in equation (2.15).

Firstly, the density of debris from the breakup at the target position must be determined. This requires the calculation of the transfer orbit that links the target position with the breakup location in the time since breakup. For the transfer orbit solution obtained, the velocity vector of the orbit at the breakup epoch and position can be determined. By vectorially subtracting the breakup orbit velocity vector from that of the transfer orbit, the $\triangle$v of the transfer orbit relative to the breakup CM is calculated. Using this $\triangle$v and referencing back to the breakup model employed, the density of debris in spread velocity space can be obtained. For the BREAKUP4.0 isotropic model, only the magnitude of the $\triangle$v is required to determine to which of the cloud shells the solution corresponds. If the $\triangle$v is larger than the cloud outer shell $\triangle$v then the target is outside the cloud and the density of debris is zero. The non-isotropic model in BREAKUP4.0 uses both the magnitude and direction of the $\triangle$v vector to determine which spread velocity space cell the target lies in. To obtain the density of debris at the target location, the transformation from spread velocity space at the breakup epoch to position space at the target position must be performed, taking into account the time between. This requires the evaluation of the state transition matrix $\Phi(\mathbf{r}, \dot{\mathbf{r}}_0)$ $(= \partial \mathbf{r}/\partial \dot{\mathbf{r}}_0)$ at the point in spread velocity space given by the transfer orbit $\triangle$v, and for the orbital transfer time. The actual density of debris encountered by the target is then calculated by dividing the spread velocity space value by the determinant of the state transition matrix, as shown in equation (2.20).

The cross-sectional area of the target with respect to the incident debris, and the

velocity of the debris relative to the target must then be determined. The relative debris velocity is obtained by calculating the velocity vector of the transfer orbit at the target position and vectorially subtracting the target orbital velocity vector. As with the debris Δv calculated at the breakup location, just the magnitude of the relative velocity or the complete vector can be utilised. The simplest method of determining A and v is to assume a constant projected cross-sectional area for the target and thus only use the magnitude of the debris encounter velocity. Using the relative velocity vector, however, also enables the direction of debris flux with respect to the target to be determined. Hence, by giving the target shape and dimensions (e.g. a simple cuboid) and an orientation relative to its orbital motion, debris fluxes and hence collision probabilities can be calculated for the individual surfaces of the target, and thus for the spacecraft as a whole. Also, by using the debris breakup Δv in conjunction with the breakup model employed to determine the mass of the fragments encountered, a measure of the possible lethality of a collision can be obtained. Here the criterion for complete object breakup given in equation (2.12) can be used. The calculation of the debris impact energy to target mass ratio ($\zeta = E_p/M_t$) for the encounter provides a simple but effective method of gauging the degree of damage such a collision would cause.

In practice, there will often be more than one transfer orbit that can provide the link between target and breakup positions in the required transfer time. This becomes increasingly the case as the debris cloud evolves and wraps repeatedly around the Earth. The above procedure must, therefore, be carried out for each transfer orbit solution obtained, and the contributions summed at every target position to determine the resultant collision risk.

Transfer orbit solution

The Gauss-Lambert, or transfer orbit, problem is well documented in the literature and a number of different methods have been proposed for its solution. These include the algorithm of Sun et al [90], the method of Gooding [87] and the original method proposed by Gauss, which is described in [95]. The approach adopted in TARGET,

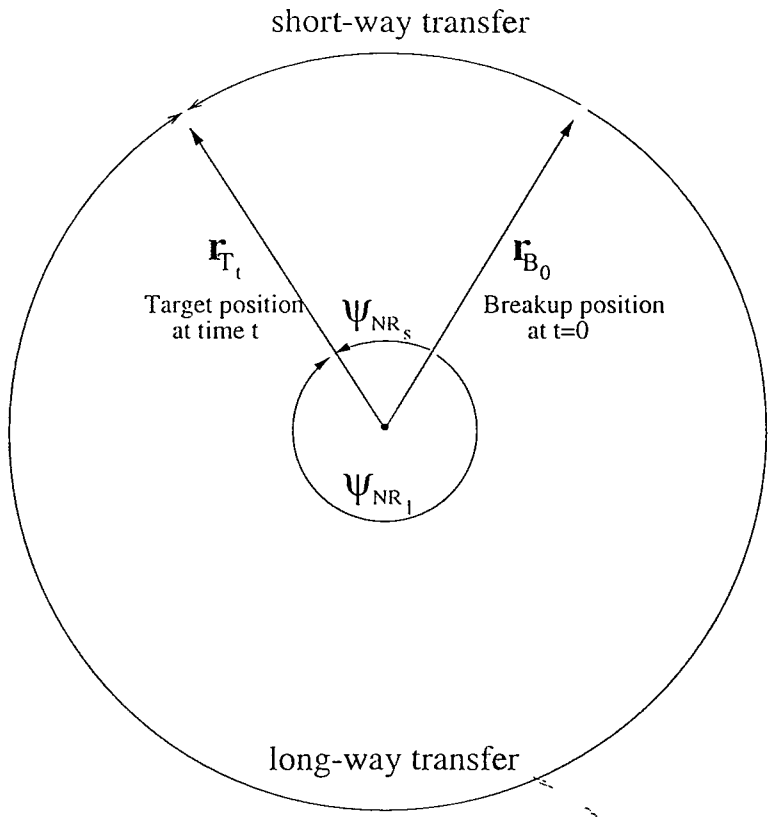

Figure 6.2: Short- and long-way orbital transfers

however, is that recommended in [104], where universal variables are employed to provide an analytic solution to the problem.

Given two position vectors and an orbital transfer time, there are at least two ways that the orbital transfer can be performed. A 'short-way' transfer occurs when the net range angle ψ_{NR} between the two position vectors is less than or equal to π radians in the direction of the transfer. The transfer orbit, therefore, forms a minor arc between the two position vectors. A 'long-way' transfer forms a major arc, with $\psi_{NR} > \pi$. The two possibilities are shown in Figure 6.2, where circular transfer orbits are depicted for simplicity. In the cloud-target problem being considered here, the transfer direction and net range angle are determined from the orbital motion of the debris and the target satellite, and the cross product of the breakup and target position vectors. Only the transfer which corresponds to debris orbiting in the same direction as the breakup CM is considered. Retrograde Δvs of the order of twice orbital velocity would be required for debris to sustain orbits in the opposite

sense to the parent orbit. In LEO such Δvs are prohibitively high (> 15km/s). At higher altitudes, GEO for example, the Δvs required are considerably less, but the likelihood of such ejection velocities being produced is also much lower. Collisions at or near GEO would not contain sufficient energy for such a spread of debris to be generated. On-orbit explosions are also incapable of dispersing debris to such a degree.

Multi-revolution orbital transfers are possible for fragmentation debris and indeed are prevalent a few hours after a breakup. Here the debris describes one or more orbits before arriving at the target position. At any given time post-breakup, the range of orbit revolutions to consider is given from the maximum and minimum debris orbital periods. The minimum orbital period used corresponds to the debris in the lowest energy orbit that has not already re-entered the atmosphere. For each orbital transfer to be considered in the search range, the determination of the transfer orbit is an iterative process, with the variable iterated upon, Z, being the square of the difference between the eccentric anomalies of the target and breakup positions on the transfer orbit, $Z = (E_{T_t} - E_{B_0})^2$. The procedure for solving for Z and hence determining the transfer orbit is as follows [104].

- Step 1 : The orbital geometry parameter A is calculated from

$$A = D\sqrt{r_{B_0} r_{T_t}(1 + cos(\psi_{NR}))} \tag{6.1}$$

  where D denotes the direction of the orbital transfer and is equal to 1 for a short-way transfer, and -1 for a long-way transfer. The orbit radii r_{B_0} and r_{T_t} are normalised with respect to the Earth's radius.

- Step 2 : An initial guess for Z is made from the orbital transfer geometry and the number of debris orbit revolutions being considered.

- Step 3 : The normalised transfer time, Δt, given by the estimate of Z is calculated from

$$\Delta t = X^3 S + A\sqrt{Y} \tag{6.2}$$

where

$$X = \sqrt{Y/C} \tag{6.3}$$

$$Y = r_{B_0} + r_{T_t} - A\frac{(1 - ZS)}{\sqrt{C}} \tag{6.4}$$

$$\begin{aligned} C &= \frac{1 - cos\sqrt{Z}}{Z}, \; Z \neq 0 \\ &= 1/2, \; Z = 0 \end{aligned} \tag{6.5}$$

and

$$\begin{aligned} S &= \frac{\sqrt{Z} - sin\sqrt{Z}}{Z^{3/2}}, \; Z \neq 0 \\ &= 1/6, \; Z = 0. \end{aligned} \tag{6.6}$$

- Step 4 : If the difference between $\triangle t$ and the actual orbital transfer time is less the tolerance adopted, then the value of Z can be accepted. If convergence has not been achieved, a new estimate for Z is calculated using a customised Newton-Raphson root-solver algorithm and the procedure loops back to step 3.

- Step 5 : Once convergence has been achieved, the transfer orbit velocity vectors at the target and breakup positions are given by

$$\mathbf{v_{B_0}} = \frac{\mathbf{r_{T_t}} - f\mathbf{r_{B_0}}}{g} \tag{6.7}$$

and

$$\mathbf{v_{T_t}} = \frac{\dot{g}\mathbf{r_{T_t}} - \mathbf{r_{B_0}}}{g} \tag{6.8}$$

where

$$f = 1 - \frac{Y}{r_{B_0}}, \tag{6.9}$$

$$g = A\sqrt{Y}, \tag{6.10}$$

and

$$\dot{g} = 1 - \frac{Y}{r_{T_t}}. \tag{6.11}$$

The transfer orbit is thus determined. The above method does not take the effects of orbital perturbations into consideration, however, implicitly assuming ideal, Keplerian, orbital motion. In fact there is no known analytical method in the literature for solving the transfer orbit problem for perturbed orbital motion. Chapter 5 showed that the effects of atmospheric drag and the Earth's oblateness can have a significant effect on debris cloud growth, even in the short-term. Completely ignoring these 'real life' perturbing forces would severely affect the integrity and scope of usage of program TARGET. The approach adopted, therefore, is to combine the inherently analytical method outlined above with a numerical minimisation routine to form a generalised hybrid transfer orbit solution algorithm. The ideal transfer orbit solution returned by the universal variable method above is fed into a customised positional difference minimisation routine. The minimisation technique employed is a modified simplex method [100], iterating on the positional difference between the actual target position and that estimated by propagating the transfer orbit solution to the target position epoch.

Any of TRAJECTORY2.0 propagation methods 4-6 can be utilised in TARGET. Whichever method is chosen is used to propagate the target orbit and also the debris transfer orbits. Propagation method 4 is Keplerian motion and so provides a check to the ideal transfer solution returned by the universal variable algorithm. Methods 5 and 6 introduce the effects of J_2 and atmospheric drag into the problem. The use of an orbit propagator to check/perturb the initial transfer orbit solution also provides an opportunity to ensure that the orbit calculated does not re-enter enroute to the target position. This is particularly important when method 6 is used and atmospheric drag is considered. Any solutions that stray below the minimum allowed orbital altitude are dismissed from further consideration.

The combined analytical and numerical transfer orbit solution scheme is computationally intensive, particularly once the debris cloud has wrapped around the Earth several times. A number of measures are, therefore, taken to speed-up and optimise the solution search procedure of program TARGET. A solution 'save and record' methodology is adopted to ensure that the best possible solution estimates

are fed to the minimisation algorithm because this is where most of the program's calculation time is spent. The perturbation effects considered in methods 5 and 6 result in transfer orbit solutions which can differ considerably from the ideal estimate. So, instead of using freshly-calculated ideal estimates every time-step, the perturbed solutions calculated and saved on the previous time-step are employed. The quality of the saved solutions is continually monitored and if a saved solution is found to 'go astray' and provide a worse estimate for the transfer orbit than the ideal answer, then it is discarded. All the solutions obtained for each time-step are recorded and checked against one-another to ensure that there is no duplication.

An additional speed-up measure is introduced into the transfer orbit solution algorithm for propagation method 6. As with EVOLUTION3.0, the propagation method 6 implementation in TARGET uses the King-Hele drag model and mean element variations. Every time a new solution to the transfer orbit problem is tested, the mean drag variations for the orbit need to be calculated. This process is extremely time-consuming. Hence, to minimise the computation time spent calculating mean drag variations afresh for each orbit, da/dE and de/dE are determined by interpolating between values in a look-up table. The look-up table is generated by auxiliary program MEAN_DRAG_CALC and consists of values of da/dE and de/dE calculated for a range of semi-major axes and orbital eccentricities. When propagation method 6 is used, the mean drag variation database created by MEAN_DRAG_CALC is read in by program TARGET. Each time the mean drag variations for an orbit need to be calculated, the data array is accessed and linear-logarithmic interpolation is employed across the two-dimensional $a - e$ matrix to yield an estimate for each drag derivative. The $a - e$ matrix and the interpolation technique are both optimised to ensure that the quality of the derivative calculation is maintained. Debris orbits with values of a and e outside the look-up table range, on hyperbolic trajectories for example, are approximated by adopting the appropriate table-boundary a and e values for drag derivative calculation.

State transition matrix calculation

To transform the debris density in spread velocity space determined from the transfer orbit solution breakup $\triangle$v to actual debris density (i.e. in position space) at the target location requires the calculation of the state transition matrix which links the two state spaces and epochs. As with the transfer orbit problem above, a number of different methods are available for calculation of Φ, several of which are reviewed in [83]. Arguably the most elegant of these is the method of Goodyear [88], which provides an efficient closed-loop solution to the problem for ideal orbital motion. Although a number of algorithms have been developed which attempt to incorporate perturbation effects into the problem, once again no universally-accepted method exists for perturbed orbital motion. For complete generality, a numerical approach is, therefore, adopted in TARGET. The state transition matrix $\partial \mathbf{r}/\partial \dot{\mathbf{r}}_0$ is calculated by using the following small $\triangle \mathrm{v}(=\partial \dot{\mathbf{r}}_0)$ approximation,

$$\frac{\partial \mathbf{r}}{\partial \dot{\mathbf{r}}_0} \approx \frac{\Delta \mathbf{r}}{\Delta \dot{\mathbf{r}}_0}, \qquad as\ \Delta \dot{\mathbf{r}}_0 \rightarrow \mathbf{0}. \tag{6.12}$$

The perturbations in position space produced by small perturbations in spread velocity space are calculated by determining the positional differences produced by slight ejection velocity deviations from the transfer orbit solution debris breakup $\triangle$v. The above method is completely general in its application and so can be employed for propagation methods 4, 5 and 6.

Target orientation with respect to debris flux

For the cuboidal spacecraft model employed by TARGET, the probability of collision on each of the target surfaces is determined by resolving the debris encounter velocity into components expressed in the embedded target body-axis frame. Each component is then processed separately and the overall 'spacecraft' collision probability is calculated by summing the component contributions. The use of an orthogonal coordinate system with the body axes pointing out along the surface normals results in each of the debris velocity components being normal to a target surface. The target cross-sectional area in each case is, therefore, simply the relevant face

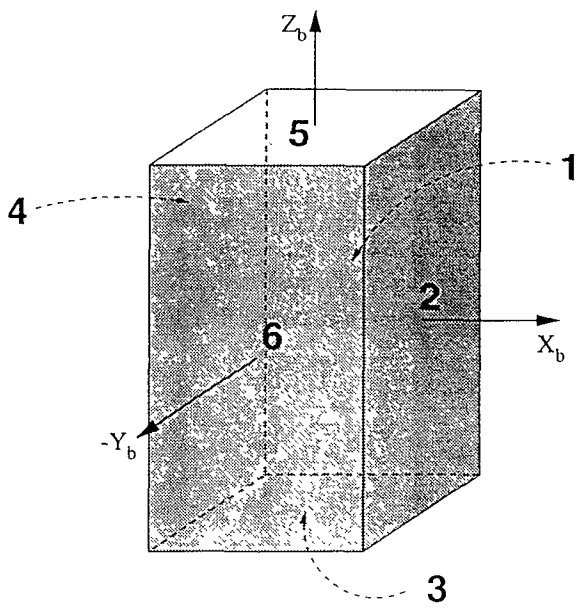

Figure 6.3: Target surface numbering scheme with respect to spacecraft body axes.

area. Figure 6.3 depicts the body axis and surface numbering scheme employed, where $(\mathbf{X_b}, \mathbf{Y_b}, \mathbf{Z_b})$ denotes the body-axis frame.

To transform the relative debris-target encounter velocity calculated from the transfer orbit solution to a vector in the target body-axis frame, the orientation of the target with respect to its orbital motion must be specified. The simplest approach is to suppose that the target maintains one face Earth-pointing, with the body-axis frame coincident with the orbiting axis frame, i.e. the positive body $\mathbf{Y_b}$ axis pointing out along the orbit radius and the body $\mathbf{Z_b}$ axis in the same sense as the orbital angular momentum vector. This is the default condition in TARGET. The default target flight orientation to surface number mapping is shown in Figure 6.4 and Table 6.1, where $(\mathbf{X_o}, \mathbf{Y_o}, \mathbf{Z_o})$ denotes the orbiting axis frame.

Not all spacecraft maintain one face Earth-pointing, however, and even those that do initially may become offset with respect to their nominal attitudes, e.g. LDEF. Some spacecraft can be flown in a number of different configurations, e.g. the space shuttle. To allow for these situations, the body axes of the target spacecraft can be rotated with respect to the orbiting frame. Roll, pitch and yaw angles are used to rotate the target about the orbiting X, Y and Z axes respectively. Rotations of

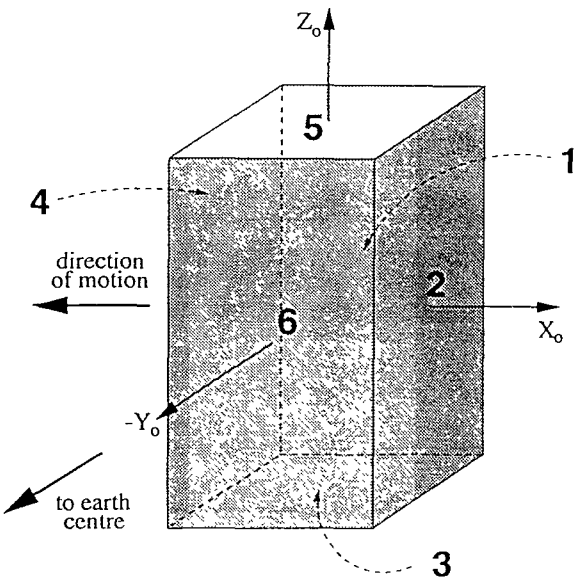

Figure 6.4: Default target in-flight orientation.

Surface number	*Flight orientation*
1	Space
2	Trailing
3	Negative orbit normal
4	Ram
5	Orbit normal
6	Earth

Table 6.1: Default target in-flight orientation.

integer multiples of 90 degrees result in exact target surface to 'direction surface' mappings being produced, where the direction surfaces are the planes normal to the positive and negative orbiting axis pointing directions.

6.3 Assessment of Target Survivability

Collision probability gives an indication of the relative severity of the orbital environment within which a spacecraft is operating, and the likelihood of 'any' collision with a piece of debris. But what does this information actually mean to the spacecraft designer or operator? An estimate, in isolation, of the chances of a spacecraft 'getting hit' is not particularly useful. Predictions of debris encounters should be ac-

companied by information detailing how damaging collisions would be, should they occur. From this, the likelihood of actual spacecraft or mission failure following a debris encounter can be assessed.

If the generic, cuboidal, spacecraft representation employed by TARGET is combined with 'real' satellite data (physical dimensions, subsystem locations, impact hardness/shielding etc) then a simple model of an actual spacecraft can be developed. Using this model, along with assumed or specified criteria regarding spacecraft/mission survivability following an impact, the failure of the spacecraft itself or one or more of its payload functions can be predicted. To enable such investigations to be performed, the spacecraft model in TARGET is divided up into 512 cells, eight divisions in each of the three body axis dimensions. Each spacecraft cell is assigned a component number which in turn details the cell's purpose, density and impact survivability. Cells which are not designated as belonging to a particular sub-system or component group can be assigned as being either structural or empty. This 'building-block' spacecraft representation is extremely versatile and can model any type of spacecraft configuration. The model resolution can be improved if required by increasing the number of cells. External systems and appendages can be accounted for by extending the cell structure out from the baseline cuboid. If such external features are modelled then shadowing/shielding effects must also be considered. The TARGET model considers the simple cuboid shape, with an outer spacecraft skin for added impact protection. Spacecraft cells with faces on the outside of the model cuboid can either be denoted as being internal (i.e. inside the skin shield) or external. Components that are designated as being external are only protected by their own level of impact hardness.

The likely size of the encountered debris, and hence the kinetic energy (KE) associated with it, is determined by referencing back to the model used to simulate the fragmentation event which generated the debris. TARGET takes its input from program BREAKUP4.0 and can use either of the two cloud types, i.e. isotropic or non-isotropic. In the case of the isotropic continuum cloud, only the magnitudes of fragment $\triangle$vs are important. From the debris breakup $\triangle$v, the range of possible

debris masses can be determined from the relevant fragment distribution models used. In the case of the non-isotropic cloud model, the direction of the debris Δvs are also important. The catalogue of fragments produced by the model is used to determine if the ejection velocity vector in question corresponds to a region of debris from the breakup. Whereas the isotropic continuum model uses spherical Δv shells to partition the debris, the non-isotropic model divides spread velocity space up into spherical polar coordinate cells. The non-isotropic model uses the same Δvs as the isotropic model for radial partitioning, but divides each Δv shell up into 32 equal cells in azimuth and elevation. The cloud cells are numbered according to increasing Δv. Cells 1-32 correspond to the innermost shell with the lowest Δvs. Cells 33-64 are located in the second shell radially outwards, and so on. Each cell may contain any number of fragments, or none at all. Hence, in contrast to the isotropic model, there will be regions of high and low debris density for any given Δv.

The damage that would be caused by a debris impact can be determined by employing a three impact category methodology. If the debris has insufficient energy to penetrate the spacecraft outer skin or external component shielding, then the impact will be absorbed and no damage will be caused to the internal spacecraft systems. This is denoted as impact category 1. If the debris KE is sufficient to puncture the spacecraft's external protection but insufficient to completely fragment the target, then the impact will either be absorbed by the spacecraft internal structure, or, in the case of a hollow booster tank for example, the impactor will pass right through it. This is impact category 2. If the impactor has sufficient energy to result in the ratio (ζ) of debris KE to target mass being greater than 40 J/g, then the target object will be completely destroyed [58]. This is impact category 3.

Impact categories 1 and 3 are relatively straightforward to simulate, as essentially either none or all of the target spacecraft will be destroyed by the impact. Category 2, however, is considerably harder to model and no simple method exists for determining the spread of the impact 'damage zone' through a complex internal structure. The method used by TARGET is to directly relate the percentage of the target mass involved in the collision with the debris impact energy to target

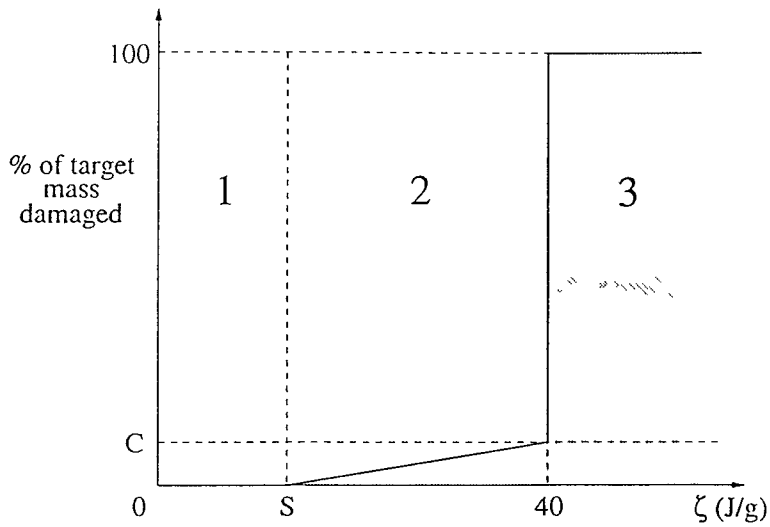

Figure 6.5: Three impact category damage model.

mass ratio ζ. This is shown graphically in Figure 6.5. The three impact categories above are represented by the three numbered zones shown in the figure. The points (S,0) and (40,C) on the figure are determined as follows. S is the debris shielding capability of either the spacecraft external skin, or the external component hit. Given the debris flux direction encountered by the target, the location of the impact is randomly selected from the cells exposed, with the probability of selecting each cell weighted according its area projected normal to the flux. From the impact cell location, the cell identification number and hence the cell details, including shield level, can be obtained. The target mass threshold for complete fragmentation, C, is obtained by relating ζ to the impact ejecta mass M_e, the mass excavated in a cratering impact. The ejecta mass can be expressed as a function of the projectile mass, M_p, and the collision velocity, v_c, thus [60],

$$M_e = M_p v_c^2 , \tag{6.13}$$

which is the same as equation (2.3). Here M_e and M_p are in grams, and v_c is in km/s. The dimensional incorrectness of equation (6.13) is discussed in Chapter 2. The criterion for complete fragmentation is then,

$$\frac{1}{2} M_p v_c^2 / M_t \geq 40/1000, \tag{6.14}$$

where M_t is the target mass in grams. Substituting M_e for $M_p v_c^2$ in equation (6.14)

and rearranging gives,

$$M_e \geq 8M_t/100, \tag{6.15}$$

i.e. the target will completely fragment if 8% or more of its mass is directly involved in the collision. This sets the value for C.

The points (S,0) and (40,C) on Figure 6.5 are joined by a straight line because M_e, and hence the percentage of the target mass damaged, is directly proportional to ζ. This relationship can be verified by considering the impact penetration depth p. For a given target-projectile combination, $p \propto v_c^{2/3}$ [42, 105, 106], and since $\zeta \propto v_c^2$, $p \propto \zeta^{1/3}$. For debris impacts, crater diameter D can be related to penetration depth by $p/D \approx 0.63$ [42]. Hence, crater volume is $\propto p^3$. So, assuming a constant or average material density, the percentage of the target mass damaged is also $\propto p^3$. And finally, combining this with $p \propto \zeta^{1/3}$, we obtain the reasonable assumption that

$$\% \text{ target mass damaged} \propto \zeta. \tag{6.16}$$

So, from the shield energy of the target cell that suffers an impact and the kinetic energy of the impacting object, the percentage of the target mass damaged can be calculated. The damage zone is spread throughout the structure by distributing the damaged mass to the cells nearest the impact location, as determined on a radial proximity basis, measured from the impact cell centroid to the neighbouring cell centroids. Sweeps with increasing damage zone radius are made until all the mass is distributed. Increments of the mean cell dimension (the cube root of cell volume) are employed. After each sweep, if damaged mass remains undistributed then each cell encountered in that sweep is considered to be completely destroyed. If the damaged mass left to be distributed is zero or negative, then the cells in that sweep are considered to be only partially damaged. Cells are tagged according to their level of damage: $\lambda = 3$ signifies complete destruction; $\lambda = 2$ denotes partial damage; and $\lambda = 1$ indicates no damage sustained. After each cell is tagged according to its level of damage, the value of λ for its component group is modified if necessary. Each component group has a criticality rating η according to whether the group is critical to the operation of the spacecraft as a whole (mission critical, $\eta = 3$), to a

Parameter	*Value=1*	*Value=2*	*Value=3*
Impact category	No damage	Partial damage	Complete breakup
Cell damage rating λ	No damage	Partial damage	Complete destruction
Component criticality rating η	Non critical	Function critical	Mission critical

Table 6.2: Damage assessment numbering scheme.

particular payload (function critical, $\eta = 2$) or is non-critical ($\eta = 1$). The highest value of λ sustained by any of the component group's cells is used to determine the whole component group's level of damage. The impact category, damage level and component criticality level numbering schemes are summarised in Table 6.2. Redundancy is not considered in individual subsystems, i.e. one destroyed component cell is taken to be sufficient to terminate the component group's operation.

6.4 TARGET Description

6.4.1 TARGET Versions

TARGET constitutes the fourth and final main module in the SDS software suite. Three different versions of the program have been used in publications [107, 108, 109, 110, 111, 111, 112], parts of which are reproduced in this section. Version 3.0 of TARGET employed the method of universal variables for the solution of the transfer orbit problem, as described in section 6.2, but with no positional error minimisation facility. Goodyear's [88] algorithm was utilised for evaluation of the state transition matrix determinant, or Jacobian. The analysis performed by TARGET3.0 was, therefore, limited to ideal orbital motion. A constant cross-sectional area was assumed for the target satellite and only the magnitude of the debris encounter velocity was calculated. Included in TARGET3.0 was a simple, non-directional, representation of the LEO debris environment based on the NASA engineering model [113] for comparison of cloud-related collision probability values with those predicted from the background population. This was the version of TARGET used in [107, 108, 111].

TARGET3.0 was upgraded to version 3.1 for comparison purposes with The Aerospace Corporation's program DEBRIS3.1 in [109]. TARGET3.1 has the facility for non-directional or directional collision probability calculation. An option for the determination of the relative direction of the debris flux was introduced in TARGET3.1, so enabling collision probabilities to be calculated for the individual surfaces of the target spacecraft, as described in the previous section. The output took the form of either collision probability, debris density or debris flux time-histories, or alternatively cumulative collision probability as a function of debris mass, encounter velocity direction or magnitude, or target surface number.

The latest version of TARGET is 4.0. It is the modelling approach of TARGET4.0 that was described in some detail in the previous two sections. The effects of J_2 and drag on the orbits of the target satellite and debris cloud are modelled using the analytic-numerical hybrid transfer orbit solution method and the state transition matrix determinant is calculated numerically. Directional debris collision probabilities are calculated and damage assessments are performed on the cellular, cuboidal, target representation for both isotropic and non-isotropic debris cloud models. TARGET4.0 was employed in [112] to investigate the likelihood of a debris cloud encounter leading to payload or even mission failure for a target spacecraft.

6.4.2 Program Operation

Single satellite analysis

TARGET4.0 operates in a similar fashion to BREAKUP4.0, TRAJECTORY2.0 and EVOLUTION3.0. *targ4_control* contains the main program inputs, including the propagation method to be employed, the time-step to be used and the number of time-steps to be considered. Program TARGET4.0 uses TRAJECTORY2.0 orbit propagation methods 4 to 6. For method 6, the drag derivative look-up table produced by MEAN_DRAG_CALC is loaded from *mean_drag4.dat*. The dimensions, mass, drag coefficient, outer skin shield energy and orbit attitude of the target satellite are all by default read in from *targ4_control*. For analyses where a full damage assessment is required, however, the parameters above and the target component

cell structure and specifications are read in from file *targ#.sat*, where # ranges from 1 to 5. Any one of five stored target satellite cell models can thus be utilised. The remaining program inputs from *targ4_control* define the orbital environment in terms of solar activity and re-entry altitude, and specify the cloud type to be employed. If the isotropic cloud model is chosen (cloud type 1) then cloud shell data is read in from BREAKUP4.0 output file *break4_iso.dat*. The outer cloud shell number (1-8) to be used is specified in *targ4_control*. This allows the cloud size to be controlled explicitly. As ejection velocity is, to a first approximation, inversely dependent upon fragment size, neglecting the outer cloud shell(s) enables the smaller debris to be filtered out of the subsequent analysis if required. This, for example, enables analyses which only want to consider trackable or non-shieldable fragments to be performed. For cloud type 2, the non-isotropic cellular spread velocity space is read into TARGET4.0 from *break4_cells.dat*. The orbit of the breakup CM is taken from BREAKUP4.0 input file *break4_control*.

A further input to TARGET4.0 from *targ4_control* is the radius of the target 'encounter zone' to be employed. This defines a spherical volume around the target position inside which all debris encounters are considered. In practice, this can be considered to be analogous to the space shuttle 'manoeuvre box' discussed in Chapter 1, or alternatively as an indication of the uncertainty associated with the positions of the target and the debris.

Output from TARGET4.0 is made to a number of data files. The target position at each epoch considered is output to file *targ_pos.dat*, along with the total collision probability calculated for that time-step. More detailed collision hazard information is output every time-step to file *targ_haz.dat*. This includes the magnitude and direction of the debris velocity with respect to the target, the collision probability calculated for each of the spacecraft surfaces, and also the kinetic energy of the largest fragments encountered. If a target cell model is used, details on the number of impacts predicted, their locations and the potential damage to the spacecraft is written to file *targ_cells.dat*. Component damage information is output to *targ_cpts.dat*

Satellite constellations

Satellite constellations can be considered by TARGET4.0 when the program is run in constellation mode. This is activated when the number of target satellites specified in *targ4_control* is greater than 1. Additional input is then taken from *const4_control*. The constellation configuration is set in *const4_control* by specifying the number of orbital planes in the constellation and also the satellite phasing strategy to be employed. The analysis assumes that the satellites in the constellation have a common semi-major axis, inclination and orbit eccentricity. The number of orbital planes specified, N, must divide into the number of satellites in the constellation exactly otherwise the configuration chosen is deemed to be invalid. The number of satellites in each orbit plane, M, is thus assumed to be the same. The intra-planar separation window, θ, which represents the angular separation between satellites within an orbital plane, is obtained very simply using $\theta = 2\pi/M$. Two plane-plane phasing strategies are currently employed. The first is based upon that utilised in [114], where the inter-plane separation window ϕ is calculated from $\phi = \theta/N$. ϕ is the angular separation between all the satellites in the constellation and represents the angular separation between satellites as they fly through the orbit plane intersection nodes. Constellations must always be designed to ensure that satellites in different orbit planes do not arrive at the nodes at the same time, otherwise a direct collision between satellites may occur. The second satellite phasing option is based upon the method outlined in [115]. This is described in more detail in section 6.5.6, where the Iridium^{TM} constellation is examined.

TARGET4.0 can consider satellite constellations of up to 1000 satellites, for unlimited-length simulations. Enormous data files could thus be produced if the same high-resolution collision hazard information output for single satellite analyses was created for every satellite in a large constellation. Several different output options are, therefore, made available to allow for the different size constellations modelled and varying output data requirements. Collision hazard and satellite position data can be output to either a single constellation file or alternatively to individual satellite files. If the single file option is selected, collision hazard informa-

tion can be output either after every debris encounter or once per orbit revolution. Full, single-satellite, hazard output can made for each constellation satellite to an individual file if required, however.

6.5 TARGET Case Studies

6.5.1 Overview

The modelling capabilities of program TARGET are illustrated here by several examples. Possible candidates for the target objects to be considered include remote-sensing and communications satellites, risk objects such as nuclear power sources, manned vehicles such as the space shuttle, the Russian space station Mir and the future international space station Alpha, and any number of the proposed large satellite constellation concepts, e.g. Iridium™ and Teledesic. The effects of constellation satellite and launch vehicle breakups on Iridium™ and Teledesic type constellations are examined later on in this section. The future ESA polar platform (PPF) ENVISAT-1 is used as the focus of novel single-target analyses, and to illustrate the general working of the program and the different modelling options available.

6.5.2 Single Target Parametric Analysis

Introduction

ENVISAT-1, which is currently due for launch in 1998, has an on-orbit mass of around 8 tonnes and with its solar array and ASAR (Advanced Synthetic Aperture Radar) antenna deployed has a maximum cross-sectional area of around $40m^2$. The proposed orbit (approximately 800km circular, 98.7 deg. inclination) is, in fact, already a particularly hazardous one, corresponding to a peak in the background debris flux [30]. Fragmentation events during the platform's orbital lifetime would further add to this already considerable threat. To examine the nature of this potential additional risk, a comprehensive parametric sensitivity analysis is performed

Element pair	*Roles in orbit description*	*Influence on cloud-target encounters*
a, e	Determine orbit SIZE and SHAPE	TIMING and DURATION
i, Ω	Determine orbit ORIENTATION	PRIMARILY TIMING
ω, f	Determine POSITION within orbit	TIMING and DURATION

Table 6.3: Orbital element pairs.

to identify which orbits present the greatest collision hazard to the PPF, if a satellite in one of the orbits considered were to fragment. The default condition for the analysis is that PPF orbital element values are used for the breakup object unless otherwise stated. For the PPF, ω, Ω, and f_0 are all set to zero. The debris cloud is represented by a single-shell with a bounding spread velocity of 500m/s and a spatial density (in spread velocity space) of 10^6 fragments/km^3/s^3. The $\triangle$v and debris density values are chosen to be representative of a cloud of fragments 1cm in size and over. This limit is taken to model the PPF's shielding capability. Collision probabilities due to the background debris environment are calculated using the NASA engineering model [113], and all the values of collision probability, P_c, quoted are total, i.e. background plus cloud. The analysis discussed in this section was performed using TARGET3.0 and can also be found in [107] and [111].

Parametric variation methodology

The orbits of the target (PPF) and the breakup object pre-fragmentation, and their locations at the time of the breakup event, influence when, or indeed if, the PPF passes through the debris cloud. The timing of a cloud-target encounter governs the magnitude and duration of the collision probability spike produced. An encounter close to one of the cloud's pinch locations is considerably more dangerous by orders of magnitude than a passage through a more expanded section of the cloud.

The six Keplerian orbital elements $(a, e, i, \omega, \Omega, f_0)$ result in the need to vary twelve parameters when considering both the target and breakup object orbits.

There are too many variables to consider the whole variation matrix, so there must be some reduction in the number of parameters to be examined. Firstly, the effects of varying the target orbit parameters will be essentially the same as varying the breakup orbit parameters since it is in essence the relative motion between the two objects that is of interest. As a target object has been chosen to be the focus of this study, the target orbit parameters are held constant and the effects of varying the orbital elements of the breakup object are examined. Secondly, it should be also be noted that the six Keplerian orbital elements can be grouped into three pairs. These element pairs are linked in the way that they describe an orbit, and also by virtue of the influence they have when varied from their PPF values (Table 6.3). Varying the two elements within each of these three element pairs enables any cross-element dependencies and/or general trends to be observed for any element combination since, by definition, there is no inter-dependency between elements that are in different pairs. Hence, by varying only the breakup orbit parameters and adopting the 'element-pair' method outlined above, the problem can be transformed to a manageable size.

$a - e$ variations

Variation of the semi-major axis, a, and/or the eccentricity, e, of the breakup orbit affects the timing and duration of any cloud-target interceptions. As a and e are varied from their PPF values, less time is spent inside the cloud. If e is set to zero (the value used for the PPF) and a varied, a symmetrical behaviour on either side of the PPF semi-major axis value is observed. As $\triangle a$ increases, the relative velocities associated with potential collisions rise but this increase in risk is offset by fewer encounters occurring close to the cloud's pinch locations. Varying e has a similar effect. As $\triangle e$ increases, the cloud-target encounters become much shorter in duration (thinner spikes on the P_c vs time curves) but away from the cloud's pinch locations they generally have a higher level of risk associated with them. Figure 6.6 shows the collision probability curves for three different $\triangle e$s, each for a period of ten orbit revolutions. Coupling between the two elements occurs when they are

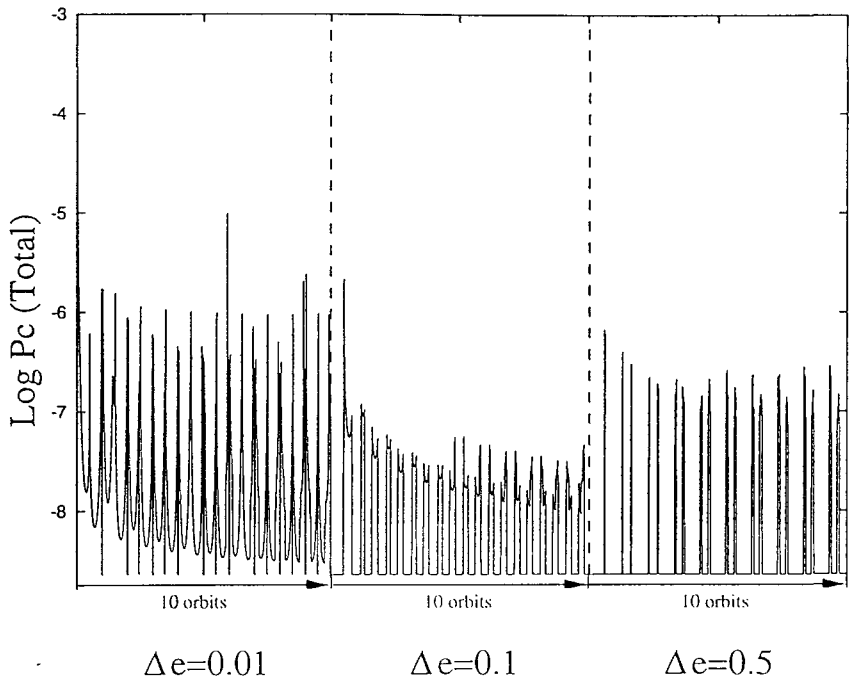

Figure 6.6: Target-breakup-object $\triangle e$ variation.

varied together, i.e. the effects of varying a are explored for a number of different values of e (e.g. Figure 6.7 gives P_c profiles as a varies for one particular value of e). The addition of small eccentricities to the breakup orbit results in the loss of the symmetrical behaviour about the PPF value of a. The most time spent in the cloud then occurs for a semi-major axis greater than that of the PPF, with the particularly spikey appearance of the curves for $\triangle a > 0$ corresponding to cloud-target encounters close to the cloud's pinch locations. Combinations of a and e that result in the breakup orbit having its apogee close to the PPF's circular orbit altitude can produce cloud-target encounters that are significantly more dangerous than would generally be the case for those values of a or e alone (longer durations, higher collision probabilities). A similar but less pronounced effect also occurs for combinations the perigees of which are close to the PPF altitude.

$i - \Omega$ variations

If the breakup being examined occurs in an orbit plane that is highly inclined with respect to the PPF orbit plane (by virtue of the difference between orbital inclinations,

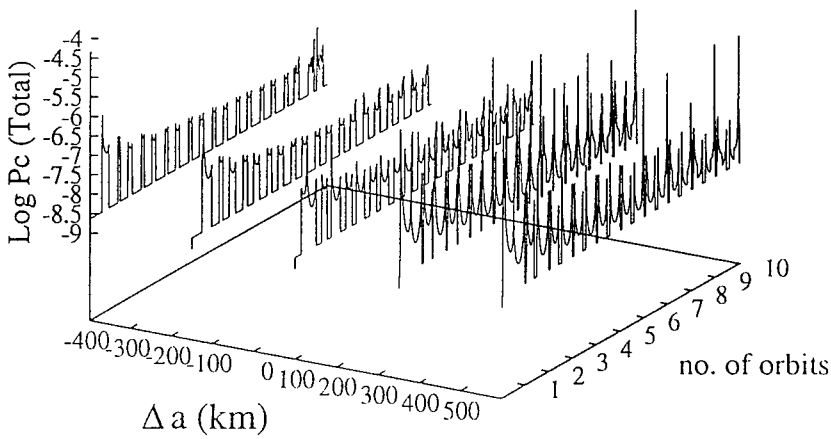

Figure 6.7: Target-breakup-object Δa variation, Δe=0.05.

Δi, and/or ascending node positions, $\Delta\Omega$) then any encounters will be relatively brief and will generally occur either at or close to the orbits' intersection points. Hence Δi and $\Delta\Omega$ govern when/if any cloud-target encounters occur but have only a relatively minor influence on their duration. Encounters will generally occur either once or twice per target orbit revolution depending upon the relative orientations of the target and breakup orbit planes and the time elapsed since the fragmentation event (Figure 6.8). The higher the values of Δi and/or $\Delta\Omega$, the longer the time until the first encounter (Figure 6.9). The magnitudes of the collision probability spikes will again be governed by two main factors; the relative debris flux velocities and the closeness of the encounters to the cloud's pinch locations. Here, the relative velocities associated with passages of the target through the cloud will generally be large, potentially as high as the sum of the target's and fragments' orbital velocities for a 'head-on' type encounter. Again, though, as with the eccentricity variation described in the previous section, the vast majority of encounters will occur away from the cloud's pinch locations.

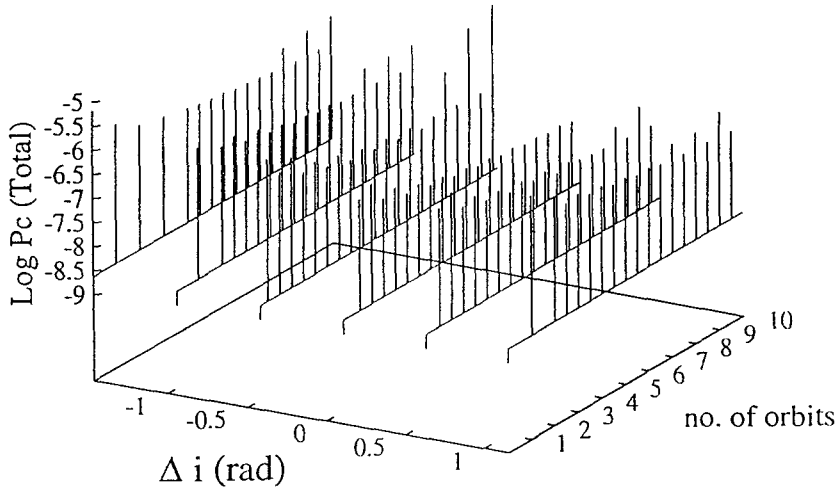

Figure 6.8: Target-breakup-object Δi variation, $\Delta\Omega=\pi/4$rads.

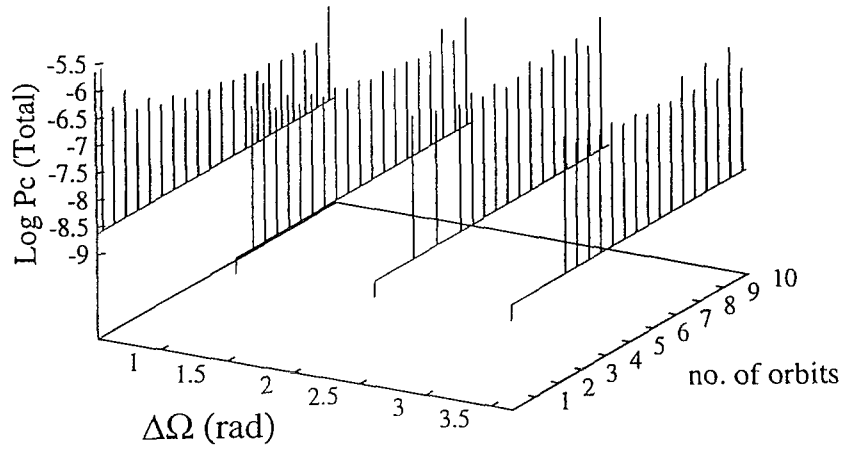

Figure 6.9: Target-breakup-object $\Delta\Omega$ variation.

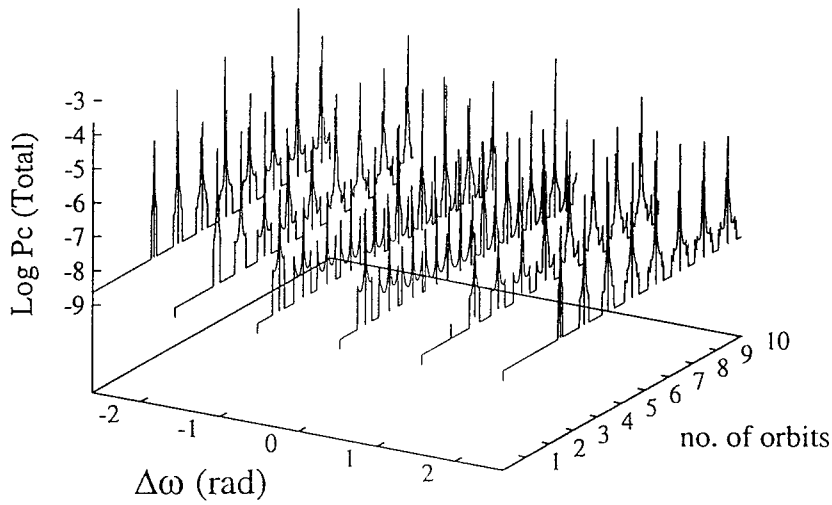

Figure 6.10: Target-breakup-object $\Delta\omega$ variation.

$\omega - f_0$ variations

For a given breakup/target orbit combination, the position of the fragmentation event within the breakup CM's orbit can significantly effect the level of risk posed to the target. The relative initial positions of the PPF and breakup object will determine how much time the PPF spends inside the cloud and, in particular, the number of encounters that are in close proximity to the cloud's pinch locations. Figure 6.10 shows that the most time is spent in the cloud for values of $(\omega + f_0)$ close to the PPF value but large collision probability spikes are registered for all starting configurations. The addition of eccentricity complicates the problem. Figure 6.11 shows that the curve representing $(\omega + f_0)$ equal for the PPF and breakup object again results in the quickest first encounter but other combinations can in fact produce the largest instantaneous levels of risk.

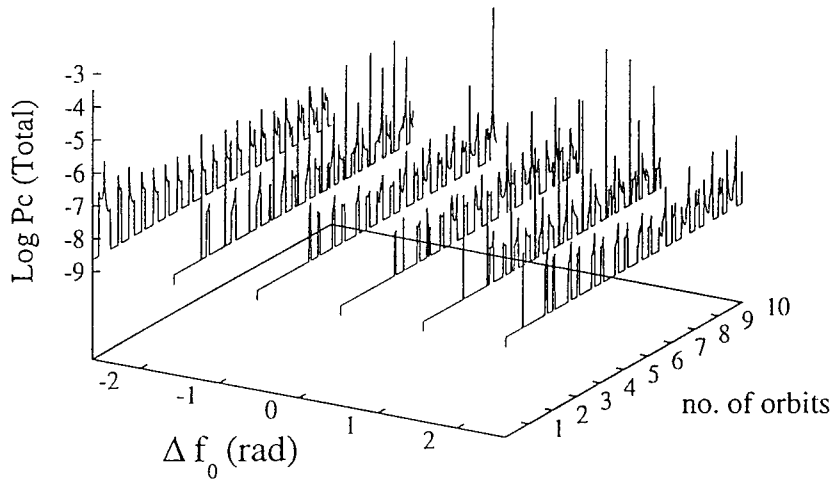

Figure 6.11: Target-breakup-object $\triangle f_0$ variation, ω=150deg., $\triangle e$=0.1.

Summary

It is shown that the collision risks associated with passages of the PPF through a debris cloud can be orders of magnitude higher than the background level. The timing and duration of cloud-target encounters are highly dependent upon the orbits of the two objects and their relative positions at the time of the breakup. Debris clouds formed from breakups in a wide range of orbits are shown to be capable of interacting with the PPF. The highest collision probabilities are produced for breakups in the same orbit plane as the PPF. No consideration is given here to the potential lethality of the debris encounters, however, and the effects of orbital perturbations are also neglected. These issues are explicitly addressed in the next two subsections.

6.5.3 Comparison of Propagation Methods

Introduction

In section 5.3.2 it was shown that the errors incurred in debris cloud evolution modelling are dependent upon the method used to propagate the fragment orbits. The estimate of collision risk posed by the cloud to spacecraft which encounter it may also, therefore, be significantly influenced by the orbit propagation method employed in the collision hazard analysis. A simple example is employed here to illustrate the effects of J_2 and atmospheric drag perturbations on the short-term collision risk to a satellite which is co-orbital with a satellite destroyed by a collision. The two satellites might be members of a constellation, for example, located in the same orbital plane but separated by an argument of latitude difference. The satellite constellation scenario, however, is addressed explicitly in section 6.5.5.

The orbital parameters used here are the same as in the first cloud-target scenario in [?], which is covered in more detail in section 6.6.3. Both the destroyed and target satellites are in 400km near-circular orbits at an inclination of 28.5 degrees. The target satellite is located 12 degrees in true anomaly ahead of the destroyed satellite. The BREAKUP4.0 isotropic cloud model is used to model the fragmentation to remove any possible effects of employing a non-isotropic fragment spread from the subsequent analysis. Six of the 8 isotropic cloud shells are used to account for Δvs up to 4km/s. TARGET4.0 is employed to determine the collision threat to the target for 12 hours following the breakup. Propagation methods 4, 5 and 6 are used in turn to investigate the effects that J_2 and drag have on the magnitudes and directions of the debris fluxes encountered.

Method comparisons

Figure 6.12 shows the collision risk predicted for the target satellite using propagation option 4 (Keplerian propagation). The cumulative collision probability is shown over time (Figure 6.12a) and target surface number (Figure 6.12b). The default target surface number to orbital attitude mapping is employed (Figure 6.4).

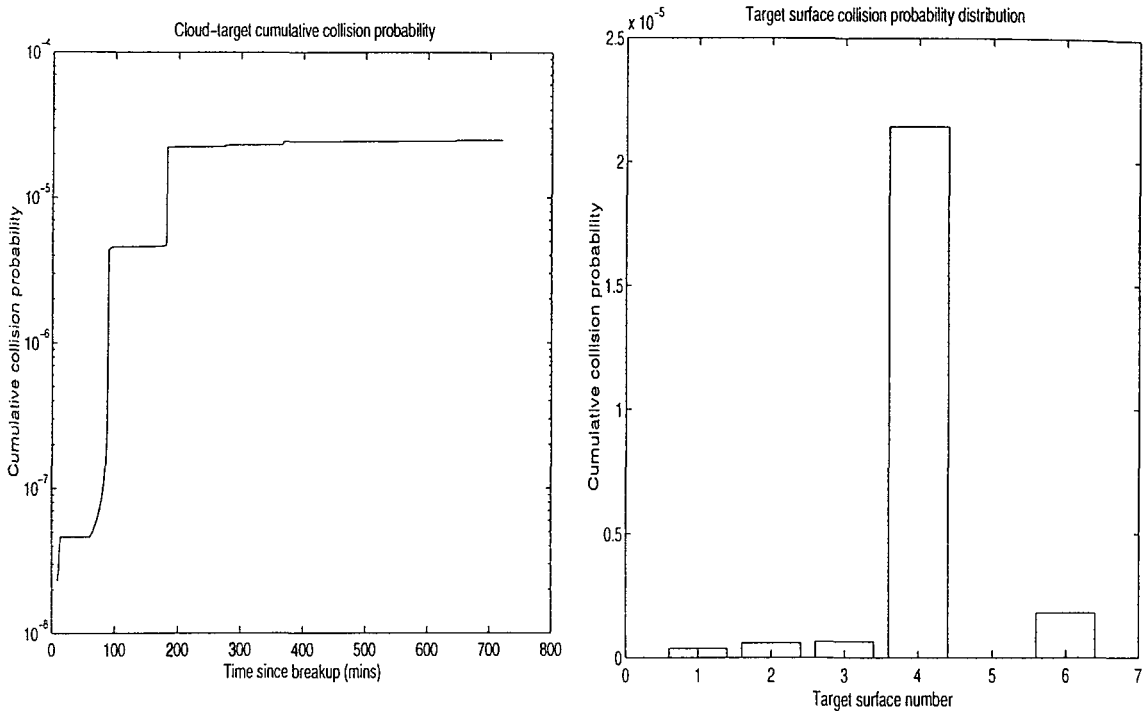

a) Cumulative collision probability versus time b) Distribution of collision risk over target surfaces

Figure 6.12: Collision probability distributions : Propagation method 4.

Figure 6.12a shows that almost all the collision probability experienced by the target satellite is due to the first three cloud encounters. The first of these high-risk events occurs soon after breakup when the density of debris is still relatively high. The second and third steps in the cumulative collision probability versus time curve correspond to target encounters with debris near the first two cloud whole-revolution pinch points. Again high debris density leads to large collision probability values. After the completion of the second orbit, post-breakup, continued debris dispersal and re-entry results in a dramatic reduction in the collision probability values calculated. The curve in Figure 6.12a, therefore, is seen to level off a few hours after the fragmentation.

Figure 6.12b shows that the target surface most at risk from debris impacts is surface 4, the ram face. This is perhaps surprising at first because the breakup occurs 'behind' the target in terms of their directions of motion. The cloud's leading section, however, is comprised of fragments ejected in a retrograde sense and these either re-enter soon after breakup or spend most of their time below the target altitude.

The fragments ejected forward (prograde) from the breakup are thrown into higher energy orbits and so orbit more slowly than the target. These fragments remain in orbit and so it is predominantly debris from this portion of the cloud that the target encounters. As the target is orbiting more quickly than this high-energy debris, the dominant encounter geometry is the target catching debris up from behind, so leading to the dominance of the ram face flux. Small debris fluxes are predicted for four of the remaining target surfaces, though, including the trailing face, surface 2. The contributions here are from debris in eccentric orbits catching the target up from behind. The negative orbit normal face, surface 3, is observed to experience a small flux. For the scenario considered here, in which the breakup occurs in the target orbit plane, ideal solutions to the transfer orbit problem (i.e. using the method of universal variables) do not result in out-of-plane encounters because the problem is two dimensional. The planes of the transfer orbits calculated are always the same as the breakup and target orbit planes. Hence no encounters can, in theory, be registered for the out-of-plane faces, numbers 3 and 5. The introduction of the numerical minimisation process into the procedure, however, removes this constraint and allows debris with out-of-plane relative velocity components to be considered.

Figure 6.13 shows the output generated by TARGET4.0 when propagation method 5 (Keplerian plus J_2) is utilised. Figure 6.13a is very similar to Figure 6.12a, with the vast majority of the end-of-run collision probability total corresponding to the three high-risk encounters described above. The inclusion of J_2 effects into the problem does not dilute the effects of these encounters markedly because the target and debris close to the cloud's centroid are subject to virtually the same perturbation forces. The pinch locations move under the action of the Earth's oblateness, as shown in section 5.3.2, but the target moves with them and so in this case virtually the same encounter pattern is observed, with only minor changes to the levels of instantaneous collision probability and the end-of-run cumulative value. Figure 6.13b shows that the distribution of collision probability over the target surfaces is somewhat different, however, with noticeable out-of-plane contributions from surface 5 and in particular surface 3. The contribution of the ram face is around 20% lower

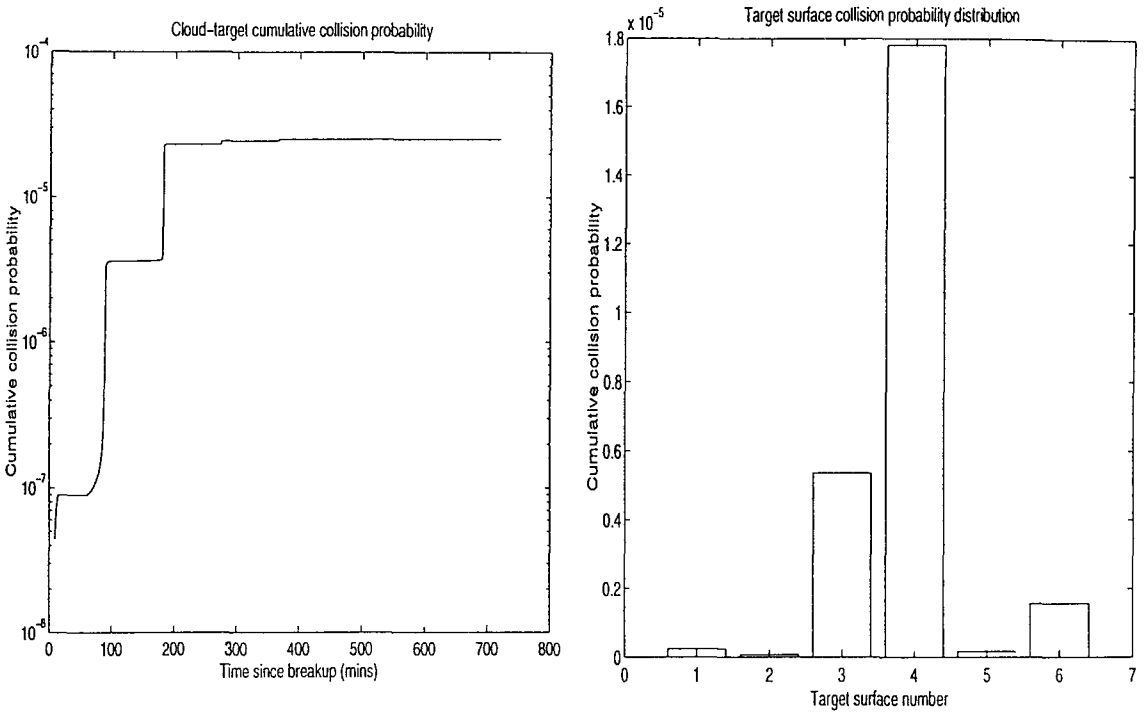

a) Cumulative collision probability versus time

b) Distribution of collision risk over target surfaces

Figure 6.13: Collision probability distributions : Propagation method 5.

than for the method 4 run, with the collision probability 'lost' from surface 4 falling on surface 3. The increased risk to the out-of-plane faces is a direct result of the J_2 perturbation force which causes the nodes of the debris and target orbits to regress at different rates due to their different orbital parameters. As stated above, debris close to the cloud centroid will be perturbed to a similar degree to the target. Nevertheless, small out-of-plane relative velocity components are produced which lead to the collision risk experienced by the orbit normal and negative orbit normal faces.

Propagation method 6 (Keplerian plus J_2 and drag) is used to assess the collision hazard to the target in Figure 6.14. The re-entry of fragments due to atmospheric drag causes a significant reduction in the debris densities around the cloud's pinch points, resulting in the smaller collision probability 'jumps' in Figure 6.14a. The effect is particularly noticeable for the first whole-revolution pinch point. The end-of-run cumulative collision probability value is around half that predicted by the method 4 and 5 simulations. Figure 6.14b, however, shows that the introduction of drag causes a large increase in the debris incident on the target space face (surface 1).

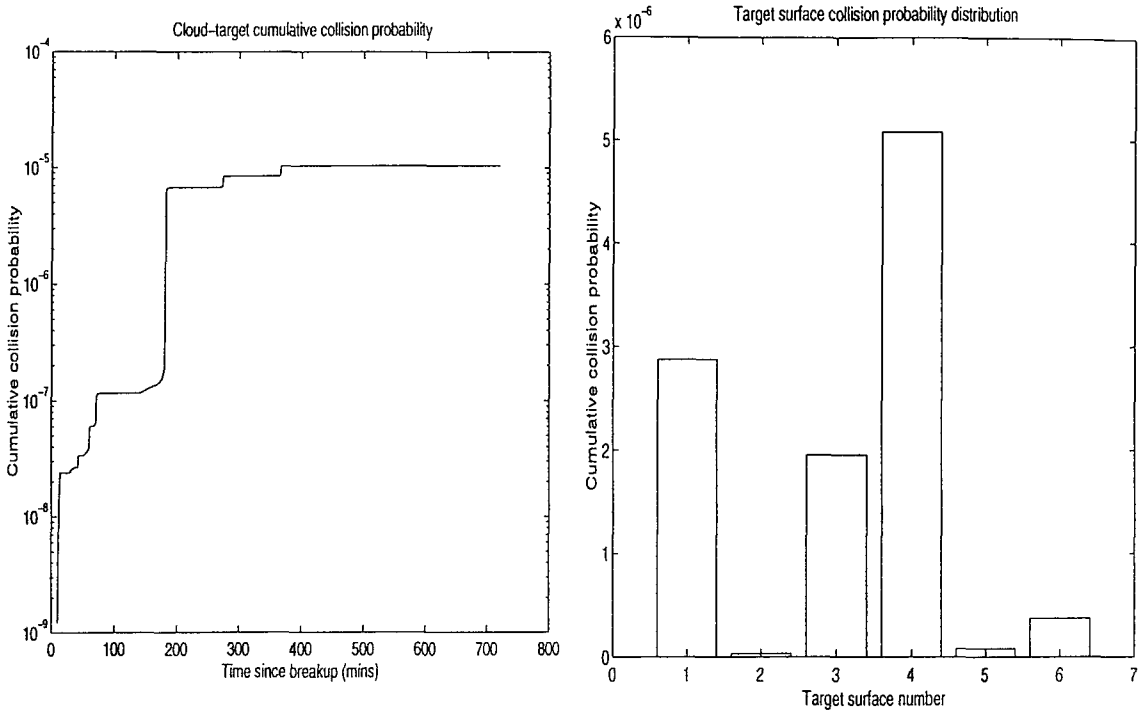

a) Cumulative collision probability versus time b) Distribution of collision risk over target surfaces

Figure 6.14: Collision probability distributions : Propagation method 6.

This is caused by the 'rain-down' effect of fragments in higher orbits than the target crossing the target orbit as they decay towards re-entry. Although these fragments are initially in higher-energy orbits than the target satellite, they will tend to decay more quickly due to their larger ballistic coefficients.

Summary

The introduction of orbital perturbations into the debris cloud collision hazard problem is seen to be capable of producing significant effects even for short-term analyses. Both the magnitude and direction of the debris flux experienced by the target object are modified. In the example considered, the introduction of J_2 and drag reduces the overall collision probability calculated for the target by approximately a factor of two, but results in significant debris fluxes being experienced by spacecraft faces normally considered to be relatively safe from debris impacts. As with the PPF analysis in the previous subsection, however, no measure of debris impact lethality

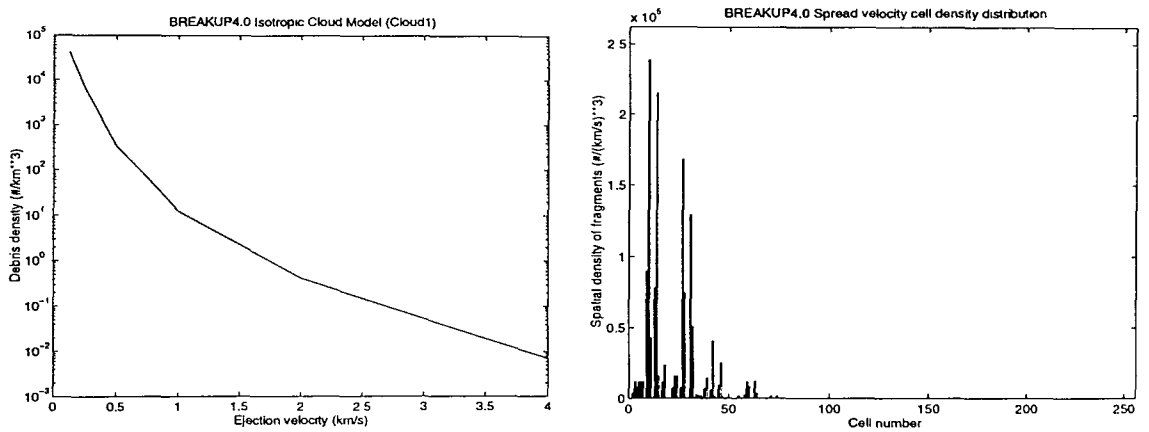

a) Isotropic model debris density distribution

b) Non-isotropic model debris density distribution

Figure 6.15: Comparison of cloud model debris density distributions.

is made here. The distribution of collision probability does not, therefore, necessarily reflect which surfaces are most at danger from damaging, high-energy impacts. In general, the action of perturbation forces serves to reduce the collision risk posed by the cloud through fragment decay and pinch zone dispersion.

6.5.4 Target damage assessment

Introduction

To illustrate the damage assessment capability of TARGET4.0, the fragmentation of the SPOT-1 rocket body is simulated using BREAKUP4.0 and the resulting debris threat to ENVISAT-1 is examined using TARGET4.0. The effect of the cloud model used to simulate the fragmentation event is examined, as is the effectiveness of a number of potential spacecraft and subsystem protective measures. The majority of the analysis discussed in this section can also be found in [112].

Breakup event

The breakup of the SPOT-1 Ariane V16 third stage rocket body has been discussed in some detail already in this thesis, with simulated breakup epoch and decayed Gabbard diagrams generated by BREAKUP4.0 and EVOLUTION3.0 being compared with actual event data in Chapters 3 and 5 respectively. In both these cases,

the fragmentation was modelled using the BREAKUP4.0 non-isotropic cloud model. The breakup of the SPOT-1 Ariane stage is a good fragmentation example to consider here because the results of the breakup simulation have already been validated and the proposed orbit of ENVISAT-1 is almost the same as that of the SPOT-1 rocket body. The debris density distributions for the event produced by the two BREAKUP4.0 cloud models are shown in Figure 6.15. For the isotropic model, the density of debris is highest near the cloud centroid and falls by several orders of magnitude towards the cloud's extremities. The eight shell cloud model produces a relatively smooth density profile. In contrast, the non-isotropic model generates a highly variable density distribution. The x-axis in Figure 6.15b is debris cloud cell number. The highest cell densities in Figure 6.15b are comparable with the highest shell density in Figure 6.15a, but most are considerably lower. The effect this has on the collision hazard posed to the target satellite is discussed in the next section.

Target satellite

Figure 6.16a shows ENVISAT-1's payload configuration with respect to its body reference frame. The solar array and ASAR (Advanced Synthetic Aperture Radar) antenna are not deployed in Figure 6.16a. The corresponding in-orbit orientation of the platform is shown in Figure 6.17. The default target flight orientation to surface number mapping is employed, as shown in Table 6.1 and Figure 6.4. The in-flight orientation of ENVISAT-1 is also depicted in Figure 6.18 [116]. The satellite is modelled using the TARGET4.0 cell model as shown in Figure 6.16b. Five payload groups are simulated. Group 1 represents the ASAR but does not model the full deployment of the antenna beyond the bounds of the target cell cuboid. Component groups 2-5 represent sections of mounted payload as opposed to individual systems. The payload cells are all externally mounted. The power and propulsion components of the platform's service module are modelled as a mission critical component group (component group 6), with the battery plate taken as being external. The remainder of the cell structure is left unassigned as component group 0 (non-critical components) and the solar array is ignored.

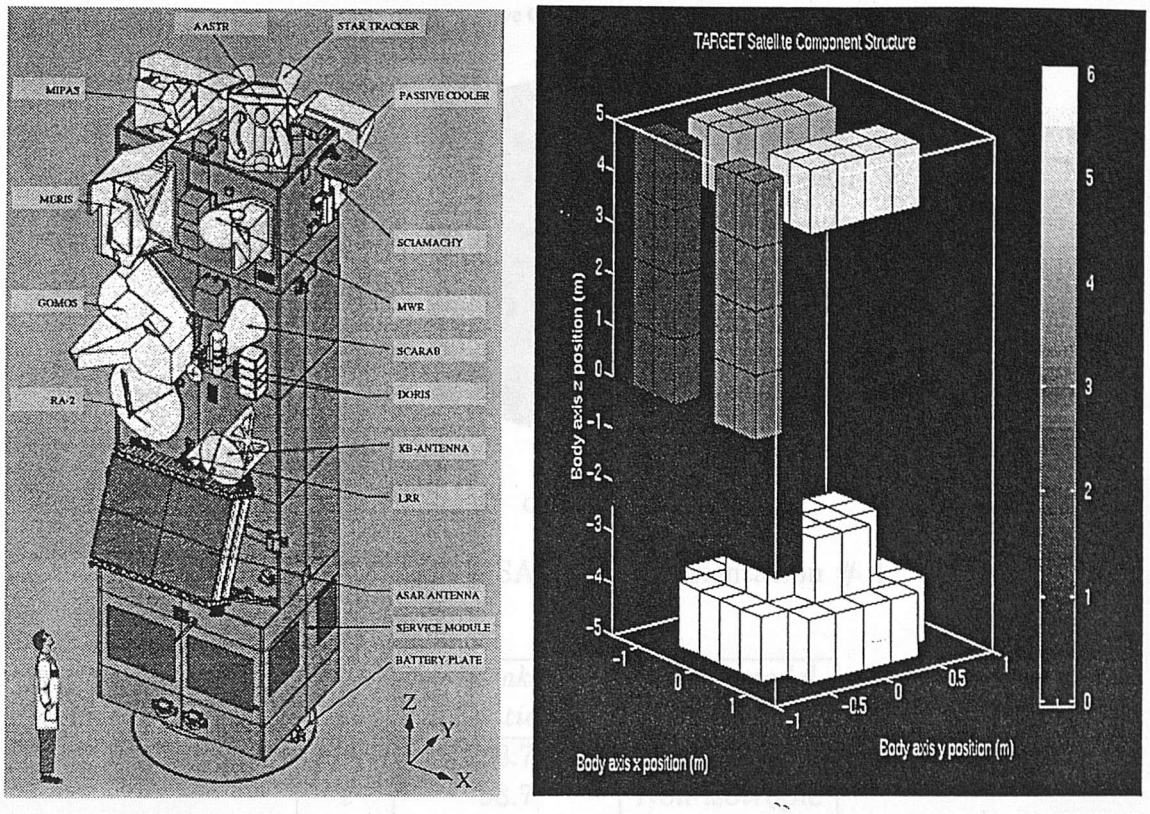

a) ENVISAT-1 payload configuration

b) ENVISAT-1 TARGET cell model

Figure 6.16: ENVISAT-1 satellite.

Hazard assessment

The collision hazard to ENVISAT-1 following an on-orbit fragmentation similar to the SPOT-1 breakup is examined. Four different scenarios are looked at, as shown in Table 6.4. The orbital parameters and model used for ENVISAT-1 are kept constant throughout. Each simulation is run for 100 minutes after the breakup with one minute time steps. The effects of atmospheric drag are neglected.

Case 1

Case 1 has the breakup occurring in virtually the same orbit as ENVISAT-1, and close to the target object. The isotropic cloud model is used with the minimum debris size considered being 0.1mm. The target outer skin and external components are assumed to have no impact shielding. The target remains inside the cloud of

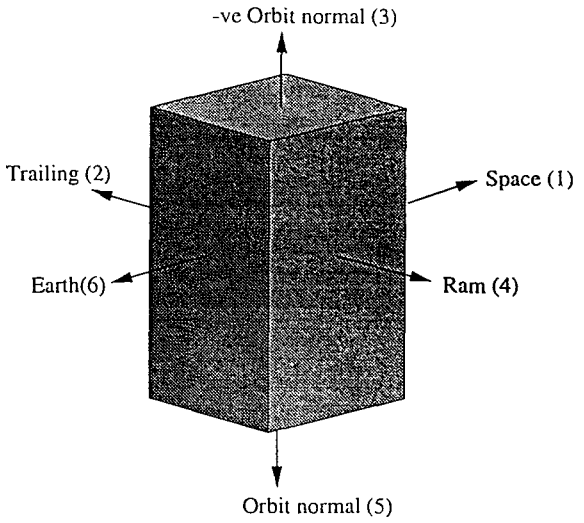

Figure 6.17: ENVISAT-1 flight orientation # 1.

Case	*Breakup inclination (°)*	*Cloud model*
1	98.7	Isotropic
2	98.7	Non-isotropic
3	28.5	Isotropic
4	28.5	Non-isotropic

Table 6.4: Test cases.

debris for the duration of the simulation, mostly very close the cloud's centroid. Figure 6.19a shows how P_c per time step varies over the run. The shape of the curve reflects the cloud's expansions and contractions, with the debris crossing the breakup plane near the half-revolution point, and converging back close to the breakup location after one full orbital revolution. These debris concentrations produce the peaks in P_c. Figure 6.19b shows that the KE of the debris encountered relative to the target is of the order of kilojoules. Spacecraft shielding is thought to be capable of protecting against debris objects of up to 1cm in size [4, 26]. The energy associated with an impact of a 1cm object at 10km/s is around 50KJ. In Case 1, therefore, a comparable level of shielding could provide ENVISAT-1 with protection from all the possible impacts predicted.

The orientation of the debris flux relative to the target is shown in Figure 6.20. From Figures 6.20a and 6.17, it can be seen that the space and trailing surfaces

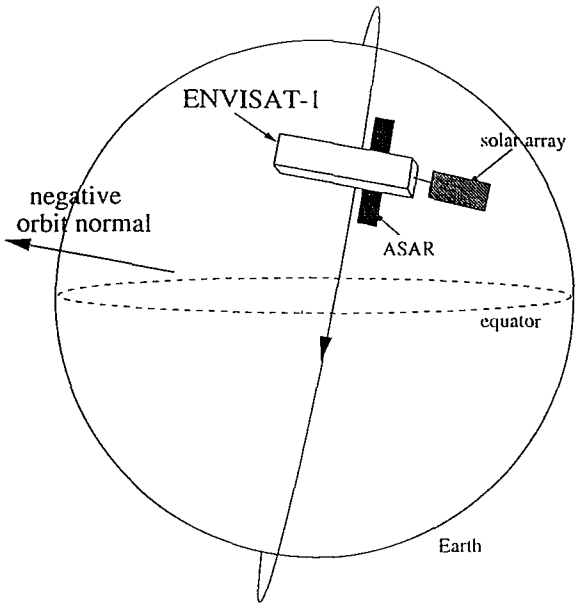

Figure 6.18: ENVISAT-1 flight orientation # 2.

account for nearly all of the collision probability, as registered in the debris encounters at the beginning and the end of the simulation. These two faces are generally regarded as being relatively safe from debris impacts due to the orbital geometries necessary to produce such encounter orientations, i.e. eccentric orbits. Figure 6.20b shows a possible spread of debris impacts, the impact locations being determined as described in section 6.3. The effect of an impact is investigated for each debris encounter. This does not mean that an impact is actually registered or indeed expected for every time step where the instantaneous value of P_c is greater than zero. The objective is purely to determine how serious each impact would be, should it occur. The damage assessment information should, therefore, always be used in conjunction with the collision probability. The spread of impacts shown in Figure 6.20b shows a dominance for the trailing and Earth-facing surfaces. From Figure 6.20a it can be seen that the space face has the highest collision probability but Figure 6.20b shows that most of the potential impact sites are on the Earth face. Figure 6.20a shows how likely each surface is to be hit over the course of the whole simulation. The collision probabilities are cumulative, summed over time, and as such do not indicate how many debris encounters actually contribute to each of the surfaces' end-of-run figures. The collision probability for surface 1 is completely dominated

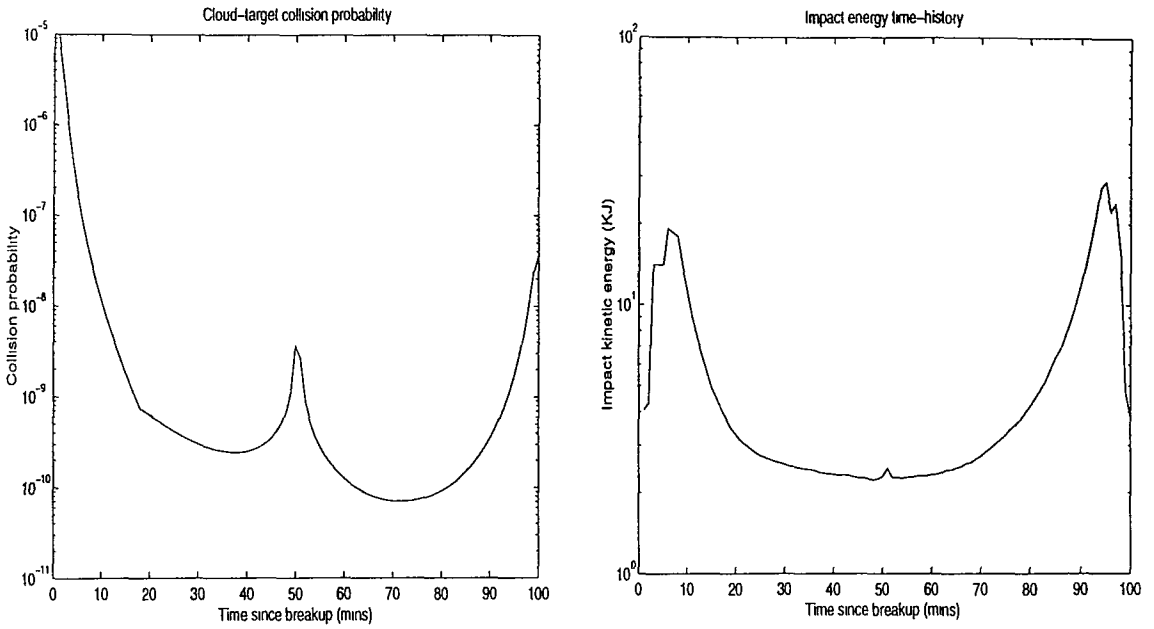

a) Case 1 collision probability

b) Case 1 encountered debris KE

Figure 6.19: Case 1 results # 1.

by the debris encounters immediately after breakup. Figure 6.19a shows that the collision probabilities for the encounters in the first few minutes of the simulation are several orders of magnitude higher than any registered in the remainder of the run. Figure 6.20b shows how many times each surface could conceivably be hit but also indicates the probability of each potential cell impact. In this case, most of the debris encounters are on the Earth face, but the surface with the greatest chance of being hit is the space face.

It is particularly interesting that the target surface with the most possible debris hits is the Earth face, as the majority of ENVISAT's payload functions are located on this side of the spacecraft. Although the chances of an impact are low, it may still be useful to know what damage such an impact would cause. The component group criticality ratings are shown in Figure 6.21a and damage levels in Figure 6.21b. Three out of the five payload groups show partial damage, as does non-critical component group 0. So, although no payload groups or mission critical components are completely destroyed in the simulation, such an impact may seriously affect the operation of the spacecraft and/or several of its payload functions.

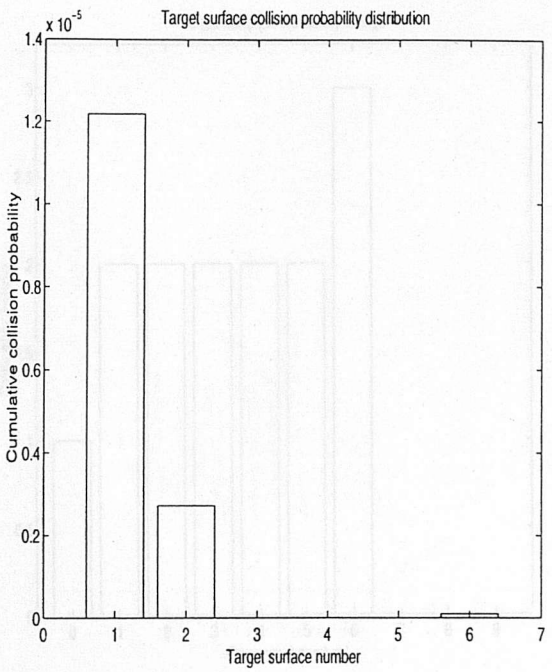

a) Case 1 surface collision probability

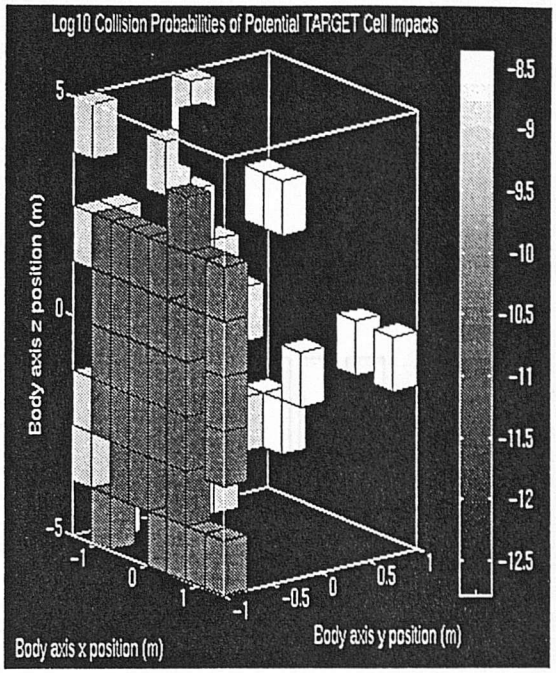

b) Case 1 distribution of debris impacts

Figure 6.20: Case 1 results # 2.

Case 2

Case 2 is identical to Case 1 but the non-isotropic cloud model is employed. The anisotropy of the spread of debris within the cloud produces the jagged collision probability and debris KE curves shown in Figure 6.22. The curves in Figure 6.22 exhibit the same underlying trends as those in Figure 6.19, but the values of collision probability and debris KE are generally around an order of magnitude lower than for Case 1. The use of the non-isotropic cloud model, therefore, not only produces a significant change in the likelihood of an impact occurring, but also affects the lethality of the debris impacts possible.

Figure 6.23 shows that the non-isotropic model has only a minor influence on the distribution of collision risk over the target surfaces. Figure 6.23a shows that a slightly higher proportion of the overall collision risk falls on the Earth face than in Case 1, but the trailing and space faces are still dominant. The spread of possible debris impacts shown in Figure 6.23b is very similar to that in Figure 6.20b.

The component group damage levels predicted for Case 2 are the same as for Case

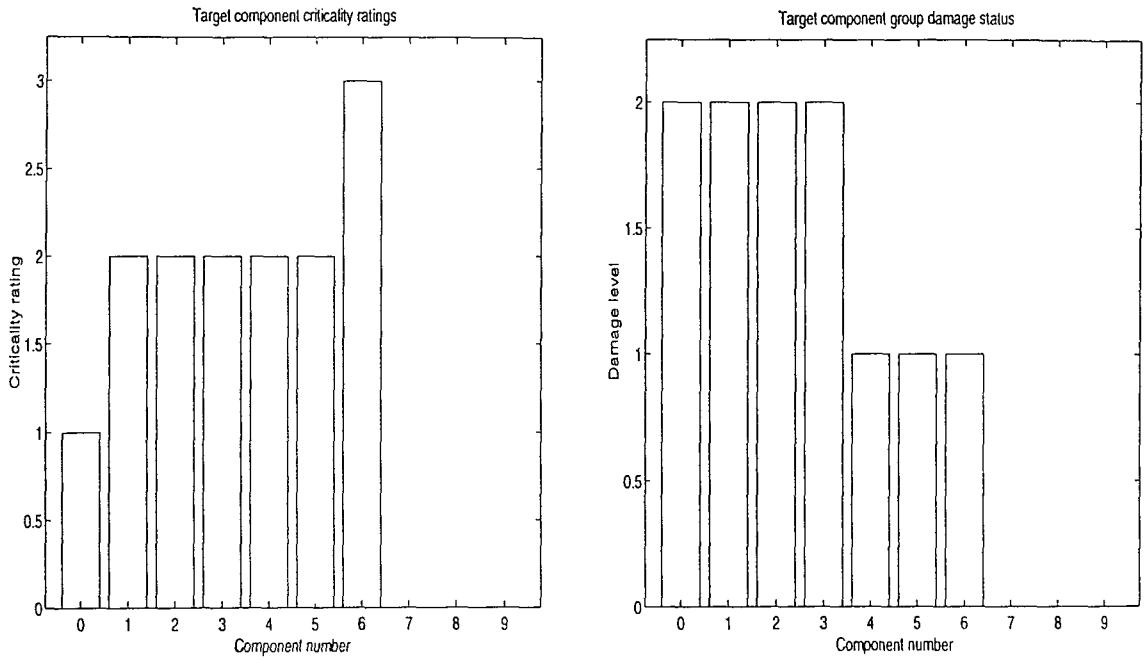

a) Case 1 component criticality ratings

b) Case 1 component group damage levels

Figure 6.21: Case 1 results # 3.

1, with partial damage to payload component groups 1, 2 and 3, and non-critical component group 0. Due to the lower debris KEs predicted in Case 2, however, the actual damage to the target produced would be generally be less than in Case 1, and the level of shielding required to protect against the impacts would be reduced.

Case 3

Case 3 has the fragmentation event in a markedly different orbit to the target, at an inclination of 28.5 degrees compared with 98.7 degrees for ENVISAT-1. The orbits and object positions at breakup are arranged so that the target encounters the debris cloud on its first orbital revolution. The two encounters shown in Figure 6.24a occur around the two orbital nodes and the peaked nature of their collision probabilities corresponds in each case to the passage of the target from the cloud's extremities, through its dense central region and out the other side. Although the relative velocities between the debris and the target are about two orders of magnitude higher than for the first two examples at around 11km/s (due to the orientation of the two orbits), the collision probabilities predicted are generally much lower. This

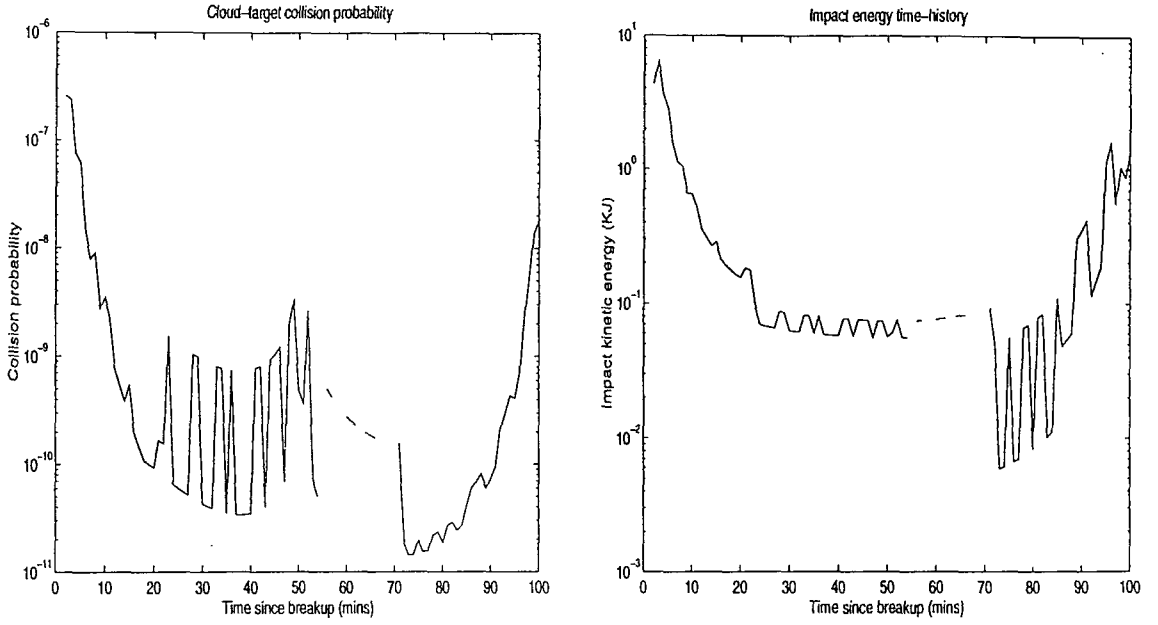

a) Case 2 collision probability

b) Case 2 encountered debris KE

Figure 6.22: Case 2 results # 1.

is because, except near the P_c peaks, the cloud is encountered well away from its centroid and so the densities of debris encountered are several orders of magnitude less than in the first two cases. The distribution of collision probability over the spacecraft surfaces is shown in Figure 6.24b. Here the ram face is dominant. The contributions from surfaces 3 and 5 are a result of the orbital geometry involved. The first encounter carries the highest risk of collision and occurs with ENVISAT-1 passing in a northerly direction through the debris cloud. This produces a debris flux on surface 5, the orbit normal face. Similarly, the second encounter occurs when the target passes through the cloud in a southerly direction and thus the debris flux is incident upon the negative orbit normal face. The collision probability for the second encounter is around an order of magnitude less than the first, however, and so the collision probability for surface 3 is correspondingly lower.

Although no debris impacts are predicted for the main payload face, surface 6, the sizes of debris KEs predicted could have serious implications not only for ENVISAT's payload functions, but for the operation of the spacecraft as a whole. The peak KEs shown in Figure 6.25a are high enough to cause complete target

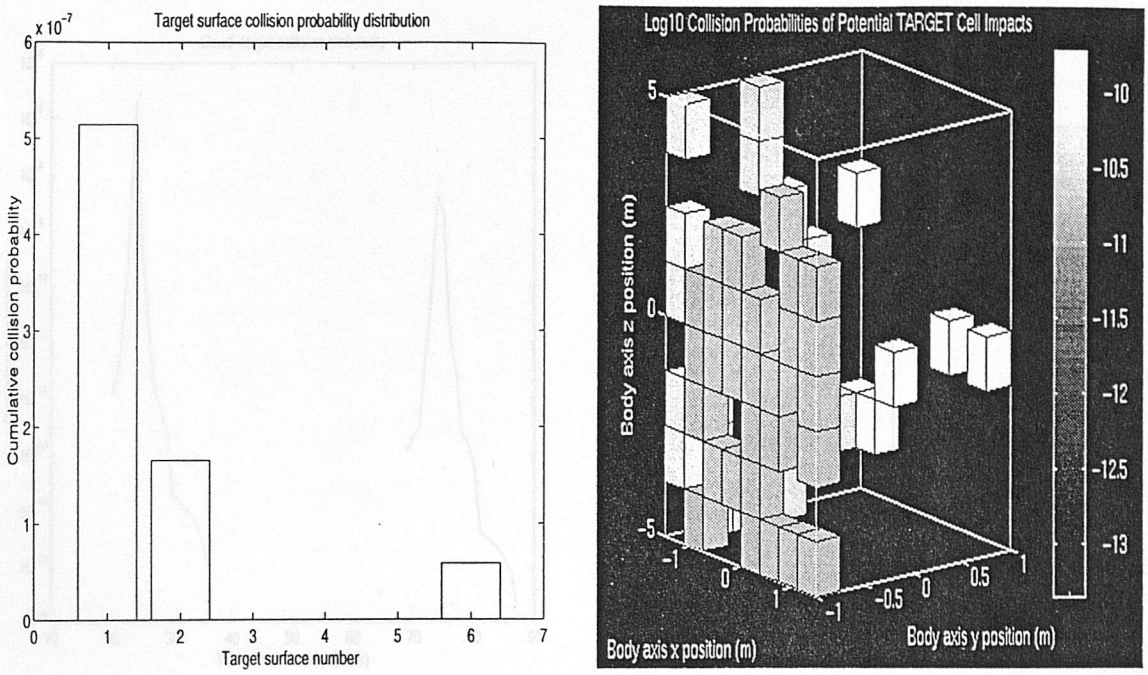

a) Case 2 surface collision probability

b) Case 2 distribution of debris impacts

Figure 6.23: Case 2 results # 2.

fragmentation should an impact occur. All spacecraft systems would, therefore, be destroyed irrespective of placement or protective shielding (Figure 6.25b).

Case 4

Using the non-isotropic debris cloud model with the same scenario as Case 3 has a dramatic effect. Only one time step out of the whole simulation registers a debris encounter. The encounter is predicted after 24 minutes and corresponds to the first peak in the Case 3 collision probability versus time curve Figure 6.24a. The potential impact associated with this encounter is, as in Case 3, of sufficient energy to completely fragment the target. The use of the non-isotropic cloud model, therefore, does not change the effect of the worst possible collision for the scenario in question. It does, however, significantly influence the likelihood of such a collision occurring. In general, cloud-target combinations will have an inclination difference between the orbits of the debris and the target object and so when encounters do occur, the target will pass through the debris cloud as in Case 3, but not necessarily close to

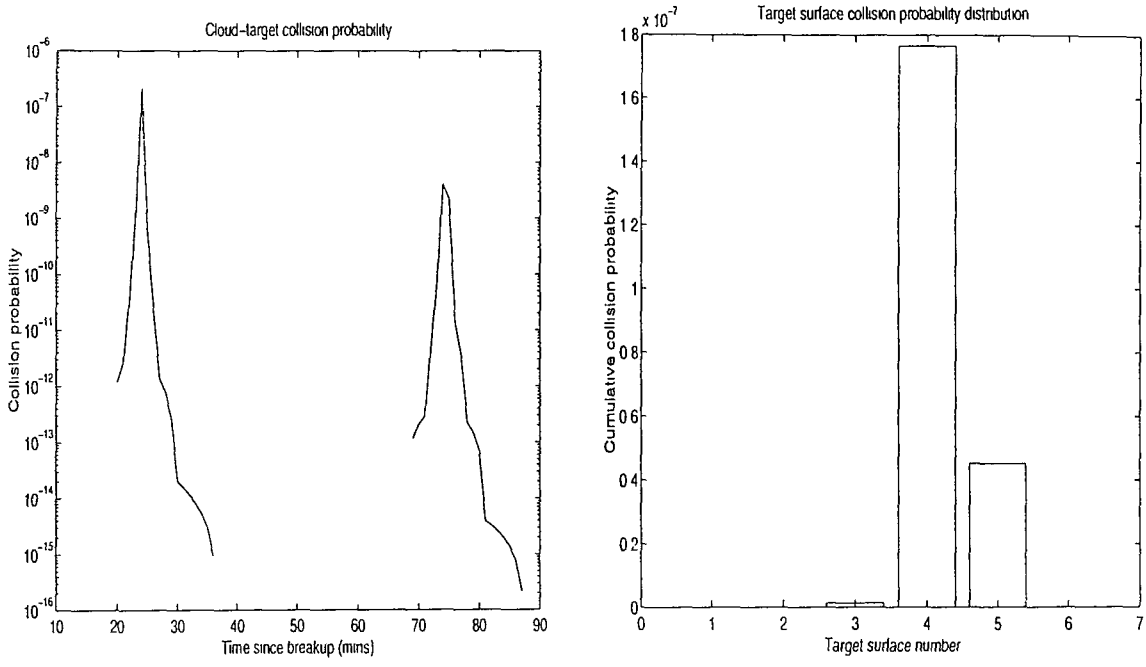

a) Case 3 collision probability

b) Case 3 surface collision probability

Figure 6.24: Case 3 results # 1.

the cloud centroid. During cloud passages, the target will spend the majority of its time in the cloud's outer regions where the density of debris is lowest. In contrast to the isotropic model, regions of space inside the non-isotropic model cloud envelope can be empty, with spread velocity cells containing no debris. Hence simply being inside the cloud's bounding envelope is not sufficient to guarantee a debris encounter. This is particularly true of explosive breakups where relatively few small fast-moving particles are generated. Case 4 highlights this fact and shows that assuming that debris clouds are 'full' of debris out to their extremities can significantly overestimate the danger they pose to spacecraft passing through them. This seems to far outweigh the effects that may be produced by any localised regions of extremely high debris density that the non-isotropic model can conceivably generate.

6.5.5 Summary

The example here shows how the BREAKUP4.0 non-isotropic fragmentation model can be directly interfaced with program TARGET4.0 to enable the effects of debris

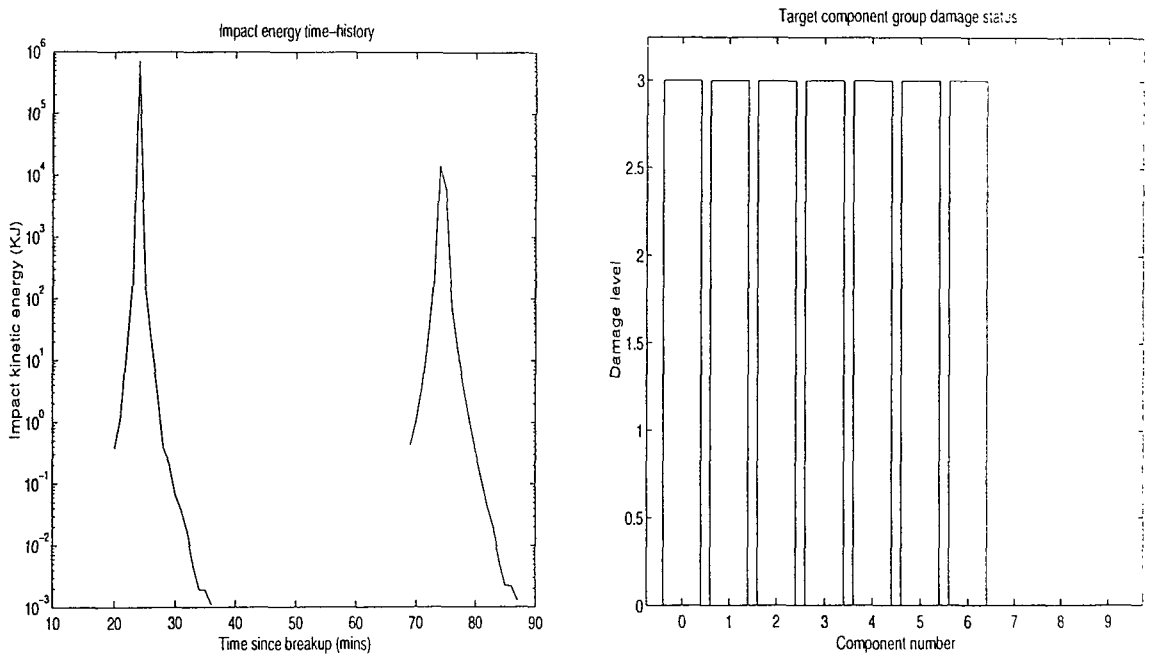

a) Case 3 debris KE

b) Case 3 component group damage levels

Figure 6.25: Case 3 results # 2.

cloud anisotropy on collision hazard analysis to be investigated. Using a model which uses cellular building-blocks to represent the target spacecraft's internal and external component structures, a simple representation of ENVISAT-1 is developed. It is shown how standard information on collision probability can be augmented by a damage assessment algorithm which relates the kinetic energy of the debris encountered to the severity of the potential impact. The test runs performed reveal that the debris cloud model employed can significantly influence the collision risk posed to the target object. Although the collision risks predicted for ENVISAT-1 are low, it is shown that impacts capable of partially disabling or even completely destroying the platform could be experienced. External components are obviously the most at risk from debris impacts. These should be hardened against minor impacts and mounted on low-risk surfaces wherever possible. None of the spacecraft surfaces are completely safe from debris hits, however, and no feasible amount of protective shielding could guard even the spacecraft internal systems against the severest debris impacts.

6.5.5 Satellite Constellations

Introduction

The possibility of a cascade fragmentation occurring within the general on-orbit population has been the subject of considerable research. Proposals for constellations of large numbers of satellites present an alternate problem. The breakup of a constellation member satellite, or launch vehicle, could result in a cascade fragmentation occurring within the framework of the constellation itself. As well as having a disastrous effect with regard to the operation of the constellation, such a breakup chain reaction would have a severe pollutive impact on the orbital environment as a whole and would increase the likelihood of a cascade fragmentation occurring within the general population. Two constellation examples are examined here, Motorola's proposed Iridium^{TM} constellation and the Calling Teledesic concept, both of which are intended for mobile cellular telephone voice and data traffic. TARGET3.0 was used for the Iridium^{TM} investigation, which has also appeared in [108]. The Teledesic analysis was conducted using TARGET4.0 and appeared in [110].

The Iridium^{TM} constellation

The original Iridium^{TM} concept [117] consisted of seventy-seven 340kg satellites in 780km circular polar orbits, evenly distributed and optimally phased in 7 orbital planes according to the phasing strategy developed in [115]. Minor adjustments were made to the orbital inclinations (to slightly less than 90^o) and the plane-to-plane phasing to simplify station-keeping and reduce the satellite collision hazard near the poles. The current configuration contains a reduced number of larger satellites. Sixty-six 689kg satellites are distributed among 6 orbital planes at 765km altitude [118, 119]. The revised constellation configuration is depicted in Figure 6.26. To maintain the same quality of ground coverage across the whole constellation, the angular separation between the planes either side of the counter-rotating interface (between planes 1 and 6) is made less than that between the other orbital planes [115].

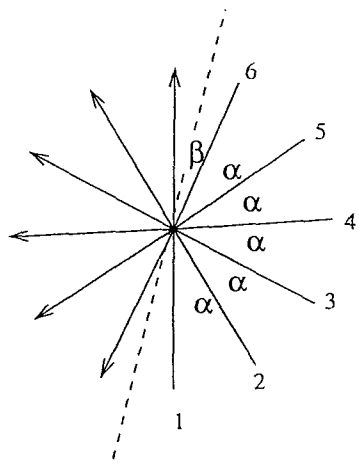

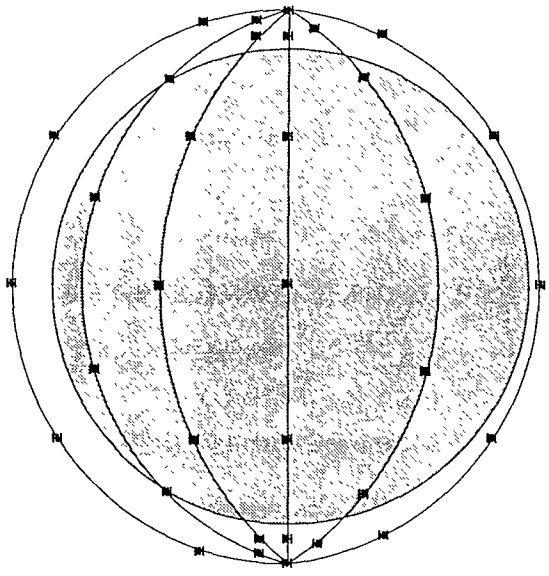

'Plan' View : Planar orientation
α = 31.4 deg.
β = 23.0 deg.

'Front' View : Six orbital planes with eleven satellites in each orbital plane

Figure 6.26: The Iridium^{TM} constellation.

Iridium^{TM} is due for completion in 1998 and Motorola has laudably included debris mitigation as a major design-driver from the outset. The multiple Proton and Delta-2 launches that will be used to form the constellation should be devoid of operational debris and initial parking orbits (460km circular) will be utilised with the satellites boosting themselves up to operational altitude after separation. The rocket second stages will be de-orbited after use and vented of residual propellant/oxidiser to prevent explosion. A similar procedure will be adopted for the constellation satellites at the end of their operational lifetimes. The batteries used on-board the satellites have also been designed with the aim of eliminating the possibility of explosion.

Launch vehicle breakup

If the Delta-2/Proton second stages are successfully made 'safe' as intended after satellite release then the risk they pose to the constellation members in place is indeed negligible. If, however, a system malfunction occurs which prevents the de-

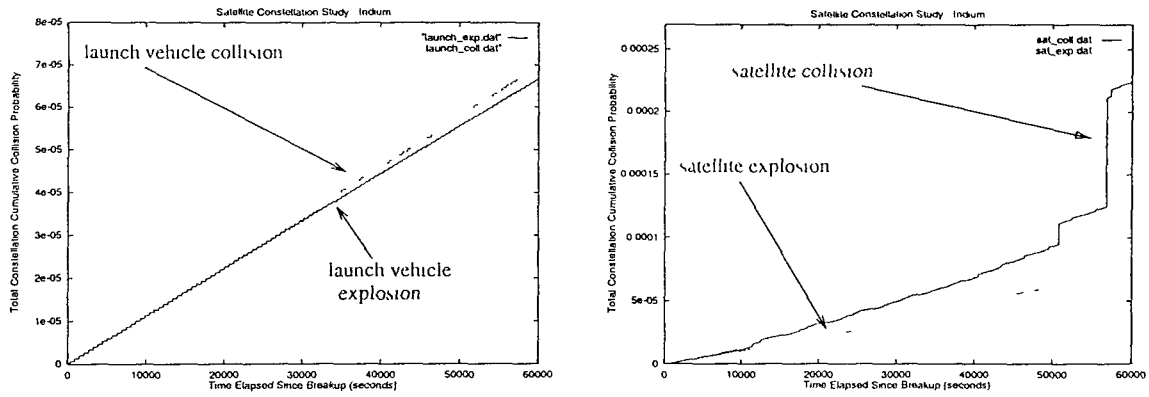

(a) Launch vehicle breakup

(b) Constellation satellite breakup

Figure 6.27: Constellation-threatening breakup scenarios.

orbiting manoeuvre from being executed, the presence of the rocket body could heighten the debris risk to the constellation. If debris were to collide with the second stage causing it to fragment, or if it were to explode, then the cloud of debris formed could impinge upon the constellation altitude. These two scenarios are modelled here.

The effects on the constellation of the fragmentation of a 900kg Delta-2 rocket body are examined. The rocket body is assumed to be in a circular parking orbit of 460km with its inclination and ascending node position both equal to that of one of the constellation planes. The constellation is assumed to be complete and a collision cross-sectional area of $10m^2$ is used for each satellite. The two rocket body fragmentation scenarios are simulated using program BREAKUP. A minimum fragment mass of 1gram is selected. This limit is taken to represent the satellites' shielding capability.

The constellation cumulative collision probability curves for both cases are shown in Figure 6.27a. The two breakup events produce very different collections of fragments but neither have any significant effect on the collision risk posed to the constellation. In the case of the explosion, the debris densities are extremely low which in turn is reflected in the values of collision probability registered. For the collision-induced breakup, the spread velocities associated with the largest fragments are extremely small and so only a few cloud-target encounters occur and those that do

are generally short-lived and at low relative velocities. The steady increase in collision probability observed is due almost entirely to the 'background' environment. The effects that the debris clouds have above this background level are barely noticeable.

Fragmentation of a constellation satellite

Active debris control, particularly with regard to battery design and end-of-life deorbit, should significantly reduce the chances of a breakup of one of the constellation satellites. The possibility of an explosive breakup will still exist, however, even if it is extremely remote. Perhaps the greatest risk comes from a collision with debris from the background population. Shielding can be employed to guard against small particles but a collision with a large piece of debris could cause a satellite to completely fragment. Again both scenarios are modelled here with the satellite fragmentations simulated using BREAKUP.

The collision probability curves for the two scenarios are shown in Figure 6.27b. The explosion curve is virtually equal again to that of the background environment, with several noticeable 'step' increases due to encounters with the highly-populated inner regions of the debris cloud. Due to these high-risk encounters, the cumulative collision probability for the remaining 65 satellites of the constellation is around 10% higher than the background level. The time period considered corresponds to 10 complete orbits of the remaining members post-breakup. The higher values of debris density found in the debris cloud produced by the collision event cause this to have a higher risk associated with it. The collision curve is noticeably steeper than the background, with two particularly high-risk encounters occurring which produce large step jumps. At the end of 10 satellite orbits, the collision curve reaches a cumulative collision probability approximately 3.5 times greater than the background.

The Teledesic constellation

The Teledesic constellation concept consists of over 800 satellites in LEO. This is over an order of magnitude more than for Iridium™. To investigate whether this dramatic increase in constellation size could lead to instability following a fragmentation, the collision-induced breakup of one of the constellation satellites is simulated. The Teledesic configuration is modelled as 800 satellites, with 80 satellites in each of 10 equally-spaced orbital planes. Each 500kg satellite is in a 700km near-circular polar orbit. Program BREAKUP4.0 is used to model the fragmentation, with debris 1mm in size and greater being considered. TARGET4.0 is used to assess the collision risk to the remainder of the constellation. The simulation is performed for 12 hours post-breakup with a time step of 1 minute. Propagation method 5 is employed to incorporate the effects of secular J_2 into the analysis. The values of collision probability quoted are per square metre of target.

Figures 6.28 and 6.29 show the collision risk calculated for the constellation distributed over time and satellite number. The collision probability time-history is obtained by summing the contributions from all the satellites during that time step. Similarly, the distribution made over satellite number is obtained by summing, for each satellite in turn, the collision probabilities registered over the duration of the simulation. Satellite number increases with true anomaly at the time of the breakup and orbit plane number. For example, satellites 1-80 reside in the plane of the breakup (satellite 1 being the breakup satellite, and plane 1 being the breakup plane), satellites 81-160 in the 'next' orbit plane (plane 2, 18^o in right ascension East of the breakup plane), and so on. Satellites with numbers 80 apart are hence the closest to being in phase.

Figure 6.28a shows the constellation collision probability versus time curve. The high-risk encounters denoted by large step increases on the curve cause the cumulative collision probability at the end of the simulation to be several times that of the background level. Figure 6.28b shows the distribution of collision probability over satellite number. The satellites in the breakup plane experience a significantly

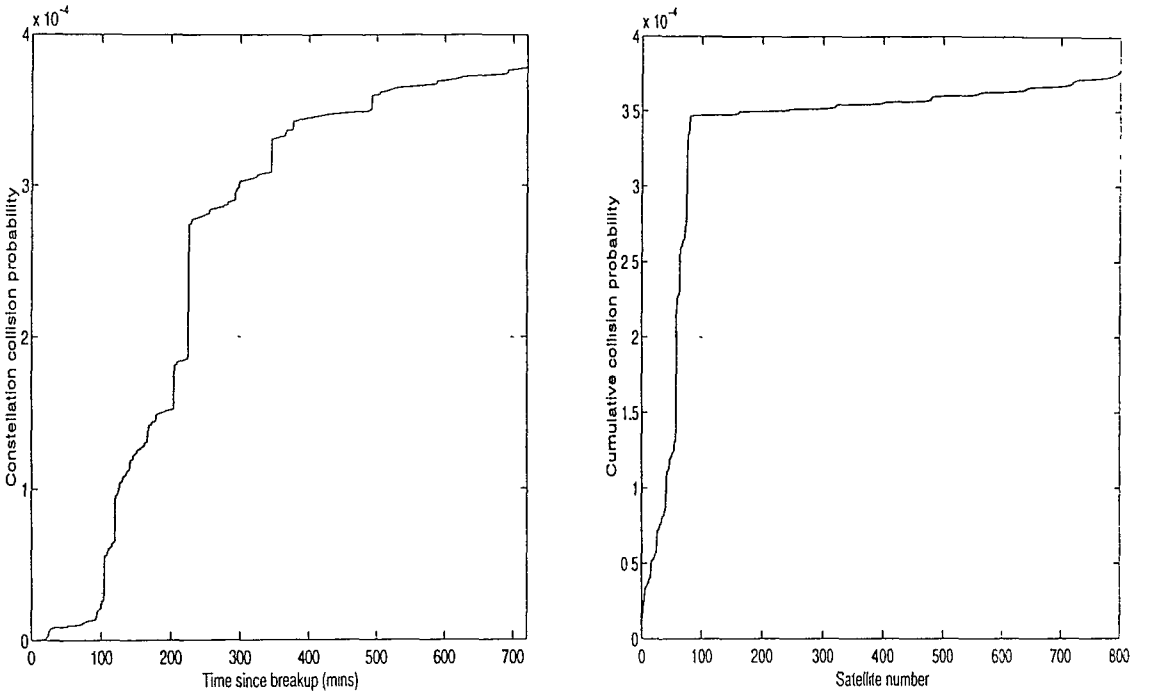

a) Constellation collision probability vs time

b) Constellation collision probability distributed over satellite number

Figure 6.28: Constellation collision probability.

higher risk of collision than the remainder of the constellation. This is due to the high values of debris density encountered by the breakup plane satellites, particularly close to the cloud's pinch locations. Although the risk of a collision is highest for satellites in the breakup plane, the risk of a damaging, or indeed catastrophic collision, is virtually negligible. This is because in the breakup plane, debris encounters predominantly occur at very low relative velocities. The inclusion of J_2 effects in the analysis does produce higher relative velocities than would be predicted by solution of the unperturbed problem, however, as out-of-plane encounters are made possible for the breakup plane satellites. This increases the breakup plane collision probabilities considerably. In the other constellation planes, debris encounters occur at much higher (typically orders of magnitude) relative velocities, as dictated by the planar geometry of the object orbits. The highest encounter velocities occur then in constellation plane 10, with such head-on encounters occurring at nearly twice orbital velocity. Figure 6.29 gives an indication of how dangerous a potential collision would be. ζ, the debris impact energy to target mass (DIE/TMASS) ratio,

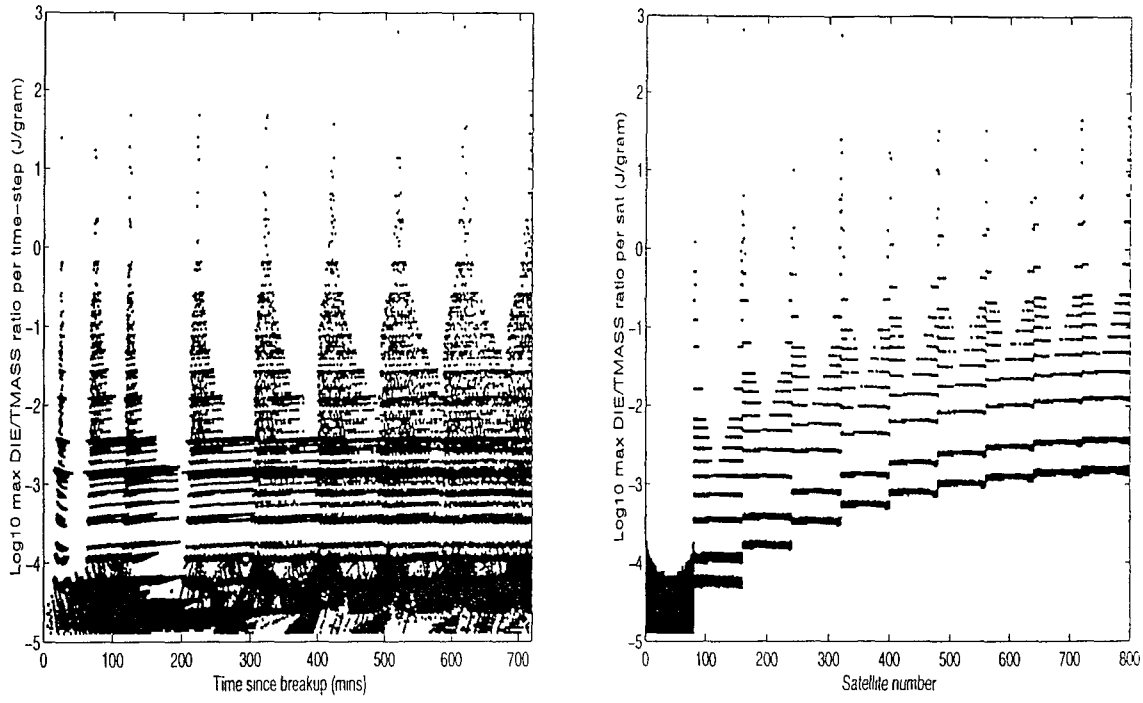

a) Time-history of potential collision damage

b) Distribution of potential collision damge over satellite number

Figure 6.29: Assessment of potential collision damage.

is again used to provide a measure of the lethality of the potential collisions. Even in the relatively short simulation described here, several values way in excess of the catastrophic threshold of 40 J/gram are predicted. This shows that the possibility of a secondary breakup cannot be completely discounted.

Discussion

The satellites in the constellation that are most likely to 'get hit' following the fragmentation of one of the constellation members are those in the plane of the breakup. The satellites most likely to be seriously damaged or even destroyed by a debris impact are those in the other orbit planes, typically those in the planes with the highest angular (i.e. right ascension) separation from the breakup plane (therefore giving highest relative velocities) and those closest to being in-phase with the breakup satellite (most likely to encounter high-density cloud regions). Although the probabilities of such dangerous collisions occurring are low, 'lethal' impacts are

possible.

There are no simple rules that can be applied to the constellation problem. Each constellation configuration and breakup scenario must be treated individually. Large constellations cannot be modelled by using smaller constellations and simply 'scaling up'. The location of the breakup not only affects which satellites in the constellation are most at risk, but also the levels of collision risk experienced. The cause of the breakup (i.e. collision-induced or explosion), and indeed how it is modelled, also influence significantly the danger to the remainder of the constellation. For example, a collision-induced breakup will produce much higher values of collision probability than an explosion due to the enormous number of small fragments generated, but the explosion will tend to produce more large fragments and hence may pose a greater risk in terms of a potentially damaging encounter.

Two specific constellations have been used as examples here. If the parameters that describe a constellation are varied, then the collision risk to the constellation following a breakup will be affected. The constellation design parameters (e.g. altitude, configuration, satellite specification) are primarily chosen to comply with the constellation's operational requirements. These parameters, however, can have important implications on the constellation's susceptibility to collision from orbital debris. If the number of satellites is increased then the risk to the system as a whole will also rise, as it will with the mass and/or size of the individual satellites. The configuration of the constellation (number of orbital planes, relative orientation/inclination of orbital planes, satellite phasing) and the constellation altitude also affect the debris risk to the system. An improvement in the satellites' shielding capability will reduce the risk to each individual satellite, and hence to the whole constellation.

Summary

The threat to a satellite constellation following the breakup of either a member satellite or a constellation launch vehicle has been examined. It has been found that the greatest threat to the constellation comes from a collision-induced breakup

of one of the satellites. Such an event would give rise to a significant increase in the debris collision probability for the constellation in the short-term. In the long-term, the likelihood of a cascade fragmentation occurring within the constellation is remote. Secondary fragmentations are a real possibility, however. With the large LEO constellations now being proposed and aggressive debris mitigation practices still being the exception rather than the rule, satellite constellations could well provide a significant pollutive threat to the orbital environment in the years to come.

6.6 TARGET Results Validation

6.6.1 Cloud-Target Encounter Detection

The cloud-encounter detection mechanism of TARGET can be illustrated, and at the same time validated, by viewing graphically the positions of the cloud and target at the time of a predicted encounter. A simple test case is employed here in which the target satellite encounters the debris cloud during its first orbital revolution post-breakup. The debris cloud from section 6.5.2 is used and ENVISAT-1 is again adopted as the target satellite.

Figure 6.30 shows the collision probability spike caused by the passage of ENVISAT-1 through the debris cloud. The collision probabilities registered during the encounter are over two orders of magnitude above the background level shown. The collision probability level falls during the course of the encounter due to the cloud's expansion over that time period. Figure 6.31 shows the positions of the PPF (represented by +) and the cloud immediately before, during and just after the encounter. The time-step (i.e. the number of target orbits described post-breakup) that each plot corresponds to is shown in the top right-hand corner of the plot window and the large circle shown in each case depicts the Earth. Propagation method 4 is used to evolve the fragment and target orbits. The collision probability spike in Figure 6.30 can be seen to correspond to the passage of the PPF through the cloud viewed graphically in Figure 6.31. For the target to be deemed truly inside the cloud, all

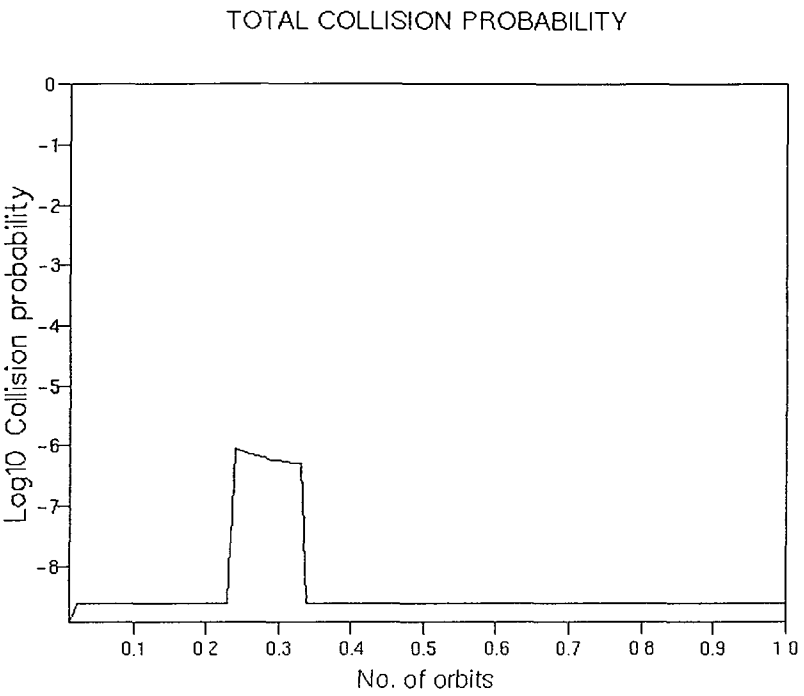

Figure 6.30: Collision probability spike caused by cloud encounter.

three planar views must show the target within the projected cloud shape. The corresponding X-Y and X-Z views can be shown to support Figure 6.31 in this case (Figure 6.32). In contrast, the evidence of just one planar view is sufficient for the object to be deemed outside the cloud.

6.6.2 State Transition Matrix Calculation

Accurate calculation of debris density is paramount to the acquisition of good quality estimates of collision probability. Once the image of the target position inside spread velocity space is determined, via the solution of the breakup location to target position transfer orbit, the calculation of debris density at the target position and epoch is reliant upon the calculation of the state transition matrix determinant. This, then, is a vital part of the overall collision probability calculation algorithm. The numerical technique employed by TARGET4.0 (and described in section 6.2.2) is compared here to the linearised analytical method developed by Ashenberg [120]. Ashenberg incorporates the effects J_2 and atmospheric drag directly into the lin-

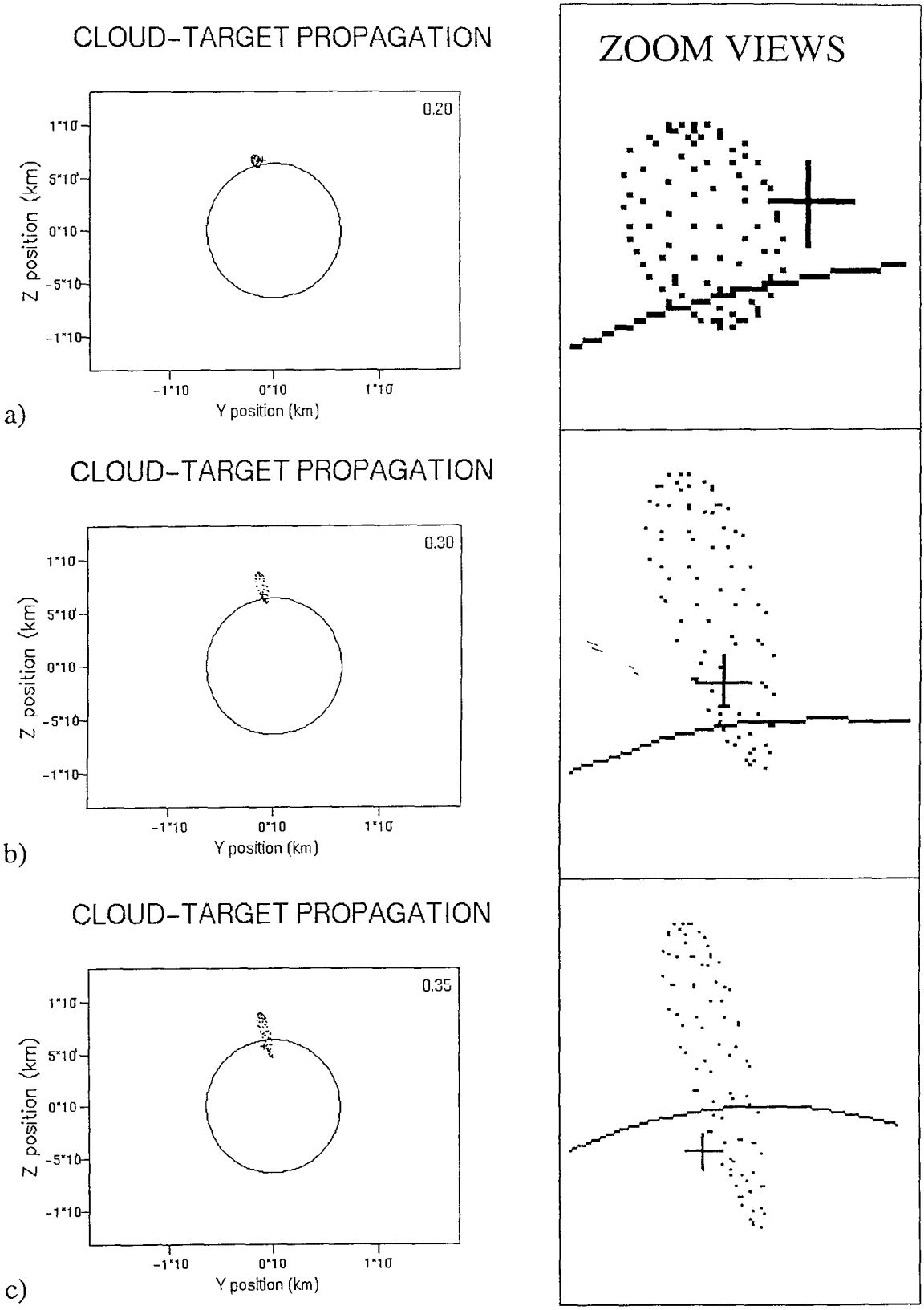

Figure 6.31: Cloud and target positions immediately before (a), during (b) and just after (c) the encounter

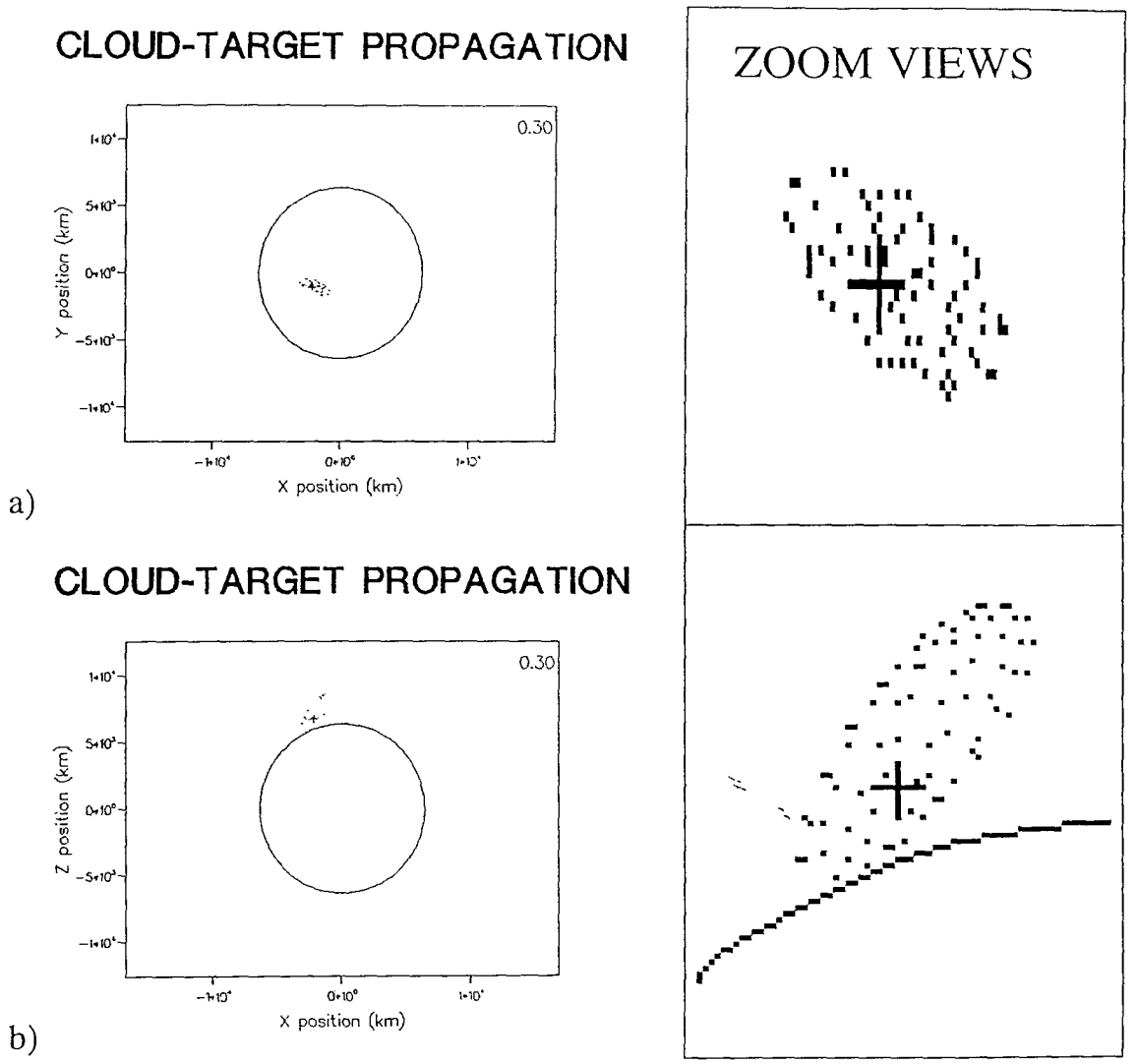

Figure 6.32: Cloud and target positions during the encounter

earised inertial frame state transition matrix, and uses the formulation developed to produce estimates of debris cloud volume. This is achieved by evaluating the state transition matrix at the breakup CM position and multiplying the state transition matrix determinant by the volume of spread velocity space (see section 2.2.7).

A numerical example in Ashenberg [120] is used to illustrate the analytical method developed. A volume versus time curve is generated for a debris cloud produced by a breakup in low Earth orbit. TARGET4.0 is used to simulate the example and to compare the two different methods of state transition matrix calculation. Figure 6.33 shows the results produced by the analytical model and TARGET4.0

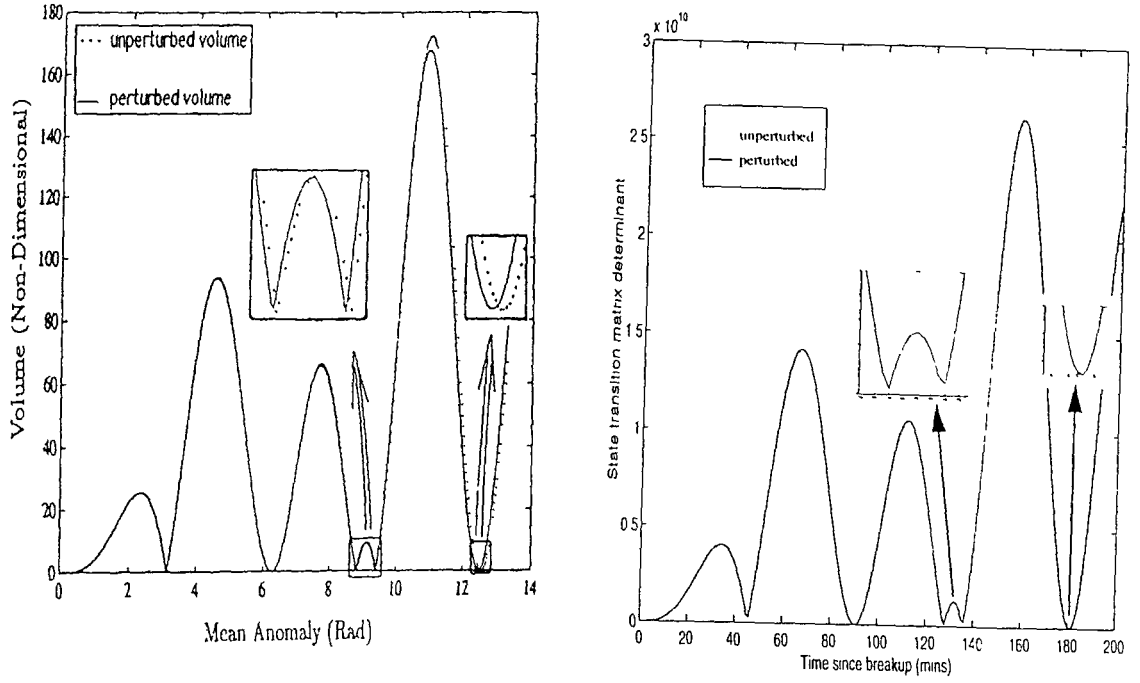

a) Ashenberg model

b) TARGET4 0 simulation

Figure 6.33: Cloud volume and state transition matrix curves.

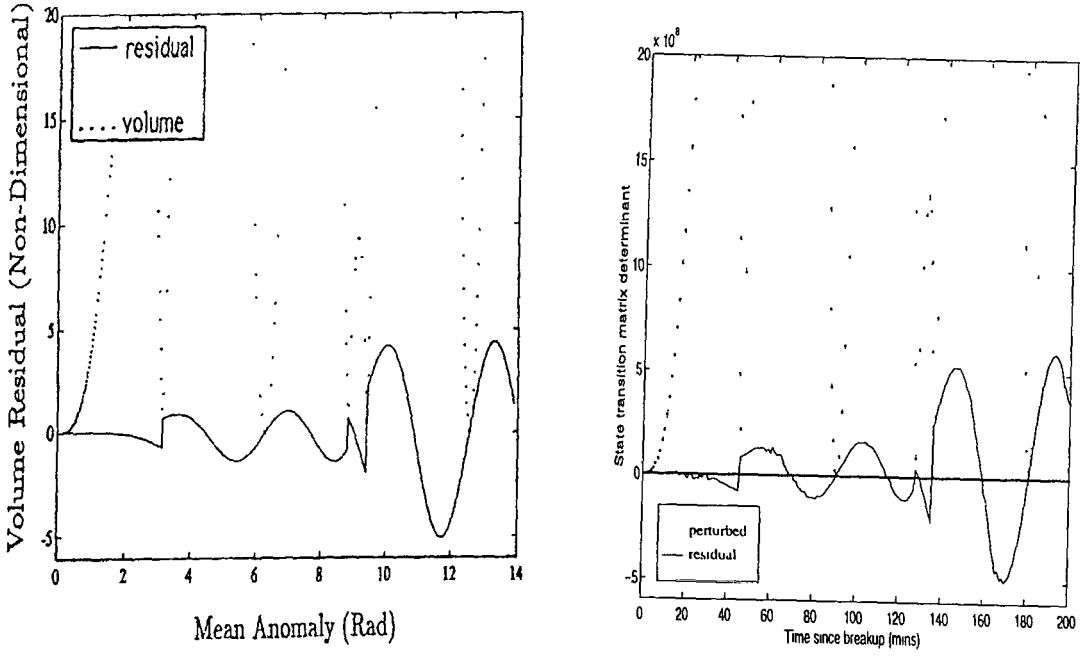

a) Ashenberg model

b) TARGET4.0 simulation

Figure 6.34: Perturbed residuals.

side-by-side, for unperturbed and perturbed orbital motion. The axes on the two plots are different but as cloud volume is directly proportional to the state transition matrix determinant and mean anomaly is directly proportional to time, the shapes and relative scalings of the two sets of curves can be compared directly. The match is extremely good with the lack of smoothness of the TARGET4.0 curves providing the only real difference between the two methods. The volume of the cloud exhibits a complex pulsating behaviour, with an underlying increasing trend but collapsing to zero at the cloud's pinch locations. The third volume trough, just before the second half-revolution pinch location, is caused by the cloud's first non-stationary pinch zone [74]. Atmospheric drag causes a slight decrease in cloud volume and also gives the pinch locations a time-shift forward as the debris orbital periods are reduced. Figure 6.34 shows perturbed volume residuals, i.e. the difference between the unperturbed and perturbed curves. Again the general matching of the Ashenberg and TARGET4.0 curves is excellent, given the inevitable noise associated with the TARGET4.0 numerical method.

6.6.3 Comparisons with Program DEBRIS

Introduction

In Chapter 5, the output from EVOLUTION3.0 was validated in part by the comparison of results with a similar model. The same approach is adopted here, and once again simulation codes developed by The Aerospace Corporation are used as benchmarks for comparison. The estimation of collision probabilities for an object passing through a debris cloud is a problem for which comparison with 'real' data is virtually impossible. Hence the comparison of results between different but similar models provides the only real opportunity to directly validate the predictions of collision hazard analyses. The dearth of suitable flight data to match against means that such comparisons can only provide a mutual, simulation, validation. Different models may be shown to be in good agreement but how realistic the models actually are is far more difficult to ascertain.

The Aerospace Corporation's programs IMPACT and DEBRIS are in essence

equivalent models to BREAKUP and TARGET, developed completely independently and using different but similar approaches, but ultimately addressing the same problems. Two comparison studies are presented here in which BREAKUP and TARGET are used to mimic case studies carried out using IMPACT and DEBRIS. The first comparison considers two simple cloud-target scenarios deliberately engineered to test and illustrate the operational capabilities of the Aerospace Corporation codes. The second study is far more interesting because it considers an actual fragmentation event and the ensuing collision risk to manned spacecraft on-orbit at the time of the event.

Comparison # 1

Introduction

Jenkin [71] contains two numerical examples to illustrate the performance of DEBRIS3.1. These examples are used to compare the output from DEBRIS3.1 and TARGET3.1. Note that the equal program version numbers are purely a coincidence. Two runs of TARGET3.1 are made for each case, one using BREAKUP3.0 to simulate the fragmentation event described and the other using pseudo-IMPACT3.0 input. BREAKUP3.0 and IMPACT3.0 were the fragmentation model versions for TARGET3.1 and DEBRIS3.1 respectively. BREAKUP3.0 used the same fragment distribution models as BREAKUP4.0, but could only produce isotropic debris clouds. The pseudo-IMPACT3.0 input is obtained by sampling the two IMPACT3.0 fragment distribution curves that are included in [71] and converting the data obtained into the correct format for input to TARGET3.1. The use of what is effectively a common breakup model enables the results produced by DEBRIS3.1 and TARGET3.1 to be compared directly. The runs which use a different fragmentation model allow the effects of the fragmentation model to be observed. This software comparison has also appeared in [109].

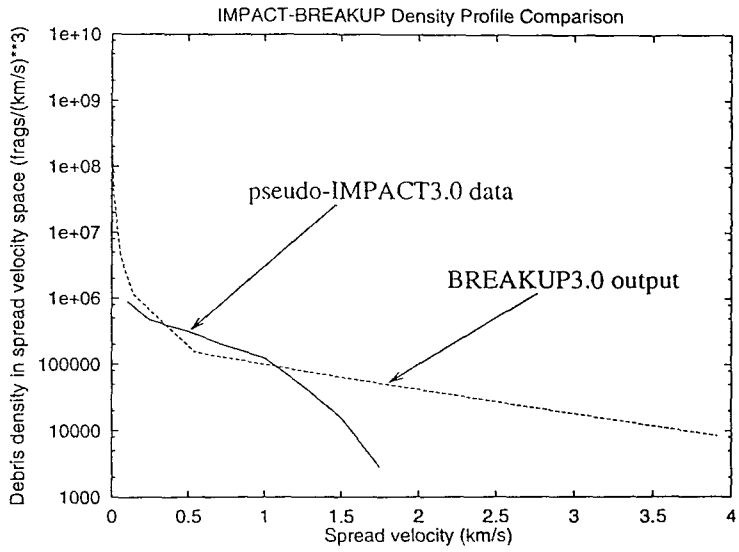

Figure 6.35: IMPACT3.0-BREAKUP3.0 comparison.

Modelling of the fragmentation event

For both the target scenarios that follow, the debris cloud is formed from a catastrophic hypervelocity collision between a 1kg fragment in a 97° inclined circular orbit and a 1200kg satellite in a 28.5° inclined circular orbit. The collision occurs at the ascending node of the destroyed satellite and the altitude for both satellites is 400km. The 1kg fragment is characteristic of a number of debris fragments that may have resulted from booster upper stage explosions in sun-synchronous orbit.

Figure 6.35 shows the fragment density versus spread velocity profiles predicted for the event by IMPACT3.0 and BREAKUP3.0. The IMPACT3.0 curve is created from pseudo-data sampled from Figure 9 in [71] and so is not to be taken as being precise. The major differences between the two curves occur at their extremities. At both the low and high spread velocity ends of the curves, BREAKUP3.0 predicts much higher (by orders of magnitude) debris densities. These significant discrepancies are primarily a function of the range of fragments considered. IMPACT3.0 models fragments in the mass range $1x10^{-6}$kg to $1x10^{-2}$kg, i.e. 4 orders of magnitude in mass. This mass range of fragments corresponds to a variation of less than 2 orders of magnitude in fragment size (approximately 0.4mm to 25.0mm). BREAKUP3.0 considers a size range of fragments spanning 4 orders of magnitude

(0.1mm to 1000.0mm). This large difference in the range of fragments modelled, along with the use of different velocity models and approaches to fragment distribution binning, cause the differences in the outputs of the two programs observed. At the low spread velocity end, the very small spread velocities predicted for the large fragments considered by BREAKUP3.0 cause the spatial densities close to the cloud centroid to be extremely high, even though the actual number of fragments located there is relatively small. At the high spread velocity end, the smaller fragments modelled by BREAKUP3.0 cause the debris cloud to be much larger than that predicted by IMPACT3.0 and, due to the sheer number of small particles predicted, much more dense in its outer regions. As the probability of collision for an object passing through a debris cloud is proportional to the density of fragments it encounters (which, in turn is determined from the breakup model), large differences in the values of debris density predicted by the fragmentation model will propagate themselves through the subsequent analysis and result in significant discrepancies in the values of collision probability calculated. In the following two examples, this is shown to be the case.

Case 1

Case 1 from [71] corresponds to a situation where the target is co-orbital with the breakup satellite but is located 12^o ahead of the destroyed satellite at the time of the breakup. Figures 6.36 and 6.37 show the debris density encountered by the target during the first 100 minutes after the breakup, as predicted by DEBRIS3.1 and TARGET3.1 respectively. From Figure 6.36 and the run of TARGET3.1 with pseudo-IMPACT3.0 in Figure 6.37, the target is seen to first enter the cloud after approximately 13 minutes but then, due to the ballistic re-entry of fragments from the cloud's leading edge, it abruptly leaves the cloud again and does not re-enter it until around 62 minutes has elapsed. It can be seen that during this encounter, in which the target passes close to the cloud's first whole-revolution pinch point, the debris density varies by nearly four orders of magnitude. The matching of results between the DEBRIS3.1 simulation and the TARGET3.1 run with pseudo-IMPACT

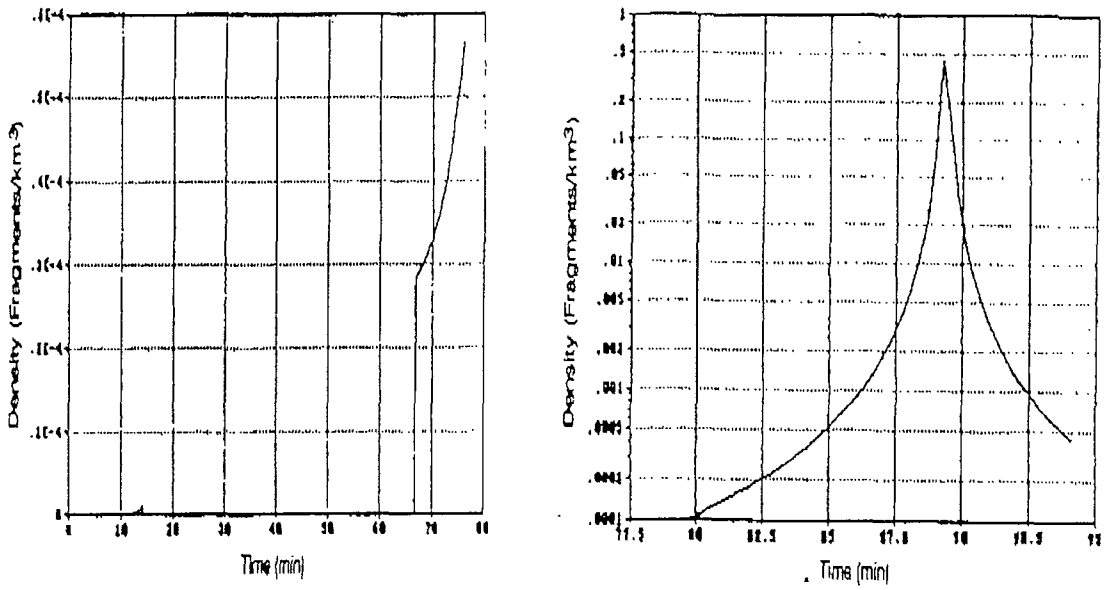

a) Fragment density during first 76 minutes

b) Fragment density during pinch point encounter

Figure 6.36: Case 1 : Fragment density encountered by target during first 100 minutes after breakup, DEBRIS3.1 simulation

input is excellent. The TARGET3.1 run with BREAKUP3.0 input produces a noticeable increase in the values of debris density encountered and also causes the first cloud-target encounter to have a much greater significance. The higher spread velocities and debris densities predicted by BREAKUP3.0 mean that the encounter lasts longer, is split into two parts and has a much higher risk associated with it.

Case 2

Case 2 from [71] involves the same debris cloud as Case 1 but this time the target is moving in a 97° inclined orbit at the same altitude as the destroyed satellite. The right ascension of the ascending node of the target orbit is 90° East of that of the destroyed satellite and the argument of latitude of the target is -56.5° at the time of the breakup. This arrangement has the target passing through the debris cloud twice during the first orbital revolution post-breakup. This can be seen from the debris density time-histories in Figure 6.38. The debris density is lower during the second encounter because the cloud is spreading out. The maximum debris densities experienced by the target are much lower than at the pinch point in Case 1, even

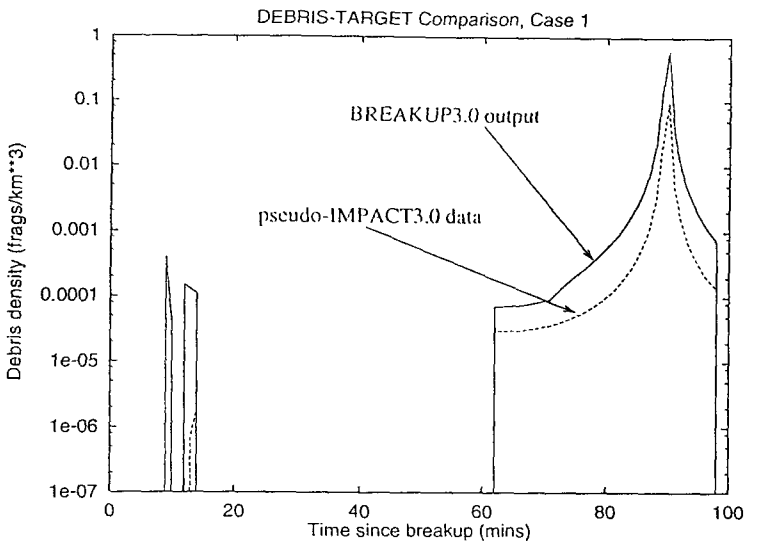

Figure 6.37: Case 1 : Fragment density encountered by target during first 100 minutes after breakup, TARGET3.1 simulation

though it passes though the cloud close to its centroid. The lower debris densities are offset, however, by higher encounter velocities. The matching of results between the equivalent DEBRIS3.1 and TARGET3.1 simulation is very good once again. As in case 1, the use of BREAKUP3.0 to model the fragmentation event is shown to produce longer higher-risk cloud-target encounters.

Figures 6.39-6.41 show the distribution of collision probability as a function of encounter velocity magnitude, azimuth angle and elevation angle. The TARGET3.1 results are generated using pseudo-IMPACT3.0 input and again are observed to be in good agreement with the DEBRIS3.1 predictions. Figure 6.39a is almost symmetrical, corresponding to the symmetrical nature of the debris flux encountered as the target passes through the debris cloud. The encounter velocities are very high and are primarily dependent upon the orientation of the cloud and target orbit planes. The empty velocity bins in Figure 6.39b can be attributed to the larger simulation step size used by TARGET3.1 compared with DEBRIS3.1. This produces fewer data points and hence fewer calculated encounter velocities. Figure 6.40 shows that the in-plane encounter direction is distributed around the satellite orbital velocity vector, i.e. the fragments are coming 'head-on'. The out-of-plane encounter direction, shown in Figure 6.41, is concentrated in two regions that are symmetric about

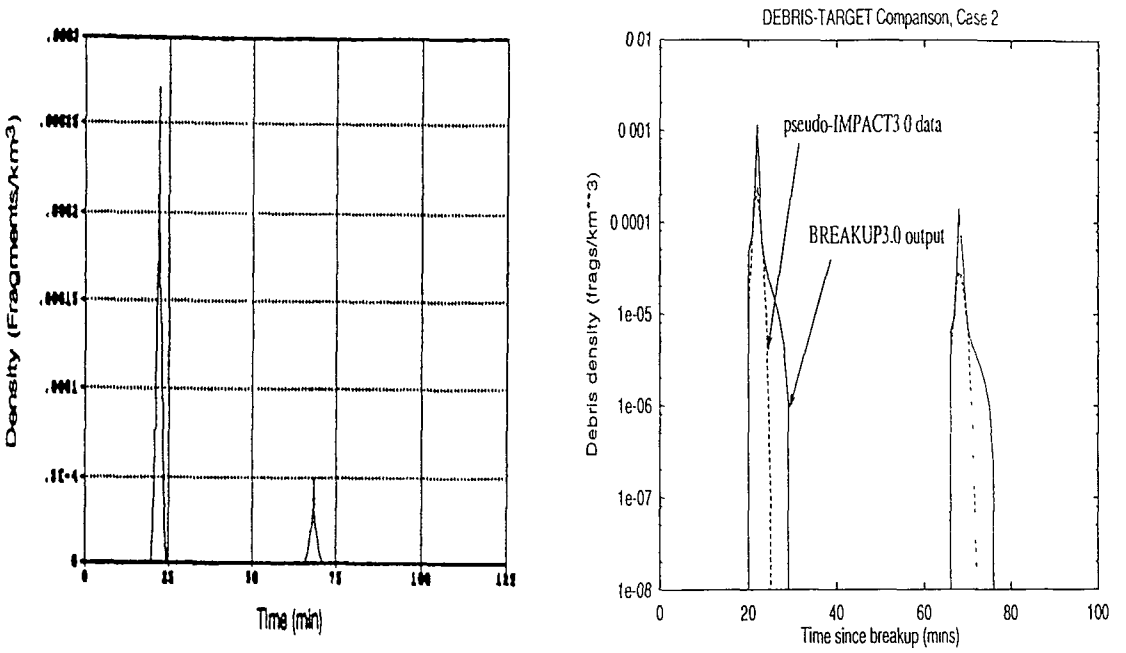

a) DEBRIS3.1 simulation

b) TARGET3.1 simulation

Figure 6.38: Case 2 : Fragment density encountered by target during first 100 minutes after breakup.

the satellite orbital velocity vector. This again is directly attributable to the angles between the two orbits at their points of intersection.

Discussion

The matching between the results of DEBRIS3.1 from [71] and those reproduced by TARGET3.1 is very good for the two cases examined. Noticeable differences are observed, however, when they are run using their respective fragmentation models. Runs of TARGET3.1 with BREAKUP3.0 input predict significantly (factors to orders of magnitude) greater risks of collision than those which use pseudo-IMPACT3.0 data. This is a direct consequence of the larger and denser cloud predicted by BREAKUP3.0. The re-entry of fragments from the leading portions of both (i.e. pseudo-IMPACT3.0 and BREAKUP3.0) debris clouds caused the cloud entry-exit behaviour observed in both the examples. If the altitudes had been higher in each case (hence no fragment re-entry over the time period considered) then the larger BREAKUP3.0 cloud would have been entered first and exited last, as one might have

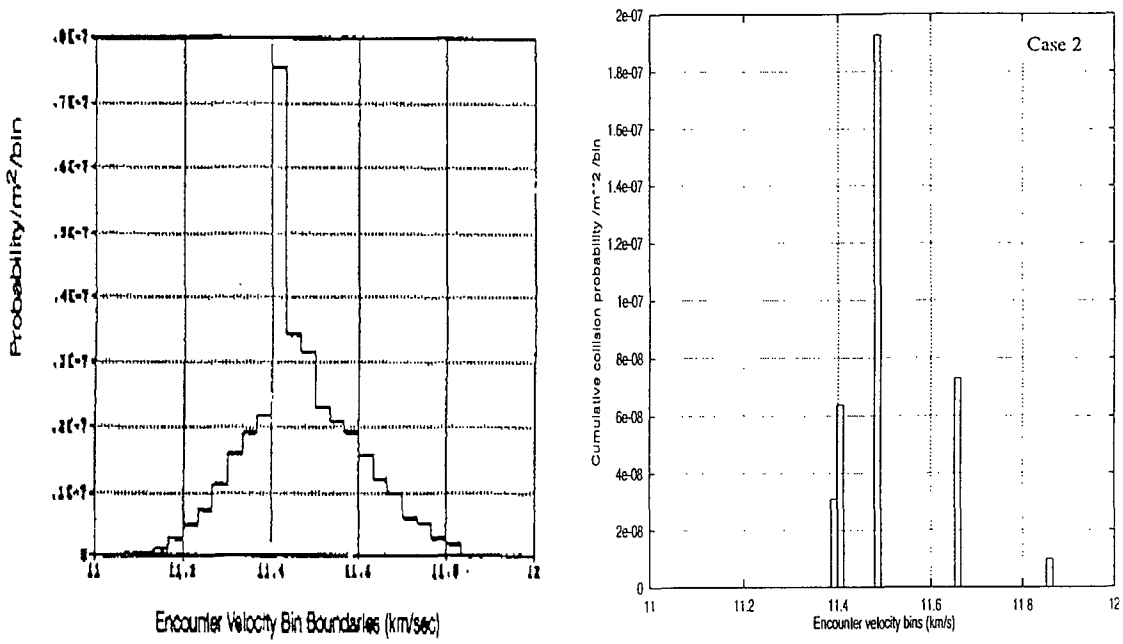

a) DEBRIS3.1 simulation b) TARGET3.1 simulation

Figure 6.39: Case 2 : Distribution of probability of collision per unit spacecraft area over fragment encounter velocity magnitude.

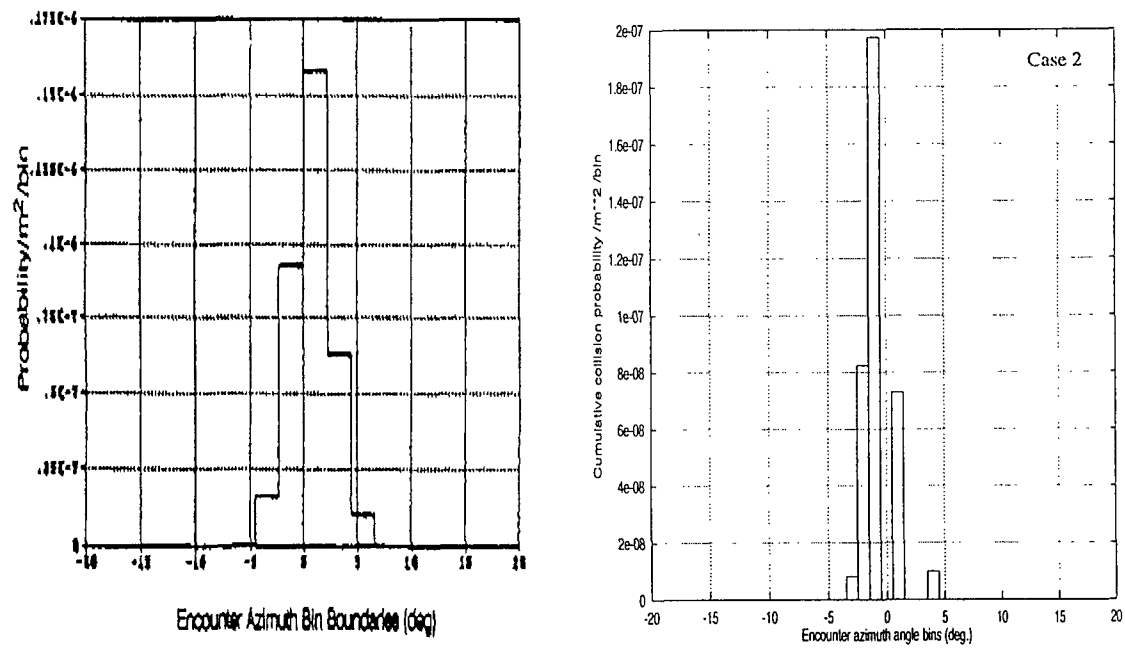

a) DEBRIS3.1 simulation b) TARGET3.1 simulation

Figure 6.40: Case 2 : Distribution of probability of collision per unit spacecraft area over fragment encounter velocity azimuth.

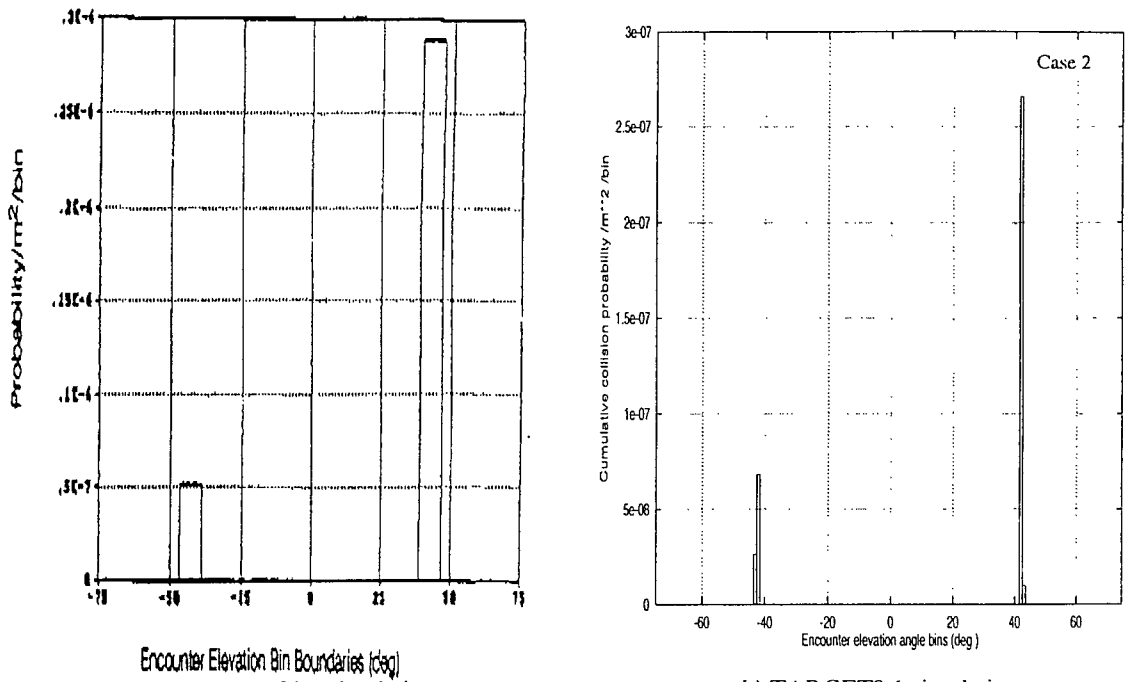

a) DEBRIS3.1 simulation

b) TARGET3.1 simulation

Figure 6.41: Case 2 : Distribution of probability of collision per unit spacecraft area over fragment encounter velocity elevation.

intuitively expected. In Case 1, the greatest difference between the two TARGET3.1 runs came in the assessment of the risk associated with the brief first cloud-target encounter. While the run with pseudo-IMPACT3.0 input predicted that the risk due to this would be negligible compared with the contribution of the pinch point fly-by, the run with BREAKUP3.0 input assigned the encounter a much greater degree of importance. Not only were collision probabilities orders of magnitude higher calculated for the encounter (higher debris densities and encounter velocities), but the encounter velocity directions meant that the trailing target surface received a significant proportion of the collision risk. The cumulative collision probability calculated for Case 1 was still dominated by potential impacts on the target ram face but the BREAKUP3.0 run showed that impacts on the trailing face are also possible, something that the pseudo-IMPACT3.0 run did not highlight. The estimation of the distribution of collision risk across the different spacecraft surfaces is important as it influences the positioning and impact-hardening of payload modules and general shielding design. In Case 2, the target spent almost twice as long inside the

BREAKUP3.0 cloud as it did inside the pseudo-IMPACT3.0 cloud. The additional risk of collision was small, however, due to the rapid fall-off of debris density away from the cloud centroid.

Comparison # 2

Introduction

On February 7, 1994, the Clementine/Titan II second stage (G-11) unexpectedly fragmented, spreading debris throughout the LEO environment. The debris cloud produced by the breakup was potentially hazardous to two manned orbiting vehicles, the U.S. space shuttle Discovery and the Russian space station Mir. A hazard analysis was performed by The Aerospace Corporation while the shuttle was still in orbit in an attempt to quantify the collision risks to the two manned vehicles. The results of the initial analysis and a follow-up study are presented in [121]. This provides an excellent opportunity for results validation on a 'real-life' example. The study involves the modelling of the fragmentation event, graphical depiction of the evolving debris cloud, and the assessment of collision hazards. It, therefore, encompasses all the major constituent simulation parts of the SDS software suite. Such a real-life analysis, carried out in real-time, also illustrates the importance of being able to accurately model fragmentation events and the short-term risk they pose to orbiting spacecraft. Had a high-risk encounter been predicted for the shuttle, for example, evasive manoeuvres could have been taken to minimise the collision risk, provided that risk exceeded acceptable levels and that the objectives of the mission were not severely impaired.

Breakup simulation

The U.S. Space Surveillance Network detected over 700 fragments from the Clementine /Titan II second stage breakup. The low altitude of the rocket orbit pre-breakup (240km near circular, 67 degrees inclination) meant, however, that a significant proportion of the debris produced is likely to have re-entered the Earth's atmosphere before it could be detected. The maximum apogee altitude of a tracked fragment

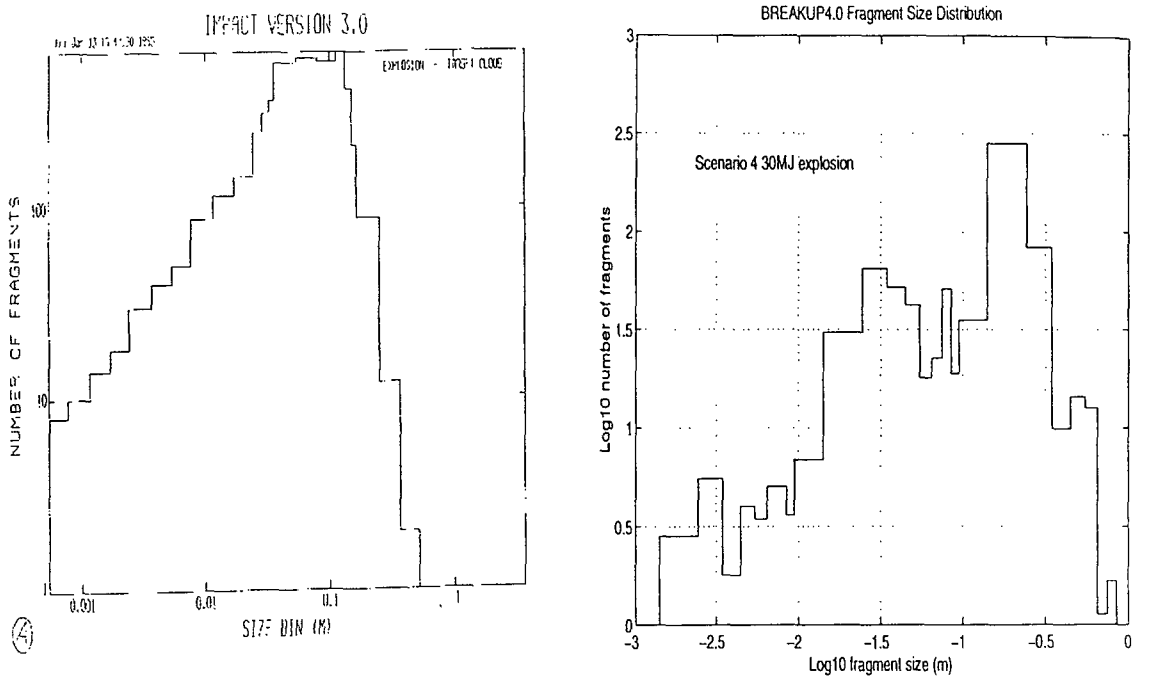

a) IMPACT simulation

b) BREAKUP simulation

Figure 6.42: Fragment size distributions of Clementine/Titan II fragmentation.

was approximately 1700km, indicating that a considerable amount of energy was associated with the fragmentation.

The fragmentation is modelled in [121] by IMPACT as an explosion with breakup energy of 30MJ. An explosion was considered to be the most likely cause of the fragmentation due to the stage's inability to vent or deplete residual fuel or oxidiser. An estimate for the energy associated with the event was determined from the spread velocities of the trackable fragments. Figure 6.42a shows the fragment number distribution for the event generated by IMPACT. 1940 fragments are produced by the simulation, with debris of around 10cm in size being the most populous. The fragment size distribution produced by BREAKUP4.0 is shown in Figure 6.42b. The fragmentation was modelled as a scenario 4 explosion with breakup energy of 30MJ. 740 fragments of 1cm in size and larger were generated. The two curves in Figure 6.42 are similar in shape, with peaks at approximately the same debris sizes, but the BREAKUP4.0 curve is more uneven due to the randomised spread made about the nominal distribution. The factor of 2.6 difference between the number

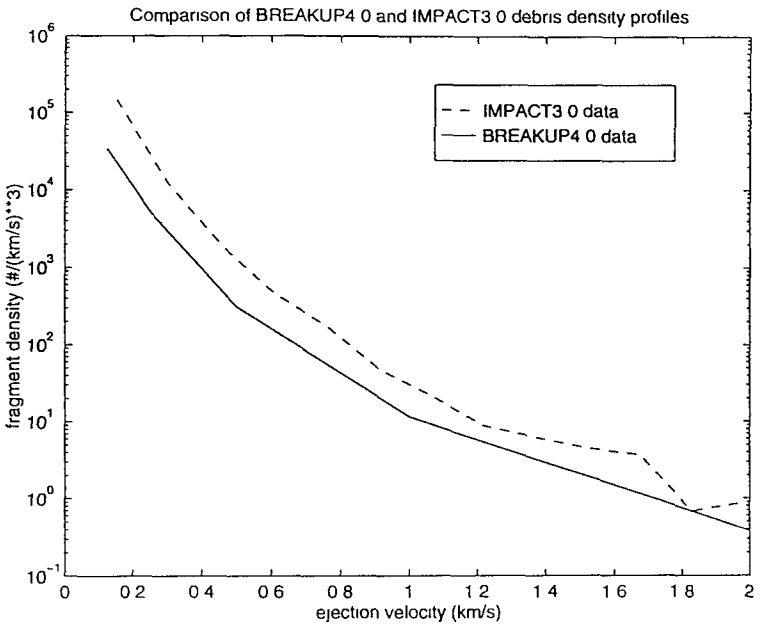

Figure 6.43: Fragment density distributions of Clementine/Titan II fragmentation.

of fragments produced by the two simulations is certainly well within the bounds of uncertainty associated with the predominantly empirical fragmentation models employed by the two codes, coupled with the effect of the BREAKUP4.0 number randomisation.

Figure 6.43 compares the debris density versus spread velocity distributions produced by the two models. The IMPACT distribution is re-plotted on the same axes as the BREAKUP4.0 curve for ease of comparison. The BREAKUP4.0 distribution is generated using the isotropic cloud model. The two curves show an almost identical tail-off of debris density with ejection velocity. The densities on the IMPACT curve are factors higher than on the BREAKUP4.0 curve, as one would expect given the difference in the numbers of fragments produced. The simulated event Gabbard diagrams are shown side-by-side in Figure 6.44. Here, the non-isotropic cloud model is employed by BREAKUP4.0. The matching of the two diagrams is excellent, with BREAKUP4.0 predicting just slightly higher maximum Δvs.

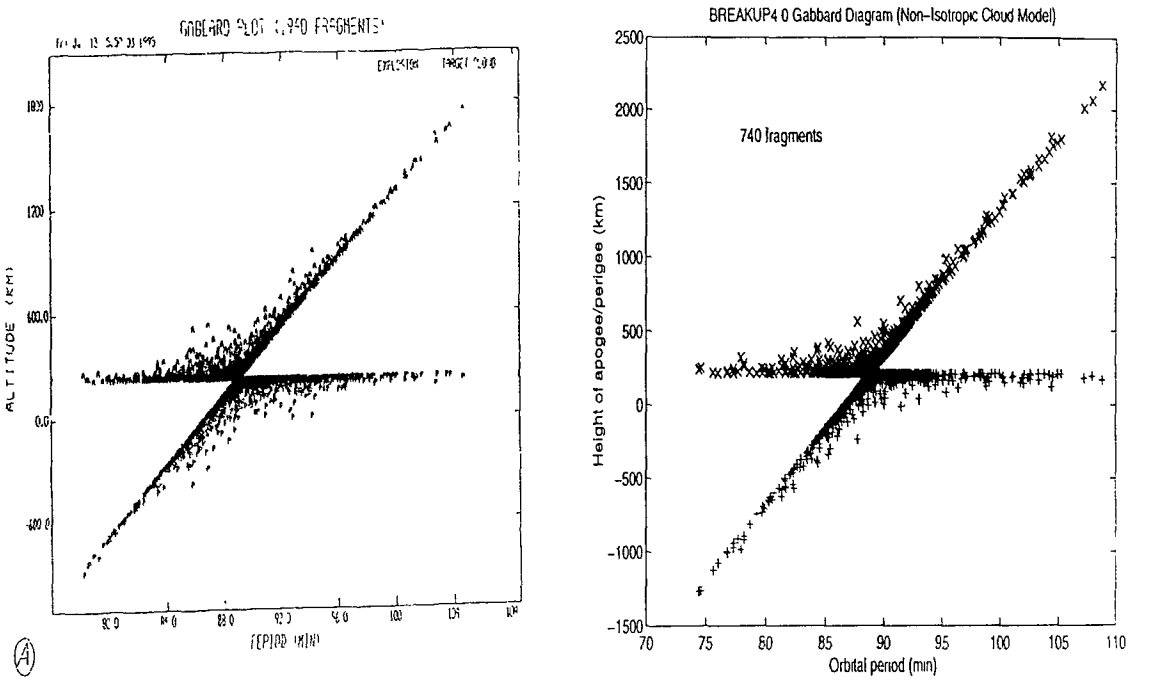

a) IMPACT simulation

b) BREAKUP simulation

Figure 6.44: Gabbard diagrams of Clementine/Titan II fragmentation.

Cloud evolution

To visualise the orbital geometry of the evolving debris cloud and the two manned vehicles, the graphical simulation program DCSIM is employed in [121]. This evolves the cloud of fragments produced by the IMPACT simulation of the breakup and the orbits of the shuttle and Mir using a Keplerian plus J_2 propagator. The orbits of both manned vehicles were over a hundred km higher than that of the Titan II stage. Discovery was moving in a near circular orbit with altitude 358km and inclination 57 degrees. Mir was in a near circular orbit at an altitude of 384km and inclination 51.6 degrees. Figure 6.45a shows the relative geometry of the debris cloud and STS-60 at the first debris cloud penetration by Discovery, approximately 34 minutes after breakup, as generated by DCSIM. The equivalent cloud-shuttle geometry produced by applying EVOLUTION3.0 with propagation method 5 to the non-isotropic BREAKUP4.0 cloud is shown in Figure 6.45b. On their own, the DCSIM and EVOLUTION3.0 figures can only provide qualitative information but they do enable the extent of the debris spread around the globe to be easily visualised, and also the

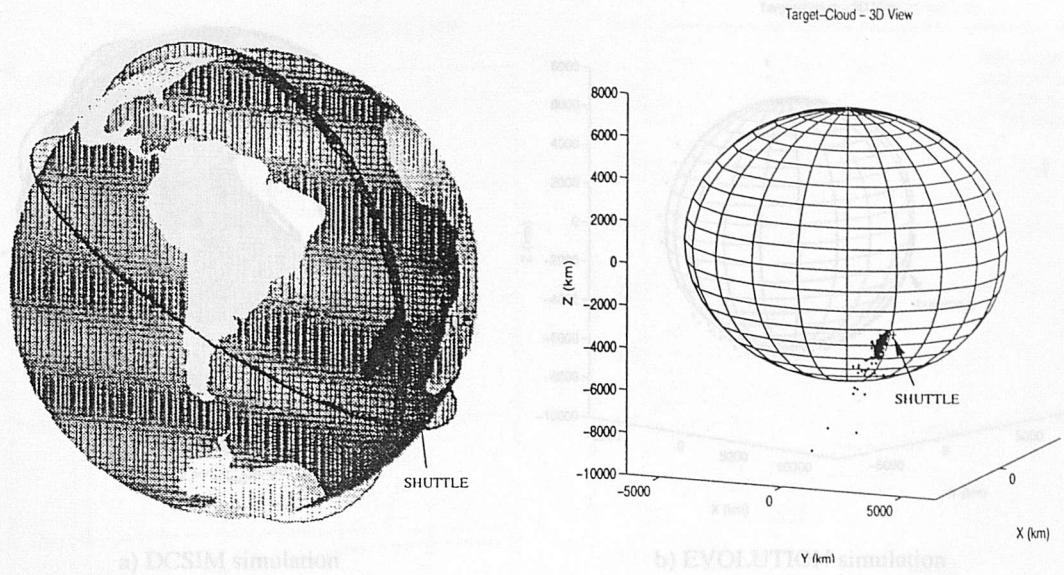

a) DCSIM simulation b) EVOLUTION simulation

Figure 6.45: Orbital geometry of cloud and shuttle at time of first encounter, 34 minutes after breakup.

locations of cloud-target encounters to be visually determined. It should be noted that a target 'encounter' with BREAKUP4.0 cloud type 2 may not necessarily be graphically depicted with the target exactly inside the cloud shape or precisely coincident with a fragment. The target may be inside a populated spread velocity cell but may still appear to be physically outside the cloud. This is a fundamental difference between the two BREAKUP4.0 cloud types and the interpretation of their evolved shapes. Being inside the graphical cloud shape is a necessary condition for an encounter with the isotropic cloud model because the cloud boundaries are depicted (c.f. section 6.6.1). The actual fragment positions are shown for the non-isotropic model cloud, but the cloud's spread velocity space cell structure is used for determining collision hazard. The cell boundaries are not shown on the EVOLUTION3.0 cloud depictions. Figure 6.46 shows the debris cloud penetration by STS-60 215 minutes after breakup. Here the shuttle appears to pass though the cloud in a region of particularly high debris density. This is substantiated by the collision hazard analysis discussed next. The general matching of debris cloud characteristics and relative target positions between the DCSIM and EVOLUTION3.0 simulations can be seen to be very good.

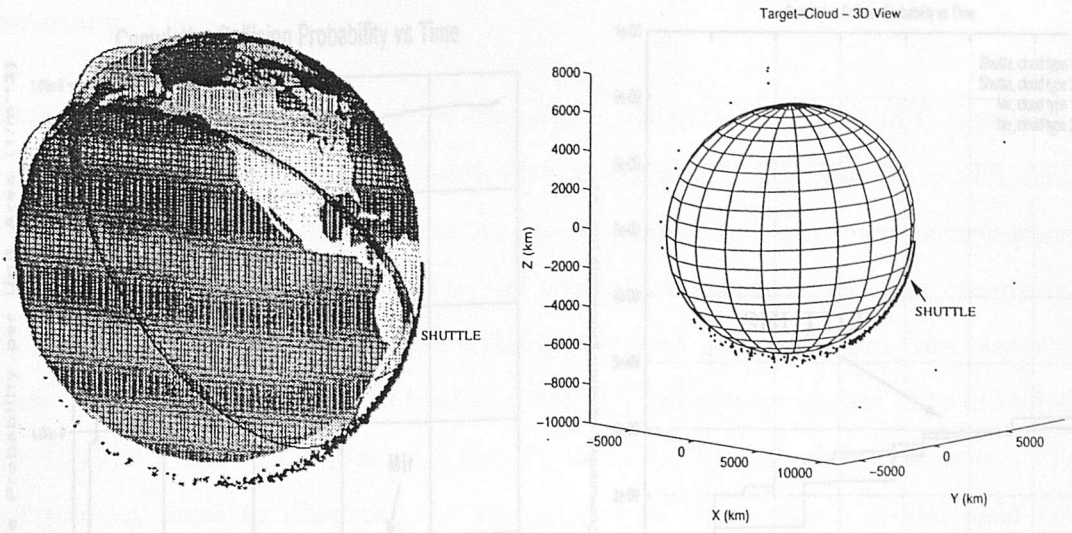

a) DCSIM simulation b) EVOLUTION simulation

Figure 6.46: Orbital geometry of shuttle and cloud at time of maximum encountered debris flux, 215 minutes after breakup.

Collision hazard analysis

To determine the collision hazard to Discovery and Mir from the Titan II debris, program DEBRIS was employed in [121], the debris cloud being defined by the IMPACT spread velocity distribution shown in Figure 6.43. The simulation was performed for four days from the breakup epoch to account for the remainder of the shuttle mission. During this time both the shuttle and Mir passed through the cloud on numerous occasions. The collision probabilities calculated for the two vehicles by DEBRIS are shown in Figure 6.47a. Only fragments of size 1cm and over are considered and the collision probabilities quoted are per square metre of target. The collision probability curves for both spacecraft are seen to level after the first day as the cloud disperses, with the collision risk to the shuttle being approximately five times that experienced by Mir. The lower risk predicted for Mir is due to the extra time taken for it to first encounter the cloud. The risks to both vehicles are relatively low, with the encounter between Discovery and the cloud 215 minutes after breakup, shown above in Figure 6.46 and evident again in Figure 6.47, proving to be the most hazardous. The collision hazards calculated using TARGET4.0 are shown in Figure 6.47b. For each vehicle, simulations are performed using both BREAKUP4.0

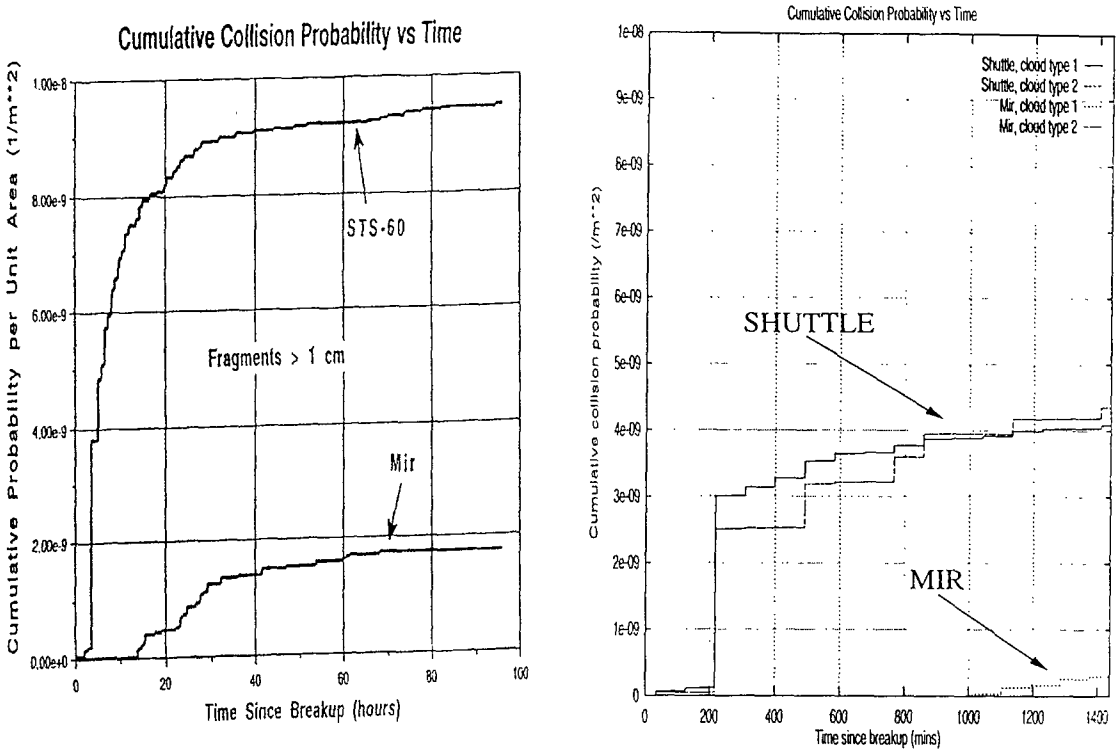

a) DEBRIS simulation b) TARGET4.0 simulation

Figure 6.47: Cumulative collision probability per unit area vs time for the shuttle and Mir.

cloud types. Once again only fragments of 1cm in size and above are considered and the collision probabilities are for unit target area. The simulations are run for 1 day only to cover the highest risk portion of the cloud's lifetime. The same scaling is used on Figures 6.47a and 6.47b for ease of comparison. The lower initial cloud densities produced by BREAKUP4.0 compared with IMPACT are seen to result in the lower collision risks predicted by TARGET4.0 compared with DEBRIS. For the shuttle, TARGET4.0 predicts cumulative collision probabilities at the end of the first day around 2.5 times lower than DEBRIS for both cloud types. This factor difference is directly in-line with the breakup model fragment density difference. The risk to Mir estimated by TARGET4.0 is around an order of magnitude less than that for the shuttle and around 6 times less than that predicted by DEBRIS. This again is due to the length of time taken for Mir to first encounter the cloud, and also the marginally greater dispersion of debris produced by BREAKUP4.0.

Summary

The two cases examined above show that while DEBRIS and TARGET appear to be in good general agreement when used with a common fragmentation model. When IMPACT and BREAKUP are used to provide input to their respective partners, noticeable differences are observed in the results produced. In the first comparison, which involved the simulation of a collision-induced fragmentation, the larger and denser BREAKUP debris cloud lead to TARGET predicting higher risks of collision than DEBRIS. For the explosive Titan II breakup, the opposite was true. These discrepancies serve to illustrate the importance of the breakup model used when attempting to assess the collision risks associated with debris clouds.

6.6.4 Comparison with the ESA MASTER Model

Introduction

The previous section covered the comparison of TARGET output with a similar debris cloud collision hazard model. It is also interesting to discover how the debris fluxes predicted by TARGET for passages of a satellite through a debris cloud compare with the fluxes on the same spacecraft predicted by a model of the background environment. The collision hazards posed by debris clouds act in addition to the ever-present threat of collision with debris from the background population and also the natural micrometeor environment. A satellite in orbit will, of course, experience the un-resolved resultant particulate environment, but at a simulation level the constituent elements are generally considered separately and so the different risks associated with each can be compared. In this section the ESA MASTER (Meteoroid And Space debris Terrestrial Environment Reference model) model [122, 123, 124] is used to examine the collision threat to a target object in a sun-synchronous low Earth orbit typical of many remote-sensing satellites, e.g. ERS-1, ERS-2 and ENVISAT-1. The threat from background debris and natural particles predicted by MASTER can then be compared with the debris cloud collision risks estimated by TARGET for ENVISAT-1 in sections 6.5.2 and 6.5.4.

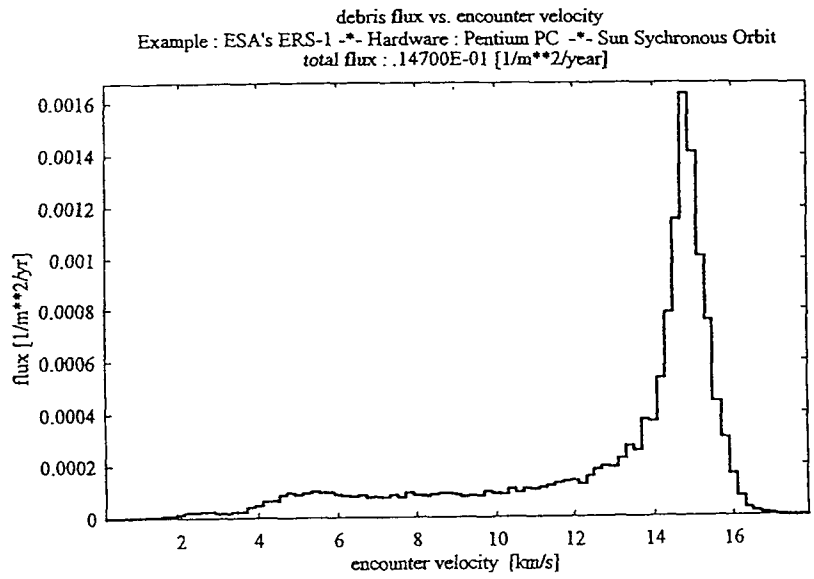

Figure 6.48: Debris flux versus impact velocity.

The ESA MASTER model

The aim of the MASTER model is the characterisation of the natural and man-made particulate environment of the near-Earth space and the evaluation of the resulting effects on space missions. The debris model is based on semi-deterministic analysis and prediction techniques, supported by data from a number of fragmentation experiments, debris observations and retrieved spacecraft surfaces. The derived fragmentation model is applied to 121 historic breakup events and a representative sample of the objects produced, along with the catalogued population, is then propagated to a common reference epoch (1995). This constitutes the MASTER reference population. The engineering application of the MASTER model allows satellites in near-circular orbits to be 'flown through' the reference population and the debris fluxes encountered to be determined. The debris model is supplemented by an analytical representation of the meteoroid environment.

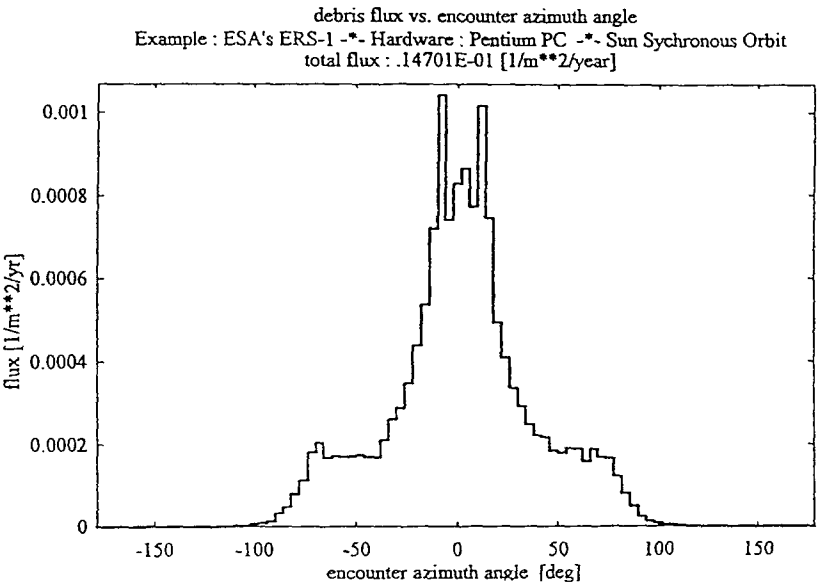

Figure 6.49: Debris flux versus impact azimuth angle.

MASTER debris fluxes on satellite in ERS-1 type orbit

In [124], the MASTER Engineering Application is used to calculate the orbit-averaged debris fluxes on a spacecraft in an ERS-1 type orbit. The orbit used for ERS-1 is virtually identical to that employed for ENVISAT-1 in sections 6.5.2 and 6.5.4. The total debris flux calculated for fragments 1mm in size and larger is $\approx 1.3 \times 10^{-2}$ impacts per m^2 per year (compared with $\approx 3.0 \times 10^{-3}$ for natural particles). The encountered debris flux versus impact velocity distribution generated is shown in Figure 6.48. The peak debris flux comes from impact velocities that are around twice the circular velocity of the target orbit altitude. From this it can be deduced that head-on encounters dominate in terms of encountered debris flux, and hence collision probability. This finding is supported by Figure 6.49 which indicates that impact azimuth angles between ± 20 degrees provide the dominant source of debris flux. The ram face of the target is thus the most at risk from debris impacts, with the absence of azimuth angles above ± 100 degrees observed suggesting that the trailing surface is the safest. The distribution of debris flux with respect to elevation angle in Figure 6.50 shows that the highest debris flux comes from within the target horizontal plane, with almost no contributions from encounters outside

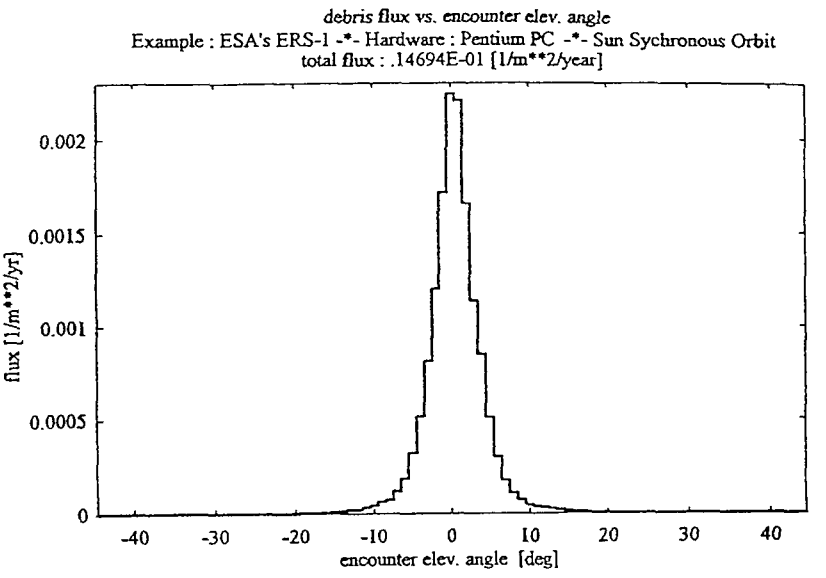

Figure 6.50: Debris flux versus impact elevation angle.

± 10 degrees.

Discussion

The average background debris flux estimated by the MASTER model for a target satellite in an ERS-1 type orbit is several orders of magnitude lower than the peak cloud fluxes that TARGET has shown can be experienced for certain breakup scenarios. The MASTER background debris flux level corresponds to a mean collision probability of $\approx 2.5 \times 10^{-8}/\mathrm{m}^2/\mathrm{minute}$. This is around an order of magnitude higher than the background collision probability calculated using the NASA engineering model [113] in section 6.5.2, but larger fragments (>1cm) were considered there. In general, whether a satellite experiences a significant increase in debris flux on passing through a cloud of fragments is dependent upon several factors. Cloud encounters soon after the fragmentation or near the cloud's pinch locations during the first few orbits post-breakup can produce order of magnitude increases in the debris flux incident upon the target object. Away from the pinch locations, the increase in collision risk is less dramatic, especially once the cloud has had time to disperse around the parent orbit. The severity and cause of the fragmentation

event is also important. For explosive breakups, such as the fragmentation of the SPOT-1 Ariane third stage modelled in section 6.5.4, the density of debris in the cloud can actually be much lower than in the background environment. Due to the energies associated with hypervelocity impacts, however, and the large numbers of small debris produced, it is estimated that the debris densities in clouds formed by collisions can be orders of magnitude higher than those experienced outside.

The debris fluxes predicted by the MASTER model suggest that by far the most likely impact scenario is a head-on collision with the ram face at virtually twice orbital velocity. The probability of an impact on one of the other faces is generally factors to orders of magnitude lower. The distribution of collision risk over the spacecraft is virtually uniform for both the Earth-Space and Orbit normal-Negative orbit normal opposite surface pairs. The examination of debris flux directionality in sections 6.5.3 and 6.5.4 showed that for an arbitrary target passage through a debris cloud, the simple impact probability distribution described above cannot be readily assumed. The relative orientation of the target and cloud orbits, and the orbit propagation scheme employed in the simulation, can produce distinctly different distributions of collision probability over the target surfaces and a wide range of possible impact velocities. The ram face is most often still found to be the most likely to be hit but the other surfaces can conceivably have comparable or possibly even greater collision probabilities associated with them, including the trailing and space faces.

6.6.5 Use of Retrieved Spacecraft Debris Impact Data

Introduction

The Long Duration Exposure Facility

The Long Duration Exposure Facility (LDEF) [37] spacecraft was deployed by the Challenger space shuttle orbiter on April 7, 1984. Placed in a nearly circular orbit at an altitude of 480km and with an orbital inclination of 28.5 degrees, its mission was to sample the near-Earth environment for 9 months. The entire spacecraft was

to be returned to Earth at the end of the mission. The scheduled return of LDEF to Earth was delayed, however, first by scheduling problems, and then by the loss of Challenger. Exceptionally intense solar maximum activity accelerated the decay of its orbit and it became clear that if LDEF was not recovered, it would re-enter the atmosphere in early 1990, with the loss of all of its data. It was retrieved at an altitude of 330 km by the crew of the Columbia on 12 January 1990, and returned to Earth on 20 January, the same day that NORAD had predicted as its most probable atmospheric re-entry date.

The LDEF vehicle was a 12-sided cylinder approximately 9.1m long and 4.3m in diameter. It was gravity-gradient stabilised, so that the long axis was always directed at the sub-satellite point on the Earth's surface. Rotation about the long axis was inhibited by a magnetic damping system. Thus, one of the long faces was always the leading, or ram face, facing the velocity direction. The opposite face was then the trailing or wake face. One end of the cylinder was always facing space, the other end always towards the Earth. The faces perpendicular to both the long axis and the velocity vector were nominally 'north' and 'south', their surface normals continuously aligned at +61.5 degrees and -61.5 degrees respectively with respect to the equatorial plane. Post-flight analysis of LDEF surfaces indicated that the spacecraft was rotated about 8.2 degrees from the intended orientation about the long axis. The normal to the leading face was rotated about 8.2 degrees away from the velocity vector, with the normal to the north face rotated 8.2 degrees towards the velocity vector.

The Interplanetary Dust Experiment

The Interplanetary Dust Experiment (IDE) [36, 45, 125, 126], one of the fifty-six experiments mounted on LDEF, was conceived to permit a discrimination between cosmic dust and orbital debris, and to characterise the dust in terms of mass, velocity, time, and trajectory. The IDE experiment occupied portions of six trays, one each on the leading and trailing faces, the Earth and space ends, and the north and south faces. High and low sensitivity dielectric detectors were calibrated to detect

hypervelocity impacts from particles down to 0.2μm and 0.5μm in size respectively. The upper detection limit for both types (representing the particle size expected to physically break the detector substrate) was 100μm in diameter. An on-board tape recorder was included to record the time of each impact, with a time resolution of approximately 13.1 seconds. Tape was only supplied for the nominal 9-month mission and ran out 348 days after LDEF deployment. Post-flight verification showed that there was only one recording anomaly during this time and no significant data were lost. About 15,000 impacts were recorded on the 459 detectors during the active phase of the mission. For the remaining 4.7 years of flight, the detectors continued to receive impacts which left physical craters, but no time-resolved information was recorded.

In contrast to data previously obtained from returned spacecraft surfaces, the controlled orientation of LDEF and high time-resolution of the IDE data provided, for the first time, a detailed, extensive data set well adapted to analysis of the spatio-temporal characteristics of orbital debris in near-Earth orbit. The IDE data showed that the particulate environment encountered was neither uniform in time nor in space. Most of the 15,000 impacts recorded by IDE occurred in groups or 'bursts'. These 'events' were of two types - 'spikes', which were single, isolated events of high intensity and 'multiple orbit event sequences' (MOES), which were a series of events separated in time by integer multiples of the LDEF orbital period. A significant finding from the good time resolution of LDEF IDE data was that the instantaneous fluxes observed could be much greater than the mean. The peak flux observed over the course of the experiment was almost 4 orders of magnitude greater than the mean value calculated. While long-term fluxes may be useful for engineering structures and similar purposes, there are circumstances where peak fluxes may be more useful. The IDE results indicate that an optical surface such as a window (which could be degraded by small particle impacts) could need replacement far sooner than would be predicted by mean fluxes.

Analysis of MOES

MOES result from the intersection of the orbit of the LDEF with that of a concentration of orbital debris. Analysis of MOES data revealed two important characteristics:

- 1. The orbital debris particle orbits are eccentric. If they were circular, the IDE detectors would register the group twice each orbit since a circular orbit must intersect LDEF's orbit (which is essentially circular) at two points.
- 2. The particles must be 'smeared out' along the orbit in a torus structure. If the particles were concentrated in a 'clump', the encounters with LDEF would not occur at integer multiples of the LDEF orbital period, unless the period of the particle orbit was the same as that of LDEF, which is unlikely in general.

In order to determine the orbits of the impacting particles in a MOES, the Method of Differential Precession was developed in [125, 126]. The goal of this method is to obtain the orbital characteristics of the particles which struck the IDE detectors during a MOES by an analysis of the time variation of the LDEF position over the series of encounters. The analysis makes use of the fact that the asphericity of the Earth induces the pole of an object's orbit to precess, resulting in a cyclic change in the position of the line of nodes of the orbit. The oblateness of the Earth also causes the line of apsides of the orbit to precess, the point of perigee advancing if the orbital inclination below 63.4^o and regressing otherwise. In general, bodies in different orbits will have different rates of these precessions, and should two of these orbits intersect, the differences in the precession rates will cause the point(s) of intersection to vary with time. If the characteristics of one of the intersecting orbits are known, the migration of the point of intersection may be used to determine the precession rates and orientation of the unknown orbit, which then may be used to calculate a family of candidate orbits.

The 'May swarm'

One of the most prominent multiple orbit event sequences observed by IDE was the 'May Swarm'. The May swarm began on May 13, 1984, and can be characterised as being of low intensity (around 3 impacts per orbit) and long duration. The May MOES lasted for over 20 days (300 LDEF orbits), with several hundred impacts recorded on the IDE trays facing in the LDEF ram direction and towards the south pole of the orbit, the majority occurring on the south-facing tray. The distribution of impacts recorded by the high-sensitivity detectors is shown in Figure 6.51. Figure 6.51 is produced by transforming the impact tray directions in the May swarm portion of the original IDE dataset [37] to TARGET surface numbers. The standard surface numbering scheme is employed (Figure 6.4) to denote the LDEF surface directions, (i.e. south=3, ram=4).

The application of the Method of Differential Precession in [125, 126] calculated the following element values for the particle orbits, at the epoch corresponding to the onset of the May swarm : a=6746.5km, e=0.0165-0.0250, i=66.55 degrees, Ω=179.0 degrees and ω=178.1 degrees. One of the candidate orbits (e=0.017) was then chosen for a series of checks on the results of the method. The first check involved the computation of the particle velocity of impact over the duration of the May swarm. These velocities were then resolved into components along the LDEF body axes in order to determine the impact speeds on the IDE trays (Figure 6.52a [126]). For this particular orbit, only the south tray and the ram-facing tray were struck, with the south impact speed being larger than that for the other tray for most of the encounter. This is in good agreement with the IDE observations of the May swarm, in which these same two trays recorded large numbers of impacts, with the south tray receiving the most hits. The second check consisted of a comparison of the sky track of the points of closest approach between the two orbits to the sky positions of the individual impacts comprising the May swarm (Figure 6.52b [126]). Again the agreement was favourable, with the sky track of close approach passing neatly through a diffuse band of impact positions.

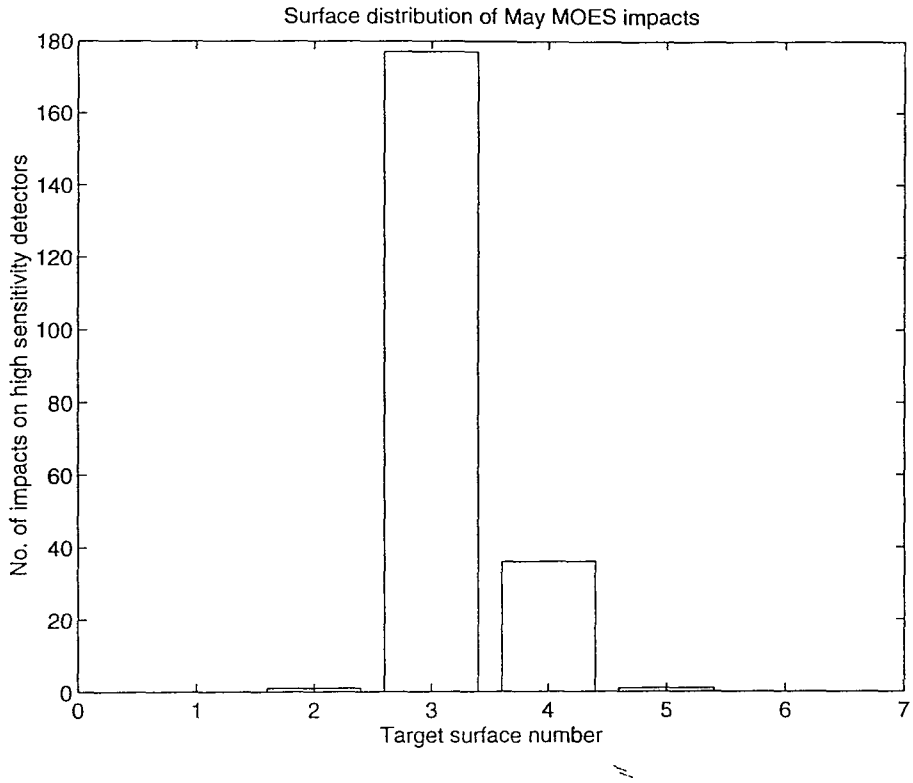

Figure 6.51: Surface distribution of May swarm impacts.

May MOES simulation using BREAKUP and TARGET

The orbital geometry and distribution of impacts associated with the May MOES can be represented using BREAKUP, EVOLUTION and TARGET. There is no 'breakup' as such in this example but the longevity of the swarm suggests that the debris ring is replenished by a source object during the time spanned by the MOES. Micron-sized particles existing at the time of the onset of the May swarm would almost certainly re-enter long before the end of the MOES under the influence of atmospheric drag and solar radiation pressure. BREAKUP4.0 is not designed to model the low-velocity ejection or shedding of debris from an object over a long time period. The ring of debris which caused the May MOES is, therefore, created by BREAKUP4.0 using a low-velocity isotropic ejection to form a ring of debris closely around the 'breakup' orbit, which is taken to correspond to the particle test orbit used in the Method of Differential Precession results checks above. The fragmentation is timed to occur long enough before the start of the MOES to allow the debris to drift completely around the orbit and form a ring-like structure. The

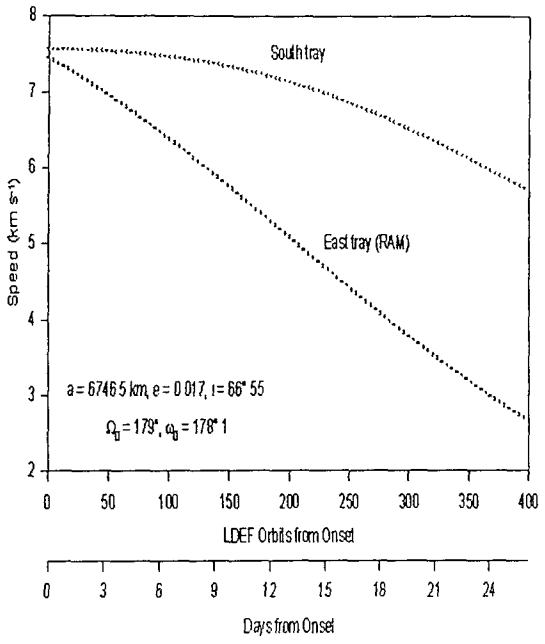

a) Particle impact speeds along IDE tray

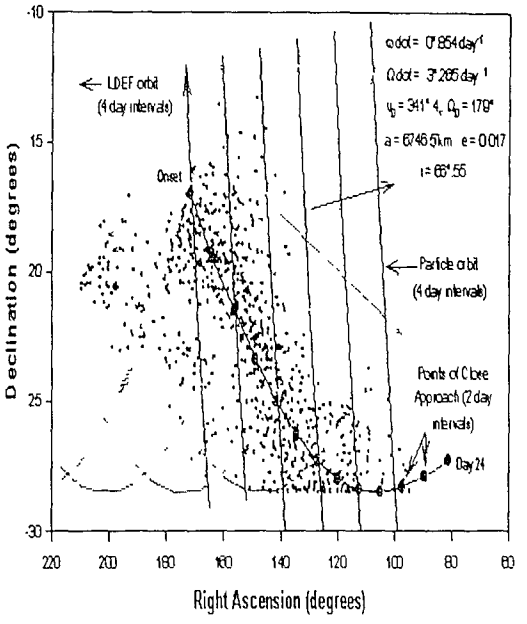

b) Sky track of close approach between particle and LDEF orbits

Figure 6.52: Orbit checking of Method of Differential Precession solution.

ring is maintained throughout the duration of the analysis by neglecting the effects of atmospheric drag from the propagation of the fragment orbits. TARGET4.0 is used to assess the collision risk to LDEF from the debris in the ring. LDEF is modelled using the simple cuboidal spacecraft representation in TARGET4.0, with the 8.2 degree offset of the spacecraft accounted for by a 'yaw' rotation about the cylinder's long axis. The size and density of fragments in the ring are unimportant in this analysis as the simulation of exact flux details and rates is not possible. Instead, simply the relative flux incident on each of the LDEF surfaces is determined, along with the debris impact velocities. Only the first day of the May swarm is represented by the simulation as this can be taken to be representative of the MOES as a whole.

The debris flux distribution predicted by TARGET4.0 is shown in Figure 6.53 along with the distribution of impacts on LDEF for the first day of the May MOES. Figure 6.53a shows that approximately the same distribution of impacts on surfaces 3 and 4 is observed for the first day of the MOES as for the event as a whole. During this time, these are the only two surfaces that are actually hit. Figure 6.53b shows that the flux distribution predicted by TARGET4.0 follows a similar pattern. The

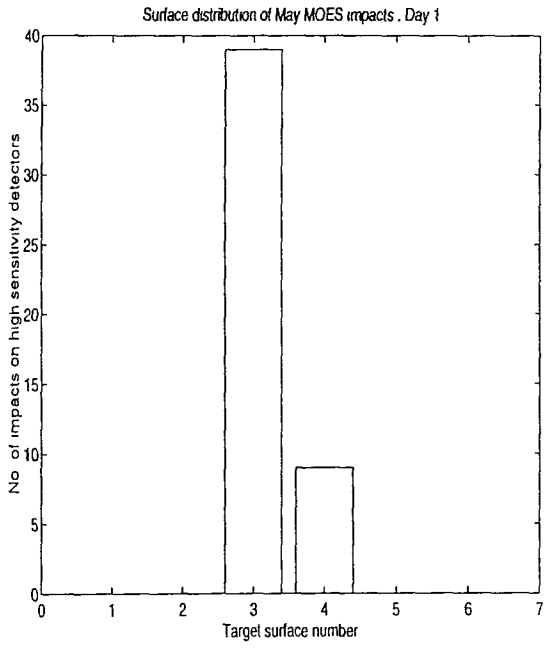

a) Impact distribution for 1st day of May MOES

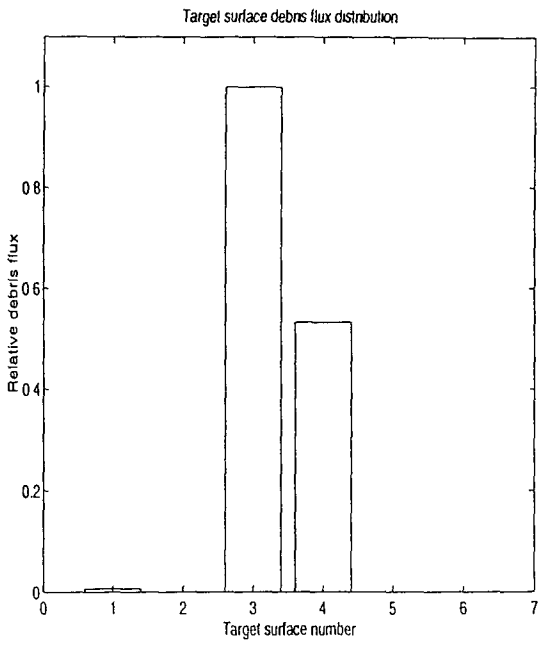

b) Distribution of encountered debris flux (normalised to surface 3 value)

Figure 6.53: Comparison of LDEF impact locations with TARGET4.0-predicted debris flux distribution.

flux levels displayed are normalised to the south face flux. TARGET4.0 predicts a proportionally higher flux contribution from the ram face than is suggested from the impact data. Obtaining an exact match would have been unlikely, however, as uncertainties in the orbits of both LDEF and the debris, and the statistical inability to be able to translate incident fluxes and hence collision probabilities directly and exactly into actual numbers of impacts, mean that only estimates of impact numbers and locations can ever be made.

Summary

The IDE data provides a valuable and unique spatio-temporal insight into the extreme anisotropy of the near-Earth particulate environment. A significant proportion of the untracked orbital debris population seems to be contained in debris swarms or clouds, with particle densities possibly orders of magnitude higher than the estimated mean. A direct simulation of the swarms of debris experienced by the IDE is beyond the scope of programs BREAKUP and TARGET as the particles

involved are too small. The micro-particulates detected by the experiment are most likely to have been generated by continuous or long-duration sources, e.g. from spacecraft surface degradation, fuel leakage or solid rocket motor ejecta. Hypervelocity impacts are another candidate source of very small debris, but the compound uncertainties involved in the orbit propagation of such particles and the modelling of their generation mean that being able to satisfactorily match micro-particulate impacts with potential collision victims is an extremely difficult task. The far less ambitious simulation attempted here with BREAKUP4.0 and TARGET4.0 shows that the May MOES experienced by the IDE was almost certainly caused by a ring of debris in an eccentric orbit, with the distribution of impacts recorded being directly attributable to the orbital geometry involved.

Chapter 7

Conclusions

7.1 Overview

The modelling of on-orbit fragmentations and the hazard they pose to orbiting spacecraft is a complex problem. The organisation of this thesis has reflected the multi-stage nature of the overall problem, which in turn also provides a logical subdivision of module tasks in the suite of simulation codes. Most of the thesis has concentrated upon the simulation software developed, the methodologies employed and the use of the programs in case studies and results validation exercises. This is entirely appropriate as the software developed represents the bulk of the work carried out for the PhD degree and is the medium through which the novel developments made are illustrated and tested.

This concluding and summarising chapter is subdivided in the same way as the thesis and the main programs in the SDS software suite. Each of the aspects of debris cloud modelling considered is briefly summarised and the novel developments made in the work described here are clearly outlined. The major findings from the numerous analyses performed are re-iterated and the implications of the findings to spacecraft operation and design are discussed where appropriate.

7.2 Breakup Modelling

Empirical and semi-empirical breakup models are employed almost without exception in debris cloud and orbital environment simulations. These are by far the easiest and quickest methods to implement and such techniques generally offer a good first approximation to the events they attempt to model. Uncertainties still exist in even the most widely used and accepted of these models, however. The very nature of fragmentation events generally precludes the formation of simple, meaningful, analytical representations. Modelling the physics of impacts and explosions results in complex formulae and the need for considerable computing power. Each fragmentation scenario must also be treated individually. The use of empirically-derived relationships, which describe a breakup in terms of the numbers, masses and velocities of the fragments produced, in conjunction with analytical equations which enforce the principles of conservation of mass, momentum and energy, is considered to be an acceptable compromise. The versatility and speed of the approach almost always outweigh any potential misgivings regarding the absolute accuracy and widespread applicability of the models.

No new fragment distribution equations or breakup models were developed here because this was not the objective of the work, nor was such an undertaking practical or appropriate. Instead a selection of the best known and validated fragment distribution expressions was employed and the emphasis was placed on how these distributions were utilised in producing debris clouds. In particular, the generation and usage of non-isotropic debris ejection velocity spreads was investigated and a new parametric technique was developed for biasing the nominally random selection of ejection directions to explicitly control the shape of the debris cloud. The model proved to be simple to use, is extremely versatile in its application and has been validated successfully through the use of actual breakup event data. The transformation of the non-isotropic debris spread into a spherical polar coordinate spread velocity cell structure has also enabled non-isotropic debris clouds to be used in collision hazard assessments for the first time. The significance of this development is discussed in section 7.5.

7.3 Fragment Trajectory Calculation

Accurate calculation of the trajectories of the fragments produced by a breakup event is fundamental to any study which seeks to explore the complex dynamics of a debris cloud, determine its lifetime or estimate the collision risk posed to spacecraft which encounter it. Hence trajectory calculation, although not strictly a task specific to the modelling of debris clouds, is a topic of sufficient importance to warrant special and separate consideration.

Numerous methods have been proposed in the literature for the fast and efficient determination of fragment locations post-breakup, utilising both linearised and full equations of motion, and also relative and geocentric inertial reference frames. A number of these methods have been examined in this thesis and implemented for the first time into a single computer code for convenient and direct comparison. The simplest of these, the linearised state transition matrix methods, are seen to break-down once the debris has begun to disperse around the parent orbit. A novel second-order state-transition matrix method has, therefore, been developed here to investigate the useful limits of such relative motion techniques. The new method is seen to offer a considerable improvement over the linearised approaches but is found to break down itself once the debris has become more than half an orbit revolution either ahead of or behind the breakup centre of mass.

For simulations of more than a few hours and breakups of realistic severity, the full equations of motion need to be employed and debris orbits propagated in a geocentric inertial frame. A large number of orbit propagation techniques are available, ranging from straightforward analytic Keplerian propagation to high-accuracy specialised numerical integration schemes. The main requirements for the orbit propagator used in the debris cloud evolution and collision hazard assessment studies described in this thesis were speed of operation, ease of implementation and an acceptable level of accuracy. Speed was a major driver because debris cloud evolution involves the propagation of a large number of orbits, and the numerical minimisation routine in the collision hazard determination code iterates on the propagator. The

approach adopted was the analytical addition of perturbation effects to Keplerian motion. This technique was considered to provide the optimum fulfilment of the above selection criteria. Only orbit perturbations due to the Earth's oblateness and atmospheric drag are modelled because these are the dominant perturbation forces for the orbital regimes and fragment sizes considered. All the analyses performed in the thesis consider objects and debris in low Earth orbit and very small particles ($< .1mm$) are generally ignored to concentrate upon potentially damaging debris. The analytical orbit propagation scheme was validated by simulating the orbits of several real satellites. The comparisons showed that in each case the analytical technique provided a reasonable approximation to the actual orbit data.

7.4 Debris Cloud Evolution

Given an orbit propagator and suitable output from a breakup model, the task of evolving a debris cloud is relatively straightforward. The cloud shape at any given epoch post-breakup is formed by propagating all the fragment orbits to the time in question and calculating the debris positions. How the cloud represents the actual locations of the debris of which it is formed is dependent upon the type of breakup model employed, however. For the non-isotropic cloud model, each orbit propagated and position calculated corresponds to an individual fragment, or a macro-fragment which represents a number of particles of a common size. The relationship between the points which form the cloud and the actual debris positions is, therefore, a direct one-to-one mapping. If an isotropic continuum cloud model is evolved then the cloud shape represents a bounding three-dimensional envelope inside which all the debris is contained.

The cloud evolution simulations performed in this thesis show that the behaviour of a debris cloud is extremely complex. The dynamics of a cloud in unperturbed orbital motion, however, are well-known and documented. The explicit consideration of the effects of orbit perturbations on the short-term behaviour of debris clouds is something that has not been previously addressed in the literature. The use of the

analytic orbit propagation technique to model the effects of J_2 and drag perturbations on the growth of a debris cloud in the first few hours after breakup shows that the locations of highest debris density are shifted and the densities reduced when compared with the ideal case. Accurate determination of the locations of debris concentrations following a fragmentation event and the levels of debris density associated with them is important for the assessment of collision risks for spacecraft which encounter them, as discussed in the next section.

The results from the cloud evolution analyses are validated in two ways, firstly through the comparison of the cloud shapes predicted for a benchmark example with those produced by another cloud model, and secondly through the generation of decayed Gabbard diagrams and comparison with actual event data. The combination of the breakup model non-isotropic cloud representation and the debris evolution software tool is shown to form a realistic and integrated facility for modelling fragmentation events and the subsequent spread of the debris produced.

7.5 Collision Hazard Assessment

The collision hazard posed by a debris cloud to spacecraft which pass through it acts in addition to that routinely experienced as a result of the background environment. Due to the passage of natural particles through near Earth space and the remnants of man's exploits in orbit, the orbital environment poses a constant, but variable, hazard to all spacecraft which operate within it. Explosions and collisions between objects in orbit only serve to increase this hazard, and can do so dramatically for short periods of time following an event. The main objective of the PhD research programme has been to quantify the additional collision hazard caused by breakup events and investigate the likelihood of collisions occurring for a variety of cloud-target scenarios.

The use of probabilistic continuum dynamics in the area of debris cloud collision hazard assessment has produced a major step forward in the scope and realism of the simulations that can be performed. The method circumvents the need for an

overly simplistic breakup, cloud representation and evolution of the cloud shape for complex three-dimensional encounter detection considerations. The generalisation of the algorithm presented in this thesis is a novel implementation of the basic method. This, in conjunction, with the application of the technique in a variety of case studies, constitutes a unique investigation into the extent to which on-orbit breakup events can impact upon specific space systems.

Studies on single target objects show that collision probabilities can increase not just by factors but by orders of magnitude if an object encounters a debris cloud close to an orbital constriction point or the centroid of the cloud. Orbit perturbations can significantly influence the collision risks predicted, as can the type of breakup model employed. The assumption of ideal orbital motion may overestimate the likelihood of a collision due to the dispersive properties of atmospheric drag and the Earth's oblateness. Also, the use of an isotropic continuum cloud model will generally lead to more debris encounters being predicted than would actually be the case because the cloud is assumed to be completely full of debris, equally spread in all directions.

A new approach to collision damage assessment has been developed which directly relates the damage caused by a debris impact to the kinetic energy of the impactor and the mass of the target object. This model, used in conjunction with an equally novel building-block representation of the target spacecraft and the power of the probabilistic continuum dynamics approach, enables the possibility of payload or even mission failure following an impact to be investigated. The combination of raw collision probability data with such damage assessment information creates a much fuller picture of the potential danger posed by debris clouds to orbiting spacecraft, and so is of much greater use to the spacecraft operator or designer. It was found that debris cloud encounters can produce collision geometries where the satellite faces most at risk are those that are considered to be the safest in normal operations (e.g. trailing, space, Earth). Impacts of sufficient severity to either partially disable or completely destroy an operational satellite were shown to be possible.

The highly topical subject of satellite constellations has also been examined, with

the associated debris risk to constellation configurations based upon the Iridium™ and Teledesic concepts investigated. Special attention was given to the issue of a chain reaction occurring within the framework of a constellation as a direct result of a constellation satellite or launch vehicle breakup. It was found that the greatest threat to a constellation comes from the collision-induced breakup of one of its satellites, with such an event producing a significant collision probability increase for the constellation in the short-term. In the long-term, the likelihood of a cascade fragmentation occurring within a constellation was found to be remote. Secondary debris impacts were shown to be a real possibility, however, including the possibility of secondary catastrophic fragmentations.

The collision hazard analysis algorithm was validated primarily through the comparison of results with another computer code, the Aerospace Corporation's DEBRIS. This program was developed completely independently to the model presented here and although it addresses the same fundamental problem and does so in a similar fashion, the implementation of the probabilistic continuum dynamics method contains a number of basic differences. Furthermore, the version of DEBRIS used to generate the published results used for comparison does not possess many of the features present in the model developed here. The consideration of atmospheric drag, a direct interface with a non-isotropic cloud model, the use of a cellular target spacecraft representation and impact energy-related damage assessment algorithm, and a built-in satellite constellation facility are all novel advances in the area of debris cloud collision hazard analysis that have been presented in this thesis.

The agreement observed between the two simulation codes provided a good degree of mutual results validation and was well within the bounds of uncertainty introduced by the fragmentation models employed. The simulation of the Clementine/Titan II breakup was a particularly important exercise as this not only represented a real-life fragmentation event for which a collision hazard analysis was performed while the cloud was still fairly young but also a situation where two manned spacecraft were in orbit at the time of the fragmentation and which subsequently encountered the debris cloud. This example showed that modelling breakup

events and the short-term collision hazards they pose is not purely an academic exercise but is a capability which can be required and used in an actual operational spaceflight scenario.

Comparison with the ESA MASTER model showed that the risks associated with debris cloud encounters are markedly different from those experienced from the background environment, in both the magnitudes and the directions of the debris fluxes encountered. The impact velocities and geometries resulting from a cloud-target encounter are highly variable and dependent upon the orbital geometry involved and the severity of the fragmentation. It is shown that the target ram face will not always receive the majority of debris hits.

The calculation of collision probabilities and encounter geometries for the passage of an object through a debris cloud is something that is extremely difficult to validate with real data. Impact data from retrieved spacecraft surfaces offer the only real, tangible, evidence of the orbital debris environment. Up until now, only the LDEF IDE experiment has provided the spatio-temporal resolution of debris impacts necessary to reveal the existence of debris clouds and to enable their orbits to be determined. A subset of this data is used in this thesis to successfully simulate the collision geometry of one of the debris swarms experienced by the IDE, but because the particles are not generated by a fragmentation event as such, only relative fluxes can actually be simulated.

7.6 Further Work

The IDE data provides a valuable and unique spatio-temporal insight into the extreme anisotropy of the near-Earth particulate environment. A significant proportion of the untracked orbital debris population seems to be contained in debris swarms or clouds, with particle densities possibly orders of magnitude higher than the estimated mean. These particles are created by a variety of sources, including spacecraft surface shedding, liquid leakage and solid rocket motor firings. Being able to model such sources of debris in addition to actual 'fragmentation' events would

enable data like that obtained from the IDE experiment, and more recently from Euromir, to be simulated directly. Dealing with very small particles has its difficulties, however, and their large surface area-to-mass ratios would require special attention in orbit propagation, with solar radiation pressure and aerodynamic drag being of considerable importance. The collision hazard analysis algorithm may also need special refinement to cope with the additional orbit perturbation effects introduced. The coupling of a debris generation model with a collision risk assessment tool to directly simulate IDE-type debris swarm impacts is conceptually almost identical to the analysis described in this thesis which focuses upon the debris from breakup events. Indeed, much of the same code could be utilised for such a purpose. Being able to analyse and understand data from spaceflight experiments is extremely important and so such an avenue of work is of particular interest.

Another possible area for future work would be the improvement of the transfer orbit solution procedure used in the collision hazard analysis code. For fragmentation events that produce large debris ejection velocities, and studies that look to compute collision probabilities over days rather than hours for example, long program run times can result due to the number of possible debris orbits that need to be considered. There is no time-scale beyond which the probabilistic dynamics approach should not be used, but simulation run times may themselves be considered to put a limit on the usefulness of the technique. The incorporation of perturbation effects, particularly J_2, into the analytical part of the algorithm would considerably enhance the initial solution estimates passed to the numerical minimisation routine and hence would reduce simulation run times accordingly. Speed of program operation is especially important when considering large satellite constellations.

A final suggestion for an avenue of future work relates to the representation of the target spacecraft and the assessment of impact damage. The use of a more realistic spacecraft model would enable effects such as shielding from solar arrays and deployed antennae to be explored and a more detailed study of the effects of a debris impact on the operation and survivability of the spacecraft to be investigated. The determination of impact damage following a predicted debris encounter essentially

takes the problem full circle. The modelling of debris impacts and explosive fragmentations is fundamental to the whole debris cloud-target satellite collision hazard assessment problem. The use of the best existing breakup models and the continued improvement of the models used is, perhaps, the single most important factor in producing realistic predictions of the collision risks to spacecraft from fragmentation debris.

7.7 Summary

The SDS software suite and the work described in this thesis represents the state-of-the-art in debris cloud modelling. The integrated structure of the software developed enables a wide variety of analyses to be conducted and simulations of both historic and potential future orbital fragmentation events to be performed. Although more work needs to be done in many of the areas examined, several major advances are presented here which should help pave the way to a better understanding of the orbital debris environment and the associated risks to spacecraft which operate within it.

Appendix A

Relative Motion Equations

The relative motion of a debris fragment with respect to its parent locus is examined. The coordinate frame used in this analysis is shown in Figure A.1. The X and Y axes are in the parent orbital plane with the Y axis directed radially and the X axis directed along the local horizontal. The Z axis completes a right-handed triad. (i,j,k) denote unit vectors along the X, Y and Z axes respectively. Point O is the inverse-square force centre, θ is the angular position of the target vehicle and ω is its angular speed.

The motion of the i^{th} particle relative to the parent locus is given by,

$$\frac{d^2\mathbf{R}_i}{dt^2} = \mu[\frac{\mathbf{r}}{r^3} - \frac{\mathbf{r}_i}{r_i^3}], \tag{A.1}$$

where $\mathbf{R}_i$ is the position vector of the i^{th} particle relative to the target, $\mathbf{r}$ and $\mathbf{r}_i$ are the inertial position vectors of the target and i^{th} particle respectively, and μ is the Earth's gravitational constant. $\mathbf{r}$ is given by

$$\mathbf{r} = r\mathbf{j} \tag{A.2}$$

and

$$\mathbf{r}_i = X\mathbf{i} + (Y + r)\mathbf{j} + Z\mathbf{k}. \tag{A.3}$$

where (X,Y,Z) are the coordinates of the particle relative to the parent, i.e.

$$\mathbf{R} = X\mathbf{i} + Y\mathbf{j} + Z\mathbf{k}. \tag{A.4}$$

Using equations (A.1-A.4) and

$$\omega = \dot{\theta}\mathbf{k}, \tag{A.5}$$

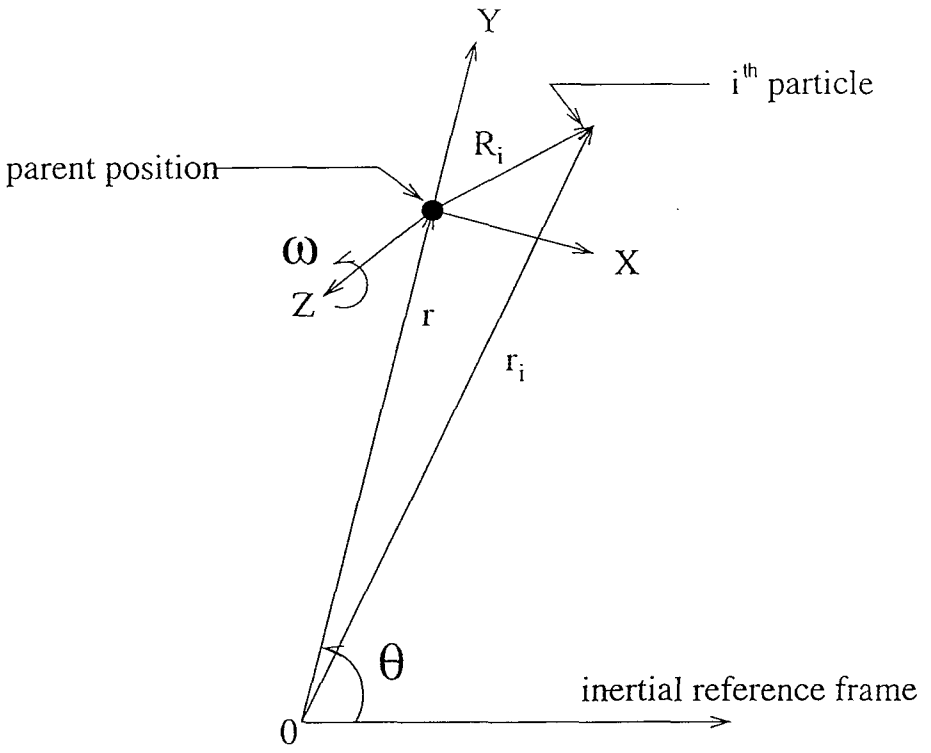

Figure A.1: Coordinate system

the equations of motion of the particle in terms of the rotating coordinate system can be obtained. In scalar form these are,

$$\ddot{X} - Y\ddot{\theta} - 2\dot{Y}\dot{\theta} - \dot{\theta}^2 X + \mu X/r_i^3 = 0, \tag{A.6}$$

$$\ddot{Y} + X\ddot{\theta} + 2\dot{X}\dot{\theta} - \dot{\theta}^2 Y + \mu(-\frac{1}{r^2} + (Y+r)/r_i^3) = 0, \tag{A.7}$$

$$\ddot{Z} + \mu Z/r_i^3 = 0, \tag{A.8}$$

where

$$r_i = [X^2 + (Y+r)^2 + Z^2]^{\frac{1}{2}}. \tag{A.9}$$

It is convenient to introduce the following non-dimensional variables,

$$x = X/a,\ y = Y/a,\ z = Z/a,\ \rho = r/a,\ T = (\mu/a^3)^{\frac{1}{2}}t, \tag{A.10}$$

where a is the semi-major axis of the parent orbit and t is time. In terms of these variables, equations (A.6-A.8) become,

$$x'' - y\theta'' - 2y'\theta' - \theta'^2 x + x/\rho_i^3 = 0, \tag{A.11}$$

$$y'' + x\theta'' + 2x'\theta' - \theta'^2 y - \frac{1}{\rho^2} + (y+\rho)/\rho_i^3 = 0, \tag{A.12}$$

$$z'' + z/\rho_i^3 = 0, \tag{A.13}$$

where

$$\rho_i = [x^2 + (y+\rho)^2 + z^2]^{\frac{1}{2}} \tag{A.14}$$

and primes denote differentiation with respect to T. By assuming that the distance between particle and the parent position is small compared to a, an approximation to the differential equations can be obtained by using the binomial expansion of the denominator function described in equation (A.14). Retaining only the linear and quadratic terms, this leads to,

$$x'' - y\theta'' - 2y'\theta' + [(\frac{1}{\rho^2}) - \theta'^2]x - (\frac{3xy}{\rho^4}) = 0, \tag{A.15}$$

$$y'' + x\theta'' + 2x'\theta' - [(\frac{2}{\rho^2}) + \theta'^2]y - (\frac{3}{2\rho^4})(x^2 - 2y^2 + z^2) = 0, \tag{A.16}$$

$$z'' + \frac{z}{\rho^3} - (\frac{3yz}{\rho^4}) = 0. \tag{A.17}$$

If the parent orbit is nearly circular then the time dependence of the angular rate and the orbit radius can be expressed through the use of series expansions in eccentricity e [127]. In non-dimensional form and retaining only linear terms, these expansions are,

$$\theta' = 1 + 2ecos(T - T_p), \tag{A.18}$$

$$\rho = 1 - ecos(T - T_p) \tag{A.19}$$

where T_p is the normalised time of periapsis passage.

If the non-linear terms are omitted and the parent orbit is circular, equations (A.15-A.17) revert to the Clohessy-Wiltshire (CW) equations [73] (denoted by the subscript c),

$$x_c'' - 2y_c' = 0, \tag{A.20}$$

$$y_c'' + 2x_c' - 3y_c = 0, \tag{A.21}$$

$$z_c'' + z_c = 0. \tag{A.22}$$

Using the initial conditions,

$$x_c(0) = y_c(0) = z_c(0) = 0, \tag{A.23}$$

(i.e. the breakup occurs at the origin of the rotating frame) and

$$x_c'(0) = x_0', \; y_c(0) = y_0', \; z_c(0) = z_0', \tag{A.24}$$

the solution of the CW equations is,

$$x_c = (4sinT - 3T)x_0' + 2(1 - cosT)y_0', \tag{A.25}$$

$$y_c = 2(cosT - 1)x_0' + (sinT)y_0', \tag{A.26}$$

$$z_c = (sinT)z_0'. \tag{A.27}$$

In matrix form, these equations become,

$$[X_c] = [M][X_0'], \tag{A.28}$$

where $[X_c]$ is the particle position vector, $[X_0']$ is the initial velocity vector and $[M]$ is known as the state transition matrix.

This solution can be improved upon by employing the method of differential corrections. By defining δx, δy and δz as follows,

$$x = x_c + \delta x, \; y = y_c + \delta y, \; z = z_c + \delta z, \tag{A.29}$$

and substituting into equations (A.15-A.17), the differential equations governing the variations of δx, δy and δz can be obtained. These equations can be greatly simplified by neglecting the smaller terms, e.g. $x_c\delta x$, $e\delta x$, ex_c^2, e^2y_c. The resulting differential equations are,

$$\delta x'' - 2\delta y' = 3x_cy_c + e[(4y_c' + x_c)cos(T - T_p) - 2y_csin(T - T_p)], \tag{A.30}$$

$$\delta y'' + 2\delta x' - 3\delta y = \frac{3}{2}(x_c^2 - 2y_c^2 + z_c^2) + e[(10y_c - 4x_c')cos(T - T_p) + 2x_csin(T - T_p)], \tag{A.31}$$

$$\delta z'' + \delta z = 3y_cz_c - 3ez_ccos(T - T_p). \tag{A.32}$$

The initial conditions for δx, $\delta x'$, etc, are all zero, because the general initial conditions are satisfied by x_c, y_c and z_c. Since the variation equations are a set of linear differential equations with known 'forcing functions', the determination of the solutions is relatively straightforward. For convenience, the solution can be split into two parts, indicated by,

$$\delta x = \delta x^o + e\delta x^e, \ \delta y = \delta y^o + e\delta y^e, \ \delta z = \delta z^o + e\delta z^e, \tag{A.33}$$

where the superscript o denotes the solution for the circular target orbit case, while the quantities δx^e, δy^e, and δz^e reflect the first-order eccentricity effect on the solution. The solutions are of the form,

$$\begin{aligned}
&\delta x^p = A_0^p + A_1^p sinT + A_2^p cosT + A_3^p sin2T + A_4^p cos2T + A_5^p T + A_6^p T sinT + A_7^p T cosT + \\
&A_8^p T^2, \\
&\delta y^p = B_0^p + B_1^p sinT + B_2^p cosT + B_3^p sin2T + B_4^p cos2T + B_5^p T + B_6^p T sinT + B_7^p T cosT + \\
&B_8^p T^2, \\
&\delta z^p = C_0^p + C_1^p sinT + C_2^p cosT + C_3^p sin2T + C_4^p cos2T + C_5^p T + C_6^p T sinT + C_7^p T cosT + \\
&C_8^p T^2,
\end{aligned} \tag{A.34}$$

where, for convenience, the superscript p can denote either o or e and the A_n^p, B_n^p, C_n^p are constants. The coefficients in the solutions for δx^o, δy^o and δz^o are given by,

$$\begin{aligned}
A_0^o &= -3x_0'y_0' \\
A_1^o &= -10x_0'^2 - 2y_0'^2 - 2z_0'^2 \\
A_2^o &= 2x_0'y_0' \\
A_3^o &= -x_0'^2 + \tfrac{1}{4}y_0'^2 + \tfrac{1}{4}z_0'^2 \\
A_4^o &= x_0'y_0' \\
A_5^o &= 6x_0'^2 + \tfrac{3}{2}y_0'^2 + \tfrac{3}{2}z_0'^2 \\
A_6^o &= 3x_0'y_0' \\
A_7^o &= 6x_0'^2
\end{aligned}$$

$$\begin{aligned}
B_0^o &= 3x_0'^2 - \tfrac{3}{2}y_0'^2 + \tfrac{3}{4}z_0'^2 \\
B_1^o &= -7x_0'y_0' \\
B_2^o &= -5x_0'^2 + 2y_0'^2 - z_0'^2
\end{aligned}$$

$$
\begin{aligned}
B_3^o &= 2x_0'y_0' \\
B_4^o &= 2x_0'^2 - \tfrac{1}{2}y_0'^2 + \tfrac{1}{4}z_0'^2 \\
B_5^o &= 6x_0'y_0' \\
B_6^o &= 6x_0'^2 \\
B_7^o &= -3x_0'y_o' \\
B_8^o &= -\tfrac{9}{2}x_0'^2
\end{aligned}
$$

$$
\begin{aligned}
C_0^o &= \tfrac{3}{2}y_0'z_0' \\
C_1^o &= -x_0'z_0' \\
C_2^o &= -2y_0'z_0' \\
C_3^o &= -x_0'z_0' \\
C_4^o &= \tfrac{1}{2}y_0'z_0' \\
C_7^o &= 3x_0'z_o'.
\end{aligned}
\tag{A.35}
$$

The coefficients for δx^e, δy^e and δz^e are given by the following,

$$
\begin{aligned}
A_0^e &= -3x_0's - \tfrac{1}{2}y_0'c \\
A_1^e &= 6y_0's \\
A_2^e &= 6x_0's + 2y_0'c \\
A_3^e &= 3x_0'c - \tfrac{3}{2}y_0's \\
A_4^e &= -3x_0's - \tfrac{3}{2}y_0'c \\
A_5^e &= -3x_0'c - 3y_0's \\
A_6^e &= -3x_0's \\
A_7^e &= -3x_0'c
\end{aligned}
$$

$$
\begin{aligned}
B_0^e &= -4x_0'c - 3y_0's \\
B_1^e &= -x_0's - 2y_0'c \\
B_2^e &= 2x_0'c + 4y_0's \\
B_3^e &= 2x_0's + y_0'c \\
B_4^e &= 2x_0'c - y_0's \\
B_6^e &= 3x_0'c \\
B_7^e &= -3x_0's
\end{aligned}
$$

$$
\begin{aligned}
C_0^e &= -\tfrac{3}{2} z_0' s \\
C_1^e &= -z_0' c \\
C_2^e &= 2 z_0' s \\
C_3^e &= \tfrac{1}{2} z_0' c \\
C_4^e &= -\tfrac{1}{2} z_0' s
\end{aligned}
\tag{A.36}
$$

where $s = sinT_p$ and $c = cosT_p$. Any coefficients not listed in equations (A.35) and (A.36) are zero. In matrix form the solutions become,

$$
[X] = [X_c] + [\delta X^e] + [\delta X^o] = [M_e][X_o'] + [M2][X2_o'] , \tag{A.37}
$$

where $[X]$ is the resultant particle position vector, $[X_c]$ is the position vector as calculated using CW equations, $[\delta X^o]$ is the differential correction due to second order relative distance terms, $[\delta X^e]$ is the differential correction due to linear eccentricity terms, $[M_e]$ is the eccentricity-modified version of the CW state transition matrix, $[X_o']$ is the initial velocity vector, $[M2]$ is the second order relative distance correction matrix and $[X2_0']$ is a vector of second order initial velocity component products.

Bibliography

[1] S. Vinals-Larruga and R. Jehn. DISCOS User's Manual. Technical report, European Space Agency, European Operations Centre, Darmstadt, Germany, January 1995.

[2] D.S. McKnight (editor). Orbital Debris Monitor (ODM), 1995.

[3] T.Furniss. Dangerous Debris. *Flight International*, pages 34–35, 23-29 November 1994.

[4] H. Klinkrad and R. Jehn. The Space Debris Environment of the Earth. *ESA Journal, Vol.16, No.1*, pages 1–11, 1992.

[5] D.J. Kessler. The Current and Future Environment: An Overall Assessment. In *University of Chicago Symposium on Preservation of Near-Earth Space for Future Generations*, 1992.

[6] H.A.Baker. *Space Debris: Legal and Policy Implications.* Utrecht Studies in Air and Space Law, Martinus Nijhoff Publishers, 1989.

[7] W. Flury. Options for Controlling Orbital Debris. In *First European Conference on Space Debris, Darmstadt, Germany, ESA SD-01*, pages 633–642, 1993.

[8] D. McKnight. Determining the Cause of a Satellite Fragmentation : A Case Study of the Kosmos 1275 Breakup, Paper IAA 87-573, 1987.

[9] W. Flury, G. Janin, R. Jehn, and H. Klinkrad. Space Debris in Elliptical Orbits. In *18th International Symposium on Space Technology and Science, Kagoshima, Japan*, pages 2353–2362, 1992.

[10] D.J. Kessler. Orbital Debris Environment for Spacecraft in Low Earth Orbit. *Journal of Spacecraft and Rockets, Vol.28, No.3*, pages 347–351, May-June 1991.

[11] P. Eichler and D. Rex. Debris Chain Reactions. In *Orbital Debris: Technical Issues and Future Directions, AIAA, NASA and DoD Sponsored Conference, Baltimore, Maryland, NASA CP-10077*, pages 187–195, 1990.

[12] D.J. Kessler. Collisional Cascading : The Limits of Population Growth in Low Earth Orbit. *Advances in Space Research, Vol.11, No.12*, pages 63–66, 1991.

[13] C.R. McInnes. An Analytical Model for the Catastrophic Production of Orbital Debris. *ESA Journal, Vol.17*, pages 293–305, 1993.

[14] R.C. Reynolds and P. Eichler. A Comparison of Debris Environment Projections using the EVOLVE and CHAIN Models. *Advances in Space Research, Vol.16, No.11*, pages 127–135, 1995.

[15] S.Y. Su and D.J. Kessler. Contribution of Explosion and Future Collision Fragments to the Orbital Debris Environment. *Advances in Space Research, Vol.5, No.2*, pages 25–34, 1985.

[16] J.P. Loftus Jr. Orbital Debris Minimisation and Mitigation Techniques. In *18th International Symposium on Space Technology and Science, Kagoshima, Japan*, pages 2389–2396, 1992.

[17] R.D. Lorenz. Space Debris and its Utilisation. In *40th Congress of the International Astronautical Federation, Beijing, China (Paper IAF-ST-89-001)*, 1989.

[18] S.P. Deshpande and S.F. Green. Can Objects in Geostationary Transfer Orbits (GTO) Affect the Debris Population at Low Earth Orbit (LEO). In *Hypervelocity Impacts in Space, University of Kent at Canterbury*, pages 100–106, 1991.

[19] R. Akiba, N. Ishii, and Y. Inatani. Behaviour of Alumina Particles Exhausted by Solid Rocket Motors. In *Orbital Debris: Technical Issues and Future Directions, AIAA, NASA and DoD Sponsored Conference, Baltimore, Maryland, NASA CP-10077*, pages 146–151, 1990.

[20] L. Friesen, A. Jackson, H. Zook, and D. Kessler. Results in Orbital Evolution of Objects in the Geosynchronous Region. In *Orbital Debris: Technical Issues and Future Directions, AIAA, NASA and DoD Sponsored Conference, Baltimore, Maryland, NASA CP-10077*, pages 160–169, 1990.

[21] L. Friesen, A. Jackson, H. Zook, and D. Kessler. Analysis of Orbital Perturbations Acting on Objects in Orbits Near Geosynchronous Earth Orbit. *Journal of Geophysical Research, Vol.97, No. E3*, pages 3845–3863, March 25 1992.

[22] S.H. Vaughan and T.L. Mullikin. Long-Term Behaviour of Inactive Satellites and Debris Near Geosynchronous Orbits. In *AAS/AIAA Spaceflight Mechanics Meeting, Albuquerque, New Mexico, (Paper AAS 95-200)*, 1995.

[23] A.G. Bird. Special Considerations for GEO - ESA. In *Orbital Debris: Technical Issues and Future Directions, AIAA, NASA and DoD Sponsored Conference, Baltimore, Maryland, NASA CP-10077*, pages 152–159, 1990.

[24] V.A. Chobotov. Disposal of Spacecraft at End of Life in Geosynchronous Orbit. *Journal of Spacecraft and Rockets, Vol.27, No.4*, pages 433–437, July-August 1990.

[25] D.S.F. Portree and J.P. Loftus Jr. Orbital Debris and Near-Earth Environmental Management : A Chronology. Technical report, NASA Reference Publication 1320, December 1993.

[26] M. Lambert. Shielding Against Natural and Man-Made Space Debris: A Growing Challenge. *ESA Journal, Vol.17, No.1*, pages 31–42, 1993.

[27] D.S. McKnight and G. Lorenzen. Collision Matrix for LEO Satellites, Paper AIAA 88-4240-CP, 1988.

[28] A. Rossi and P. Farinella. Collision Rates and Impact Velocities for Bodies in Low Earth Orbit. *ESA Journal, Vol. 16*, pages 339–348, 1992.

[29] E.G. Stansbery, D.J. Kessler, T.E. Tracy, M.J. Matney, and J.F. Stanley. Characterization of the Orbital Debris Environment from Haystack Radar Measurements. *Advances in Space Research, Vol.16, No.11*, pages 5–16, 1995.

[30] G. Dittberner and D.S. McKnight. Collision Risk in Sun-Synchronous Low Earth Orbit. *Advances in Space Research, Vol.13, No.8*, pages 187–190, 1993.

[31] M. Beech and P. Brown. Space-Platform Impact Probabilities. *ESA Journal, Vol.18*, pages 63–72, 1994.

[32] M. Beech and P. Brown. Impact Probabilities on Artificial Satellites for the 1993 Perseid Meteoroid Stream. *Orbital Debris Monitor, Vol.8(1)*, pages 9–11, 1 April 1995.

[33] M. Beech, P. Brown, and J. Jones. The Potential Danger to Space Platforms from Meteor Storm Activity. *Quarterly Journal of the Royal Astronomical Society, Vol.36, No.2*, pages 127–152, 1995.

[34] J.A.M McDonnell. The LEO Microparticulate Environment: LDEF's 5.75 Year Perspective on Orbital Debris and Meteoroids. In *First European Conference on Space Debris, Darmstadt, Germany, ESA SD-01*, 1993.

[35] A.F. Whitaker and D. Dooling. LDEF Materials Results for Spacecraft Applications - Executive Summary, NASA CP-3261, March 1995.

[36] S.F. Singer. Orbiting Particle Clouds– Properties, Prevention and Protection. In *First European Conference on Space Debris, Darmstadt, Germany, ESA SD-01*, pages 143–148, 1993.

[37] Long Duration Exposure Facility (LDEF) Archive System (World Wide Web site:- http://setas-www.larc.nasa.gov/setas/ldef.html).

[38] A. Cordelli, A.Rossi, C. Pardini, L. Anselmo, and P. Farinella. Long-Term Evolution of Debris Clouds Generated by Explosions in Earth Orbits. In *Advances in the Astronautical Sciences, Vol.87, Pt 1*, pages 349–366, 1994.

[39] J. Zhang and D.J. Kessler. Orbital Debris and Meteoroid Population as Estimated from LDEF Impact Data. In *LDEF - 69 Months in Space, Third Post-Retrieval Symposium, NASA CP 3275, Pt 1*, pages 373–384, 1993.

[40] A.E. Potter. Small Orbital Debris Measurement : Recent Advances and Future Problems. In *18th International Symposium on Space Technology and Science, Kagoshima, Japan*, pages 2369–2376, 1992.

[41] J. Zhang, D.Rex, and H. Sdunnus. Orbital Debris Model in the Submillimeter Region and its Validation with Impact Data. In *Hypervelocity Impacts in Space, University of Kent at Canterbury*, pages 277–281, 1991.

[42] J.C. Mandeville and L. Berthoud. From LDEF to EURECA: Orbital Debris and Meteoroids in Low Earth Orbit. *Advances in Space Research, Vol.16, No.11*, pages 67–72, 1995.

[43] G. Drolshagen, J.A.M. McDonnell, T. Stevenson, R. Aceti, and L. Gerlach. Post-Flight Measurements of Meteoroid/Debris Impact Features on EURECA and the Hubble Solar Array. *Advances in Space Research, Vol.16, No.11*, pages 85–89, 1995.

[44] D. Steel. The Space Station Will Eat Itself. In *Hypervelocity Impacts in Space, University of Kent at Canterbury*, pages 271–276, 1991.

[45] J.D. Mulholland, S.F. Singer, J.P. Oliver, J.L. Weinberg, W.J. Cooke, N.L. Montague, J.J. Wortman, P.C. Kassel, and W.H. Kinard. IDE Spatio-Temporal Impact Fluxes and High Time-Resolution Studies of Multi-Impact Events and Long-Lived Debris Clouds. In *LDEF - 69 Months in Space, First Post-Retrieval Symposium, NASA CP 3134, Pt 1*, pages 517–527, 1991.

[46] D.S. McKnight. Analysis of Shuttle Window Impact Data. In *Hypervelocity Impacts in Space, University of Kent at Canterbury*, pages 191–195, 1991.

[47] D.L. Talent and F. Vilas. A Space-Based Concept for a Collision Warning Sensor. In *AIAA Space Programs and Technologies Conference, Huntsville, Alabama*, 1990.

[48] F. Vilas, M.F. Collins, P.C. Kramer, G.D. Arndt, and J.H. Suddath. Collision Warning and Avoidance Considerations for the Space Shuttle and Space Station Freedom. In *Orbital Debris: Technical Issues and Future Directions, AIAA, NASA and DoD Sponsored Conference, Baltimore, Maryland, NASA CP-10077*, pages 50–58, 1990.

[49] C. Mazza. *Software Engineering Standards (derived from European Space Agency PSS-5.* Prentice Hall, 1994.

[50] A. Tan, F. Allahdaddi, S. Maethner, and J. Winter. Satellite Fragmentation: Explosion vs Collision. *Orbital Debris Monitor, Vol.6(2)*, pages 8–13, 1 April 1993.

[51] N.L. Johnson and D.S. McKnight. *Artificial Space Debris.* Krieger Publishing, Malabar, Florida, 1991.

[52] G.M. Chernyavskiy, N.L. Johnson, and D.S. McKnight. Identification and Resolution of an Orbital Debris Problem with the Proton Launch Vehicle. In *First European Conference on Space Debris, Darmstadt, Germany, ESA SD-01*, pages 575–580, 1993.

[53] N.L. Johnson. Preliminary Analysis of the Fragmentation of the SPOT-1 Ariane Third Stage. In *Orbital Debris from Upper Stage Breakup, Progress in Astronautics and Aeronautics, Vol.121*, pages 41–106, 1989.

[54] K.G. Henize and R.H. Rast. Potential Spot-1 R/B-Cosmos 1680 R/B Collision. In *Orbital Debris from Upper Stage Breakup, Progress in Astronautics and Aeronautics, Vol.121*, pages 163–165, 1991.

[55] K.G. Henize, C.A. O'Neill, M.K. Mulrooney, and P. Anz-Meador. Optical Properties of Orbital Debris. *Journal of Spacecraft and Rockets, Vol.31, No.4*, pages 671–677, July-August 1994.

[56] G.D. Badhwar and P.D. Anz-Meador. On-Orbit Breakup Characteristics. In *Orbital Debris: Technical Issues and Future Directions, AIAA, NASA and DoD Sponsored Conference, Baltimore, Maryland, NASA CP-10077*, pages 128–137, 1990.

[57] R.R. Dasenbrock, B. Kaufman, and W.B. Heard. Satellite Disintegration Dynamics. In *Advances in the Astronautical Sciences, Vol.33*, pages 73–91, 1975.

[58] W.J. Tedeschi, J.C. Connell, and D.S. McKnight. Development of Orbital Debris Spacecraft Breakup Models. In *AAS/AIAA Astrodynamics Specialist Conference, Durango, Colorado, (Paper AAS 91-366)*, 1991.

[59] W.J. Tedeschi, J.C. Connell, D.S. McKnight, F. Allahdadi, A. Reinhardt, R.D. Hunt, and D.M. Hogg. Determining the Effects of Space Debris Impacts on Spacecraft Structures. *Acta Astronautica, Vol.26, No.7*, pages 501–512, 1992.

[60] D.S. McKnight. Determination of Breakup Initial Conditions. *Journal of Spacecraft and Rockets, Vol.28, No.4*, pages 470–477, July-August 1991,.

[61] A.S. Ganeshan, S.C. Rathnakara, and S. Banerjee. Modelling the Low Earth Space Debris Environment. *Journal of Spacecraft Technology, Vol.4, No.2*, pages 52–59, 1994.

[62] R.C. Reynolds. A Review of Orbital Debris Environment Modelling at NASA/JSC. In *Orbital Debris: Technical Issues and Future Directions, AIAA, NASA and DoD Sponsored Conference, Baltimore, Maryland, NASA CP-10077*, pages 89–109, 1990.

[63] V.A. Chobotov, D.B. Spencer, D.L. Schmitt, R.P. Gupta, D.T. Knapp, and R.G. Hopkins. Dynamics of Debris Cloud Motion and the Collision Hazard to Spacecraft Resulting. Technical Report TOR-0086A(2420-02)-1, SD-TR-88-96, The Aerospace Corporation, El Segundo, California, January 1988.

[64] F. Jonas, K. Yates, and R. Evans. Comparisons of Debris Environment Model Breakup Models, Paper AIAA 93-0166, 1993.

[65] V.A. Chobotov and D.B. Spencer. A Review of Orbital Debris Modelling at the Aerospace Corporation. In *Orbital Debris: Technical Issues and Future Directions, AIAA, NASA and DoD Sponsored Conference, Baltimore, Maryland, NASA CP-10077*, pages 89–109, 1990.

[66] A. Reinhardt, W. Borer, and K .Yates. Long-Term Orbital Debris Environment Sensitivity to Spacecraft Breakup Parameters. *Advances in Space Research, Vol.13, No.8*, pages 207–214, 1993.

[67] R. Madler and R.D. Culp. Sensitivity of the LEO Orbital Debris Environment to Satellite Breakup Parameters. In *AAS/AIAA Spaceflight Mechanics Meeting, Albuquerque, New Mexico, (Paper AAS 95-201)*, 1995.

[68] S.Y. Su. Comments on the Explosion Models from the Equilibrium Density Profile of Small Debris Objects. *Advances in Space Research, Vol.16, No.11*, pages 107–111, 1995.

[69] V.A. Chobotov and D.B. Spencer. Debris Evolution and Lifetime Following an Orbital Breakup. *Journal of Spacecraft and Rockets, Vol.28, No.6*, pages 670–676, November-December 1991.

[70] K.R. Housen. The Short-Term Evolution of Orbital Debris Clouds. *The Journal of the Astronautical Sciences, Vol.40, No.2*, pages 203–213, April-June 1992.

[71] A.B. Jenkin. DEBRIS : A Computer Program for Debris Cloud Modelling. In *44th Congress of the International Astronautical Federation, Graz, Austria, (Paper IAA 93-746)*, 1993.

[72] R. Crowther. Orbital Evolution of Space Debris Due to Aerodynamic Forces. *Advances in Space Research, Vol.13, No.8*, pages 167–170, 1993.

[73] W.H. Clohessy and R.S. Wiltshire. Terminal Guidance System for Satellite Rendezvous. *Journal of Aerospace Sciences, Vol.27*, pages 653–658,674, September 1960.

[74] A.B. Jenkin. Analysis of the Non-Stationary Debris-Cloud Pinch Zone. In *AAS/AIAA Astrodynamics Conference, Victoria, British Columbia, Canada, (Paper AAS 93-625)*, 1993.

[75] D.B. Spencer. The Effects of Eccentricity on the Evolution of an Orbiting Debris Cloud. In *Advances in the Astronautical Sciences, Vol.65, Pt 1*, pages 791–807, 1987.

[76] M.L. Anthony and F.T. Sasaki. Rendezvous Problem for Nearly Circular Orbits. *AIAA Journal, Vol.3, No.9*, pages 1666–1673, September 1965.

[77] D.S. McKnight. A Phased Approach to Collision Hazard Analysis. *Advances in Space Research, Vol.10, No.3-4*, pages 385–388, 1990.

[78] R. Jehn. Dispersion of Debris Clouds From In-Orbit Fragmentation Events. *ESA Journal, Vol.15, No.1*, pages 63–77, 1991.

[79] R. Crowther. Modelling the Short-Term Evolution of Orbital Debris in Circular Orbits. *Journal of Spacecraft and Rockets, Vol.31, No.4, Engineering Notes*, pages 709–711, July-August 1994.

[80] J.W. Frye. Collision Probability Estimate Method For Impact Generated Low Earth Orbit Space Debris Clouds. *Advances in The Astronautical Sciences, Vol.76, Pt I*, pages 287–309, 1991.

[81] R.S. Hujsak. Non Linear Dynamical Model of Relative Motion for the Orbiting Debris Problem. *Journal of Guidance, Control, and Dynamics, Vol.14, No.2*, pages 460–465, March-April 1991.

[82] J.L. Arsenault, K.C. Ford, and P.E. Koskela. Orbit Determination Using Analytic Partial Derivatives of Perturbed Motion. *AIAA Journal, Vol.8, No.1*, pages 4–12, January 1970.

[83] A.B. Jenkin and M.E. Sorge. Debris Clouds in Eccentric Orbits. In *AIAA Space Programs and Technologies Conference, Huntsville, Alabama, (Paper AIAA 90-3903)*, 1990.

[84] W.B. Heard. Dispersion of Ensembles of Non-Interacting Particles. *Astrophysics and Space Science, Vol.43*, pages 63–82, 1976.

[85] W. Kaplan. *Advanced Calculus.* Addison Wesley, Reading, Massachusetts, 1973.

[86] R.S. Hujsak. Dynamical Methods for Calculating Debris Density, Paper AIAA 92-4439-CP, 1992.

[87] R.H. Gooding. A Procedure for the Solution of Lambert's Orbital Boundary-Value Problem. *Celestial Mechanics, Vol.48, No.2*, pages 145–165, 1990.

[88] W.H. Goodyear. Completely General Closed Form Solution for Coordinates and Partial Derivatives of the Two-Body Problem. *The Astronomical Journal, Vol.70, No.3, (Errata Vol.70, p524)*, pages 189–192, April 1965.

[89] A. Jenkin. Personal communication, August 1994.

[90] F.T. Sun, N.X. Vinh, and T.J. Chern. Analytic Study of the Solution Families of the Extended Godal's Time Equation for Lambert's Problem. *The Journal of the Astronautical Sciences, Vol.35, No.2*, pages 213–234, April-June 1987.

[91] N.L. Johnson. History of On-orbit Satellite Fragmentations. Technical report, Teledyne Brown Engineering, Second Edition, February 1986.

[92] M. Rycroft, editor. *The Cambridge Encylopedia of Space.* Cambridge University Press, 1990.

[93] A.E. Roy. *Orbital Motion.* Adam Hilger, 1991.

[94] D.G. King-Hele. *Satellite Orbits in an Atmosphere.* Blackie, 1987.

[95] P.R. Escobal. *Methods of Orbit Determination.* John Wiley and Sons Inc., 1965.

[96] CIRA-72. Cospar International Reference Atmosphere 1972. *Academie Ver-Lag*, Berlin 1972.

[97] T.E. Sterne. *An Introduction to Celestial Mechanics.* Interscience Publishers Inc., New York, 1960.

[98] J. de Lafontaine and S.C. Garg. A Review of Satellite Lifetime and Orbit Decay Prediction. Technical report, University of Toronto, Institute for Aerospace Studies, June 1980.

[99] Y. Kozai. The Motion of a Close Earth Satellite. *The Astronomical Journal*, pages 367–377, 1959.

[100] W.H. Press. *Numerical Recipes : The Art of Scientific Computing.* Cambridge University Press, 1986.

[101] K.J. Ball and G.F. Osborne. *Space Vehicle Dynamics.* Oxford University Press, 1967.

[102] C.J. Brookes and F.C.E. Ryland. Air Density at Heights Near 300km, From Analysis of the Orbit of China 2 Rocket (1971-18b). *Planetary and Space Science, Vol.25, No.11*, pages 1011–1020, 1977.

[103] D.M.C. Walker. The Last 14 Days of Skylab 1 : Orbit Determination and Analysis. *Proceedings of the Royal Society of London, A387*, pages 187–217, 1983.

[104] J.E. White R.R. Bate, D.D. Mueller. *Fundamentals of Astrodynamics.* Dover Publications, 1971.

[105] W.P. Schonberg and R.A. Taylor. Exterior Spacecraft Subsystem Protective Shielding Analysis and Design. *Journal of Spacecraft and Rockets, Vol.27, No.3*, pages 267–274, May-June 1990.

[106] A.G. Williams. A Model for Evaluation of the Hazard to Spacecraft Due to Man-Made Orbital Debris. Master's thesis, Faculty of the University College, Northrop University, Inglewood, California, July 1987.

[107] S.P. Barrows, G.G. Swinerd, and R. Crowther. Assessment of the Short-Term Collision Hazard Resulting from an On-Orbit Fragmentation Event : Polar Platform Case Study. In *AIAA/AAS Astrodynamics Specialist Conference, Scottsdale, Arizona, NASA CP 9411*, pages 265–274, 1994.

[108] S.P. Barrows, G.G. Swinerd, and R. Crowther. The Cascade Fragmentation of a Satellite Constellation. *Advances in Space Research, Vol.16, No.11*, pages 119–122, 1995.

[109] S.P. Barrows, G.G. Swinerd, and R. Crowther. A Comparison of Debris Cloud Modelling Techniques. In *AAS/AIAA Spaceflight Mechanics Meeting, Albuquerque, New Mexico, (Paper AAS 95-187)*, 1995.

[110] R. Crowther, H. Stokes, R. Walker, S. Barrows, and G. Swinerd. Characterisation of the Potential Impact of Space Systems on the Orbital Debris Environment. In *Space Environment, Legal and Safety Issues, Timothy D. Maclay, editor, Proc. SPIE 2483*, pages 88–99, 1995.

[111] S.P. Barrows, G.G. Swinerd, and R. Crowther. Debris Cloud Collision Hazard Analysis : Polar Platform Case Study. *Journal of Spacecraft and Rockets, Vol.32, No.5*, pages 905–911, 1995.

[112] S.P. Barrows, G.G. Swinerd, and R. Crowther. Assessment of Target Survivability Following a Debris Cloud Encounter. In *Proceedings of the 1st International Workshop on Space Debris, Moscow, October 9-11*, 1996.

[113] D.J. Kessler. Orbital Debris Environment for Spacecraft Designed to Operate in Low Earth Orbit. Technical Report NASA TM 100471, April 1989.

[114] R. Crowther. Implications of Space Debris for Constellation Survivability and Design. In *First European Conference on Space Debris, Darmstadt, Germany, ESA SD-01*, pages 565–570, 1993.

[115] W.S.Adams and L.Rider. Circular Polar Constellations Providing Continuous Single or Multiple Coverage Above a Specified Latitude. *The Journal of the Astronautical Sciences. Vol.35, No.2*, pages 155–192, 1987.

[116] B. Pfeiffer, B. Gardini, and J. Cendral. Envisat and the Polar Platform : The Concept and its History. *ESA Bulletin, No.76*, pages 8–13, November 1993.

[117] R.E.Penny Jr and P.A.Swan. Orbital Debris Mitigation the Iridium way, Paper COSPAR 92-B.8-M.55, 1992.

[118] R.E.Penny Jr. Iridium Debris Mitigation Practices. In *First European Conference on Space Debris, Darmstadt, Germany, ESA SD-01*, pages 571–574, 1993.

[119] A. Wilson (editor). *Space Directory 1993-4*. Janes.

[120] J. Ashenberg. Perturbed Volume of Orbiting Debris. *Journal of Spacecraft and Rockets, Vol.31, No.3*, pages 526–528, 1994.

[121] A.B. Jenkin, D.L. Mains, and M.E. Sorge. Debris Study of the Clementine/Titan II Upper Stage Breakup. In *AAS/AIAA Spaceflight Mechanics Meeting, Albuquerque, New Mexico, (Paper AAS 95-199)*, 1995.

[122] H. Klinkrad, H. Sdunnus, and J. Bendisch. Development of the ESA Space Debris Reference Model. *Advances in Space Research, Vol.16, No.11*, pages 93–102, 1995.

[123] H. Klinkrad, W. Flury, H. Sdunnus, and D. Rex. Use of Debris Measurement Data for Verification and Improvement of ESA's MASTER Model. In *Proceedings of the 1st International Workshop on Space Debris, Moscow, October 9-11*, 1996.

[124] H. Sdunnus. Meteoroid and Space Debris Terrestrial Environment Reference Model : Final Report. Technical Report ESOC Contract 10453/93/D/CS, ESA, July 1995.

[125] W.J. Cooke, J.P. Oliver, and C.G. Simon. The Orbital Characteristics of Debris Particle Rings as Derived from IDE Observations of Multiple Orbit Intersections with LDEF. In *LDEF - 69 Months in Space, Third Post-Retrieval Symposium, NASA CP 3275, Pt 1*, pages 361–371, 1993.

[126] J.P. Oliver, S.F. Singer, J.L. Weinberg, C.G. Simon, W.J. Cooke, P.C. Kassel, W.H. Kinard, J.D. Mulholland, and J.J. Wortman. LDEF Interplanetary Dust Experiment (IDE) Results. In *LDEF - 69 Months in Space, Third Post-Retrieval Symposium, NASA CP 3275, Pt 1*, pages 353–360, 1993.

[127] F.R. Moulton. *An Introduction to Celestial Mechanics.* The Macmillan Co., New York, 1914.